ROYAUME DU MAROC
Université Mohammed V - RABAT -
جامعة محمد الخامس – الرباط –
Faculté des sciences
كلية العلوم
CENTRE D'ETUDES DOCTORALES - SCIENCES ET TECHNOLOGIES

N° d'ordre: 3786

THESE

En vue de l'obtention du : ***DOCTORAT***

Structure de Recherche *: Laboratoire de Matière Condensée et Sciences Interdisciplinaires URL-CNRST*
Discipline *: Sciences de la Matière Physique*
Spécialité *: Sciences des Matériaux*

Présentée et soutenue le 17/06/2023 par :

Houda JEBARI

Experimental, DFT, and Monte-Carlo investigations of Sillenite materials: Photocatalysis and photovoltaic applications.

JURY

Abdallah EL KENZ	PES,	Université Mohammed V, Faculté des Sciences–Rabat	Président
Mohammed ABD-LFEDIL	PES,	Université Mohammed V, Faculté des Sciences–Rabat	Rapporteur/Examinateur
Abdelmajid AINANE	PES,	Université Moulay Ismail, Faculté des sciences–Meknès	Rapporteur/Examinateur
Abdeljalil RACHADI	PH,	Université Mohammed V, Faculté des Sciences–Rabat	Rapporteur/Examinateur
Abdelilah BENYOUSSEF	PES, Expert,	Académie Hassan II des Sciences et Techniques–Rabat	Examinateur
Omar ELBOUNAGUI	PH,	Université Mohammed V, Faculté des Sciences–Rabat	Examinateur
Najim TAHIRI	PA,	Université Mohammed V, Faculté des Sciences–Rabat	Invité
M'hamed TAIBI	PES,	Université Mohammed V, Ecole Normale Supérieur–Rabat	Co-Directeur
Hamid EZ-ZAHRAOUY	PES,	Université Mohammed V, Faculté des Sciences–Rabat	Directeur de Thése

Année Universitaire : 2022/2023

✉ Faculté des Sciences, avenue Ibn Battouta, BP. 1014 RP, Rabat–Maroc
☎ 00212 (05) 37 77 18 76 🖷 00212(05) 37 77 42 61; http://www.fsr.um5.ac.ma

Dedication

I dedicate this thesis to:

My grandfathers, grandmother, and uncle (may God have mercy on them),

My dearest mother ***Souad TAHIRI*** *and father* ***Thami JEBARI****, whom I love more than anyone and for the reason of what I become today. I thank you for all that you have given me, for your affection, for your trust and for your continuous presence at my side.*

My beautiful sisters ***Siham****,* ***Kaoutar****, and* ***Safae****, whom I love and who, each in their own way, have contributed to this work.*

My adorable nephews ***Malak****,* ***Amir****,* ***Ghita****, and* ***Soulaymane*** *whom encouraged me, supported me, and gave me good soul throughout my thesis.*

All the members of my family for their affection, their advice and their encouragement which were pleasantly useful to me.

Acknowledgement

This work was carried out at the Laboratory of Condensed Matter and Interdisciplinary Sciences (LaMCScI) of Mohammed V University, Faculty of Science V-Rabat under the supervision of Professor **Hamid EZ-ZAHRAOUY**, PES, and head of the Laboratory of Condensed Matter and Interdisciplinary Sciences (LaMCScI) of the Mohammed V University, Faculty of Science V-Rabat. And under the co-supervision of Professor **M'hammed TAIBI**, PES, and head of the Laboratory of Physico-Chemistry of Inorganic and Organic Materials (LPCMIO) of the Mohammed V University, Ecole Normale Supérieure–Rabat.

I would like to thank almighty **ALLAH** (**SWT**) for giving me the courage, patience, and strength during all these years of study.

I would like to thank all the people who have supported and encouraged me during the preparation of my thesis.

I would like to take this opportunity to express my gratitude. It is my pleasure to express my gratitude to my thesis supervisor, Professor **Hamid EZ-ZAHRAOUY**, for his valuable suggestions, helpful criticism, and effective advice at every stage of my thesis. I hope I was able to prove to him that I deserved his trust and that this work finally meets his expectations.

I would also like to express my sincere thanks and gratitude to my co-supervisor Professor **M'hammed TAIBI** for his precious advice and for the great experience that he has brought to me.

I would like to thank Professor **Abdallah EL KENZ** from Mohammed V University, Faculty of Sciences–Rabat, for being the president of the jury members of this thesis.

I would like to thank Professor **Mohammed ABD-LEFDIL** from Mohammed V University, Faculty of Sciences–Rabat, for reporting and reviewing this thesis.

I would like to thank Professor **Abdelmajid AINANE** from University Moulay Ismail, Faculty of Sciences–Meknés, for reporting and reviewing this thesis.

I would like to thank Professor **Abdeljalil RACHADI** from Mohammed V University, Faculty of Sciences–Rabat, for reporting and reviewing this thesis.

I would like to express my sincere thanks to Professor **Abdelilah BENYOUSSEF** from Mohammed V University, Faculty of Sciences–Rabat, resident member of the Hassan II Academy of Sciences and Techniques Rabat, who did me the honor for reporting and reviewing this thesis.

I am very pleased to express my gratitude to Professor **Omar ELBOUNAGUI** from Mohammed V University, Faculty of Sciences–Rabat, for the very constructive remarks in the theoretical part of my thesis project, and for reporting and reviewing this thesis.

My thanks go also to Professor **Najim TAHIRI** from Mohammed V University, Faculty of Sciences–Rabat, for the relevant remarks in the theoretical part of my thesis work.

I would like to thank the thesis jury for reviewing my work and giving their relevant and useful comments. It is an honor for me that they agreed to judge this work.

I am pleased to express my deepest and most respectful thanks to Professor **Azzam BELAYACHI** from Mohammed V University, Faculty of Sciences-Rabat. His human qualities, his recommendations and his constructive criticism have always been of an indisputable contribution throughout my scientific journey.

I would also like to thank Professor **Abdelmajid ELMANSOURI** from Higher Institute of Audio-visual and Film Professions-Rabat for the Raman, and optical measurements.

My thanks also go to **Mourad BOUJNAH**, Post-Doc at the Centro de Investigación y de Estudios Avanzados del I.P.N. Querétaro, México, for his very constructive remarks in our collaboration in the theoretical studies realized in this project, and for the magnetic measurements.

My thanks also go to Doctor **Lahcen BOUDAD** of the Laboratory of Physico-Chemistry of Inorganic and Organic Materials (LPCMIO) of the University Mohammed V, Ecole Normale Supérieure-Rabat, for his very useful remarks in our collaboration in the experimental investigation realized in this project.

I would also like to thank **Rachida LAMOURI**, research professor at Yeungnam University, Gyeongsan, Republic of Korea, who has supported me since my first year of thesis.

It is with a very strong emotion that I address to all the Professors of the Laboratory of Condensed Matter and Interdisciplinary Sciences (LaMCScI) the expression of my most sincere feelings of gratitude. It was essential for me to be in an optimal work intoxication, not only from the scientific point of view but also relational. I regret that I cannot thank them all individually.

I would like to thank all those who, from near or far, helped me in the realization of this work, as well as all my colleagues of the Laboratory of Physico-Chemistry of Inorganic and Organic Materials (LPCMIO), and my colleagues of the Laboratory of Condensed Matter and Interdisciplinary Sciences (LaMCScI)), to mention only the pleasure that I had to work among them.

Abstract

This thesis presents a combination of experimental and theoretical results on the physicochemical properties of iron sillenite. It is considered a promising candidate for wastewater treatment and/or photodegradation of pollutants and dyes. In addition, we explore the aluminium substitution and the effect of triaxial deformation on the physicochemical properties of $Bi_{25}FeO_{40}$ using experimental and theoretical methods, respectively. Experimentally, we successfully synthesized new $Bi_{25}Fe_{1-x}Al_xO_{40}$ sillenite compounds ($x = 0.00$, 0.20, and $x = 0.50$) at 750°C using the solid state route. Next, we prove the structural stability of $Bi_{25}FeO_{40}$ and $Bi_{25}Fe_{0.80}Al_{0.20}O_{40}$. The pure compound exhibits a structural transition from a cubic-centred phase to a monoclinic ($\gamma \rightarrow \alpha$) phase at high temperatures. This phenomenon was observed by HT–XRD and confirmed by DSC analyses and dielectric measurements. Moreover, this anomaly is also found for $x = 0.20$ and 0.50. Magnetic measurements revealed the antiferromagnetic behavior of $Bi_{25}FeO_{40}$ and $Bi_{25}Fe_{0.80}Al_{0.20}O_{40}$ below T_N. On the other hand, a paramagnetic behavior is observed for $Bi_{25}Fe_{0.50}Al_{0.50}O_{40}$. The optical properties make these materials suitable candidates for photocatalysis and photovoltaic applications. Moreover, the theoretical study based on DFT, and MCs confirms the obtained magnetic and optical results. Theoretically, we prove that $Bi_{25}FeO_{40}$ can also be used for hydrogen production in a basic solution with a pH higher than 11. To evaluate the effect of triaxial deformation on the structural, magnetic, electronic, and electrical properties, we perform a theoretical study using DFT. This allows us to predict the decrease of the electronic bandgap energy, electrical, and thermal conductivities under a compression effect of -3%. On the contrary, the electrical resistivity increases under a traction effect of +3%.

Keywords: Aluminum/Iron Sillenite; Solid-State reaction; Neel temperature; AFM; HT-XRD; FTIR; Raman; DSC; Dielectric; Photodegradation; H_2 production; DFT; MCs; Triaxial strain.

Résumé

Cette thèse présente une combinaison de résultats expérimentaux et théoriques sur les propriétés physicochimiques de la sillénite de fer. Elle est considérée comme un candidat prometteur pour le traitement des eaux usées et/ou la photo-dégradation des polluants et des colorants. En outre, nous explorons la substitution de l'aluminium et l'effet de la déformation triaxiale sur les propriétés physicochimiques de $Bi_{25}FeO_{40}$ en utilisant des méthodes expérimentales et théoriques, respectivement. Expérimentalement, nous avons synthétisé avec succès de nouveaux composés de sillénite $Bi_{25}Fe_{1-x}Al_xO_{40}$ ($x = 0{,}00$, $0{,}20$, et $x = 0{,}50$) à 750°C en utilisant la voie de l'état solide. Ensuite, nous prouvons la stabilité structurelle de $Bi_{25}FeO_{40}$ et $Bi_{25}Fe_{0.80}Al_{0.20}O_{40}$. Le composé pur présente une transition structurelle d'une phase cubique centrée à une phase monoclinique ($\gamma \rightarrow \alpha$) à haute température. Ce phénomène a été observé par XRD-HT et confirmé par des analyses DSC et des mesures diélectriques. En outre, cette anomalie est également constatée pour $x = 0{,}20$ et $0{,}50$. Les mesures magnétiques ont révélé le comportement antiferromagnétique de $Bi_{25}FeO_{40}$ et $Bi_{25}Fe_{0.80}Al_{0.20}O_{40}$ sous T_N. D'autre part, un comportement paramagnétique est observé pour $Bi_{25}Fe_{0.50}Al_{0.50}O_{40}$. Les propriétés optiques font de ces matériaux des candidats appropriés pour la photocatalyse et les applications photovoltaïques. De plus, l'étude théorique basée sur la DFT et les MCs confirme les résultats magnétiques et optiques obtenus. Théoriquement, nous démontrons que $Bi_{25}FeO_{40}$ peut également être utilisé pour la production d'hydrogène dans une solution basique avec un pH supérieur à 11. Afin d'évaluer l'effet de la déformation triaxiale sur les propriétés structurelles, magnétiques, électroniques et électriques, nous réalisons une étude théorique à l'aide de la DFT. Ceci nous permet de prédire la diminution de gap énergétique électronique, du conductivité électrique et thermique sous un effet de compression de -3%. Au contraire, la résistivité électrique augmente sous un effet de traction de +3%.

Mots clés : Sillénite de Fer/Aluminium ; Réaction à l'état solide ; Température de Néel ; AFM ; HT-XRD ; FT-IR ; Raman ; DSC ; diélectrique ; photo-dégradation ; production de H_2 ; DFT ; MCs ; déformation triaxiale.

Résumé détaillé

Les résultats présentés dans ce manuscrit de thèse font partie d'un projet de recherche consacré à l'étude théorique et expérimentale des propriétés physicochimiques de la sillénite de fer. Expérimentalement, l'effet de la substitution de l'aluminium sur les propriétés structurelles, thermiques, diélectriques, magnétiques et optiques de la sillénite de fer a été étudié. Théoriquement, nous explorons les propriétés pertinentes de $Bi_{25}FeO_{40}$ et l'effet de la déformation triaxiale sur leurs propriétés structurelles, magnétiques, électroniques et électriques.

De nouveaux composés de sillénite $Bi_{25}Fe_{1-x}Al_xO_{40}$ ($x = 0.00$, 0.20, et $x = 0.50$) ont été synthétisés en utilisant la voie de réaction à l'état solide. L'analyse de diffraction des rayons X (XRD) indique que tous les matériaux élaborés ont une structure cubique centrée avec le groupe d'espace I23, et l'augmentation des paramètres de maille avec la concentration de l'aluminium est mise en évidence. La morphologie des échantillons est étudiées par microscopie électronique à balayage. L'effet du dopage à l'aluminium a également été étudié par spectroscopie Raman et infrarouge.

Les diagrammes de diffraction des rayons X à haute température (HT-XRD) ont montré que la phase mère présente une transition structurelle d'une phase cubique centrée (γ-$Bi_{25}FeO_{40}$) à une phase monoclinique (α-$Bi_{25}FeO_{40}$) à des températures élevées (au-delà de 700 K). Ce phénomène a également été constaté par l'analyse calorimétrie différentielle à balayage (DSC) et mesures diélectriques à 671 K. De plus, cette transition est également observée pour $x = 0.20$ et 0.50 à 682 et 679 K, respectivement, ce qui est dû à l'apparition d'une relaxation activée thermiquement.

Les mesures magnétiques ont révélé le comportement antiferromagnétique de $Bi_{25}FeO_{40}$ et $Bi_{25}Fe_{0.80}Al_{0.20}O_{40}$ au-dessous des températures de Néel d'environ 268 et 265K, respectivement. Par ailleurs, un comportement paramagnétique est observé pour $Bi_{25}Fe_{0.50}Al_{0.50}O_{40}$. Les bandes d'absorption élevées dans le spectre visible et les énergies directes de la bande interdite comprises entre 2,02 et 2,11 eV.

D'autre part, nous avons exploré les propriétés physiques du sillénite de fer $Bi_{25}FeO_{40}$, à l'aide des calculs ab-initio en se basant sur la théorie de la densité

fonctionnelle (DFT) et la simulation de Monte-Carlo (MC). On a prouvé que $Bi_{25}FeO_{40}$ est un semi-conducteur d'une bande interdite directe de 2,38 eV. Les propriétés optiques du composé étudié mettent en évidence une absorption significative de la lumière dans les régions des longueurs d'onde ultraviolettes et visibles. En plus de son application photo-catalytique pour la dégradation des polluants et des colorants, le matériau $Bi_{25}FeO_{40}$ peut également être utilisé pour la production d'hydrogène dans une solution basique dont le pH est supérieur à 11. Ce matériau présente des propriétés électriques importantes et un comportement antiferromagnétique a également été démontré au-dessous de 255 K, qui est en bon accord avec les résultats expérimentaux.

L'effet de la déformation triaxiale sur les propriétés structurelles, magnétiques, électroniques et électriques de $Bi_{25}FeO_{40}$ a été aussi examiné à l'aide de la DFT. Cette étude a été réalisé pour évaluer la stabilité de la phase mère $Bi_{25}FeO_{40}$ sous contrainte de traction et de compression. Après une déformation compressive de -3% le long de l'axe x, un changement dans le mécanisme d'hybridation s-p entre les orbitales Bi-6s et 6p et les orbitales O-2s et 2p se produit. Cela permet de réduire la valeur énergétique de la bande interdite électronique jusqu'à 1,38 eV. Ceci est dû au changement de la longueur des liaisons entre Bi-Bi, Bi-O1, Bi-O2(i), Bi-O2(ii), Bi-O2(iii) et Bi-O3 sous l'effet de la déformation le long du même axe.

Les conductivités électrique et thermique se comportent de manière similaire sous traction et compression, avec une amélioration sous compression de -3%. En revanche, la résistivité électrique a diminué sous l'effet de la traction de +3 %. Le signe positif du coefficient Seebeck suggère une conduction du matériau à travers des porteurs des charges positive, ce qui permet au $Bi_{25}FeO_{40}$ d'être un semi-conducteur de type P avec et sans effet de déformation. Ceci révèle que la déformation le long des axes x, y et z de -3% à +3% n'a pas d'impact sur le mécanisme de conduction de $Bi_{25}FeO_{40}$, ainsi que sur les propriétés magnétiques, qui restent inchangées sous déformation de traction et de compression.

Les résultats obtenus font des matériaux étudiés des candidats potentiels pour les cellules solaires à colorant (DSSC), ainsi que des photo-catalyseurs prometteurs pour la photo-dégradation des colorants et des polluants, qui peuvent être facilement recyclés et collectés par séparation magnétique.

List of Figures

List of Tables

List of abbreviations

BFO_{40}	$Bi_{25}FeO_{40}$
Bcc	body-centred cubic
PC	photocatalysis process
DSSC	Dye-Sensitized Solar Cells
SSR	Solid-State reaction
XRD	X-ray diffraction
HT-XRD	High temperature X-ray diffraction
FT-IR	Fourier transform infrared
SEM	Scanning Electron Microscopy
DRS	Diffuse Reflectance Spectroscopy
DSC	Differential Scanning Calorimetry
SQUID	Superconducting Quantum Interference Device
M_s	Saturation magnetization
M_r	Remanent magnetization
H	Magnetic field
H_c	Coercive fields
ZFC	zero-field cooled
FC	field cooled
WC	Weiss constant
T_N	Neel Temperature
DFT	Density functional theory
MCs	Monte Carlo simulation

AFM	Antiferromagnetic
FM	Ferromagnetic
DFT	Density Functional Theory
GGA	Generalized Gradient Approximation
LSDA	Local Spin Density Approximation
KS	Khon Sham
MT	Muffin-Tin
APW	Augmented-Plane-Wave
LAPW	Linearized-Augmented-Plane-Wave
FP-LAPW	Full Potential Linearized-Augmented-Plane-Wave
MC_S	Monte Carlo simulation
K_B	Boltzmann constant
D	The relative ratio
DOS	Density of state
BS	Band structure

Content

General introduction

Due to increasing environmental problems and energy deficiencies around the world, the demand for clean and reliable energy conversion technologies has generated great interest worldwide [1,2]. In addition, human and aquatic life has been dangerously affected by wastewater that contains toxic organic dyes from several types of pollutants, such as paint, textiles, cosmetics, and printing [3]. Furthermore, many antibiotics cannot be completely metabolized by human or animal organisms and may be released into wastewater through urinary excretion [4,5]. Additionally, common wastewater treatment methods such as biodegradation, adsorption, flocculation, and coagulation … represent a secondary source of pollutants [6]. The most cost-effective method used for this issue is the photocatalysis process consisting in splitting water using sunlight [5,7].

Semiconductor photocatalysts has shown promise as a technology for removing toxic organic contaminants from water [8]. However, they are applied in powder form, which makes separation and recycling after treatment extremely difficult. This not only results in the loss of the photocatalyst, but also in secondary pollution by photocatalyst particles. The introduction of various magnetic nanoparticles such as magnetite, maghemite, ferrites, and sillenites, etc. into the photocatalyst matrix has recently become an area of intense research, as it allows for easy separation of the photocatalyst from the treated water using an external magnetic field [5,9,10]. Further, this process requires semiconductors with narrow bandgap energy, redshift absorption, and appropriate CB and VB edge positions for the reduction and oxidation reactions [11].

Sillenite materials, with the general formula $Bi_{12}MO_{20}$ (M=Ge, Ti, Ga, Fe, Bi, V, etc.), as new photocatalysts with a high photocatalytic activity, are receiving increasing attention [12]. So far, sillenites such as $Bi_{12}TiO_{20}$, $Bi_{12}SiO_{20}$ [13], $Bi_{24}Ga_2O_{39}$ [14], and $Bi_{24}AlO_{39}$ [15] have reported high photocatalytic properties due to the Bi-O polyhedra in $Bi_{12}MO_{20}$ crystals. The BiO_7 polyhedron results in a dipole moment of 0.174 Debye, which is believed to eliminate electron-hole pair recombination and greatly facilitate the photocatalytic activity of the catalysts.

Among sillenite materials, iron-sillenite $Bi_{25}FeO_{40}$ has attracted much interest due to its physical/chemical properties and technological applications such as gas sensing, digital memory, piezoelectric, photorefractive, photoconductive, and electro-optic properties [16,17]. $Bi_{25}FeO_{40}$ is similar to γ-Bi_2O_3 formed by doping γ-Bi_2O_3 with iron metal oxides; γ-Fe_2O_3 [16]. It is considered as an efficient photocatalyst due to its structure with M = $Bi_{0.5}Fe_{0.5}$, which includes a lot of oxygen and ionic vacancies [18], allowing the reduction of the recombination of electron–hole pairs. Consequently, Fe-doping leads to hybridization of energy levels and modification of the electronic structure, which is responsible for extending the photo-absorptivity to the visible light region (<623 nm) and enhancement of the photocatalytic activity of Fe-doped Bi_2O_3, knowing that Bi_2O_3 has a bandgap energy tends to 2.78 eV [19]. Iron-sillenite has a wide variety of applications, including sensors [20], batteries [21], electrocatalysis for nitrogen fixation via the NRR process (N_2 Reduction reaction) [22], Dye-Sensitized Solar Cells applications (DSSC) [23,24], H_2 production [25], and for environmental pollution remediation, wastewater, and/or water treatment, degradation of pollutants, and dyes using the photocatalysis process (PC) [5,26–38].

The present work is articulated around two main parts, namely a first part devoted to the presentation of an overview of the basic concepts, comprising two chapters. The first one is a generalization of the different notions necessary to understand and interpret the results obtained. The second chapter concerns the description of the various experimental techniques and theoretical methods used in this manuscript. The second part is assigned to the experimental and theoretical obtained results and includes three chapters. Chapter III deals with the synthesis and the study of the structural, vibrational, thermal, dielectric, magnetic, and optical properties of novel sillenite materials $Bi_{25}Fe_{1-x}Al_xO_{40}$. Chapter IV focuses on the theoretical studies of the pristine compound ($Bi_{25}FeO_{40}$), synthesised, and characterised in the previous chapter. Moreover, the last chapter presents the theoretical investigation of the triaxial strain effect on the structural, magnetic, electronic, and electrical properties of iron-sillenite $Bi_{25}FeO_{40}$.

Finally, a general conclusion will summarize the main results of the work presented in this thesis and establish the perspectives that will be realized in the next step.

Part I

Background information

Chapter I

Basic concepts of the magnetic states and bibliography study of sillenite materials

This chapter presents generalities and basic concepts, allowing the reader to fully understand the various notions represented and discussed in this manuscript. In the first section, we focus on the description of sillenite-like materials. Then, we introduce an overview of the iron-sillenite $Bi_{25}FeO_{40}$, specifying its structure, synthesis method, properties, and different applications, which will be outlined in the second section. The last one is devoted to the presentation of the basic knowledge on the magnetic states.

1. Bibliography of sillenite materials

1.1. Introduction

Currently, a lot of research is focused on the study of multifunctional materials, in which several properties can be potentially exploited. Sillenites are known as multifunctional materials because they are applicable in different fields. This type of material is currently attracting considerable interest due to its numerous properties such as photorefraction, photoconduction [39–42]. These properties have potential applications in electro-optics, acoustics, and piezotechnics [39–42]. They are also well known for their physicochemical properties and their technological applications in the fields of sensing and data storage, as well as in other applications related to environmental issues [42–46]. Among the sillenite-based materials, we will focus in this manuscript on the study of the iron-sillenite materials because of their diverse properties.

1.2. Sillenite materials

1.2.1. Introduction

Sillenite is a mineral with the chemical formula of $Bi_{12}MO_{20}$, where, M = Si, Ga, Ge, Mn, Fe [13,42,47,48]. This family of structures is named after the Swedish chemist Lars Gunnar Sillén, who studied it for the first time in 1937. They are found in Australia, Europe, China, Japan, Mexico, and Mozambique. Sillenites refer to a class of bismuth compounds that are isostructural to $Bi_{12}SiO_{20}$, whose parent structure is γ-Bi_2O_3, a metastable form of bismuth oxide Bi_2O_3 [49]. According to M. Devalette et al. the sillenites can be described by the following formula; $Bi_{12-x}M_xO_{20\pm\delta}$, $Bi_{12}(Bi_{4/5-nx}M^{n+}_{5x}\square_{\frac{1}{5}-(5-n)x})O_{19.2+nx}$, and/or $Bi_{12}(Bi_{4/5-nx}M^{n+}_{5x})O_{19.2+nx}$, where M = Group II–VIII elements [13,50]. In addition, V. M. Skorikov et al. reported that sillenites exist only in systems comprising bismuth oxide [50].

1.2.2. Structural description

Based on the phase equilibrium studies of Bi_2O_3-M_xO_y systems, the sillenite phases can be formed at M = Rb, Mg, Zn, Cd, B, Al, Ga, In, Tl, Si, Ge, Ti, Pb, P, V, As, Nb, Cr, Mo, W, Mn, Fe, Co, Ni, Ru, and Ir and their stability depends on the stoichiometry of the regents [50]. Approximately, 60 sillenites compounds with the formula of $Bi_{12-x}M_xO_{20\pm\delta}$, have been synthesised. The M^{n+} cations of $Bi_{12-x}M_xO_{20\pm\delta}$ could take various oxidation degree; 2+ (Cd^{2+}, Co^{2+}, and Zn^{2+}, …), 3+ (Ga^{3+}, Fe^{3+}, and Cr^{3+}, …), 4+ (Si^{4+}, Ti^{4+}, and Mn^{4+}, …), and 5+ (V^{5+}, As^{5+}, and P^{5+}, …) [51–63].

The crystallin structure of $Bi_{12}MO_{20}$ (M ≡ Bi or other metal cations) can be described as MO_4 tetrahedra separated by bismuth oxygen structures, that occupy the octahedral sites and compose a centred–cubic lattice, with the space group of I23 (No.197). As shown in Figure I.1, the tetrahedral sites can be occupied in position 2a by cations with four oxidation states (e.g., Mn^{4+}, Si^{4+}, Ge^{4+}, Ti^{4+}, ...) composing ideal tetrahedral bonds via oxygen. It can be also occupied by other elements with oxidation states different from four, which can be incorporated into the tetrahedral sites via oxygen vacancies, partial occupation of the 2a sites by Bi^{3+} or Bi^{5+} ions, to achieve a charge balance [13,18].

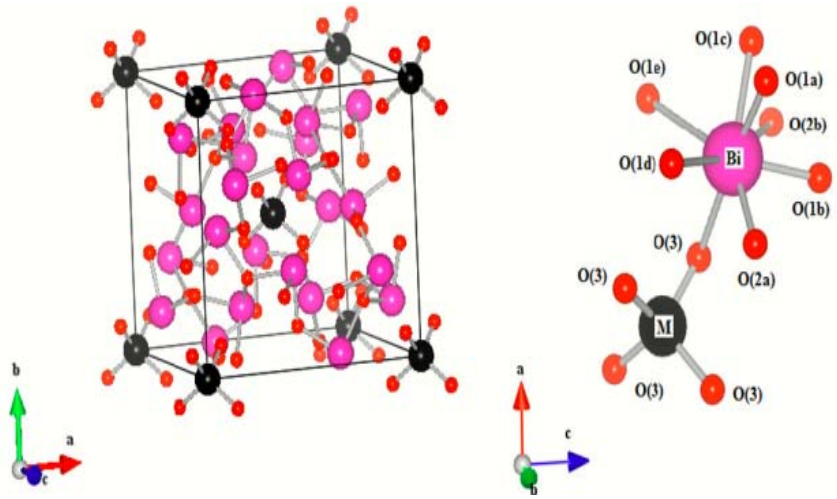

Figure I.1: The crystallin structure of sillenite material; (Octahedral sites occupied by the bismuth oxides and the tetrahedral one occupied with M oxides) [64].

The phase diagram presented in Figure I.2, shows possible combinations between Bi_2O_3 and Fe_2O_3 [13,65,66]. The stoichiometry of Fe^{3+} and Bi^{3+} must be exact and precise. A slight excess of Bi^{3+} will result in the production of bismuth oxide, Bi_2O_3, or the very similar sillenite, $Bi_{25}FeO_{39}$ / $Bi_{25}FeO_{40}$. On the other hand, a surplus of Fe^{3+} will initiate the formation of iron-rich phases such as mullite $Bi_2Fe_4O_9$. Although these secondary phases

are supposed to have little or no impact on the stoichiometry [67]. In the following section, we will make a brief description of the $Bi_{25}FeO_{40}$ structure.

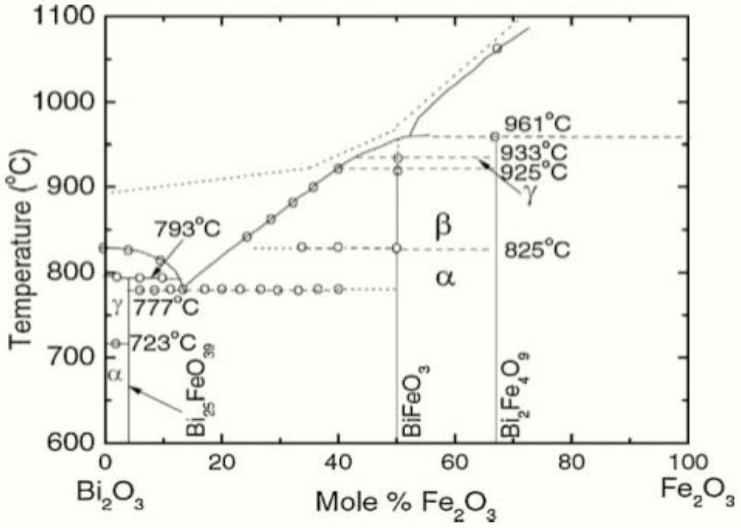

Figure I.2: Diagramme des phases des ferrites de bismuth [64].

2. Iron-sillenite semi-conductor

2.1. Iron-sillenite structure

$Bi_{25}FeO_{40}$ is a sillenite semiconductor, crystallized in a centred–cubic structure, where Fe atoms occupy the tetrahedral site with a 2a-Wyckoff position, while the octahedral sites are filled by Bi atoms with a 24f-Wyckoff position [68]. Iron-sillenite has a lattice parameter of about 10.18 Å and the atomic positions presented in Table I.1 [16,68].

Table I.1: Atomic positions of iron-sillenite $Bi_{25}FeO_{40}$ [68].

	X	*Y*	*Z*	*Wykoff positions*
Bi	*0.17635*	*0.31796*	*0.01409*	*24f*
Fe	*0*	*0*	*0*	*2a*
O1	*0.6346*	*0.7521*	*0.9887*	*24f*
O2	*0.6885*	*0.6885*	*0.6885*	*8c*
O3	*0.8926*	*0.8926*	*0.8926*	*8c*

Overall, an ideal sillenite is characterized by the tetravalence of M atoms, as in Mn^{4+} and Fe^{4+} forming ideal sillenites, such as $Bi_{12}FeO_{20}$ and $Bi_{12}MnO_{20}$ [39,47]. Furthermore,

Valant et al. [69] developed the general formula of sillenite materials, $Bi_{12}(Bi_{4/5-nx}M_{n+5x})O_{19.2+nx}$, describing the possible homogeneity area, depends on the charge of the tetrahedral M^{n+} cations. According to Infante et al. [68] iron-sillenite exhibit two possible chemical formulas; $Bi_{25}FeO_{40}$ and $Bi_{25}FeO_{39}$. Contrariwise, Devalette et al. [13] and Craig et al. [18] revealed that one Bi cation per unit cell exists in the 5+ oxidation state following the formula $Bi_{24}^{3+}(Bi^{5+}Fe^{3+})O_{40}$. Moreover, the octahedral sites are occupied by the Bi^{3+} creating BiO_5E-polyhedrons ($E = 6s^2$ inert electron pair). The tetrahedral sites are shared by Bi^{5+} and Fe^{3+} cations [18].

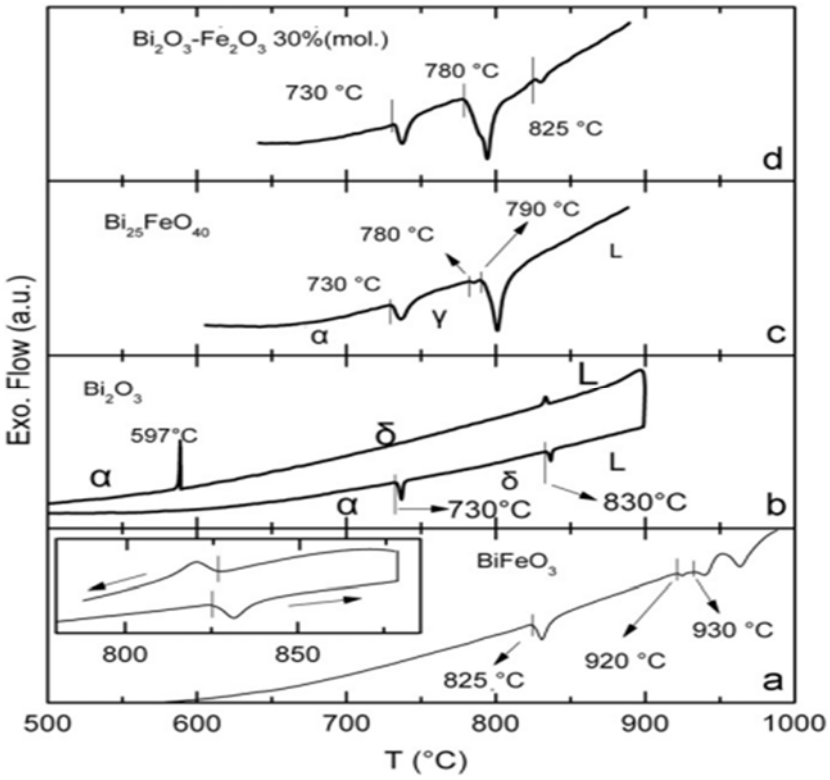

Figure I.3: DSC experiments measured in air, for the possible phase transition of (a) $BiFeO_3$ powder, (b) Bi_2O_3 powder, (c) $Bi_{25}FeO_{40}$ powder and (d)Bi_2O_3–Fe_2O_3 30 mol% mixture [64].

Lu et al. and Harwig report from the DSC measurements (Figure I.3) a phase transition of iron-sillenite from monoclinic phase to the bcc structure at 1030 K (From α-$Bi_{25}FeO_{40}$ to γ-$Bi_{25}FeO_{40}$) was observed under heating. As well as for Bi_2O_3, a phase transition from monoclinic to face-centred cubic phase occurred at 1030 K (from α-Bi_2O_3 to δ-Bi_2O_3). Further, during cooling under the melting point, two types of phase transitions can arise for Bi_2O_3 structure, producing two metastable intermediate phases with a slight temperature difference of about 10 K; from δ-Bi_2O_3 to γ-Bi_2O_3 at 939 K, then from γ-Bi_2O_3

to α-Bi_2O_3 at 904 K and/or from δ-Bi_2O_3 to β-Bi_2O_3 at 950 K, then from β-Bi_2O_3 to α-Bi_2O_3 at 952 K [49,64].

2.2. Synthesis method of iron-sillenite; solid-state reaction (SSR)

The size, morphology, and properties of iron-sillenite is controlled by several criteria: the method of elaboration, the precursors used, the calcination temperature as well as the initial conditions of the synthesis. To optimise those parameters, various synthetic routes were developed such us; solid–state reaction [70,71], sol-gel method [72], hydrothermal method [42], combustion-like process [16], molten salt growth [45], and co-precipitation method [46], allowing the production of $Bi_{25}FeO_{40}$ with a particle size ranging from 25 nm to 10 μm [17,73].

In this thesis, we synthesize $Bi_{25}FeO_{40}$ via the solid–state reaction (SSR) process. This technique presents a set of advantages such as the reduction of toxic waste quantities, the ease of large-scale reproducibility, the reduction of costs, etc … However, obtaining homogeneous phases sometimes requires multiple thermal treatments at high temperature and several intermediate grindings.

The solid–state synthesis protocol can be summarized in four main steps:

- **Choice and preparation of precursors:** in general, the choice of precursors depends on the reaction conditions and the expected nature of the desired product. In some cases, and before being weighed, the reagents must be carefully dried to remove moisture.
- **Mixing of the precursors:** this step allows the homogenization of the mixture, as well as the reduction of the size of the grains, and the increase of their reactivity. Generally, the grinding of powders is carried out either with a mortar or by using laboratory mixing devices.
- **Shaping:** in some cases, and to promote the reactivity of the precursors, the powder is shaped into granules. Uniaxial hydraulic presses are often used for this step.
- **Thermal treatment:** consists in putting the mixture through a thermal cycle under controlled atmosphere. During this step, the reagents react by solid phase diffusion phenomena to compose the desired phase. The thermal treatment depends essentially on the form and the reactivity of the reagents.

2.3. Applications of iron-sillenite semi-conductor

Iron sillenite $Bi_{25}FeO_{40}$ exhibits high absorption in the ultraviolet area (UV), elsewhere in the visible range, with a direct band gap ranging from 1.78 eV to 2.81 eV [16], [66]. These values of bandgap energy values are in good agreement with the criteria for an efficient photocatalyst, which will be discussed in next section (2.4). Moreover, Köferstein et al., Wu et al, and others have reported different magnetic behaviours of iron-sillenite namely; paramagnetic, super-paramagnetic and spin glass state [7,16,74]. These behaviours depend on the synthesis process and/or stoichiometry of this material. Currently, this type of material is attracting great of interest due to the new perspectives for industrial applications it offers. They presents a wide variety of applications, including sensors [20], batteries [21], electrocatalysis for nitrogen fixation via the NRR process (N_2 Reduction reaction) [22], Dye-Sensitized Solar Cells applications (DSSC) [23,24], H_2 production [25], and for environmental pollution remediation, wastewater, and/or water treatment, pollutant and dye degradation using the photocatalysis process [5,26–38]. Recently, many studies have been conducted to investigate the potential properties of $Bi_{25}FeO_{40}$ as a promising photocatalyst, that can be simply recycled and collected by magnetic separation, washed, centrifugated, and dried [30,75–77].

The photocatalytic activity of $Bi_{25}FeO_{40}$ powders has been evaluated by multiple method. As a results, it is considered as an effective compound for photodegradation of rhodamine B (RhB) [25,44,45], for the removal of methylene blue (MB) [30,35,77]. Moreover, it considered as promising photocatalyst for the photodegradation of methyl violet (MV) [33], decoloration of methyl orange (MO) [72,76]. Besides, iron-sillenite is a promising photocatalyst for the degradation of ciprofloxacin (CIP) [35], 2,4-DCP [45], and Acid Yellow (AY-17) [46]. In addition to photocatalytic activity for dye degradation, $Bi_{25}FeO_{40}$ reports an efficient photocatalyst for water treatment from various types of pollutants such as: removal of phenol and p-chlorophenol [36], the tetracycline hydrochloride (TCH) [28], the bisphenol A (BPA) [29], sulfamethoxazole (SMX) [5], the tetracycline (TC) [30].

2.4. The mechanism and bases of photocatalytic water splitting

Photocatalytic performance depends on several parameters that act together to enhance the photocatalytic response. Photocatalysis is an electrochemical process that

consists of the movement of photogenerated electrons and holes between a semiconductor and an electrolyte.

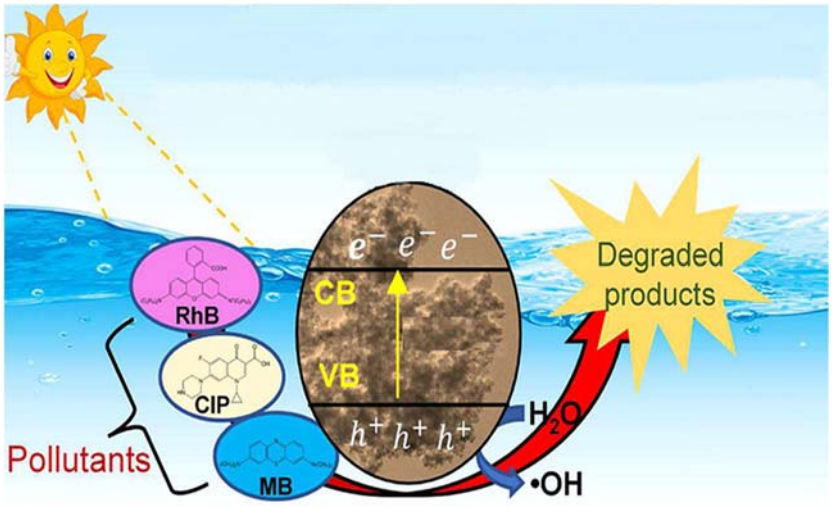

Figure I.4: The photocatalytic mechanism of iron-sillenite $Bi_{25}FeO_{40}$ for colorants and pollution photodegradation, such us ; RhB, CIP, and MB [35].

Figure I.4 illustrates the photocatalytic mechanism implemented in this manuscript; the semiconductor is $Bi_{25}FeO_{40}$, and the electrolyte can be a dye solution such as the RhB, CIP, and/or MB or another pollutant.

Iron-sillenite particles are first distributed in the electrolyte solution (dye and/or pollutant), then after irradiation under sunlight, the electrons in their valence band (VB) are excited towards the conduction band (CB). This is due to the absorption of the visible light by the electrons (e^-–VB). Then the generation of holes (h^+) in the $Bi_{25}FeO_{40}$–VB. In general, an electrolyte in equilibrium possesses one or more redox couples with precise redox potentials. If the potential of the photogenerated electrons of the semiconductor is lower than one of these redox couples, the electrons penetrate in the electrolyte to carry out the reduction of this couple. Similarly, if the photogenerated hole potential of the semiconductor is higher than a redox couple, the holes enter the electrolyte to oxidize it. The reduced and oxidized species can initiate the responsible reaction for degradation of the electrolyte.

As an example, for RhB degradation, the photogenerated e^- react with the surface area adsorbed O_2 to create O_2^- ($E^0_{O_2/O_2^-}$= –0.16 V vs. NHE), which will be an additional reaction of RhB allowing the degradation. Thus, the photocreated h^+ react with the OH^-, produced from ionized water molecules (H_2O) ($E^0_{OH^-/^*OH}$= 2.38 V vs. NHE). Then, the

produced OH^- oxidize RhB. Hence, a photocatalyst must have a CBM lower than –0.16 V to perform the first reaction and VBM greater than 2.38 V to properly conduct the second one. Further, the photogenerated holes can only operate the second reaction [78]. The photocatalytic mechanism of the studied compound for RhB degradation can be described as follow:

$$Bi_{25}FeO_{40} + hv \rightarrow Bi_{25}FeO_{40}\ (h^+) + Bi_{25}FeO_{40}\ (e^-) \quad (I.1)$$

$$h^+ + H_2O \rightarrow {}^*OH + H^+ \quad (I.2)$$

$${}^*OH + RhB \rightarrow H_2O + CO_2 \quad (I.3)$$

Adding to the CBM and VBM levels of the photocatalyst, a lower optical band gap energy, and the absorbance region of the solar light might enhance the PC activity. Moreover, the smaller particle size and higher surface area increase the degradation performance of PC [25,78]. The value of VBM and CBM energies of the photocatalyst can be calculated using following equations:

$$E_{VB} = \chi - E_0 + 0.5E_g \quad (I.4)$$

$$E_{CB} = E_{VB} - E_g \quad (I.5)$$

where, E_{VB} and E_{CB} are the valence band and the conduction band edge potentials, respectively. χ is the absolute electronegativity of a semiconductor, and E_0 is the energy of free electrons on the hydrogen scale ($E_0 = 4.5$ eV) [25]. Otherwise, the relative effective mass ratio (D) of photogenerated electrons and holes is a characteristic parameter that can be used to evaluate the performance of a photocatalyst and estimate the charge separation efficiency [11].

The relative ratio (D) is another parameter that allows the evaluation of the photocatalytic activity. It plays a significant role in photocatalysis and evaluated using the formula described in the equation (I.6). In general, a higher D value means a higher probability of separation of photo-induced electron-hole pairs, and therefore a lower recombination rate to stimulate the photocatalytic activity [79].

$$D = m_h^*(m_0) / m_e^*(m_0) \quad (I.6)$$

3. Magnetic states

To better understand and properly study the magnetic properties of sillenite materials in this part, we will describe in this section the basic knowledge about magnetic states.

As early as 1820, experiments conducted by the Danish physicist and chemist Hans Christian Oersted demonstrated the correlation between magnetism and electrical phenomena, by generating magnetic fields from an electric current [80]. The study of this electricity-magnetism interaction was also carried out by other researchers such as M. Faraday and N. Tesla, leading to the formulation of Maxwell's equations and representing the basic postulates of electromagnetism [81]. However, the understanding of the fundamental nature of magnetism and its origin was only obtained thanks to quantum theory. Indeed, it has been revealed that the magnetic aspect of materials comes from electrons and that the electronic configuration of the ions that compose the material is the basis of its magnetic character. On the other hand, the electromagnetic interaction comes from two sources of magnetism, namely the orbital magnetism due to the movement of electrons around the nucleus producing the orbital magnetic moment and the intrinsic magnetism due to the rotational movements of electrons on themselves inducing the spin magnetic moment (Figure I.5).

The magnetic contributions from these orbital (μ_L) and spin angular moments (μ_S) are expressed as follows [82]:

$$\vec{\mu}_L = -\frac{g_L \mu_B}{\hbar}\vec{L} \quad \text{(I.7)}$$

$$\vec{\mu}_S = -\frac{g_S \mu_B}{\hbar}\vec{S} \quad \text{(I.8)}$$

where g_L and g_S are the orbital and spin gyromagnetic factors, respectively. $\vec{L}$ and $\vec{S}$ are the orbital and spin angular momentum operators, respectively. μ_B is the Bohr magneton and $\hbar$ the reduced Planck constant.

In materials with one or more magnetic atoms, the direction and sometimes even the modulus of the magnetic moments depend on several factors such as the nature and environment of the magnetic ions, the temperature, and the applied magnetic field. Materials can therefore be classified according to their response under the action of an

external magnetic field. This response is evaluated by a quantity χ known as magnetic susceptibility [83] :

$$\vec{M} = \chi \vec{H} \tag{I.9}$$

where,

$$\chi = \frac{\delta M}{\delta H} \tag{I.10}$$

hence, M is the magnetization, H is the magnetic field, and χ is the magnetic susceptibility.

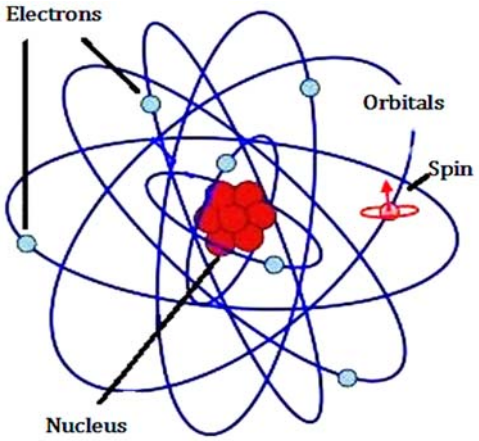

Figure I.5: Schematic illustration of the atom.

In general, magnetic states are classified into disordered magnetic states (diamagnetic, paramagnetic states) and ordered magnetic states (ferromagnetic, antiferromagnetic and ferrimagnetic states).

3.1. Diamagnetic state

When all electrons in a material subjected to a magnetic field, they are oriented in the opposite direction to the applied magnetic field (Figure I.6). Diamagnetic materials are materials that contain only non-magnetic atoms; the magnetization is induced by the applied magnetic field and disappears when this field is no longer present. Since its origin comes from the deformation of electronic orbitals under the action of an external magnetic field. However, the diamagnetic component of magnetic materials is generally small compared to the components of other magnetic orders. Moreover, the susceptibility of diamagnetic materials is independent of temperature (Figure I.7 (b)) [84,85].

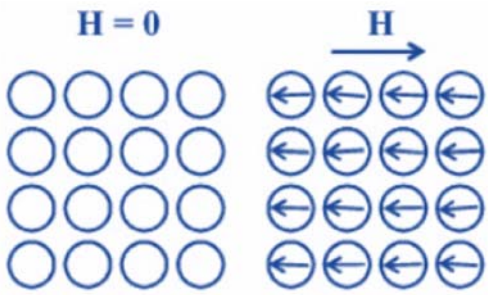

Figure I.6: Magnetic field effect on diamagnetic materials, where the magnetization in the opposite direction to the external magnetic field at H ≠ 0.

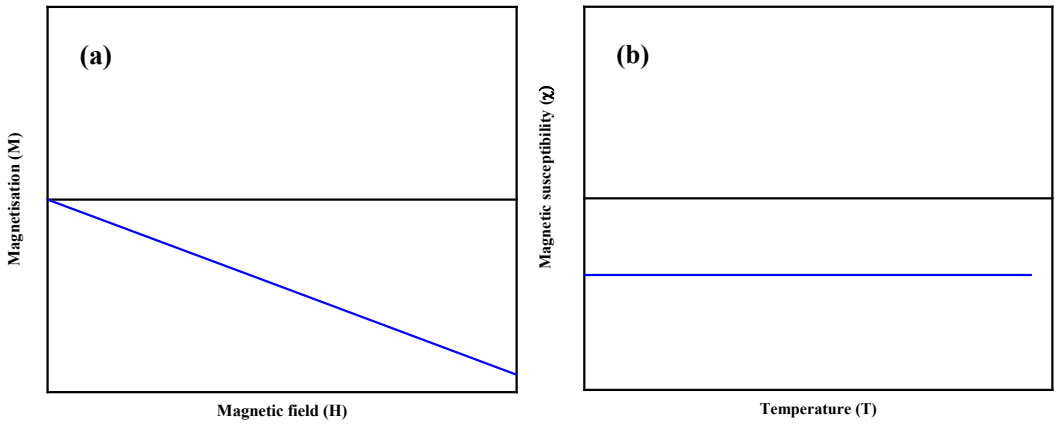

Figure I.7: (a) Variation of the Magnetisation (M) as function of the external magnetic field of diamagnetic materials (H). (b) Thermal evolution of the magnetic susceptibility χ of diamagnetic materials.

3.2. Paramagnetic state

In paramagnetic state, the atoms carry a magnetic moment whose orientation is random. The inter-atomic or inter-molecular distances are larger enough that the moments do not interact with each other. In the absence of an external magnetic field, paramagnetic materials are only subjected to thermal agitation and the overall magnetization is zero. Under the action of an external magnetic field and contrary to diamagnetic materials, the magnetization of paramagnetic materials is oriented in the same direction as the applied field, inducing an increase of the latter. When the exciting field is cancelled, these magnetic moments regain their disorder and compensate on average, so that the total magnetization becomes zero (figure I.8) [86]. On the other hand, as the temperature increases, thermal agitation tends to misalign the moments, reducing the magnetic susceptibility (χ) of the material (Figure I.9). This effect of temperature for

paramagnetic materials is expressed as function of the Curie constant C and the temperature T, by the Curie's law as follow [87]:

$$\chi = \frac{C}{T} \tag{I.11}$$

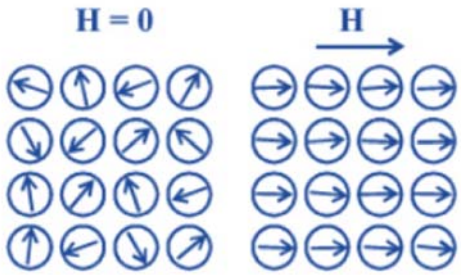

Figure I.8: Magnetic field effect on paramagnetic materials, where the magnetization in the same direction to the external magnetic field at H ≠ 0.

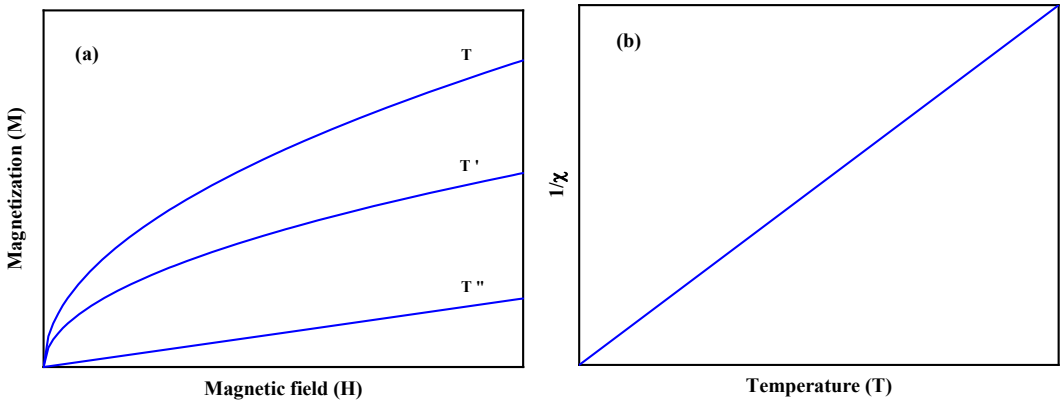

Figure I.9: (a) Variation of the Magnetisation (M) as function of the external magnetic field (H) of paramagnetic diamagnetic materials for (T " > T ' > T). (b) Thermal evolution of the magnetic susceptibility χ of paramagnetic materials.

3.3. Ferromagnetic state

Ferromagnetic materials are characterized by the existence of spontaneous magnetization (SM), which can orient itself along the direction of an applied magnetic field and occur even in the absence of the latter (Figure I.10) [88]. At the microscopic scale, ferromagnetic media are structured into domains of uniform magnetization, known as Weiss domains, separated by Bloch walls [89]. The total magnetization is given by the sum of the magnetizations of the different Weiss domains. When a magnetic field is applied, these Weiss domains progressively change their magnetization as a function of the applied magnetic field, so that domains whose magnetization is oriented in the direction of the applied magnetic field increase at the expense of other domains.

The application of a magnetic field (H) progressively orients the moments in the direction of the field, inducing a hysteretic behavior of the magnetization (M) as a function of the magnetic field (H) [90]. When all the domains are oriented, the saturation magnetization (M_S) is obtained. When the applied field returns to zero, the magnetization decreases to the remanent magnetization (M_r). A certain coercive field (H_C) is then required to bring the magnetization back to zero. By applying a sufficiently strong opposite magnetic field, the magnetization no longer follows the initial trajectory and shows a hysteretic behavior as a function of the external magnetic field (Figure I.11).

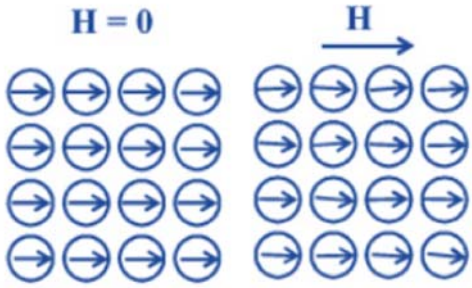

Figure I.10: Magnetic field effect on the ferromagnetic materials, where the magnetization is non null with and/or without applying an external magnetic field ($H \neq 0$ or $H = 0$, respectively).

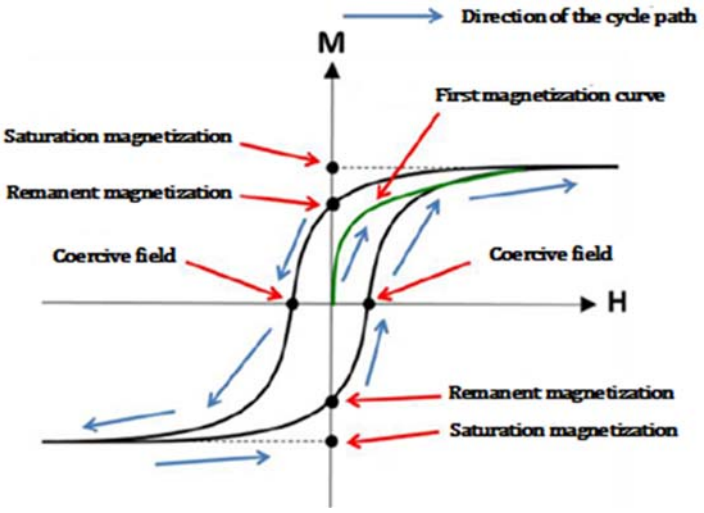

Figure I.11: Schematic illustration of the hysteresis loop of ferromagnetic materials [91].

There are two subgroups of ferromagnetic materials (Figure I.12) [91]: soft and hard ferromagnetism. The first one, is characterized by their remanent magnetization (M_r), their hysteresis loop and their coercive excitation (H_c). Thus, they can react to a weak external magnetic field. On the other hand, hard ferromagnetism presents a significant

hysteresis cycle. Moreover, their remanent magnetization (M_r), their coercive excitation (H_c) and their hysteresis losses are important.

The thermal agitation disorders the magnetic moments as function of the temperature, then the spontaneous magnetization decreases. Above a certain temperature called the Curie temperature (T_c), the spontaneous ferromagnetic magnetization (M_s) becomes zero and the material goes to the paramagnetic state (Figure I.13). The magnetic susceptibility thus follows the Curie-Weiss law [92] :

$$\chi = \frac{C}{T - T_C} \qquad \text{(I.12)}$$

where C is the Curie constant.

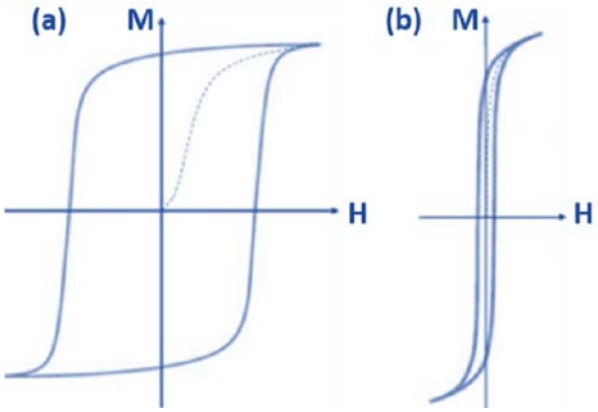

Figure I.12: Hysteresis loops of; (a) hard and (b) soft ferromagnetic materials [92].

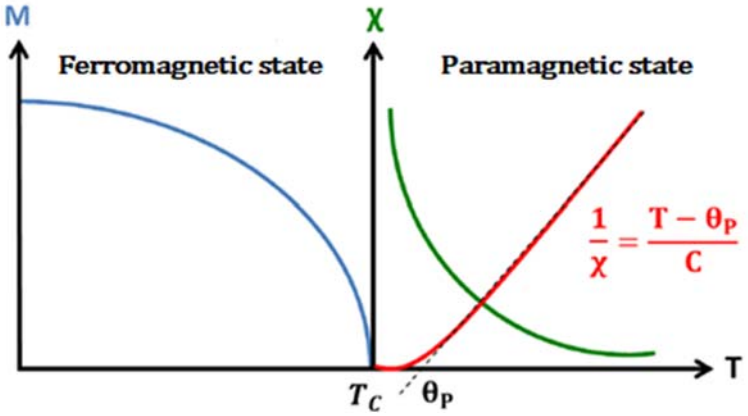

Figure I.13: The thermal evolution of the magnetization M and magnetic susceptibility χ of ferromagnetic materials [92].

3.4. Antiferromagnetic state

In antiferromagnetic materials, the moments interact with each other in such a way as to have an antiparallel alignment with respect to each other and thus a zero overall

magnetic moment (Figure I.14). Indeed, antiferromagnetic materials are formed by two sublattices coupled by negative exchange interactions, oriented antiparallel [84,86].

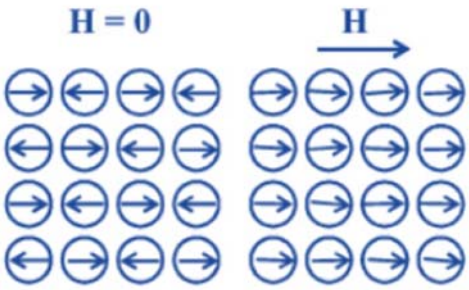

Figure I.14: Magnetic field effect on the antiferromagnetic materials, where the magnetization is null in the absence of the external magnetic field ($M = 0$ for $H = 0$) and it is non null in the presence of the external magnetic field ($M \neq 0$ for $H \neq 0$).

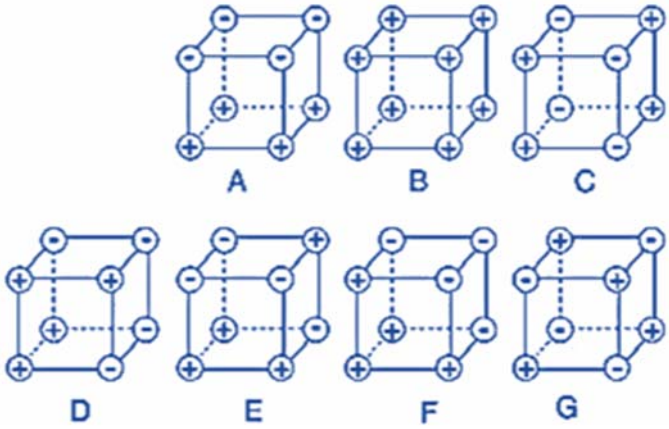

Figure I.15: Schematic illustration of the various types of the antiferromagnetic materials.

According to the number of parallel (FM) and antiparallel (AFM) neighbors of each spin, seven antiferromagnetic structures can be distinguished; Antiferromagnetic order type A (AFM-A), type B (AFM-B), type C (AFM-C), type D (AFM-D), type E (AFM-E), type F (AFM-F), type G (AFM-G) (Figure I.15) [93–100]:

- AFM-A: whose intraplanar coupling is parallel, while the interplanar coupling is antiparallel. Each spin is surrounded by 4 FM neighbors and 2 AFM neighbors (i.e., Antiferromagnetic coupled ferromagnetic plans) [94].
- AFM-B: is a ferromagnetic order as signified above [95].
- AFM-C: in which the atoms have an antiparallel coupling along the same plane and parallel between two planes. Thus, each spin has 2 FM neighbors and 4 AFM neighbors (i.e., ferromagnetically coupled antiferromagnetic plans) [96].

- AFM-D: it is an antiferromagnetic in the diagonals (i.e., AFM in the cross-crossing stripes) [98].
- AFM-E and AFM-F: it is an antiferromagnetic with ferrimagnetic plans [97,99].
- AFM-G: in which the inter and intraplanar couplings are both antiparallel. Therefore, each spin is surrounded by six antiparallel neighbors (i.e., AFM in all directions) [100,101].

In accordance with ferromagnetic materials, the magnetic character of antiferromagnetic systems is influenced by temperature (figure I.16) [102]. In fact, the antiparallel character manifests itself up to a certain critical temperature, known as Neel temperature (T_N), beyond which the magnetic moments become disordered, and the material becomes paramagnetic. In this paramagnetic state, the magnetic susceptibility follows the Curie-Weiss law [103]:

$$\chi = \frac{C}{T + \theta} \tag{I.13}$$

with C is Curie constant and θ a temperature constant below T_N.

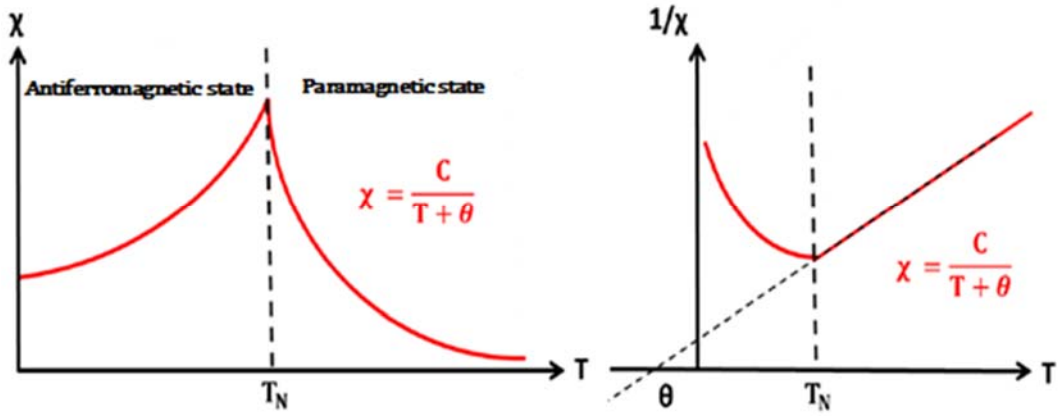

Figure I.16: The thermal evolution of the magnetization M and magnetic susceptibility χ of Antiferromagnetic materials.

3.5. Ferrimagnetic state

As well as for the antiferromagnetic systems, ferrimagnetic materials are characterized by the existence of two sublattices of antiparallel magnetizations, with non-equal magnetic moments. This non-compensation of magnetic moments induces spontaneous magnetization, giving these materials a behavior very similar to that of ferromagnetic materials [103,104].

This antiparallel alignment occurs up to a critical temperature corresponding to the Curie temperature T_C, at which the thermal fluctuations destroy the spin arrangement, and the material passes to the paramagnetic phase (figure I.17). Above T_C, ferrimagnetic materials present a magnetic susceptibility whose thermal variation follows the Curie-Weiss law expressed as follows [105]:

$$\chi = \frac{C}{T - \theta} \tag{I.14}$$

where, C is the Curie constant, T is the temperature and, θ is the Weiss temperature.

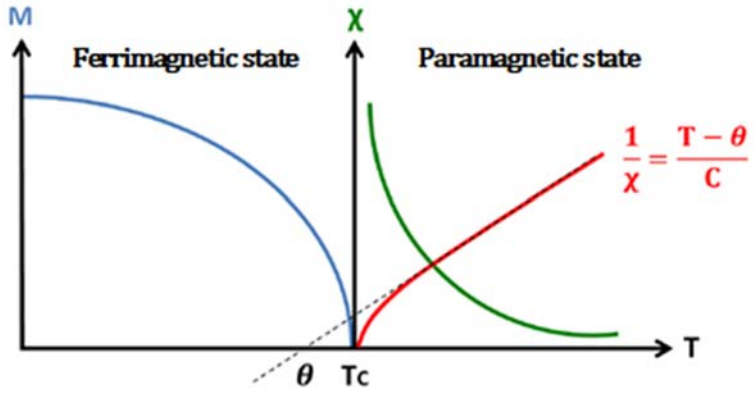

Figure I.17: The thermal evolution of the magnetization M and magnetic susceptibility χ of ferrimagnetic materials.

3.6. Weak ferromagnetism or uncompensated antiferromagnetic

There are antiferromagnetic materials where the magnetic moments of the two sublattices A and B are not perfectly antiparallel and the angle between the magnetization vectors $\vec{M}_A$ and $\vec{M}_B$ has a slight slope with respect to π as mentioned in Figure I.18. This is allowing the appearance of a weak spontaneous magnetization, which well known as weak ferromagnetic behavior.

Although L. Neel explained the appearance of this phenomenon by the presence of stoichiometric defects or ferromagnetic impurities, this hypothesis was definitively abandoned after the observation of a ferromagnetic moment in materials with controlled stoichiometry [106]. Years later, Guiot et al. explained the appearance of a weak spontaneous magnetization based on the presence of imperfections in the crystal lattice [107]. Considering this hypothesis, Dzyaloshinskii al. constructed a model to describe weak ferromagnetism [108]. Then, he introduced an asymmetric term known by the Dzyaloshinskii-Moriya interaction, based on symmetries, which was named after Moriya

when he discovered that the mechanism of this interaction is partly based on the spin-orbit coupling [109,110].

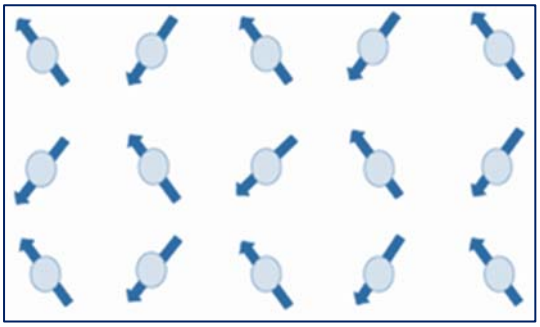

Figure I.18: Schematic illustration of the weak ferromagnetic behaviour in the antiferromagnetic materials.

5. Conclusion

In this chapter, we have implemented the basic concepts necessary to understand the characteristics of sillenite materials as they are considered as a promising photocatalyst for water treatment, pollutant and/or dye degradation.

Chapter II

Experimental and computational methods

In this chapter, we will present an overview of the various experimental techniques and theoretical methods used in this thesis. In the first part, we will present the experimental techniques such as X-Ray diffraction (XRD), Fourier transform infrared spectroscopy (FT-IR), Raman spectroscopy, scanning electronic microscopy (SEM), optical diffuse reflectance spectroscopy (DRS), differential scanning calorimetry (DSC), dielectric, and magnetic measurements. The second part is devoted to the exposition of the basic concepts of the computational methods used in this thesis, namely density functional theory (DFT) and Monte Carlo Simulation (MCs)). A first principal calculation based on density functional theory (DFT) was used to determine the structural, electronic, optical, photocatalytic, electrical, and magnetic properties of the studied materials at 0K. Then, the magnetic properties will be studied at finite temperature using Monte Carlo simulation.

1. Experimental techniques

1.1. X-ray powder diffraction analysis

X-ray diffractometry is an analytical technique in crystallography based on the interaction of the X-rays with the closely spaces lattice of atoms in a crystal. The produced pattern is recorded and then analyzed to reveal the nature of the lattice. This allows us to study and understand the crystallized materials from the collected pattern. From the XRD of the powder's collected pattern, we can quickly identify materials and changes occurred in width or positions of the peaks, determine crystalline size, purity, and texture of the crystals using the Bragg's law [111,112]. This law was developed in 1914, establishes the diffraction relationship between the wavelength of an incoming beam and the d-spacing of a diffracting crystal. A diffraction peak is obtained only when the distance travelled by the rays after reflection from successive crystal planes differs by an integral multiple of wavelengths, according with the Bragg's equation [113].

$$n\lambda = 2d_{hkl} \sin\theta \qquad \text{(II.1)}$$

where n, λ, d_{hkl}, and θ are the order of reflection, the incident X-ray wavelength, the distance between two crystallographic planes (called "interarticular distance), and the incident angle, respectively. This diffractometer with Bragg-Brentano θ–2θ geometry is equipped with an X-ray source using the K_α radiation of copper (Figure II.1). The intensity diffracted by the sample is measured with a scintillation point detector, that moves in concert with the sample and picks up the intensity diffracted by the crystallites in reflection. As the sample rotates by an angle θ, the detector rotates by an angle 2θ so that it is always in the Bragg position relative to the

reticular planes parallel to the sample surface and thus collects the rays diffracted by them [111].

The identification of the phases present in the obtained products is performed by X-ray diffraction powder. The analysis at room temperature is performed with a Shimadzu LabxXRD-6100 diffractometer, equipped with a copper anticathode (λ_{cu} = 1.5406 Å). The allotropic transformations in the pristine compound were checked by X-ray diffraction at different temperatures (500, 700, 900 and 1000 K) using the same equipment. The samples were heated from 300 K to 1000K with a heating rate of 10 K/min and while holding the temperature for 20 min during each recording. The substituted compounds were processed by XRD at room temperature. The cell parameters of the studied compounds were refined by means of AFMPOU software [114].

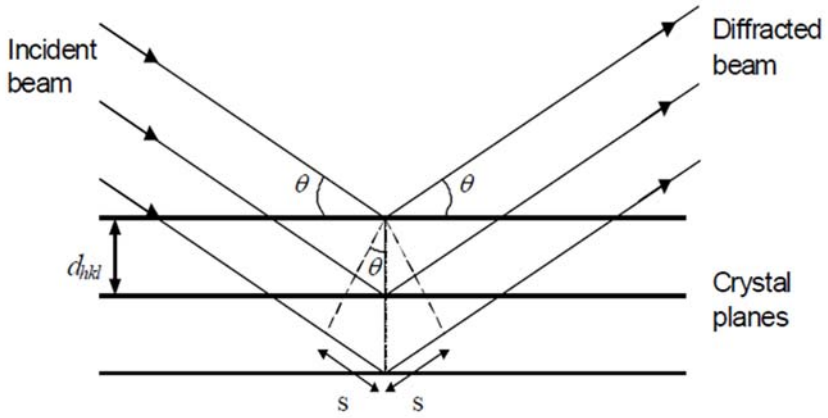

Figure II.1 : Schematic representation of the Bragg-Brentano mode geometry XRD analysis Bragg-Brentano mode (θ–2θ) [115].

1.1. Spectrometric Methods

1.1.1. Fourier transform infrared spectroscopy (FT–IR)

Fourier transform infrared spectroscopy is a technique used to study the interaction between infrared radiation and matter, based on the phenomenon of absorption of incident infrared radiation on the sample (gas, solid or liquid). It allows, through the detection of vibrations characteristic of chemical bonds, to analyse the chemical functions present in the material. Because of the less energetic aspect of infrared light (compared to ultraviolet (UV) or visible light), the energy absorbed by the material does not allow the passage of electrons from one electronic level to another. However, it allows the vibration of bonds between atoms. This

absorption occurs selectively, depending on the vibrations excited in the sample. When the wavelength of the light beam is close to the vibration energy of the molecule, it absorbs the radiation and a decrease in the reflected or transmitted intensity is recorded.

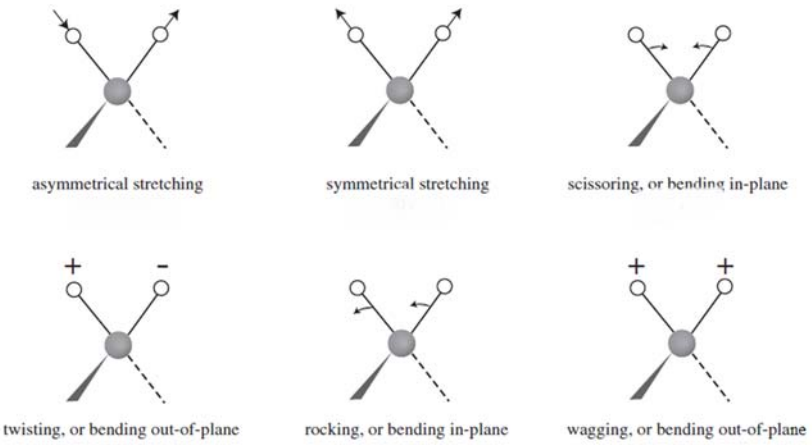

Figure II.2: Main vibration modes of the bonds [116].

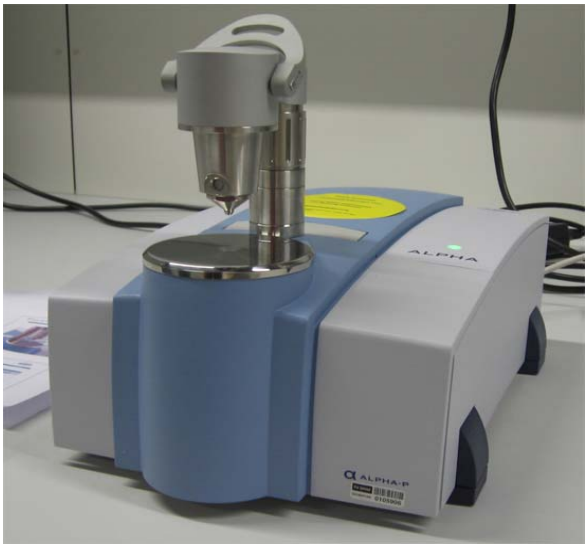

Figure II.3: Infrared spectrometer ALPHA (Platinum–ATR), used for FTIR spectroscopy.

Indeed, each bond has its own oscillation frequency known as resonance frequency. When this bond interacts with an electromagnetic wave having the same frequency, the bond absorbs the radiation and vibrates. This allows us to study the different bonds present in the material. There are several modes of vibration (Figure II.2); stretching (change in the length of a bond), bending (change in the angle between two bonds), Rocking (change in angle between a group of atoms), Wagging (change in angle between the plane of a group of atoms), and Twisting (change in the angle between the planes of two groups of atoms) [114].

Infrared analysis (IR) of the different samples was carried out using a Fourier transform infrared spectrometer (FTIR) of the Bruker Platinum-ATR type operating in transmittance mode, with a spectral measurement range extending from 400 to 4000 cm^{-1} (Figure II.3). The active modes of vibration can be determined using group theory. The position of these absorption bands will depend on the difference in electronegativity of the atoms and their mass.

1.1.2. Raman Spectroscopy

Raman spectroscopy is another vibrational spectroscopic technique based on the inelastic scattering of light by matter which was first discovered in 1928 by Chandrasekhra Venkata Raman [117]. Scattering occurs when an electromagnetic wave encounters a molecule or passes through a lattice. The process of this scattering can be visualized in figure II.4, presenting both the Stokes and anti-Stokes shifts. Raman scattering is characterised by frequencies $v_0 \pm v_m$, where v_0 and v_m are the incident and vibrational frequency of a molecule, respectively. The $v_0 - v_m$ and $v_0 + v_m$ are called Stokes and anti-Stokes scattering, respectively (Figure II.4) [117].

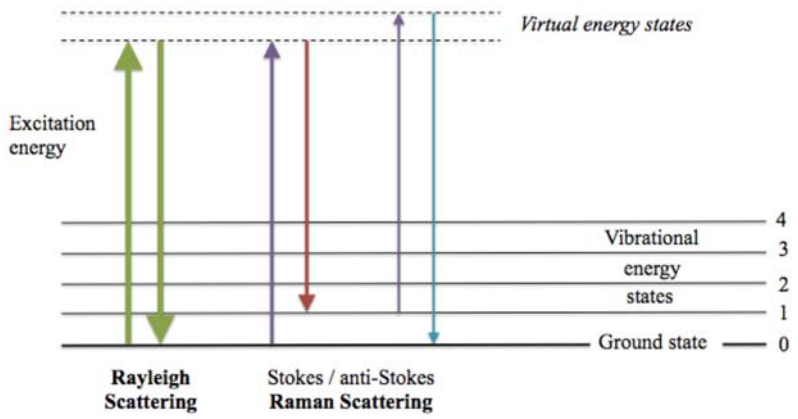

Figure II.4: Energy interactions in Raman scattering (right) and Rayleigh scattering (left). Energy is shifted in Raman scattering due to interactions with vibrational states causing scattered light to return at a slightly different wavelength. The line thicknesses represent the intensity of the signal. Explanations of arrows: green = Rayleigh scattering, purple = Raman Scattering, red = Stokes scattering, and blue = anti-Stokes scattering [118].

A Raman spectrometer measures the vibrational frequency (v_m) as a shift from the frequency of the incident light (v_0) and the observed Raman shift of the Stokes and anti-Stokes scattering is a direct measure of the vibrational energies of the molecules under investigation [117]. In Rayleigh scattering, a photon interacts with a molecule, to further polarise the electron cloud and raise it to a virtual energy state (Figure II.4). The molecule quickly drops back down

to its ground state and a photon is released. Since the molecule drops back to its initial state, the energy released in the photon must be the same as the energy from the initial photon. The frequency and wavelength are therefore the same and since the photon can be released in any direction, scattering is the result. In Raman scattering, a photon loses or gain energy resulting in a changed frequency and wavelength. The vibrational energy levels in the ground state of the molecule controls the energy increase or decrease. When the molecule rises from a ground state to a virtual state and drops back to a (higher energy) vibrational state then the scattered photon has less energy than the incident photon (v_0-v_m), and therefore a longer wavelength. This is called Stokes scattering. When the molecule is positioned in a vibrational state to begin with and drops back to its ground state then the scattered photon has more energy (v_0+v_m), and therefore a shorter wavelength. This is called anti-Stokes scattering.

Raman spectroscopy can analyse solids, liquids, and gases. This technique is considered as a fast technique and a good quality spectrum can be obtained in just a few seconds. It's a non-destructive analysis which allows for further investigation with other analyses, which can generate two- and three-dimensional images of the sample simultaneously. This technic provides subtle information such as crystallinity, phase, intrinsic stress/strain, and polymorphism. However, Raman spectroscopy cannot analyse metals and the induced fluorescence may obscure the Raman spectrum. An accurate database is necessary to interpret the spectrum. Moreover, heating from the laser radiation can destroy the sample or cover the Raman spectrum.

Figure II.5. illustrates the construction of a typical Raman spectrometer. The monochromatic light is beamed through a window and filters lead the light to the sample. Optical filters are used to selectively block Rayleigh scatter whilst allowing Raman scatter to pass through to the spectrometer. A set of mirrors gathers the reflected light from the sample and focus it through the entrance slit to the double grating monochromator. A Charge-Coupled Device (CCD) detects the scattered light, transforms the light into a spectrum, and records the intensity of Raman scattering in arbitrary units by wavelength. This intensity is then normalized by the strongest or most defined peak and can provide a qualitative explanation of the molecular structure. In other words, when a laser is focussed onto a molecule, the molecule starts to vibrate. This vibration is characteristic for the structure of that mineral. The vibration modes change the way the wavelength of light is perceived. If this information is plotted where y-axis represents the intensity of the light and x-axis the wavelength of that light, a specific

pattern occurs. The entire spectral pattern can normally be associated with a specific mineral or a specific substance.

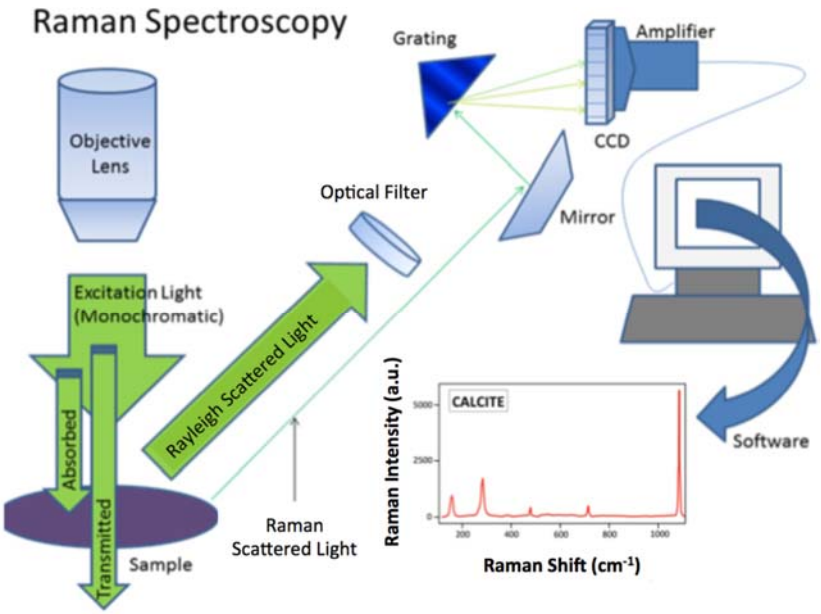

Figure II.5: The construction of a typical Raman spectrometer. A laser is beamed onto the sample and optical filters block Rayleigh scatter whilst allowing Raman scatter to pass to the detector. The result is a Raman spectrum that can provide a qualitative explanation of the molecular structure [118].

1.1.3. Scanning electronic microscopy (SEM)

Scanning electron microscopy (SEM) is an analytical technique that allows the study of the microstructure of materials (in the powder or solid state): shape, porosity, as well as the size, distribution and microcracking of grains. The operation of this microscope is essentially based on electron-matter interactions, using secondary electrons coming from inelastic shocks between bound electrons belonging to the target atoms and incident electrons released by an electron gun through a thermo-ionic emission (Figure II.6). Indeed, an electron beam is generated by a suitable source, in this case a tungsten filament or an electron gun. This electron beam, accelerated by a high voltage, passes through a system of apertures and lenses to produce a thin beam of electrons scanning the surface of the sample. The electrons emitted by the beam are collected by an appropriately placed detector. The coupling of the signal of these secondary electrons released with the scanning of the beam, allows the topographic analysis of the target [119]. The equipment used is a scanning electron microscope Tescan Vega 3, using a voltage of 10 kV [120].

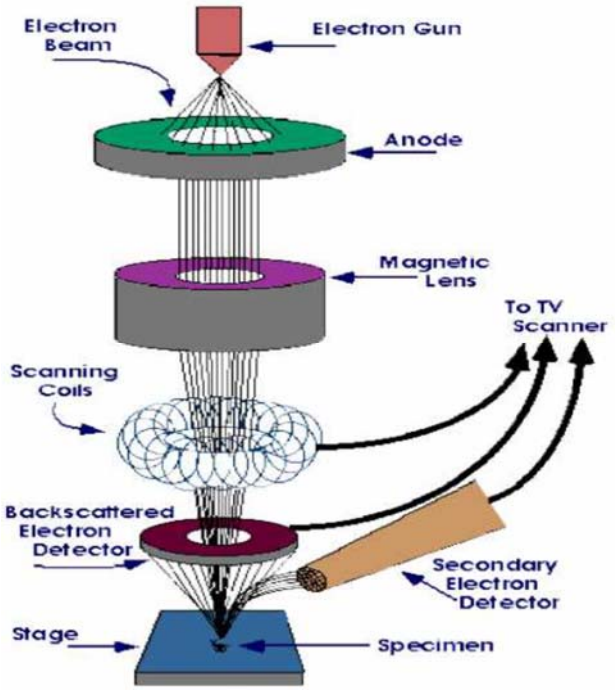

Figure II.6: The schematic illustration of the scanning electron microscopy [119].

1.1.4. Optical Diffuse Reflectance Spectroscopy (DRS)

Diffuse reflectance spectrophotometry (UV-Vis) is a quantitative analysis technique to study the optical properties (absorbance, transmittance, and reflectance) and to observe vibrational, rotational, and electronic transitions of liquids and solids. To measure the global reflectance of a solid sample, the sample is placed behind the integrating sphere. The light coming from the source is reflected by the sample and then by the inner surface of the integrating sphere before reaching the detector. This process allows us to measure the diffuse reflectance of the sample. In addition, the specular reflectance can in turn be obtained from the global and diffuse reflectance data [121]:

$$R_{diffuse} = R_{global} - R_{specular} \quad \text{(II.2)}$$

The spectra were recorded in reflectance mode with respect to the wavelengths, to estimate the nature and the value of the band gap E_g of the different materials synthesized. Optical diffuse reflectance absorption measurements were recorded at room temperature by means of a Specord ®210 Plus–Analytik Jena UV-Visible spectrometer. It is equipped with a 150 mm ILN-925 integrating sphere.

1.2. Differential Scanning Calorimetry analysis (DSC)

Differential Scanning Calorimetry (DSC) is a characterization technique that consists in following the thermal behavior of a given material, by studying the amount of heat released or absorbed when it undergoes physical or chemical transformations. The DSC method consists in determining the enthalpy variation of a sample. This analysis consists of measuring the heat flux necessary to maintain the equality between its temperature and that of an inert reference material. Whose physical properties do not undergo sudden changes along the studied temperature range (figure II.7). Therefore, these variations in heat flux correspond to variations in the specific heat of the sample [122]. DSC measurements were performed using a Setaram121 apparatus. The thermograms were recorded under argon atmosphere over a temperature range of 25–800°C, with a heating and cooling rate of 10°C/min.

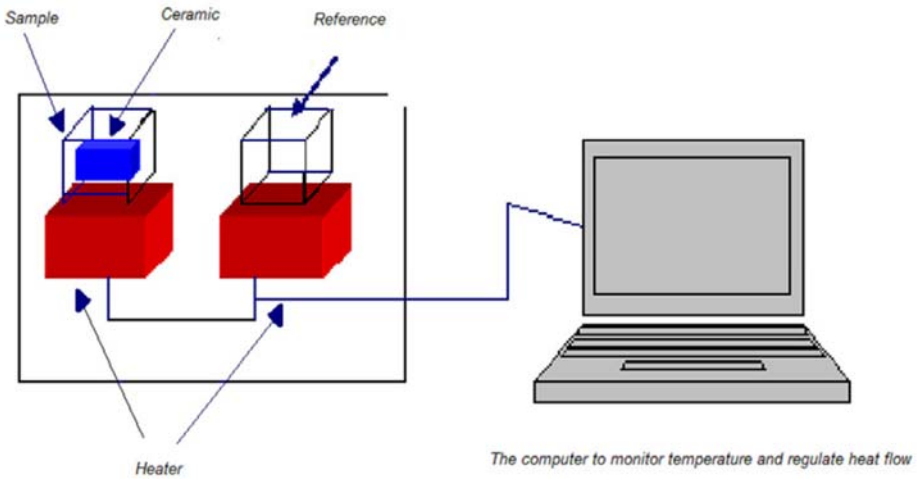

Figure II.7: Schematic dispositive of DSC measurements [122].

1.3. Dielectric Measurements and impedance spectroscopy

1.3.1. Sample preparation

The studied samples were compressed with a hydraulic press to form a pellet and then sintered at a temperature of 600°C. The opposite flat sides of the sample are coated with conductive layers of silver lacquer to create a flat capacitor and provide electrical contact. The dried pellet is placed between two platinum electrodes, connected to wires of the same nature ensuring electrical continuity to the outside of the cell.

1.3.2. Dielectric measurements

The dielectric cell contains a Hewlett Packard 4284A bridge (HP4284A), an oven and a thermocouple. This bridge, characterized by its wide frequency range (20 Hz to 1 MHz), allows to measure a very wide range of capacitance values from pF to several hundred nF while maintaining good accuracy. Dielectric measurements were performed over a wide range of frequencies and the thermal evolution of the dielectric quantities was followed for temperatures between 25 and 525°C at three different frequencies: 10 kHz, 100 kHz, and 1 MHz. Measurements of capacitance (C) and dissipation factor (tan(δ)) allow the determination of the values of the dielectric constant. The dielectric constant is also called relative permittivity (ε'_r) and electrical conductivity (σ). The capacitance C displayed on the measuring bridge is the sum of the sample's own capacitance C_e and that of the vacuum cell C_0:

$$C = C_e + C_0 \tag{II.3}$$

where,

$$C_e = \varepsilon_0 . \varepsilon'_r \frac{S}{e} \tag{II.4}$$

hence,

$$\varepsilon'_r = \frac{e}{\varepsilon_0 S} (C - C_0) \tag{II.5}$$

and,

$$\sigma = 2\pi . f . \varepsilon_0 . \varepsilon'_r . \tan(\delta) \tag{II.6}$$

where, f is the measurement frequency, ε_0 is the dielectric permittivity of vacuum, while S and e are the area and thickness of the sample (pellet) respectively.

1.3.3. Impedance spectroscopy

Impedance spectroscopy (IS) is an experimental technique for studying the electrical characteristics of materials (single crystal, polycrystalline or amorphous). The experimental data contains three variables, namely the real and imaginary electrical component and frequencies, as well as four interrelated electrical response formalisms: impedance (Z*), admittance (Y*), relative permittivity (ε*), and electrical modulus (M*) [123]. Therefore, data can be presented in many formats that highlight the different electrical characteristics of a

sample. The general approach is to apply a voltage to the sample and measure the corresponding response current as the frequency is swept.

The impedance response of a material is usually represented by separate arcs when its real part (Z') is plotted against its imaginary part (Z") (Figure II.8). These arcs represent the different electrical aspects of the sample, so that the low-frequency arc reflects the grain boundary response, while the high-frequency arc represents the grain response. In some cases, another arc, usually attributed to the electrodes, is shown in the low frequency domain. It should be noted that in many materials, the electrical response of the grains and grain boundaries appear as overlapping arcs. The arcs in the impedance response diagram can also be modelled with equivalent circuits. This provides numerical values for the various electrical aspects of a material [124].

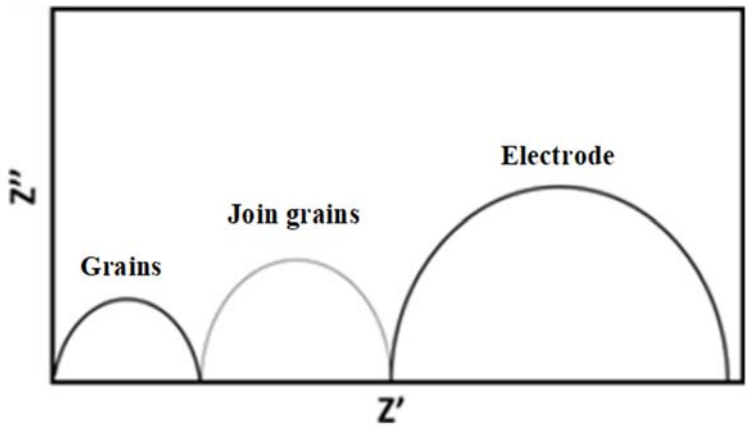

Figure II.8: The three possible impedance response illustration [125].

1.4. Magnetic measurements (SQUID Magnetometer)

Magnetization measurements M(H,T) were performed using a SQUID MPMS3 magnetometer [126], under an applied magnetic field of 100 Oe and 2000 Oe over the temperature range [2 K–400 K]. Likewise, the hysteresis curves were recorded at 10 K and 300 K with a maximum applied field of 4T. This instrument allows the determination of anisotropy and magnetic susceptibility. This apparatus is controlled by a computer system that records the digital data for each successive measurement. During the magnetization measurement, the sample is moved in a homogeneous magnetic field between two detection coils. The measurement is based on the detection of the variation of the magnetic flux induced by an abrupt displacement of the sample parallel to the magnetic field present between the coils. This flux variation is proportional to the magnetic moment per unit mass of the sample, generates

an electromotive force integrated over the whole sample displacement. The schematic of SQUID MPMS3 magnetometer is shown in Figure II.9.

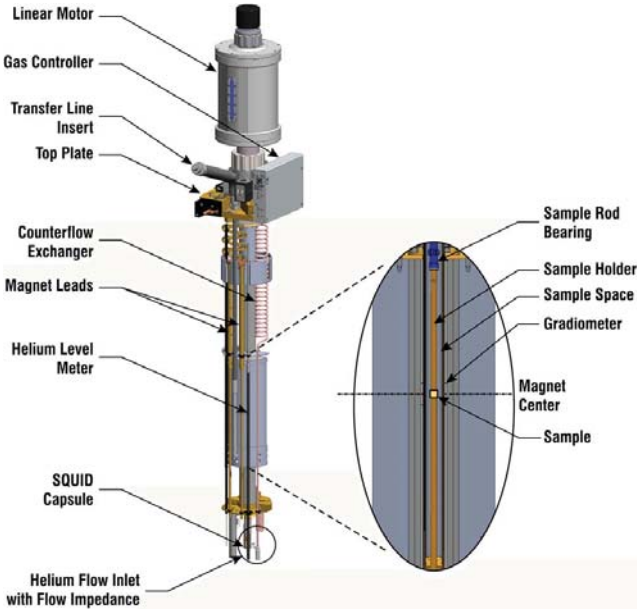

Figure II.9: Schematic diagram of MPMS3 SQUID [127].

2. Computational methods

2.1. Density Functional Theory

2.1.1. Introduction to Density Functional Theory

Density functional theory (DFT) is considered as the most used quantum methods for determination of the physical and/or physicochemical properties of a given system, in the fields of solid state. Systems containing many electrons. The density functional theory DFT was established on the basis of the theoretical formalism and based on the quantum mechanics, proposed by Pierre Hohenberg, Walter Kohn and Lu Sham in the mid-1960s [128,129]. This formalism allows the resolution of Schrödinger equation only for limited number of input data, trough the resolution of electron density instead of the all-electron wave function. In this section, we will present the basis of the functional theory (DFT), and the implemented approximations in the presented thesis. Thus, define the equation that involved in a system made of nuclei and electrons and leading to the development of the Kohn-Sham equation.

2.1.1.1. Schrödinger equation

The Schrödinger equation is a linear partial differential equation that governs the wave function of a quantum-mechanical system. It was established in its primitive form in 1926 by Erwin Schrödinger and was generalized by Paul Dirac just three years later. Paul Dirac [130] has emphasized on the difficulty of solving the equations of quantum mechanics and desirability of developing practical methods of applying quantum mechanics to explain complex systems.

During the same period, Thomas [131] and Fermi [132] proposed a tractable scheme for solving the many-electron problem, in which the electron density *n(r)* is regarded as central variable rather than the wave function, and the total energy of a system is written as a functional $E_{TF}[n(r)]$. This Thomas-Fermi model is viewed as the predecessor to modern DFT [132]. However, its accuracy is limited by the errors due to the inaccurate representation of kinetic energy, exchange energy, and the complete neglect of electron correlation. In the subsequent decades, physicists made great efforts on solving Schrödinger-type equations with local effective potentials and enhancing several numerical methods [133–136], that have been critical for carrying out density functional calculations. The famous Kohn-Sham equation was created by Kohn and Sham since 1965, to execute the DFT [137]. To resolve this equation for a complex system, the Kohn-Sham equation allowing the reduction to a tractable problem of non-interacting electrons moving in an effective potential. Which can lead to an explanation of the main features of complex atomic systems without too much computation.

The Schrödinger equation is a differential equation, describes the representation of the wave function Ψ of a quantum particle's motion under the influence of an external potential V(r). The external potential might be the Coulomb electrostatic potential due to the nuclei of the atoms. It is described via the following equation:

$$\widehat{H}\psi(\vec{r},t) = -i\hbar\frac{\partial\psi(\vec{r},t)}{\partial t} \qquad \text{(II.7)}$$

where $\psi(\vec{r},t)$ is the wave function and $\widehat{H}$ is the Hamiltonian of the system:

$$\widehat{H} = -\frac{\hbar^2}{2m}\nabla^2 + \widehat{V}(\vec{r},t) \qquad \text{(II.8)}$$

hence, $-\frac{\hbar^2}{2m}\nabla^2$ corresponds to the kinetic energy term and $\widehat{V}(\vec{r},t)$ to the external potential. In our case, we will use the stationary equation [138], which for a system with N electrons and M nuclei, is written as follows:

$$\hat{H}\psi_i(\vec{r}_1, \vec{r}_2, \ldots \vec{r}_N, \vec{R}_1, \vec{R}_2, \ldots \vec{R}_M) = E\psi_i(\vec{r}_1, \vec{r}_2, \ldots \vec{r}_N, \vec{R}_1, \vec{R}_2, \ldots \vec{R}_M) \quad \text{(II.9)}$$

And $\hat{H}$ is the Hamiltonian operator of the system. The coordinates $\vec{r}_i$ and $\vec{R}_i$ collect the space and spin variables of the electron i and nucleus k, respectively. The Hamiltonian operator $\hat{H}$ can be decomposed as:

$$H_{Total} = T_n + T_e + V_{nn} + V_{ne} + V_{ee} \quad \text{(II.10)}$$

where T_n and T_e correspond to the kinetic energy of the nuclei and the electrons, respectively. V_{nn}, V_{ne} and V_{ee} represent the potential energy of the electrostatic energy between nucleus-nucleus, nucleus-electron, and electron-electron, respectively. Considering the high number of degrees of freedom (3 N+3 M) and interactions involved in three-dimensional multi-body problems, their exact processing proved to be an impossible task. In view of the impossibility of finding an exact solution to equation (II.10) in the case of N-body poly-electronic systems, it is necessary to use simplifying approaches.

2.1.1.2. Born-Oppenheimer approximation

The Born-Oppenheimer approximation assumes that the motion of electrons can be decoupled from that of nuclei, under the assumption that electrons are lighter and much faster, and a first approximation takes into account an evolution of electrons in a potential created by fixed atoms [138,139]. The nuclear wave function can be described as:

$$\psi(\vec{r}, \vec{R}) = \psi_n(\vec{R})\psi_e(\vec{r}, \vec{R}) \quad \text{(II.11)}$$

Which means that the Hamiltonian of the equation (II.10) can written as:

$$H_{Total} = T_e + V_{ne} + V_{ee} \quad \text{(II.12)}$$

Allowing the elimination of all Hamiltonian terms involving the nuclei. However, this is not enough to solve the Schrödinger equation due to the complexity of the electron-electron interactions. For this reason, we often found that Born-Oppenheimer coupled to the Hartree approximation.

2.1.2. Hartree-Fock approximation

This approximation is considered as the basis of almost all ab initio methods. The exact solution to the equation (II.9) can only made the hydrogen atom. This is attributed to the absence of the multiple coulombic repulsion terms present in the polyelectronic system. To

avoid this drawback, the Hartree approximation, that considered the first approximation studied the multi-electron wave function as the product of single-particle (single-electron) functions, designated by the term (orbital). The wave function of the system is described as follow:

$$\psi_i(\vec{r}_1, \vec{r}_2, \vec{r}_3 \dots \vec{r}_N) = \psi_i(\vec{r}_1).\psi_i(\vec{r}_2).\psi_i(\vec{r}_2) \dots \psi_i(\vec{r}_N) \quad \text{(II.13)}$$

Coulombic repulsion is considered as an average effect and each electron is treated independently but in an effective potential determined by integration over the wave functions of the other electrons. Thus, the Hartree approximation is a mean-field approximation replacing the complicated many system problem by simple problems in a mean-field potential [140]. However, as the electron is a fermion, the total wave function must be antisymmetric with respect to the exchange of any two particles, which is neglected by Hartree approximation.

To overcome this issue, the Pauli exclusion principal is taking in account and implemented in the Hartree-Fock approximation [141–143]. In this approximation, the multi-electronic wave function is expressed as a Slater determinant constructed from N single-electronic wave functions ψ_i.

$$\psi(x_1, x_2, x_3 \dots, x_N) = \frac{1}{\sqrt{N!}} \begin{bmatrix} \psi_1(x_1) & \psi_2(x_1) & \dots & \psi_N(x_1) \\ \psi_1(x_2) & \psi_2(x_2) & \dots & \psi_N(x_2) \\ \vdots & \vdots & \ddots & \vdots \\ \vdots & \vdots & & \vdots \\ \psi_1(x_N) & \psi_2(x_N) & \dots & \psi_N(x_N) \end{bmatrix} \quad \text{(II.14)}$$

where $\frac{1}{\sqrt{N!}}$ is a constant of normalization.

This approximation is appropriate for resolving the Schrödinger approximation, exclusively for molecular physics. While it can only handle simple systems with few electrons, like small molecules [144]. It does not consider electronic correlations effects, whilst the treatment of large systems such as solids remains difficult to apply. Indeed, the ground state corresponds to a global minimum over a much larger set of functions than the one covered by a Slater determinant. Nevertheless, it is shown that the ground state is approached progressively by writing it as a sum of Slater determinants. This would make the calculation numerically very heavy. For this reason, the density function theory is often used, because of its computational simplifications.

2.1.3. Principle of density functional theory

The solution of the Schrödinger equation containing N-electrons must be treated with coarse methods to adequately reproduce the physical quantities containing the most information. However, it is possible to recompose the problem using appropriate theorems and approaches. Currently, density function theory would have attracted much interest, if not for the context of the theorem established by Kohn-Sham, which made it useful along with ground state functional approaches to describe real multi-electronic systems. The idea of this theory originated in the work of Thomas and Fermi in 1927 [128,145]. However, their approaches are not sufficiently adapted to electronic structure calculations.

This approach clarifies the basis of DFT. Earlier, Thomas and Fermi excluded the interactions between electrons, considering the system as a homogeneous gas and its kinetic energy as a function of the local density. The two authors ignored the exchange correlation defects that appear between electrons. However, this defect was rectified by Dirac in 1930 [146], who introduced the local exchange approach. The main objective of DFT is to determine the ground state properties of a given system composed of a fixed number of electrons interacting with nuclei using only information about the electron density ρ. Thus, we must first establish what the electron density of the system is to determine its ground state properties.

2.1.3.1. Hohenberg-Kohen theorems

Far from the Hartree-Fock approach where the energy of the system depends on the wave function, the density function theory expresses the energy as a function of the electronic density. This procedure simplifies the solution of the Schrödinger equation. The density functional theory was developed in 1964 and 1965, with the publications of Hohenberg and Kohn [147,148]. The two theorems are as follows:

Theorem 1: This theorem highpoints the unique relationship between the external potential and electronic density. Since the electronic density determines the number of electrons, it also uniquely determines the wave function and thus the electronic properties of the system. The total ground state energy of an interacting N-electron system in the presence of an external potential is a unique function of the electronic density ρ:

$$E = E(\rho) \qquad \text{(II.15)}$$

Theorem 2: This theorem is characterized by the enormous simplification of the solution of the Schrödinger equation, due to the reduction of the problem with 3N variables to a problem of a scalar function in 3-dimensional space. It is identified by the definition of the ground state density with the energy minimization of the system. All other properties are functional of the ground state density:

$$E(\rho_0) = \min\left(E(\rho)\right) \tag{II.16}$$

2.1.3.2. Kohen-Sham equations

In 1965, Walter Kohn and Lu Sham considered a virtual system of N-independent electrons (i.e., Vee = 0 in equation III. 6), which the ground state is the Slater determinant containing of the N-orbitals ψ_i of the electrons and whose electron density is the same as that of the real system of interacting electrons. Similarly, the Schrödinger equation is recombined in terms of the so-called Kohn-Sham equation, which is actually a Schrödinger equation with a real potential in which quasiparticles are moving [149,150]. Walter Kohn and Lu Sham introduced the real density by the self-consistent solution of the set of single-particle Schrödinger equations, known as the Kohn-Sham equations:

$$\left\{-\frac{1}{2}\nabla^2 + V_{KS}(r)\right\}\varphi_i(r) = \varepsilon_i\varphi_i(r) \tag{II.17}$$

$$\rho(r) = \sum_{ioccup} |\rho_i(r)|^2 \tag{II.18}$$

$$V_{KS}(r) = V_{ext}(r) + V_{XC}(r) + V_H(r) \tag{II.19}$$

where $V_{ext}(r)$ is the external potential formed by the nuclei and $V_{XC}(r)$ is the potential of the exchange-correlation energy, defined by the following formula:

$$V_{XC}(r) = \frac{\partial E_{XC}[\rho(r)]}{\partial\rho(r)} \tag{II.20}$$

hence, $V_H(r)$ is the classical Hartree potential given as:

$$V_H(r) = \int \rho(r)\frac{1}{|r-r'|}.dr' \tag{II.21}$$

The total energy of the system is obtained by solving the Kohn-Sham equations and described with the following equation:

$$E(r) = \sum_{ioccup} \varepsilon_i + \int \frac{\rho(r).\rho(r')}{|r-r'|}.dr.dr' + E_{XC}(\rho).\int V_{XC}(r)\rho(r).dr \qquad \text{(II.22)}$$

One can notice the identical presentation of equation (II.17) and the Schrödinger equation. However, it is only an equivalence, because the eigenvalues of the Kohn-Sham equation are pure vibrational parameters. Therefore, do not strongly signify the eigen-energies of the system and the eigenvectors are not the real electronic wave functions.

2.1.3.3. Exchange-correlation approximation

The only uncertainty in the Kohn-Sham approach is the exchange correlation term. The actual complexity of this term makes it difficult to solve the Kohn-Sham equations, nevertheless this functional can be subject to local or quasi-local density approaches. The most basic types of the exchange correlation approach are Local Density and Generalized Gradient Approximations (LDA and GGA).

Local Density Approximation (LDA): The local density approach (LDA) transforms DFT from an exact N-body theory into an approximate but very useful and widely used theory. In the local density approach (LDA), it is assumed that the electron density can be treated locally as a uniform gas [151]. In other words, this approach involves the following two assumptions:

- The exchange-correlation effects are mainly provided by the density at point $\vec{r}$.
- The density $\rho(\vec{r})$ is a slowly varying function of $\vec{r}$.

Therefore, in the presented LDA formalism, it was considered that the $E_{XC}[\rho(\vec{r})]$ contribution to the total energy of the system can be accumulated from each portion of the nonuniform gas as if it were locally uniform. The LDA approach implies that the exchange-correlation term of the total ground state energy can be described according to the given expression:

$$E_{XC}^{LDA}(r) = \int \rho(r)\, \varepsilon_{XC}^{hom}\big(\rho = \rho(r)\big).dr \qquad \text{(II.23)}$$

where ε_{XC}^{hom} is the exchange-correlation energy for a uniform density of an electron gas. The local spin density approach (LSDA) is another version of the LDA that allows to consider the electronic spin. The exchange-correlation energy E_{XC}^{LDA} is then a function of the two spin densities (upper and lower) and equation (II.23) becomes:

$$E_{XC}^{LSDA}(\rho\uparrow,\rho\downarrow) = \int \rho(r)\,\varepsilon_{XC}^{hom}\big(\rho\uparrow(r),\rho\downarrow(r)\big).\,dr \qquad \text{(II.24)}$$

Generalized Gradient Approximation (GGA): A first step to enhance the treatment of the exchange-correlation energy is to make the $E_{XC}[\rho(\vec{r})]$ function dependent not only on the electron density $\rho(\vec{r})$ but also on its gradient $[\nabla\rho(\vec{r})]$. With this modification, the $E_{XC}[\rho(\vec{r})]$ accounts for the non-uniformity of the electron gas [152,153].

In the GGA formalism, the contribution of $E_{XC}[\rho(\vec{r})]$ to the total energy of the system can be accumulated from each non-uniform portion of the gas as if it were locally non-uniform. This simplification implies the following form of $E_{XC}[\rho(\vec{r})]$:

$$E_{XC}^{GGA}[\rho(\vec{r})] = \int \rho(r)\,\varepsilon_{XC}[\rho(\vec{r}),|\nabla\rho(\vec{r})|].\,dr \qquad \text{(II.25)}$$

where $\varepsilon_{XC}[\rho(\vec{r}),|\nabla\rho(\vec{r})|]$ represents the exchange-correlation energy as a function of the electronic density and its gradient. The GGA functions significantly increase the accuracy of the calculations compared to the description provided by the LDA, for the binding energy of the molecules. Thus, this approach provides a better explanation of the equilibrium volumes, elastic moduli, optical and magnetic properties of compounds compared to the LDA approach.

2.1.4. Solving Kohen-Sham equations

In this section, we will implement two most common methods to solve the Kohn-Sham equations. These methods are the full potential linearized augmented plane wave (FP-LAPW) and the pseudopotential methods.

2.1.4.1. Full-Potential Linearized Augmented Plane Wave (FP-LAPW)

The Full-Potential Linearized Augmented Plane Wave (FP-LAPW) method which was invented by Andersen is an improvement of the Augmented Plane Wave (APW) method developed by Slater [154,155]. This method is based on the self-consistent solution of the Kohn-Sham equations in two arbitrary regions of the elementary mesh (Figure II.10):

- **Region I:** Corresponds to non-overlapping atomic spheres (A and B) of the Muffin-Tin radius R_{MT}, wherein a series of linear combinations of radial and angular functions are used.
- **Region II:** The interstitial area between the atomic spheres, which can be defined by plane wave expansions.

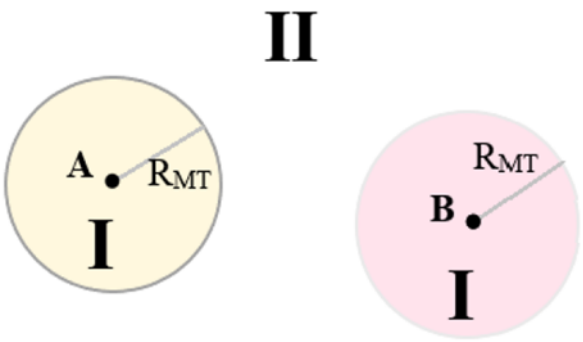

Figure II.10 : Schematic illustration of two atomic spheres A and B with radius R_{MT} (region I) and the interstitial region between the spheres (region II).

The convergence of this basis is controlled by the cut-off parameter $R_{MT} \times K_{max}$, which is the product of the radius of the smallest Muffin-Tin sphere and the cut-off energy of the wave plane basis. This method offers the possibility to consider a realistic potential. This one is not limited to the spherical component. Contrary to the methods using pseudopotentials, the core electrons are included in the calculations. Then, we obtain a rectified description of the wave functions in the vicinity of the nucleus. This method is the most accurate, but it is heavy in computation time. The whole presented framework, has been released within the WIEN2K package, that developed by Blaha and Schwarz in 1990 and based on the full potential linearized plane wave method [154,156].

2.1.4.2. The method of pseudo-potentials (Plane Wave)

A plane wave approach involves a very large number of waves to best qualify the system. One way to reduce the basis is to remove the waves whose kinetic energy is higher in absolute value than a certain energy, known as $E_{cut\text{-}off}$. However, this basis, although reduced, is not well assimilated because a very large number of plane waves are still needed to rectify the strongly bound orbitals of the core electrons.

Elements with few electrons require few plane waves, while heavy elements or transition metals will require extremely powerful computing resources. However, in most cases, valence electrons are the only ones participating in the chemical bond. The core electrons are therefore grouped with the nuclei: this approach is the pseudopotential plan wave method, that known as the frozen nucleus approximation [157]. In 1958, the first pseudopotentials method was

developed by Phillips and Kleiman. Currently, the used pseudopotentials are determined from "all-electron" calculations, which makes the method more suitable [158,159].

2.1.4.3. Computational protocol

Different codes are used to describe solids with different computation speeds and accuracies. For our study, we used two codes: WIEN2K based on the FP-LAPW method and the Quantum Espresso (PW) code.

An important part of the work consists in optimizing the structures. To optimize means to determine a structure at equilibrium and to determine its fundamental energy. On each atom of the primitive cell forces are exerted. When these forces are negligible, the atoms have reached their equilibrium position. Based on the optimized structure, the iterative calculation (self-consistent) will be applied to extract the total energy, the gap, the total momentum... We propose a scheme that summarizes the solution of the Schrödinger equation with the different approaches.

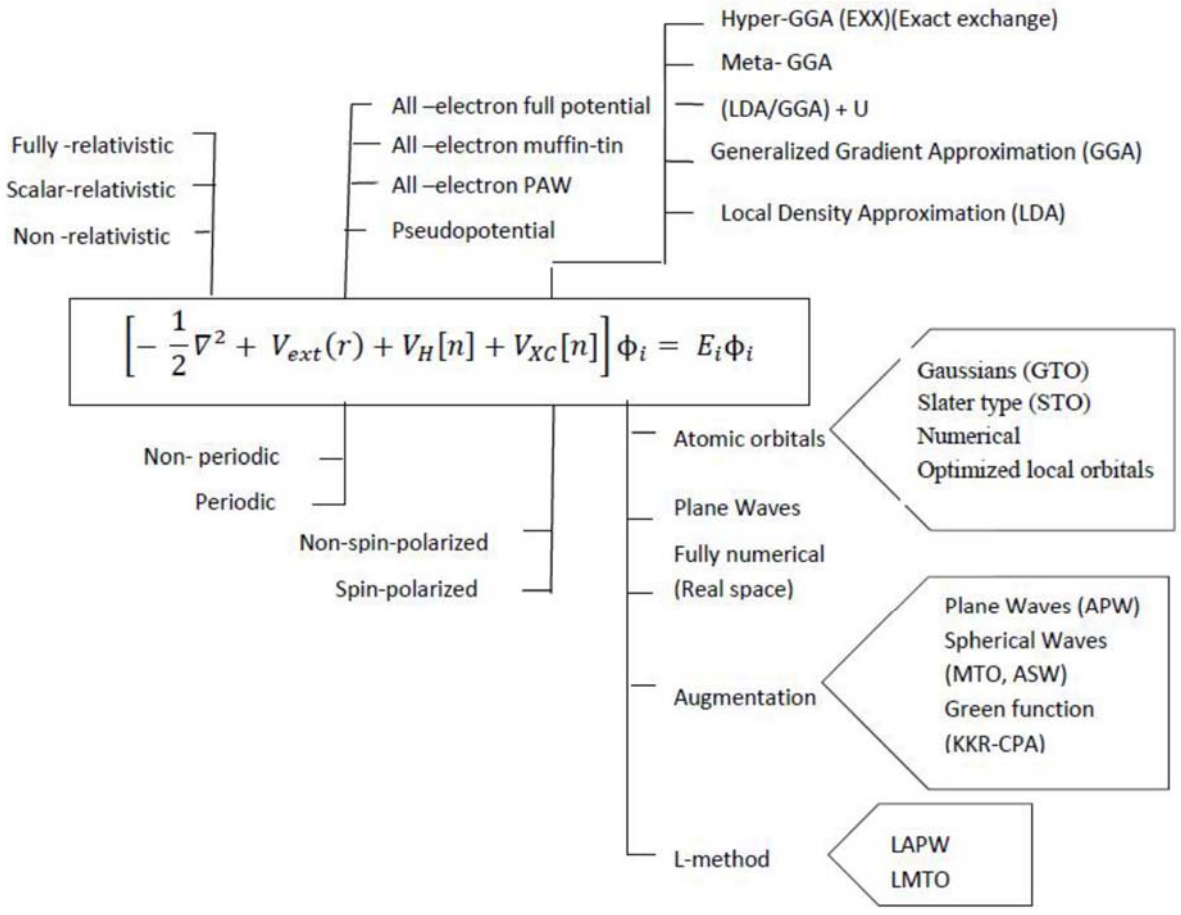

Figure II.11: Schematic representation of different methods based on DFT.

2.1.4.4. Modelling of electrical materials

Transport theory deals with the flow of charges and heat through a solid material under the effect of an external field (electric field and/or temperature gradient). The movements of the carriers (electrons or phonons) are induced by the external fields but are countered by internal diffusion processes between them and between other (quasi)-particles. There are exchanges of energy and momentum within the interactions, resulting from the finite electrical or thermal conductivity. On the other hand, the interactions lead to the conduction of carriers that are not in their equilibrium state. There are two approaches to this non-equilibrium transport, namely the Green-Kubo theory [160] and the semi-classical Boltzmann transport theory [161]. The former focuses on the transport coefficients of the current or heat flow correlation function, the latter considers the effects of various diffusions in the mechanisms of the transport properties, in terms of relaxation times. Boltzmann transport theory has proven its validity in many applications, where the calculated transport coefficients can be easily compared with experimental results. In this section, we show how to merge the electronic structure of the ab-initio approach using the DFT density function theory into the Boltzmann transport theory, to derive the electronic transport coefficients.

Basis of the semi-classical transport theory: The semi-classical transport theory is based on the direct or approximate solution of the Boltzmann transport equation determined by the semi-classical distribution function $f_n(r, k, t)$. It gives the probability of finding a particle in the region (r, r+dr) and (k+dk) at time t. The moments of the distribution function give us information about the particle density, the current density, and the energy density. The Boltzmann theory describes the electronic system by introducing the distribution function which is given by the Fermi function when the electrons are in their equilibrium states. It depends explicitly on the band n and the wave vector k which are the quantum numbers of the electronic states. In non-equilibrium states, the distribution function can depend on the spatial coordinates r and the time t, and will be characterized by $f_n(r, k, t)$. The distribution function $f_n(r, k, t)$ in the vicinity of r, can change due to the electron diffusion, external field (electric field or temperature gradient), and collisions.

Transport parameters: such as Seebeck coefficient, electrical, and thermal conductivity, etc, are obtained using the semi-classical Boltzmann transport theory implemented in the BoltzTrap code [162], [163]. The Boltzmann transport theory has proven its validity in many

applications where the calculated transport coefficients can be easily compared with experimental results.

The motion of charges under an electric field generates an electric current, whose density is given by:

$$J_e = \frac{2e}{8\pi^3}\int v(k)f(k)dk \tag{II.26}$$

where $f(k)$ is the Fermi-Dirac distribution function given by:

$$f(k) = f^0(k) + \left(-\frac{\partial f^0}{\partial E}\right) v(k)\tau(k)\left\{e\varepsilon - (\frac{\partial \mu}{\partial T} + \frac{E-\mu}{T})\nabla T\right\} \tag{II.27}$$

Similarly, the current density of heat produced by the electrons, is obtained by:

$$J_Q = \frac{2}{8\pi^3}\int v(k)[E-\mu]f(k)dk \tag{II.28}$$

With μ is the chemical potential.

Substituting equation (II.26) for both equations (II.27) and (II.28) and ignoring the f^0 term in equation (II.26), we arrive at:

$$J_e = \frac{2e}{8\pi^3}\int v(k)\, v(k)\tau(k)\left(-\frac{\partial f^0}{\partial E}\right)\left[e\varepsilon - \nabla\mu + \frac{E-\mu}{T}(-\nabla T)\right]dk \tag{II.29}$$

$$J_e = \frac{e^2}{4\pi^3}\int v(k)\, v(k)\tau(k)\left(-\frac{\partial f^0}{\partial r}\right)\left[\varepsilon - \frac{1}{e}\nabla\mu\right]dk + \frac{e}{4\pi^3\hbar}\int v(k)\, v(k)\tau(k)\left[\frac{E-\mu}{T}\right](\nabla T)dk \tag{II.30}$$

And

$$J_Q = \frac{2}{8\pi^3}\int v(k)v(k)\tau(k)\left(-\frac{\partial f^0}{\partial E}\right)\left\{e\varepsilon - \nabla\mu + \frac{E-\mu}{T}(-\nabla T)\right\}[E-\mu]dk \tag{II.31}$$

$$\begin{aligned} J_Q = {} & \frac{e^2}{4\pi^3}\int v(k)\, v(k)\tau(k)\left[\varepsilon - \frac{1}{e}\nabla\mu\right](E-\mu)\left(-\frac{\partial f^0}{\partial E}\right)dk \\ & + \tfrac{1}{4\pi^3}\textstyle\int v(k)\, v(k)\tau(k)\left[\frac{E-\mu}{T}\right](-\nabla T)(-\frac{\partial f^0}{\partial E})dk \end{aligned} \tag{II.32}$$

Let us now establish the integral:

$$K_n = \frac{1}{4\pi^3\hbar}\int v(k)\, v(k)\tau(k)[E-\mu]^n\left(-\frac{\partial f^0}{\partial E}\right)dk \tag{II.33}$$

Equations (II.30) and (II.33) can be expressed in terms of K_n:

$$J_e = e^2 K_0 \varepsilon + \frac{eK_1}{T}(-\nabla T) \quad \text{(II.34)}$$

$$J_Q = eK_1 \varepsilon + \frac{K_2}{T}(-\nabla T) \quad \text{(II.35)}$$

When there is no temperature gradient, i.e., ∇T=0 in Equation (II.34), we get:

$$J_e = \sigma \varepsilon \quad \text{(II.36)}$$

where σ is the electrical conductivity, which takes the form:

$$\sigma = e^2 K_0 \quad \text{(II.37)}$$

When the electric field is absent and only a temperature gradient exists, one might be tempted to think that the thermal conductivity is simply obtained by taking it as the coefficient of the thermal gradient in equation (II.35), i.e., under the conditions of a zero external electric field. This is a primary issue before ensuring that no electric current flows through the material. In this case, the relationship $J_e = 0$ in equation (II.34) becomes valid. Substituting equation (II.34) into equation (II.35) to eliminate the electric field gives the following results.

$$J_Q = k\,(-\nabla T) \quad \text{(II.38)}$$

Where k is the electronic thermal conductivity:

$$k = \frac{1}{T}\left[K_2 - \frac{K_1^2}{K_0}\right] \quad \text{(II.39)}$$

If we assume that there is a temperature gradient across the material, in an open circuit condition, there is no electric current, but an electric field is produced:

$$\varepsilon = \frac{K_1}{eTK_0}\nabla T \quad \text{(II.40)}$$

According to the definition of the Seebeck coefficient, we obtain:

$$S = \frac{K_1}{eTK_0} \quad \text{(II.41)}$$

2.2. Monte Carlo Simulation

2.2.1. Introduction to Monte Carlo simulation

Condensed matter systems are well known to be treated in the framework of statistical physics, which was designed primarily to study their properties. This branch of physics is based on a concept that considers that the microscopic quantities of a system closely reflect the macroscopic phenomena observed in that system. The main drawback is the huge number of particles in a condensed matter system, implying many difficult problems related to the structure and type of interactions that occur in the system, making it more difficult to find exact solutions to all the questions studied. It is therefore obvious that the solutions provided by analytical methods are only provisional solutions. For this reason, among the most used simulation techniques, the Monte Carlo method is nowadays widely used as an important alternative method to develop the understanding of complex physical systems and phenomena. Monte Carlo simulation is a fundamental technique used for solving problem that confesses probabilistic interpretation [164]. It is a computational algorithm that uses repeated random sampling to obtain numerical results at equilibrium. This type of simulation has proven useful in the study of systems with many coupled degrees of freedom, such as solids, fluids, and strongly coupled disordered materials. It is important to note that the Monte Carlo method includes several fields such as, economics, medicine, etc [165–168].

The main objective of Monte Carlo simulation is to describe the evolution of a model as a function of time. This time dependence is directly related to the Monte Carlo step, which is the basis of the process in which the model evaluates to the steady state according to a sequence of random numbers generated during the simulation. Monte Carlo simulation is based on the numerical solution of systems using a stochastic process and is therefore the most important class of numerical techniques used to solve statistical physics problems in equilibrium or nonequilibrium cases. The principle of Monte Carlo simulation is based on some basic concepts, which are described in the following section.

2.2.2. Basis concepts of Monte Carlo Simulation

Monte Carlo simulation based on the estimation of the average of a physical quantity $\langle Q \rangle$, that described following the canonical system as:

$$\langle Q \rangle = \frac{\sum_i Q_i \exp(\beta E_i)}{\sum_i \exp(\beta E_i)} \quad \text{(II.42)}$$

where $\exp(\beta E_i)$ is the Boltzmann factor, defined as the probability density of the canonical ensemble. Hence $\beta = \frac{1}{K_B T}$ with K_B is the Boltzmann constant, T is the temperature of the system, and E_i is the potential energy. The basis of Monte Carlo simulation are presented in the following steps [169]:

The choice of the sample:

The average values of the quantities obtained by the Monte Carlo simulation are calculated based on the states that the system takes over time. The system does not necessarily take all possible states during the measurements. Real systems behave as a kind of Monte–Carlo simulation during their evolution to establish their properties. The states of the material are not equiprobable but are distributed according to the Boltzmann distribution. This distribution is mainly used for the estimation of the mean value. The notion of large sample therefore consists in creating an appropriate Markov chain in which the configurations are chosen according to their weight and the Boltzmann probability.

The Markov chain:

The Monte Carlo simulation uses the Markov chain to randomly generate the configurations of the studied material. The transition to a configuration denoted "b" depends only on the previous configuration denoted "a", but not on all configurations in the state space. This means that the transition, which can follow the probability W(a→b), in a Markov chain is almost local in time. the Markov process uses several times to generate a Markov chain. We start from configuration "a" to arrive at a new configuration "b", then we put this configuration in a process to generate another configuration "c", and so on. The Markov process is specially chosen because, when it runs long enough from any state of the system, it will eventually produce a succession of states that appear with probabilities given by the Boltzmann distribution. For this, we impose two other conditions on our Markov process: ergodicity and detailed balance.

The ergodicity:

Ergodicity implies that the system can take any possible state from a given state after a sufficiently long time during the Markov process. The ergodicity condition is not satisfied if all transition probabilities of a given state are zero.

The detailed balance:

The detailed balance condition ensures that the future balance is only a Boltzmann distribution and not another distribution. If the system is in equilibrium, the probabilities of transition from one state to the same state are equal, which can be described by the following transition:

The detailed balance confirms that the future equilibrium is only a Boltzmann distribution and not another distribution. If the system is in equilibrium, the transition probabilities from one state to the same state are equal, which can be described as follow:

$$\sum_a P_a \times W(a \to b) = \sum_b P_b \times W(b \to a) \tag{II.43}$$

As W(a → b) = 1, equation (II.43) becomes.

$$\sum_a P_a \times W(a \to b) = P_a = \sum_b P_b \times W(b \to a) \tag{II.44}$$

The distribution will be the equilibrium distribution implied by the dynamics of Markov processes, if any set of transition probabilities satisfies equation (II.44). This equation does not guarantee the distribution of the system state. To validate this, we will consider the transition probabilities W(a → b) as the elements of the Markov matrix:

$$q_b = \sum_b W(b \to a) \times q_b(t) \tag{II.45}$$

In a matrix form:

$$Q(t+1) = M \times Q(t) \tag{II.46}$$

Therefore, equation (II.44) does not allow the equilibrium established by the distribution. To surmount this struggle, the detailed equilibrium condition is given as follows:

$$P_a \times W(a \to b) = P_b \times W(b \to a) \tag{II.47}$$

Generally, real systems satisfy the condition of detailed balance. For a balanced Boltzmann distribution, an additional condition is derived from equation (II.47). We can write:

$$\frac{P_a}{P_b} = \frac{W(a \to b)}{W(b \to a)} = \exp\left(-\beta(E_b - E_a)\right) \tag{II.48}$$

The main goal is to create a program established the Markov chain according to the transition probabilities.

The Acceptance:

An algorithm does not necessarily indicate the exact set of transition probabilities. However, the acceptance probability allows one to find the rectified transition probabilities of any Markov process. Subsequently, the condition W(a → b) ≠ 0 is accepted and always respects the detailed balance conditions. Hence, the transition probability can be described by:

$$W(a \to b) = g(a \to b) \times A(a \to b) \tag{II.49}$$

where,

- $g(a \to b)$ is the probability of selection. It represents the probability to get new state "b" from the old state "a" by the algorithm.
- $A(a \to b)$ is the acceptance probability, which corresponds to the probability of accepting the transition from the old state "a" to the new state "b".

The value of the acceptance probability is random between 0 and 1.

Equation (II.48) becomes:

$$\frac{P_a}{P_b} = \frac{W(a \to b)}{W(b \to a)} = \frac{g(a \to b) \times A(a \to b)}{g(b \to a) \times A(b \to a)} \tag{II.50}$$

To prevent the algorithm from being slowed down, an acceptance close to one is usually allowed. The best algorithm is therefore the one that adds the selection probability g(a → b) and takes A(a → b) ≃ 0.

2.2.3. Implementation of the Metropolis Algorithm

The Metropolis algorithm is the most used algorithm worldwide in many areas [170]. The application of this algorithm to the Ising model consists in performing a single flip attempt at each Monte Carlo step [171,172]. In this case, all selection probabilities are equals and are given by:

$$g(a \to b) = \frac{1}{N} \tag{II.51}$$

where N is the number of spins in the system.

The detailed balance equation (II.50) can consequently be inscribed as follows:

$$\frac{P_a}{P_b} = \frac{W(a \to b)}{W(b \to a)} = \frac{g(a \to b) \times A(a \to b)}{g(b \to a) \times A(b \to a)} = \exp\left(-\beta(E_b - E_a)\right) \qquad \text{(II.52)}$$

The Metropolis algorithm is carefully related to the choice of the acceptance $A(a \to b)$ and can be described as follows:

$$A(a \to b) = \begin{cases} exp\ (-\beta(E_b - E_a)) & if\ (E_b - E_a\ >\ 0) \\ 1 & elsewhere \end{cases} \qquad \text{(II.53)}$$

The transition probability W(a → b) adopts the same form as acceptance, with this choice of transition probabilities of the system tends to a stable configuration, in which the system seeks the equilibrium state.

Immediately, the implementation of the Metropolis algorithm can be presented in the following steps:

- From an initial configuration "a" of energy "E_a", a new configuration "b" of energy "E_b" is selected randomly.
- Each new configuration is tested to verify its acceptance by calculating the variation of energy $\Delta E = E_b - E_a$, according to the following conditions.
  - If $\Delta E < 0$, the new configuration "b" is accepted.
  - If $\Delta E > 0$, we generate a number randomly, r ($0 < r < 1$). If $r < \exp(\Delta E)$, the new configuration "b" is accepted. Else, the new configuration "b" is rejected.
- The process is repeated until a new configuration is obtained.

3. Conclusions

In summary, different experimental methods were used to determine the physical properties of studied sillenite materials. In addition to that, the theoretical framework presented in this manuscript was established using density functional theory (DFT) based on ab-initio methods and Monte Carlo simulation to calculate the physical properties. In particular, the first-principle calculation has been implemented with the different approaches that have been used in this thesis, to calculate the physicochemical properties of iron-sillenite.

Part II

Results and discussions

Chapter III

Experimental investigation of the physicochemical properties of novel sillenite compounds $Bi_{25}Fe_{1-x}Al_xO_{40}$

After having exposed the different experimental and theoretical protocols followed for the chemical synthesis of the iron-sillenite compound $Bi_{25}FeO_{40}$, we aim through this chapter to study their physicochemical properties and the effect of aluminium substitution on the structural, vibrational, thermal, dielectric, magnetic, and optical properties of the synthesized compound. The results presented in this chapter are obtained using different experimental techniques, namely room temperature and high temperature X-ray diffraction, scanning electron microscopy (SEM), Fourier transform infrared spectroscopy (FT-IR), and Raman analysis. The thermal behavior of the sillenite compounds will be also examined in this chapter, using the DSC measurement. The dielectric and electrical characterizations carried out by dielectric measurements and by impedance spectroscopy. Moreover, the evolution of magnetic properties of studied compounds were studied as a function of the magnetic field and the temperature. At the end of this chapter, we will present the results obtained of the optical characterization of the different synthesized compounds.

1. Synthesis of sillenite compounds $Bi_{25}Fe_{1-x}Al_xO_{40}$ (x = 0.00, 0.20, 0.50)

The synthesis of the sillenite powders $Bi_{25}Fe_{1-x}Al_xO_{40}$ (x = 0.00, 0.20, and 0.50) is performed according to the solid–state reaction procedure (SSR) using iron-oxide, bismuth-oxide, and aluminium-oxide reagents (Fe_2O_3 Sigma Aldrich, ≥ 99.9%, Bi_2O_3 Sigma Aldrich, ≥ 99.9%, and Al_2O_3 Sigma Aldrich, ≥ 99.9%, respectively).

The synthesis protocol described in Figures III.1 and III.2, and proceeds according to the following chemical reaction:

$$12.5\ Bi_2O_3 + \frac{(1-x)}{2} Fe_2O_3 + \frac{x}{2} Al_2O_3 \rightarrow Bi_{25}Fe_{1-x}Al_xO_{40} \qquad \text{(III.1)}$$

The metal oxide masses, corresponding to the desired stoichiometry, are mixed, and grounded roughly with an agate mortar for 1 hour to obtain a homogeneous mixture. The mixture of a yellow-orange color ($Bi_{25}FeO_{40}$) was placed in a platinum crucible and heated for the first time at a temperature of 500°C for 24 hours using a programmable electric furnace. The calcined powder, turning orange, and is then ground for 30 min with the same previous procedure to obtain the homogeneity of the sample. The obtained powder is treated again at a temperature of 700°C (1) for 24 h. The calcined powder becomes less

colored, afterward another calcination is done at the same temperature of 700°C (2), then at 750°C. The produced powder takes a light-yellow color (Figure III.2).

To study the effect aluminium doping on the Iron-sillenite, we will follow the same process for the synthesis of $Bi_{25}Fe_{1-x}Al_xO_{40}$ (x = 0.00, 0.20, and 0.50) compounds.

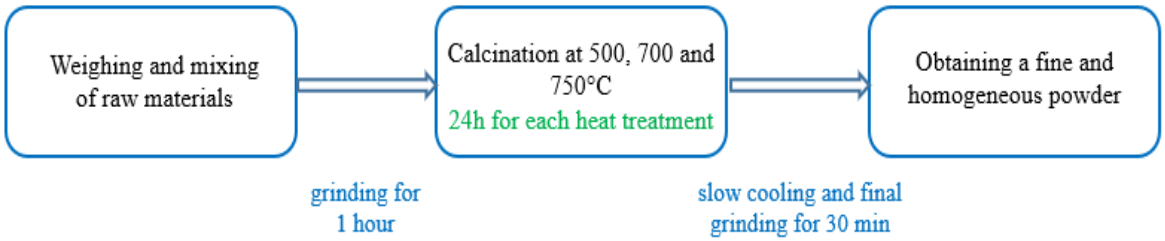

Figure III.1: Flowchart illustrating the different steps of elaboration of $Bi_{25}Fe_{1-x}Al_xO_{40}$ (x = 0.00, 0.20, and 0.50) by solid–state reaction (SSR).

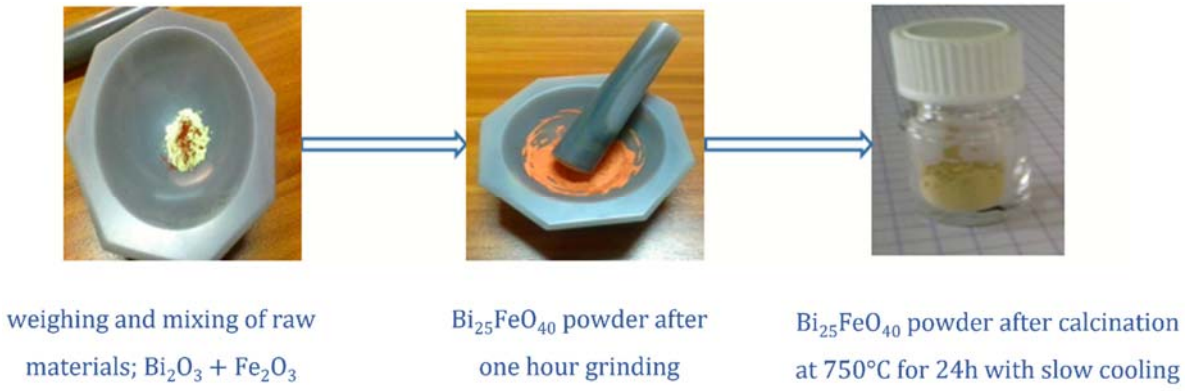

Figure III.2: Synthesis protocol of iron-sillenite by solid–state reaction at 750°C.

2. Structural and vibrational analysis of Al/Fe-sillenites

2.1. X-ray diffraction study (XRD)

The X-ray diffraction patterns of $Bi_{25}Fe_{1-x}Al_xO_{40}$ were examined at room temperature using a LabxXRD-6100 Shimadzu diffractometer, equipped with a copper anticathode (λ_{cu} = 1.5406Å). Afterward, the refinement of the cell parameters was performed using AFMPOU software [114]. Figure III.3 presents the X-ray diffraction patterns of the prepared sillenite materials $Bi_{25}Fe_{1-x}Al_xO_{40}$, where x takes values of 0.00, 0.20, and 0.50. The XRD patterns indicates that three materials are found to crystallize in the body-centred cubic (I23, No. 197). The refined cell parameters of $Bi_{25}Fe_{1-x}Al_xO_{40}$ are found to be 10.199 (2), 10.170 (1), and 10.169 (1) Å, for x = 0.00, 0.20, and 0.50,

respectively. The volumes of the samples take values of 1061.9 (6), 1051.7 (3), 1051.5 (6) $Å^3$, for x = 0.00, 0.20, and 0.50, respectively. The obtained cell parameters are consistent with the literature [16,18,68]. The sharp forms of the diffraction peaks reveal good crystallization in the sillenite-type structure [18,61,68]. Unlike the $Bi_{25}FeO_{40}$ and $Bi_{25}Fe_{0.80}Al_{0.20}O_{40}$ samples, the XRD diffractogram of $Bi_{25}Fe_{0.50}Al_{0.40}O_{40}$ displays some small peaks around 25.84°, 27.01°, and 27.48°, attributed to the monoclinic Bi_2O_3 secondary phase (α-Bi_2O_3) [16,173]. The decrease of the cell parameters as a function of the substitution ratio is explained by the larger ionic radius of the Fe^{3+} (0.49 Å) compared to that of the Al^{3+} ones (0.39 Å) (Figure III.3).

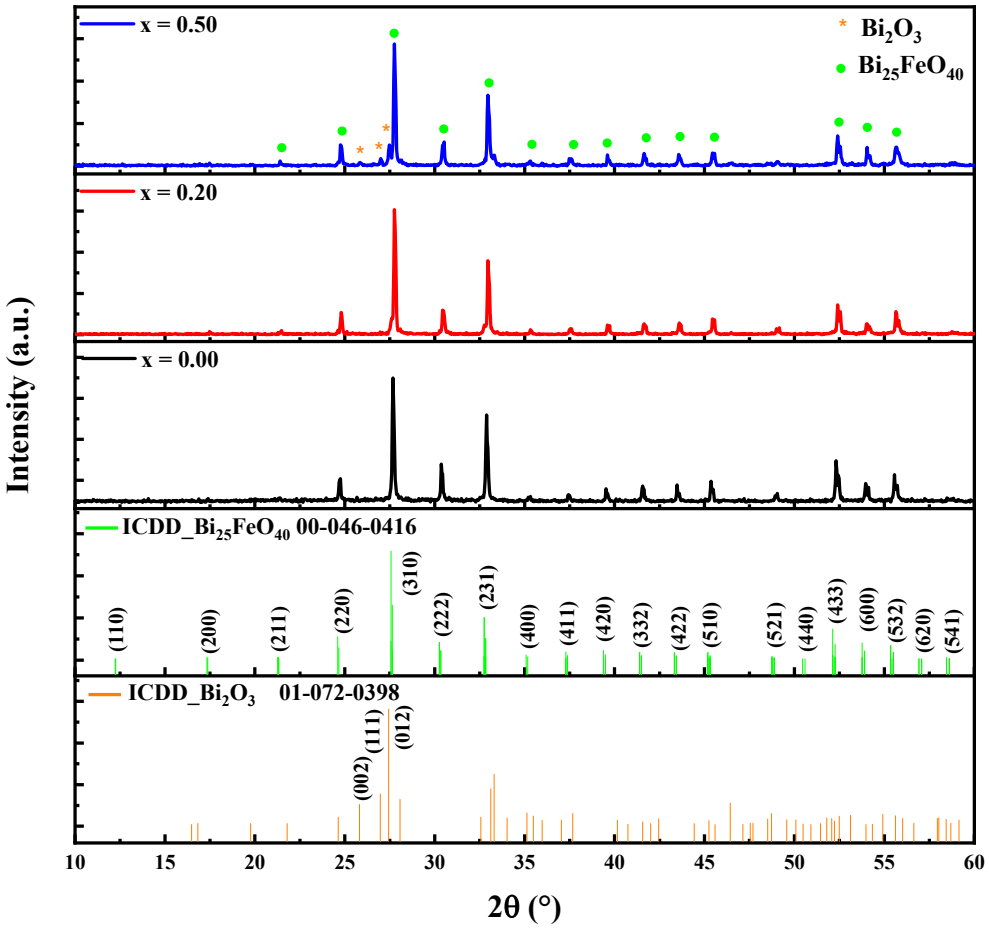

Figure III.3: XRD pattern of the synthesized $Bi_{25}Fe_{1-x}Al_xO_{40}$ (x = 0.00, 0.20, 0.50) compounds.

2.2. Morphological analysis (SEM)

The scanning electron microscopy spectra (SEM) was used to evaluate the surface morphology of $Bi_{25}Fe_{1-x}Al_xO_{40}$ compounds and presented in Figure III.4. The resulting

micrographs reflect the homogenous morphology of these sillenite materials, consisting of irregular agglomerated grains with uniformity in size and shape (Figure III.4). The average grain size of studied compounds was calculated using the ImageJ software [174] and found to be 4.04, 1.79, and 1.42 µm, for x = 0.00, 0.20, and 0.50, respectively. These results indicate that al-substitution affects the microstructure of the $Bi_{25}FeO_{40}$ sillenite system and reduce the grain size [16].

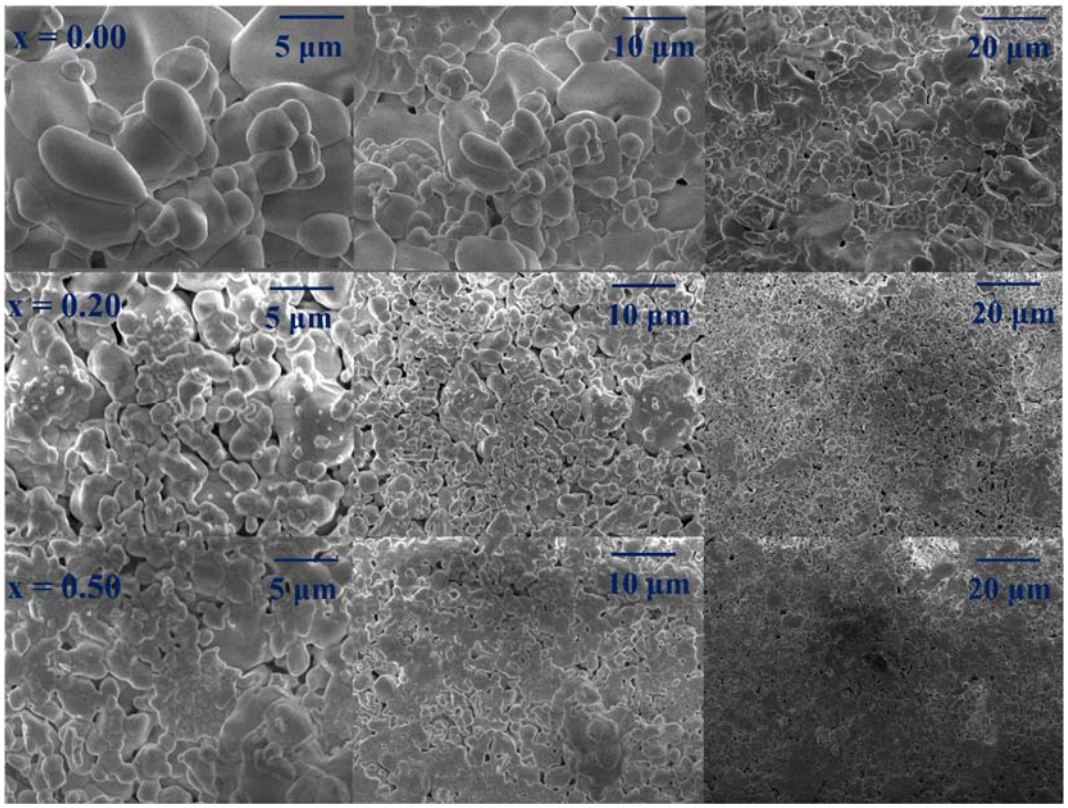

Figure III.4 : SEM morphology of $Bi_{25}Fe_{1-x}Al_xO_{40}$ (x = 0.00, 0.20 and 0.50) materials.

2.3. Infrared spectroscopy analysis (FT-IR)

Fourier transform infrared spectroscopy (FTIR) has been widely used for the interpretation of structural changes in Iron-sillenite. It was collected at room temperature, using a Bruker Platinium-ATR apparatus FT-IR spectrophotometer.

The Fourier transformed infrared spectroscopy (FT-IR) of sillenite compounds are plotted in Figure III.5. The characteristic five absorption bands of sillenite structure were observed around 438, 508, 572, 631, and 845 cm^{-1} [13,68]. The bonds situated at 438 and 508 cm^{-1} were observed for the three compounds, and corresponding to the stretching vibration of the Bi-O bonds [13,175]. Moreover, the typical bonds located at 572, 631, and

845 cm^{-1} noticed for the three as-prepared samples are associated with the Fe–O bonds stretching vibration in [FeO_4] tetrahedra [13,68]. Another bond around 673 cm^{-1} was noticed in the Al/Fe–Sillenites (for x = 0.20 and 0.50), which is attributed to the vibration modes of the Al–O–Al bonds [176]. Besides, the observed small shift of the different bands towards higher wavenumbers with increasing doping rate confirms the effect of Al-substitution on the vibrational properties and the findings derived from the XRD study. Indeed, the substitution of iron by aluminum leads to the reduction of the lattice volume and thus of the vibrational frequency of these different bonds [177].

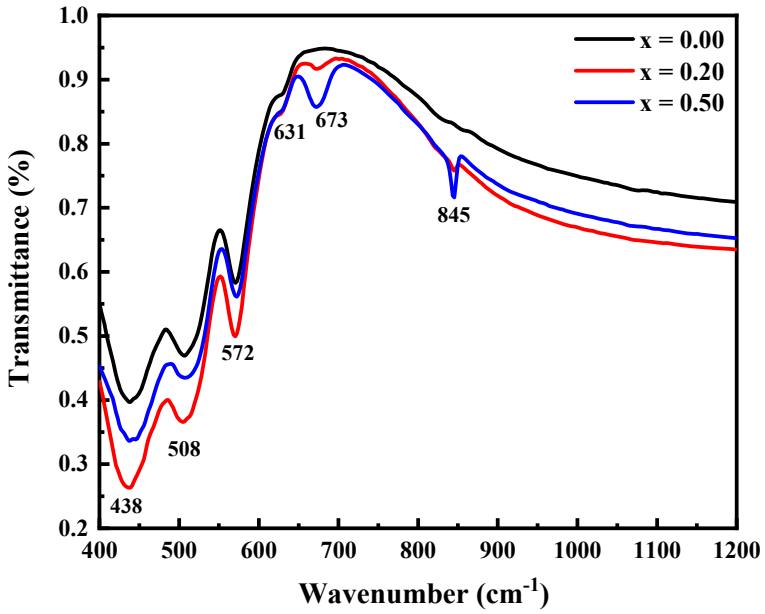

Figure III.5: FT-IR Spectra of $Bi_{25}Fe_{1-x}Al_xO_{40}$ (x = 0.00, 0.20 and 0.50) materials.

2.4. Raman analysis

The Raman spectra were obtained with a compact confocal Raman microscope with high sensitivity and spatial resolution (confotec™ MR520), contains a He-Ne laser source with an excitation wavelength of 553.99 nm. It is equipped with PMT detectors and a CCD camera for spectral measurements with Peltier cooling.

The recorded Raman spectra are shown in Figure III.6. Different characteristic peaks around 61, 125, 189, 246, 303, 516, and 812 cm^{-1} are noticed, in agreement with the literature reports for iron–sillenite [7,36,178].

The vibration modes noticed at 61, 125 cm^{-1} are attributed to Bi–O vibration bonds, whereas 189, 246 cm^{-1} are due to the vibration of the Bi–O–Bi bonds Besides, the peak at

516 cm^{-1} is related to oxygen breathing [58]. According to the group-theory, iron-sillenite contain the following vibration modes; 8A (totally symmetric), 8E (doubly degenerate), and 24F (triply degenerate). They are Raman active vibrations, expect of F symmetry are IR active. The bond observed at 125 cm^{-1} is assigned to the vibrational E and F modes of the tetrahedral FeO_4 [178]. The more pronounced difference between $Bi_{25}FeO_{40}$ and $Bi_{25}FeO_{40}$: Al is the appearance of a band at 673 cm^{-1}. This is in accordance with Refs. [181], which attribute this band to the stretching modes of Al-O bonds in sillenite type structures. The slight shift observed in the positions of Raman bands asserts the substitution effect on the different bond lengths as already reported in this paper [179,180].

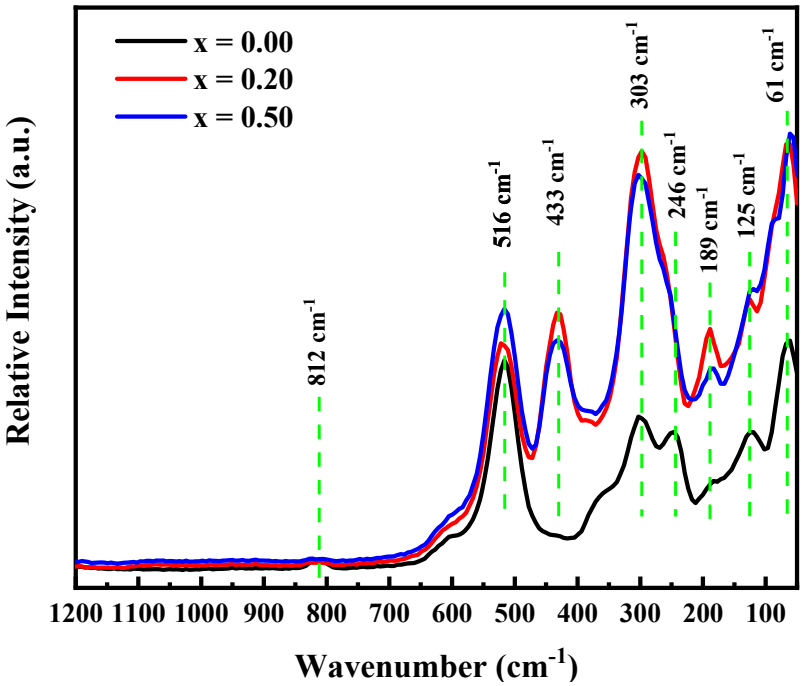

Figure III.6 : Raman spectrum of $Bi_{25}Fe_{1-x}Al_xO_{40}$ (x = 0.00, 0.20 and 0.50) materials recorded at room temperature in 50–1200 cm^{-1}.

2.5. High temperature X-ray diffraction study of $Bi_{25}FeO_{40}$ (HT-XRD)

Allotropic transformations were investigated by the high-temperature X-ray diffraction (HT-XRD) for the studied compound. Figure III.7 (a) shows the obtained HT-XRD spectra recorded at 500 K, 700 K, 900 K, and 1000 K. One can observe a displacement in the diffraction peaks towards lower angles, indicative of a change in the cell parameters during heating of the body-centred cubic iron-sillenite. Indeed, the obtained diffractogram

at 700 K shows clearly the appearance of a diffraction peak located at 25.22°(1) correspond to (220).

The appearance of doublet peaks at 27.00°, and 27.08° (2), were also noticed, that fit to (030) and (103), respectively. The observed peaks at 32.12°, and 32.22° (3) correspond to (032), and (213) (3), and 34.68° correspond to (004) (4), mentioned in the Figure III.7(b), indicating a change in the symmetry of the structure. The observed increase in cell volume reveals the expansion of the unit cell with increasing temperature, leading to a structural transition from a centred cubic structure (γ-$Bi_{25}FeO_{40}$) to a monoclinic one (α-$Bi_{25}FeO_{40}$) observed at 700 K. The affined structural parameters are reported in Table III.1.

Table III.1: Thermal evolution of lattice parameters of iron-sillenite.

T (K)	300	500	700	900	1000
a (Å)	10.199 (2)	10.241 (3)	10.177 (5)	10.211(6)	10.236 (5)
b (Å)	10.199 (2)	10.241 (3)	9.814 (6)	9.854 (7)	9.902 (7)
c (Å)	10.199 (2)	10.241 (3)	10.289 (5)	10.312 (4)	10.364 (4)
α (°)	90	90	90	90	90
β (°)	90	90	88.75 (4)	88.86 (4)	88.84 (3)
γ (°)	90	90	90	90	90
V (Å³)	1061,9 (6)	1074,2 (5)	1027,3 (6)	1037,1 (2)	1050,9 (2)

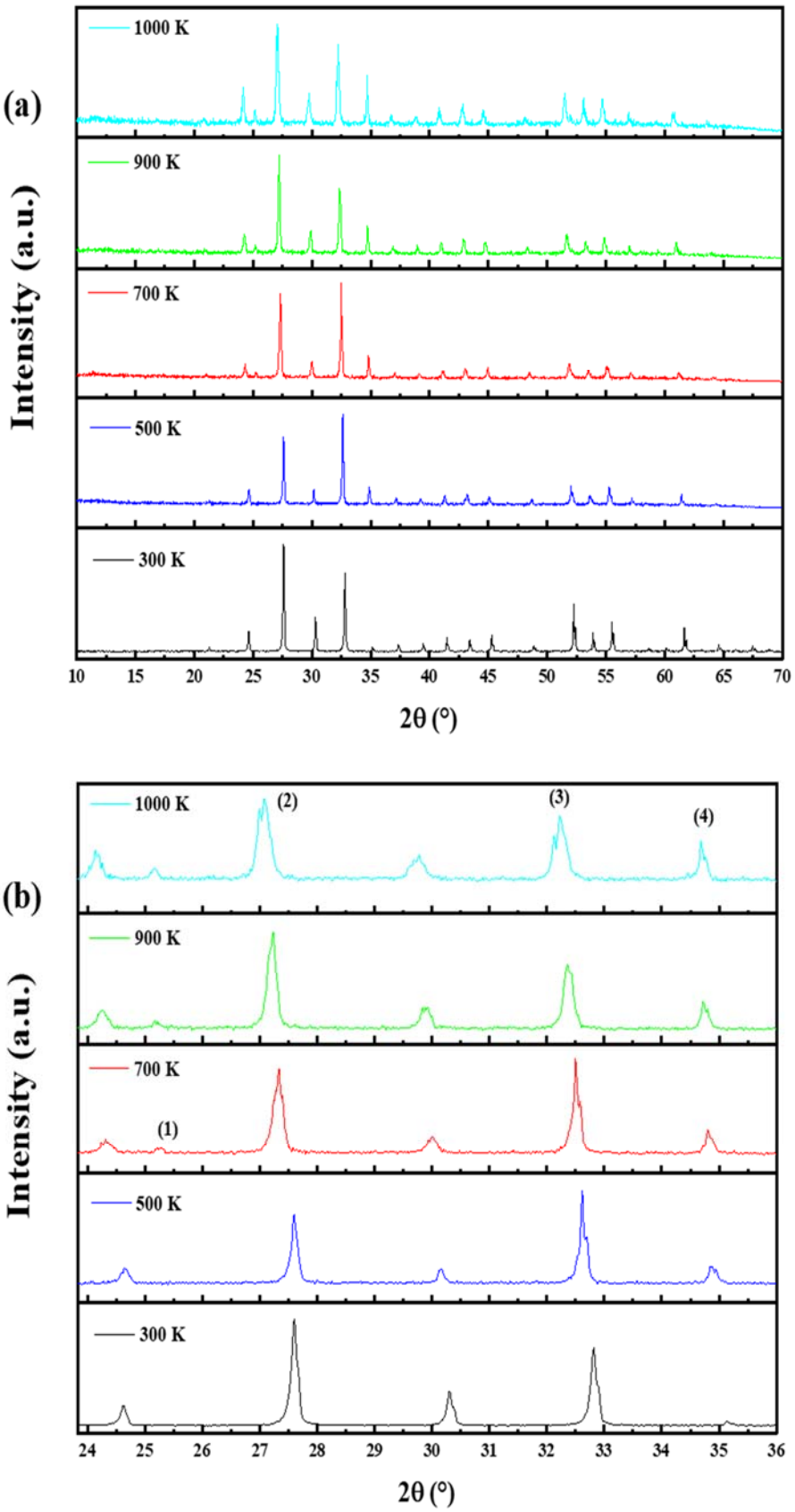

Figure III.7 : (a) High-temperature XRD patterns of iron-sillenite, (b) present the zoom view of HT-XRD.

3. Thermal analysis of Al/Fe-sillenites (DSC)

Heat flow measurements were performed to investigate the thermal properties of the materials and to relate their thermal behavior to their specific physical properties. It was carried out employing the differential scanning calorimetry (DSC) by means of a SETARAM DSC121 apparatus, with a heating and cooling rate of 10°K/min under argon atmosphere. The measurements were recorded in a wider temperature range to allow a possible detection of the whole phenomena revealed by the HT-XRD analysis (Figure III.7).

The DSC thermograms of iron-sillenite and Al/Fe-Sillenite materials recorded during both heating and cooling cycles in the temperature ranging from 450K to 1050 K and presented in Figure III.8 ((a) and (b)), respectively.

Figure III.8 (a) illustrates the endothermic peaks at 1036, 1034, and 1037 K for x = 0.00, 0.20, and 0.50, respectively. These peaks are assigned to the α→γ transition of the sillenite phase, thus similar results were reported previously by F. Oudich et al. [181]. In addition, two other endothermic peaks are noticed. The first peak occurred at 671, 682, and 679 K for x = 0.00, 0.20, and 0.50, respectively. The second peak is broad and centered between 500 and 600 K. These endothermic features are associated with the dielectric behavior of these materials, as discussed in the subsequent section. The exothermic peaks noticed at 923, 893, and 921 K during the cooling process are attributed to the γ-Bi_2O_3→α-Bi_2O_3 structural transition [49]. These findings are well consistent with those previously reported on iron–sillenite by Harwig et al. and Lu et al. [49,64] .

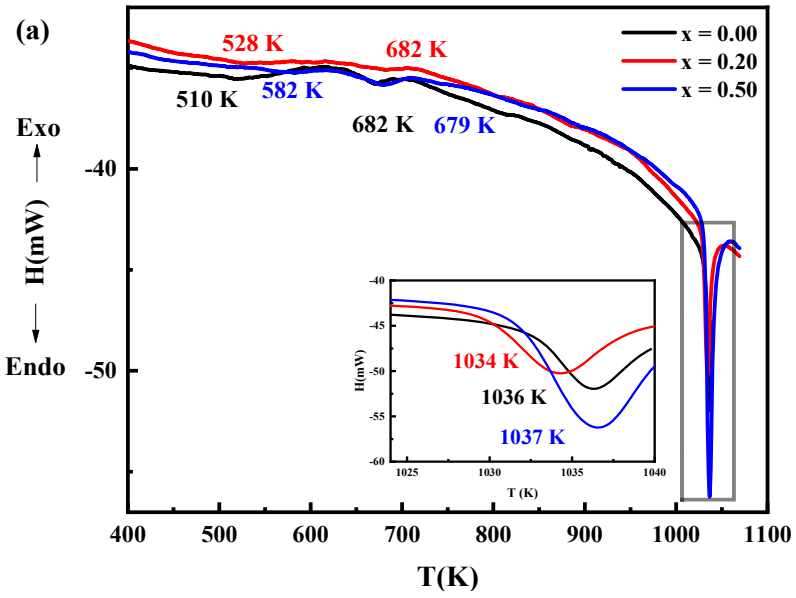

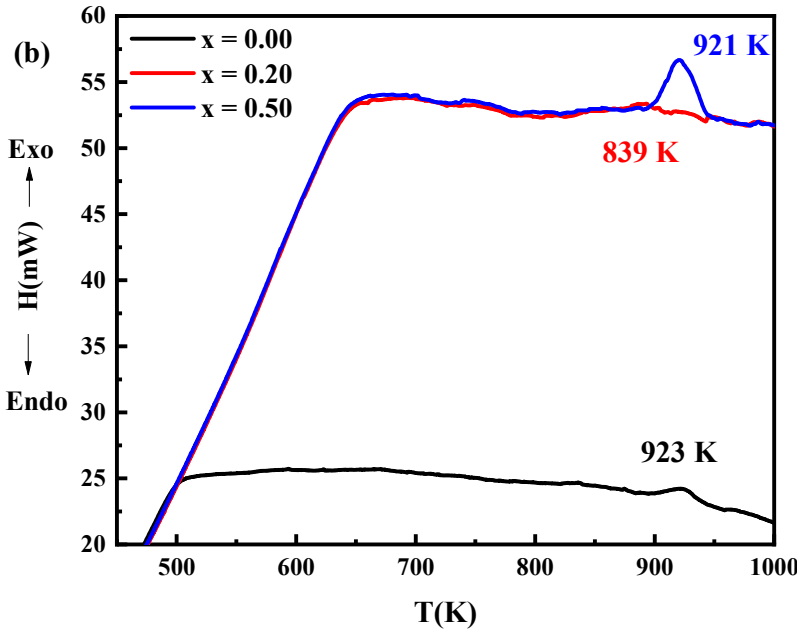

Figure III.8 : Thermal analysis thermograms of $Bi_{25}Fe_{1-x}Al_xO_{40}$ (x = 0.00, 0.20 and 0.50) phases during: (a) heating, (b) cooling.

4. Dielectric properties of Al/Fe-sillenites

Electrical and dielectric measurements were deduced from impedance spectroscopy using an LCR meter (Hewlett Packard 4284A Precision LCR Meter) as a function of frequency (10 kHz–1 MHz) and temperature (RT-700 K). For this purpose, both sides of the pellets were coated with silver paste and dried at 150 °C for 2 h in the hot air oven. The dielectric apparatus was supplied with a muffle furnace with a temperature controller and a sample holder for temperature variation studies.

4.1. Study of the dielectric permittivity and the dissipation factor as a function of frequency

The frequency evolution of the dielectric constant and losses for $Bi_{25}Fe_{1-x}Al_xO_{40}$ (x = 0.00, 0.20, 0.50) compounds at different temperatures is displayed in Figure III.9. All the compositions display the usual dielectric dispersion behavior, where the dielectric constant decays with an increase in frequency to become almost constant at higher frequencies. Usually, electronic, dipolar, interfacial, and ionic polarizations contribute to the dielectric permittivity of a material. At low frequencies, both dipolar and interfacial

polarizations are effective for dielectric permittivity. However, for higher frequencies, the electronic polarization becomes effective, and the dipole contribution becomes insignificant. The noticeable decline in the dielectric constant as frequency increases could be explained in terms of the dipolar relaxation process. At low frequencies, the space charges align with the applied electric field. However, upon increasing the frequency, the dipoles become no longer able to synchronize with the frequency of the applied field and take more time to alter their orientation in response to the field, and their contribution is reduced. This results in low values and weak dependence of ε' on the frequency.

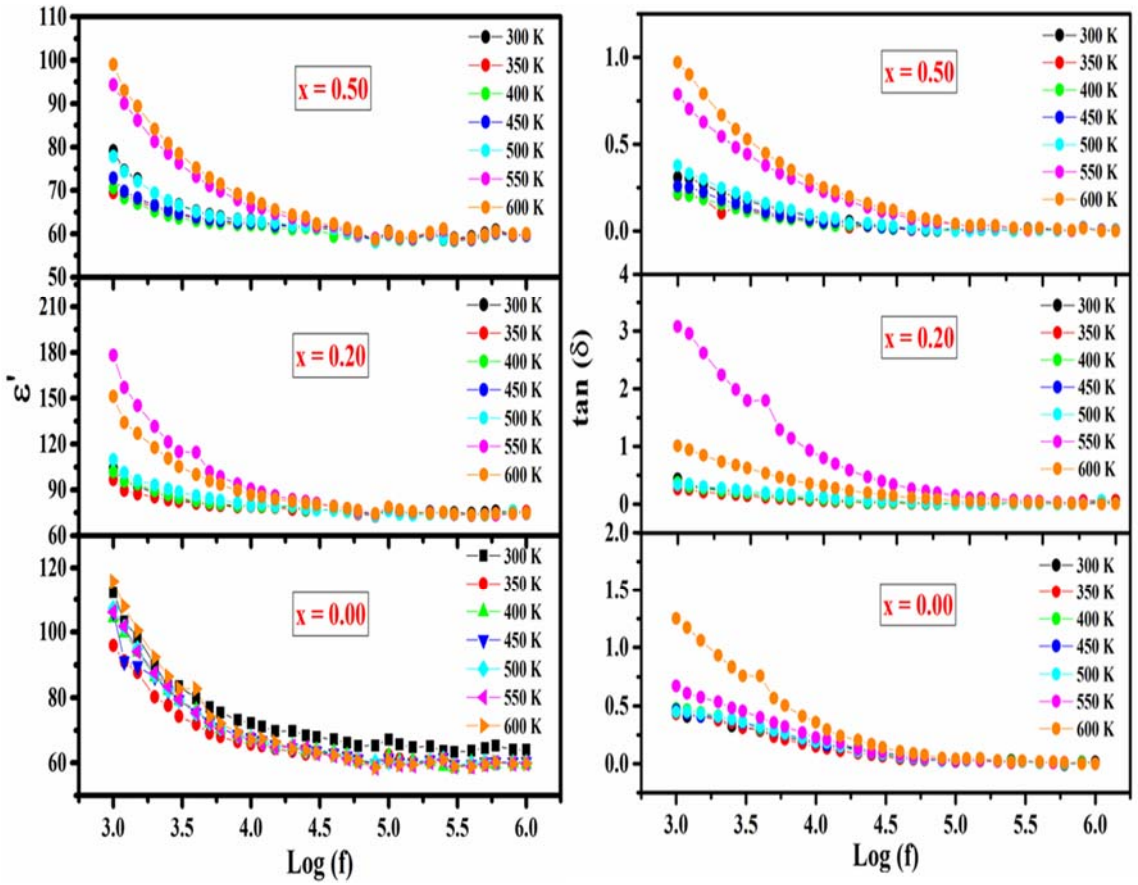

Figure III.9 : Frequency dependence of dielectric constant (ε') and loss factor (tan (δ)) of $Bi_{25}Fe_{1-x}Al_xO_{40}$ at different temperatures.

4.2. Thermal evolution of the dielectric permittivity and the dissipation factor

The temperature dependence of the dielectric permittivity and losses for all samples has been studied at different frequencies and presented in Figure III.10. Similar to most polar dielectrics [183], this material exhibits typical temperature-dependent dielectric behavior. Accordingly, both the dielectric constant and losses display a gradual variation

at low temperatures before increasing to a narrow broad peak between 470–570°K, followed by a rapid increase, potentially resulting in a peak at around 700°K, most notably for doped compounds. These phenomena are in accordance with the first two noticed broad endothermic peaks observed in the DSC thermograms. By considering various mechanisms, it is possible to provide in-depth explanations of the observed dielectric anomalies at low frequencies with respect to temperature. These include thermal-assisted electron hopping, space charge polarization resulting from electrical or structural inhomogeneities, and the presence of bismuth or oxygen vacancies due to partial loss of bismuth during the samples sintering process. The thermal-assisted electron hopping mechanism is influenced by temperature changes in the system, where higher temperatures can increase the mobility of free charge carriers. This leads to an increase in conductivity and polarization in the system, as the extra thermal energy enhances the frequency of the electron hopping mechanisms. This effect is more prominent at lower frequencies and less at higher frequencies due to the space charge effect becoming less significant. If the frequency of the hopping mechanism matches that of the applied electric field, a dielectric peak may appear as a result of resonance effects, explaining the occurrence of peaks in the observed dielectric curves. When an alternating electric field is applied to a dielectric material at room temperature, the free charge carriers within the material align themselves with the field reversals and move toward the surface of the material. This accumulation of charge on the surface of the dielectric structure is called space charge polarization. The amount of charge motion is greater at lower frequencies and less at higher frequencies due to resistance within the material. At higher temperatures, further drift in charge carrier motion occurs which can lead to an increase in conduction and dielectric constant. Furthermore, chemical imbalances may result from the partial evaporation of one or several constituents of these materials, leading to the formation of bismuth/oxygen vacancies. These vacancies have been identified as potential sources of dielectric anomalies in several studies [184,185].

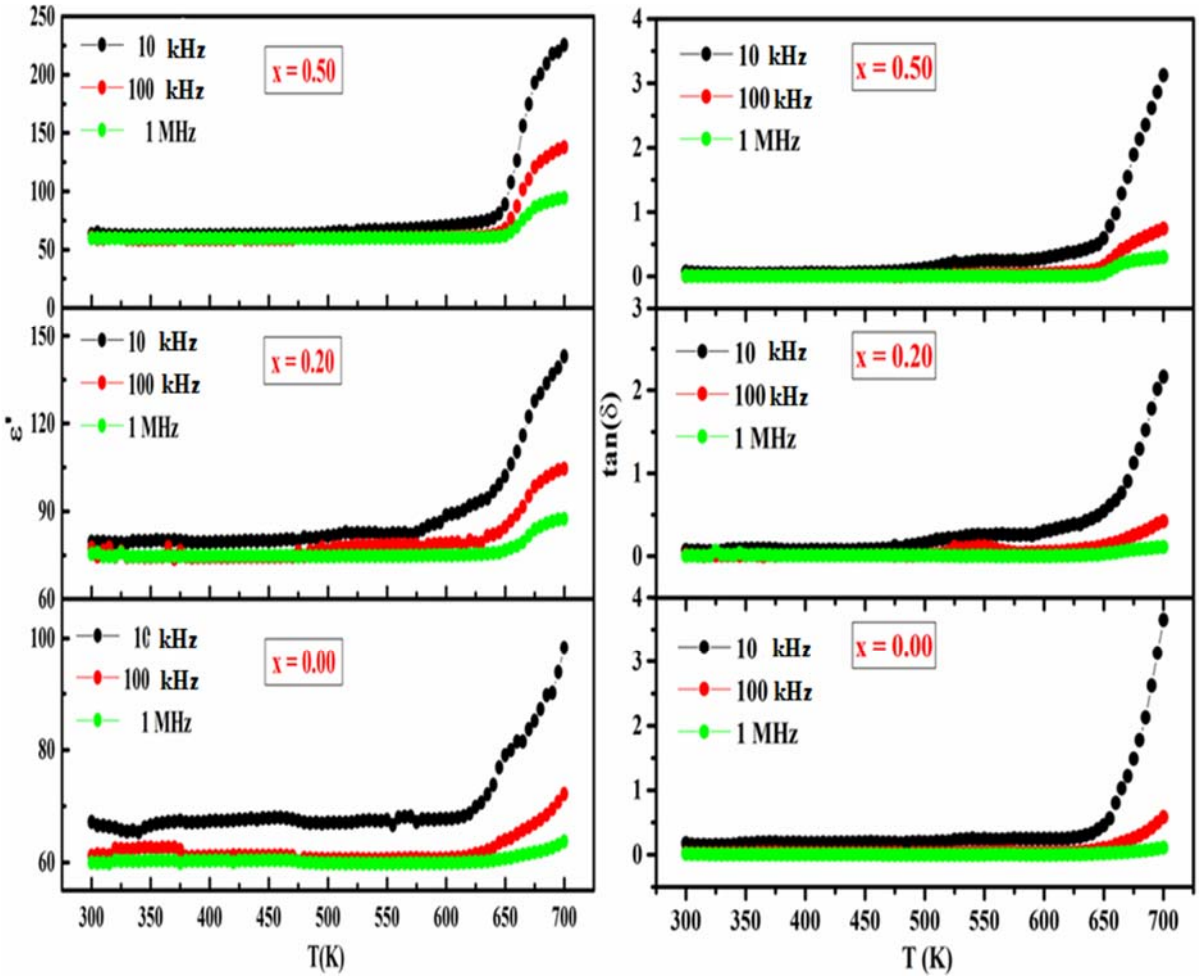

Figure III.10 : Temperature variation of dielectric constant (ε') and loss factor (tan (δ)) of $Bi_{25}Fe_{1-x}Al_xO_{40}$ at different frequencies.

4.3. Study of the electrical conductivity

Figure III.11 (a) gives the variation of AC conductivity of $Bi_{25}Fe_{1-x}Al_xO_{40}$ (x = 0, 0.2, 0.5) sillenite systems as a function of the applied electric field frequency at various temperatures. The AC electrical conductivity has been calculated based on the equation:

$$\sigma = 2\pi f \varepsilon' \varepsilon_0 \tan(\delta) \qquad \text{(III.2)}$$

where f is the frequency of the applied field, and ε_o is the dielectric permittivity in a vacuum. All the samples display an increasing trend in the AC conductivity curve relative to the increase of the charge carrier transfer rate between different localized sites along with increasing frequency. Generally, the total conductivity is expressed as the sum of two components: namely the frequency-independent DC conductivity part (σ_{DC}) and the

dispersive AC conductivity one (σ_{AC}). This type of frequency dependence can be explained by Jonsher's Power law, governed by the equation:

$$\sigma(\omega) = \sigma_{DC} + \sigma_{AC}(\omega) = \sigma_{DC} + A\omega^{S} \qquad \text{(III.3)}$$

Here $\omega = 2\pi f$ is the angular frequency, and A is a constant having the units of conductivity. The exponent s reflects the correlation degree in the system and takes a zero value in the case of random hopping, while it goes to one as the correlation in the system increases. Besides, there are two distinct cases according to Funke [186]: if $s > 1$, the charge carrier hopping occurs between adjacent sites, whereas if $s < 1$, the electron hopping is associated with a sudden hopping motion.

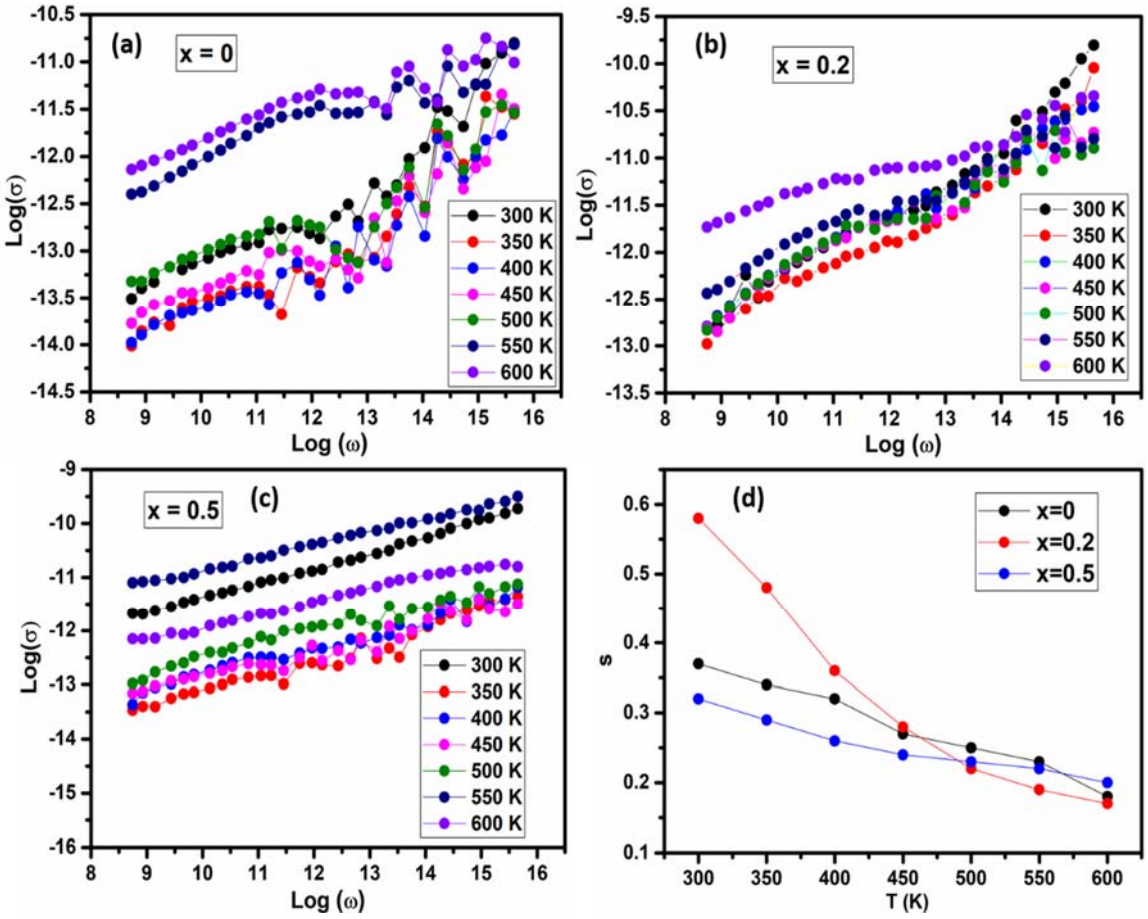

Figure III.11 : Logarithm plot of a.c conductivity versus frequency for (a) $Bi_{25}FeO_{40}$, (b) $Bi_{25}Fe_{0.2}Al_{0.8}O_{40}$, (c) $Bi_{25}Fe_{0,5}Al_{0,5}O_{40}$ samples. (d) depicts the temperature dependence of the exponents for the various compositions.

Different conduction mechanism theoretical models were developed to describe the conduction mechanism in the materials, depending on the temperature evolution of the

exponent s, correlated barrier hopping model (CBH), quantum mechanical tunneling (QMT), overlapping large polaron tunneling (OLPT), and small polaron hopping tunneling (SPT) are the various theoretical models. Here, in Figure III.11 (a) as the DC conductivity part (σ_{DC}) is mainly not present for all compositions, the conductivity component $\sigma_{AC}(\omega)$ can be described using the equation:

$$\sigma(\omega) = \sigma_{AC}(\omega) = A\omega^{S} \qquad \text{(III.4)}$$

The s values obtained from the slope of the $\log(\sigma_{AC})$ versus $\log(\omega)$ plot are represented in Figure III.11 (d). The inverse dependence of the s parameter on the temperature indicates that the correlated barrier hopping model is predominant for all compositions. Besides, the exponent (s) inferiority to unity indicates that the conduction mechanism is produced by sudden hopping. These results indicate that substitution with aluminium does not affect the conduction mechanism of the $Bi_{25}FeO_{40}$ system within the range of the realized substitution.

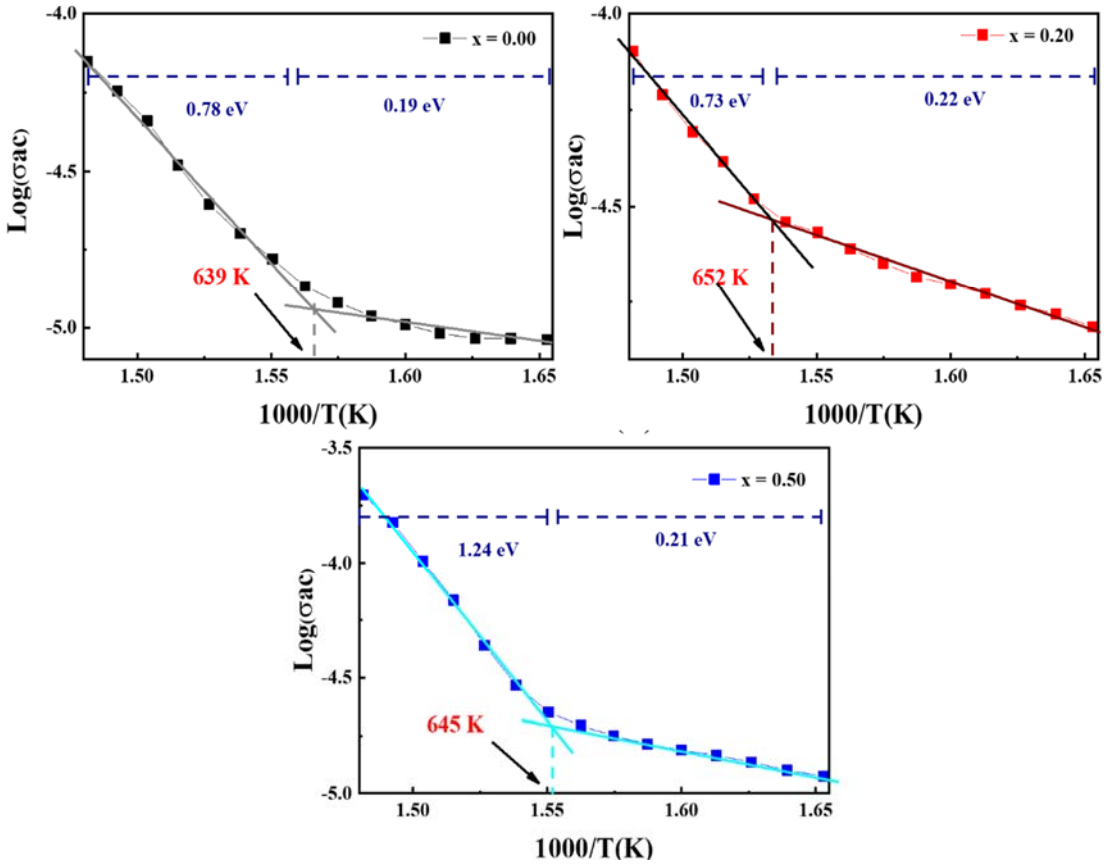

Figure III.12 : Evolution of the log(σac) versus (1000/T) of $Bi_{25}Fe_{1-x}Al_xO_{40}$ (x = 0.00, 0.20, and 0.50) at a frequency of 10 kHz.

Another parameter that can be calculated to evaluate the conduction mechanism, is the activation energies E_a. The activation energies of the sillenite compounds can be calculated from the slope of the $\log\sigma_{ac}$ vs 1000/T curve as follows [187]:

$$\sigma = \sigma_0 e^{\frac{E_a}{k_B T}} \quad \text{(III.5)}$$

where k_B and σ_0 are the Boltzmann constant and the conductivity at infinite temperature. Figure III.12 presents the inverse temperature (1000/T) dependence on the conductivity. The figure presented in Figure III.12 demonstrates the presence of two areas of conduction in the three synthesized compounds. The intersection temperature of these areas was found to be 639, 652, and 645 K for $x = 0.00$, 0.20, and 0.50, respectively. This is attributed to the phenomenon evidenced previously through both dielectric and thermal analysis. The activation energies for the first conduction domain were calculated to be 0.19, 0.22, and 0.21 eV, for $x = 0.00$, 0.20, and 0.50, respectively. Additionally, the activation energies for the second domain of conduction were found to be 0.78, 0.73, and 1.24 eV, for $x = 0.00$, 0.20, and 0.50, respectively. The significant difference between the values of the two areas indicates a change in the conduction mechanism between low and high temperatures. The activation energy values in the second region (0.70–1.25 eV) suggest that the conduction process is governed by the motion of oxygen vacancies at high temperatures [188].

4.4. Analysis by impedance spectroscopy

Figure III.13 ((a), (b), and c) illustrate the variation of the real impedance part (Z′) of the $Bi_{25}Fe_{1-x}Al_xO_{40}$ samples with frequency at various temperatures. The obtained curves demonstrate a frequency dispersion that merges at higher frequencies, resulting in a steady range indicative of a space charge release. The delay in the relaxation process induces the dispersive trend at low frequencies that may be related to space charges. Besides, the temperature dependence of Z′ is related to the high-temperature characteristics of semiconductors, as evident from both positive temperature of resistance coefficient (PTCR) and negative temperature of resistance coefficient (NTCR) features present in these materials. The imaginary impedance part (-Z″) is given in Figure III.13 ((d), (e), and (f)).

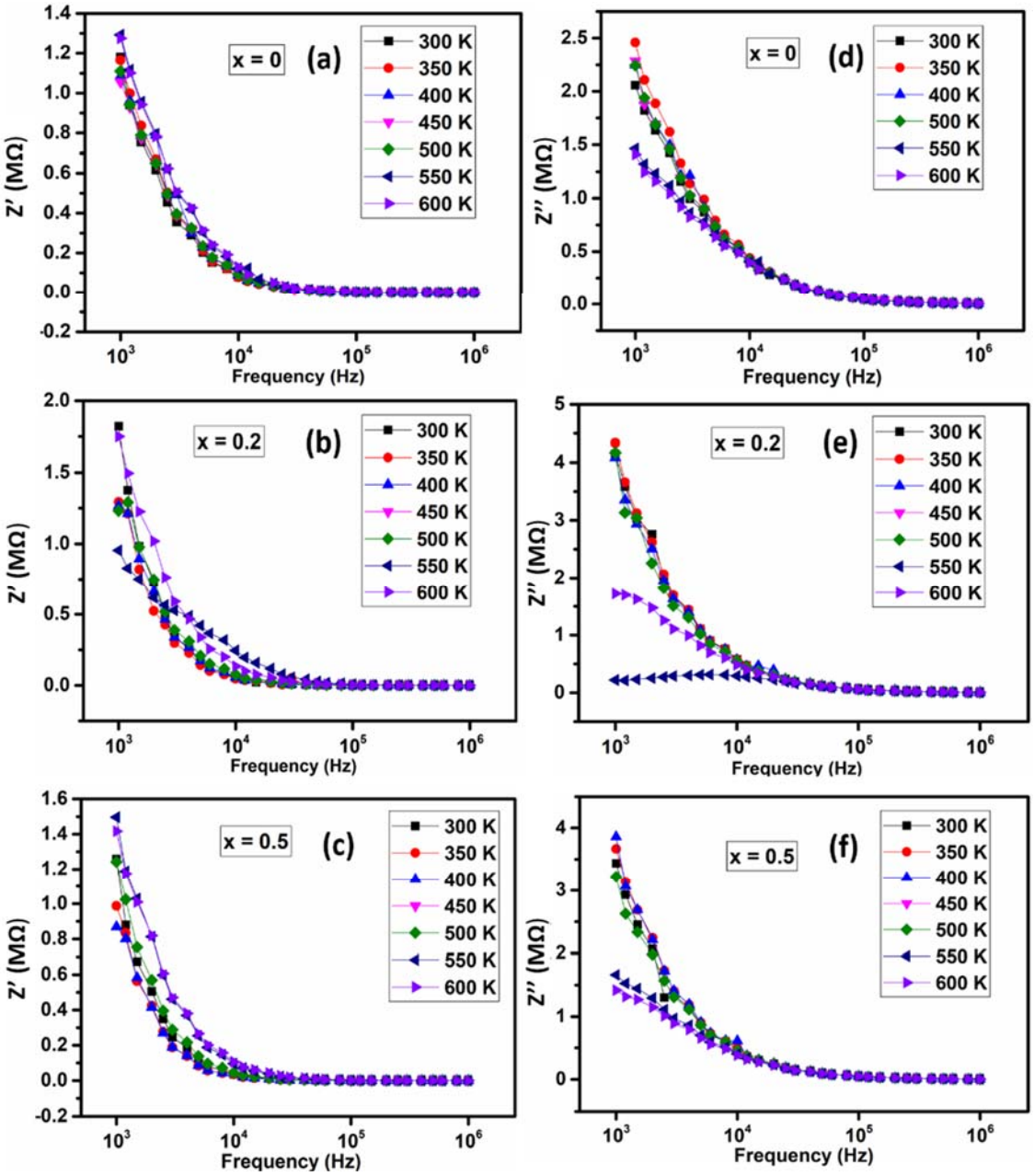

Figure III.13 : Frequency and temperature dependence of (a,b,c) real part (Z′) and (d,e,f) imaginary part (Z′′) of complex impedance of $Bi_{25}Fe_{1-x}Al_xO_{40}$ (x = 0.00, 0.20, 0.50) selenite materials.

The obtained results indicate that the imaginary part shows a higher value at low frequencies, before diminishing and merging in the high-frequency region. One can also observe that Z" variation represents a step-like anomaly at high temperatures for the $Bi_{25}Fe_{0.80}Al_{0.20}O_{40}$ pattern. The absence of this trend for the other curves is likely attributed to the fact that the peak maxima move towards frequencies below the investigated frequency range. This seems to point to the onset of a thermally activated

relaxation with distributed relaxation times. Furthermore, the merging of the -Z'' curves in the high-frequency region for all compounds is evidence of the increase in electrical conductivity along with the increase in temperature, driven by the release of space charge and the lowering of the barrier properties of these selenite materials [189].

5. Magnetic study of Al/Fe-sillenites

Magnetization measurements were performed using a SQUID MPMS3 magnetometer under an applied magnetic field of 100 Oe and 2000 Oe over the temperature range [2 K–400 K]. Likewise, the hysteresis curves were recorded at 10 K and 300 K with a maximum applied field of 4T.

5.1. Thermal evolution of the magnetization and the inverse of the susceptibility

Figure III.14 ((a) and (b)) represent the zero-field cooled (ZFC) and field cooled (FC) magnetization as a function of the temperature ranging from 100 to 400 K under an external magnetic field of (a) 0.01 T, and (b) 0.2 T, for the studied sillenite materials. Figure III.14 (c) describes the invers of the magnetic susceptibility χ^{-1} as a function of T. This is giving a better view of the transition mentioned in the magnetization versus temperature (Figure III.14 (a)). The magnetic susceptibility dependent on the Curie-Weiss law at high temperatures and defined following the above equation [190]:

$$\chi = \frac{C}{T + \theta_{CW}} \qquad \text{(III.6)}$$

where C, θ_{CW} are the Curie constant and Curie–Wiess constant, respectively.

Figure III.14 (a) shows the presence of an antiferro–paramagnetic transition for both $Bi_{24}FeO_{40}$ and $Bi_{24}Fe_{0.80}Al_{0.20}O_{40}$ compounds However, the absence of any anomalous behavior for the half-doped sillenite indicates the paramagnetic behavior of this compound in the investigated temperature range. Furthermore, the obtained results indicate the paramagnetic behavior of these materials under a higher applied magnetic field of 0.2 T (Figure III.14(b)).

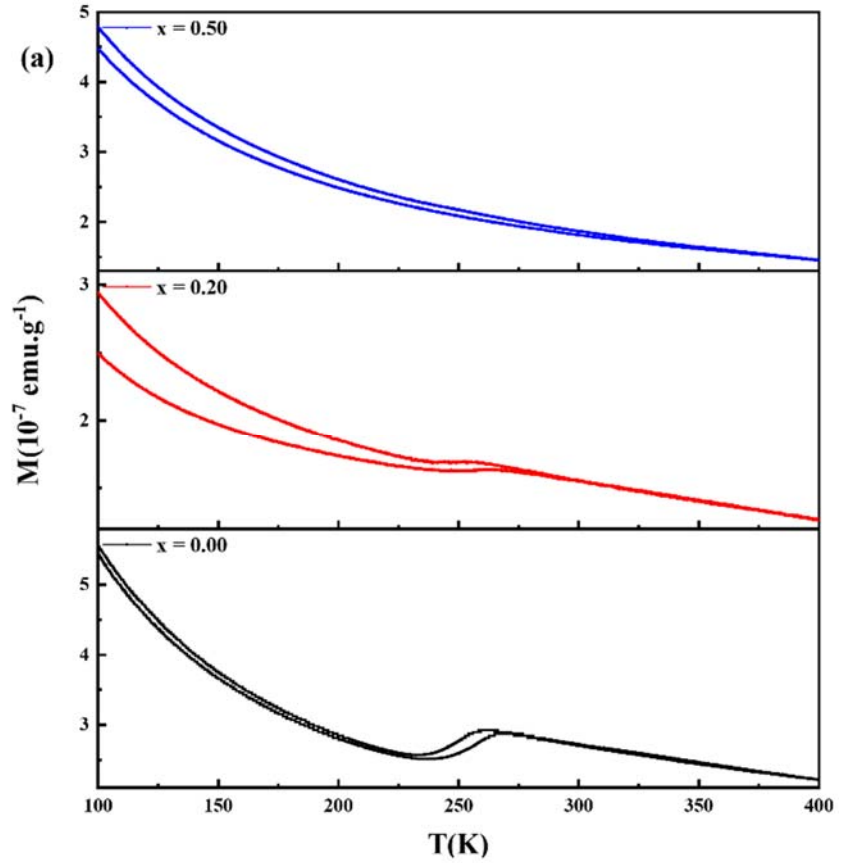
(a)
x = 0.50
x = 0.20
x = 0.00
M(10^-7 emu.g^-1)
T(K)

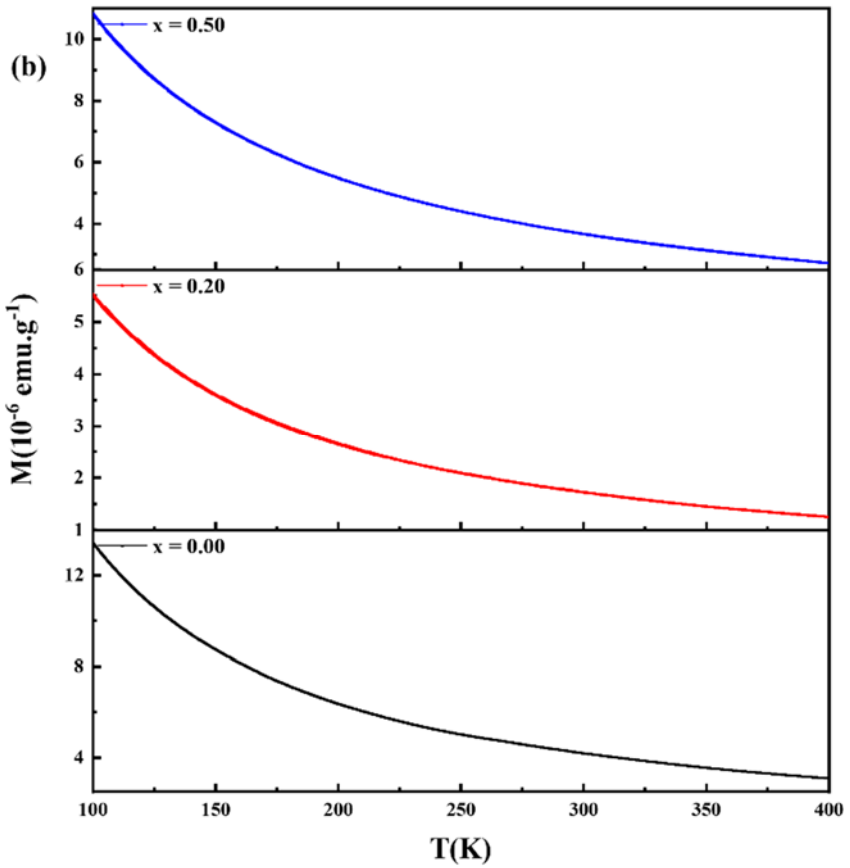
(b)
x = 0.50
x = 0.20
x = 0.00
M(10^-6 emu.g^-1)
T(K)

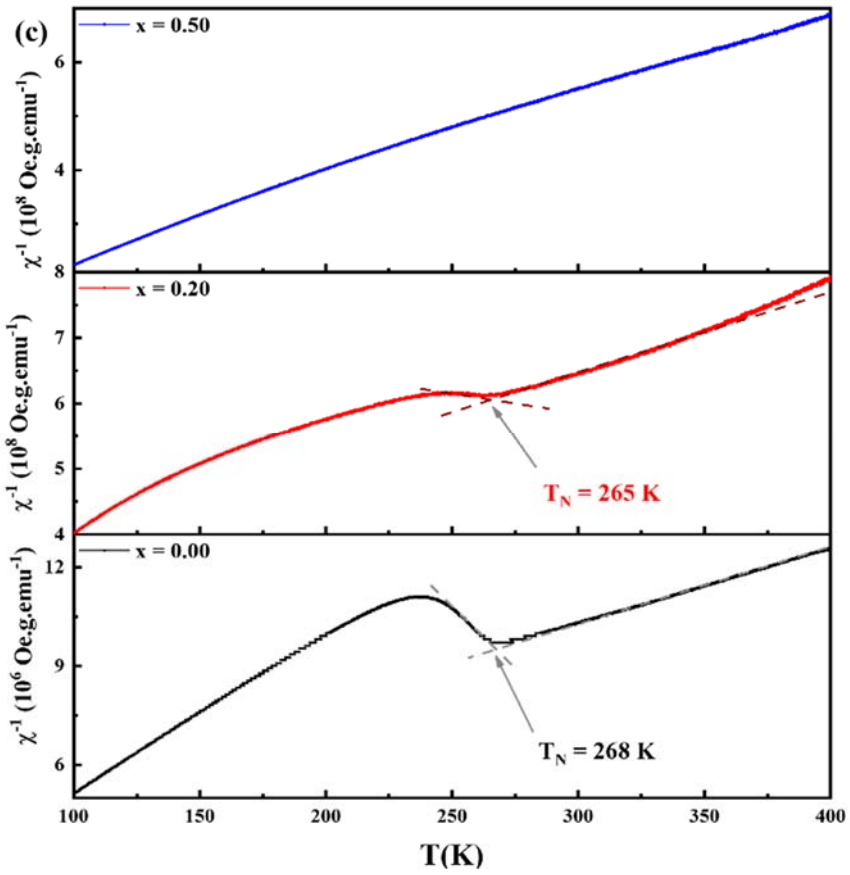

Figure III.14 : Temperature dependence of the zero-field cooled (ZFC) and field cooled (FC) magnetization of $Bi_{25}Fe_{1-x}Al_xO_{40}$ (x = 0.00, 0.20, and 0.50) measured under a magnetic field of (a) 100 Oe and (b) 2000 Oe. (c) represents the inverse of magnetic susceptibility χ^{-1} as a function of T under 100 Oe, for x = 0.00, 0.20, and 0.50.

The Curie–Wiess constant θ_{CW} take values of –150 K and –182 K for x = 0.00 and 0.20, respectively. The negative sign points on the prevalence of antiferromagnetic interactions, with T_N take values of 268 K and 265 K for x = 0.00 and 0.20, respectively. The Curie constant can be calculated using the following formula.

$$C = \frac{N_A g^2 \mu_B^2 S(S+1)}{3K_B} \qquad \text{(III.7)}$$

where N_A, k_B, g, μ_B, and S are the Avogadro number, the Boltzmann constant, the g-factor, the Bohr magneton, and the spin values of the considered compounds, respectively. The calculated Curie constant was found to be 9.18 10^{-8} m^3.K.mol^{-1}, 9.10 10^{-10} m^3.K.mol^{-1}, for x = 0.00 and 0.20, respectively. The obtained value for the substituted one is smaller than

that calculated for the pristine compound, due to the low interaction between Fe–Fe. Thus this value is approximately close to the results obtained for iron-sillenite [16].

Although the effective magnetic moment is defined as follow,

$$\mu_{eff} = g\sqrt{S(S+1)}\mu_B \quad \text{(III.8)}$$

The effective magnetic moments were calculated from the Curie constant, using equations (6) and (7). The calculated values of effective magnetic moments are 6.37 μ_B and 3.51 μ_B for x = 0.00 and 0.20, respectively. The calculated effective magnetic moment for x = 0.20 is found to be smaller than that calculated for the pristine compound. Thus, this value is lower than the theoretical value for Fe^{3+} ions in high-spin state 5.92 μ_B [16,191]. This is due to the substitution effect of non-magnetic Al^{3+} at Fe^{3+}–sites on the magnetic properties, which declines the superexchange $Fe(d^5)$–O–Bi–O–Bi–O–$Fe(d^5)$ interactions.

The slight increase in the magnetization found at this ordering temperature for the pristine material can be assigned to a weak ferromagnetic component due to the antisymmetric Dzyaloshinskii-Moriya interaction [192,193]. The observed antiferromagnetic interactions are the result of the superexchange $Fe(d^5)$–O–Bi–O–Bi–O–$Fe(d^5)$ interactions.

5.2. Hysteresis cycle measurements

Hysteresis cycles were measured to verify the presence of the mechanism highlighted above and to better understand the magnetic behavior of this compound. As an example, the variation of the magnetization Iron-sillenite compound, recorded at 10K and 300 K and plotted in Figure III.15((a), (b), and (c)).

These findings are asserted the noticed phenomena in Figure III.14. Indeed, the recorded curves at 10 K for the studied materials shown a clear hysteresis loop, with negligible coercive fields of H_c = 36, 34, and 33 Oe and remnant magnetizations (M_r) of about 2.45 10^{-6}, 1.66 10^{-6}, and 8.99 10^{-7} emu.g^{-1}, for x = 0.00, 0.20, and 0.50, respectively. The linear curve observed at room temperature asserts the paramagnetic behavior of the studied materials. Moreover, the magnetization versus the magnetic field does not reach saturation even at 4T for all compounds. It can be concluded that Aluminium substitution has no effect on the hysteresis loop behavior of iron-sillenite. However, it becomes

paramagnetic at low temperature after the substitution of 50% Al_2O_3. These results are consistent with previous reports, revealing the weak ferromagnetic behaviour of iron-sillenite with a coercivity of 10 Oe and 50 Oe [36,73].

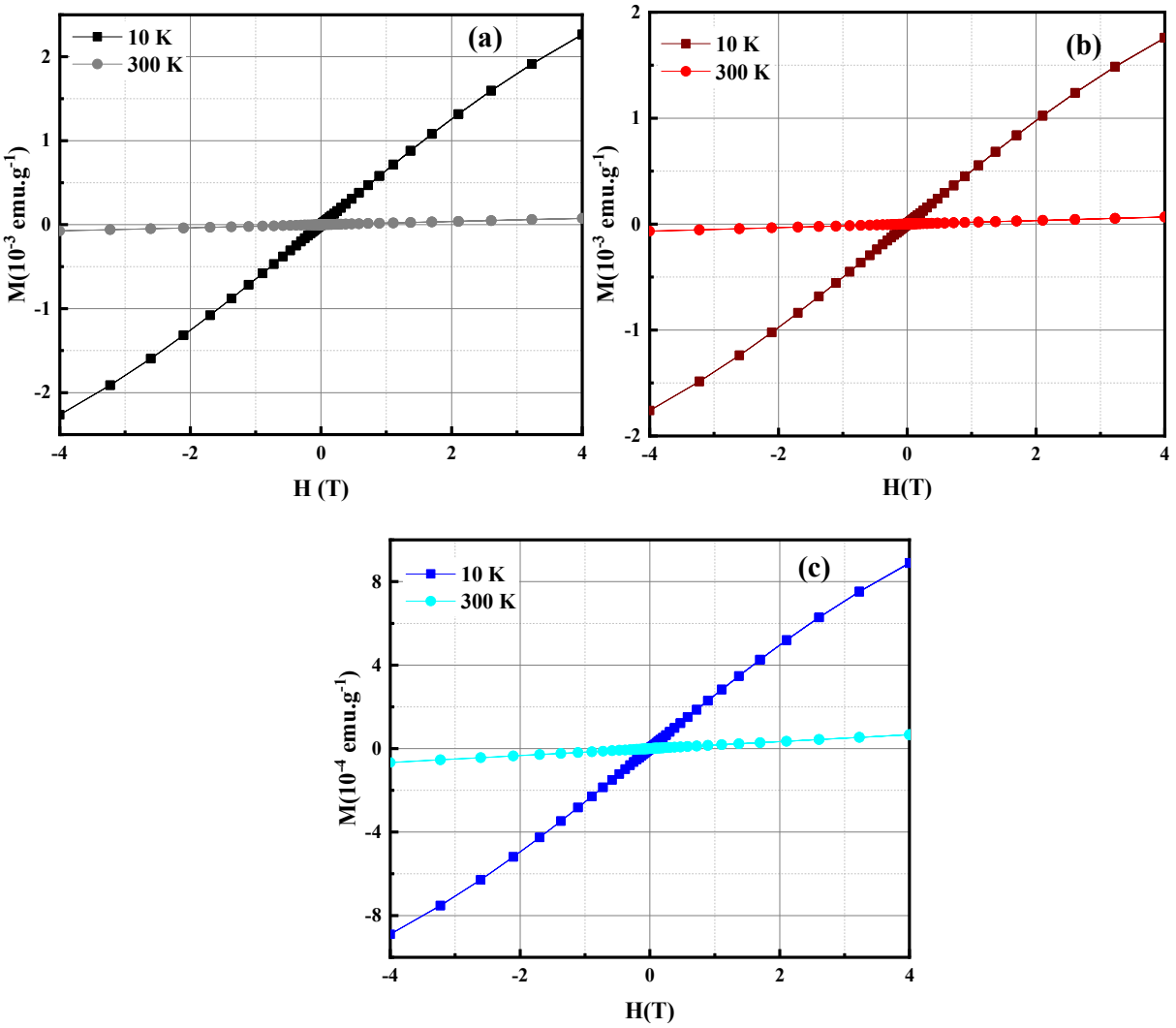

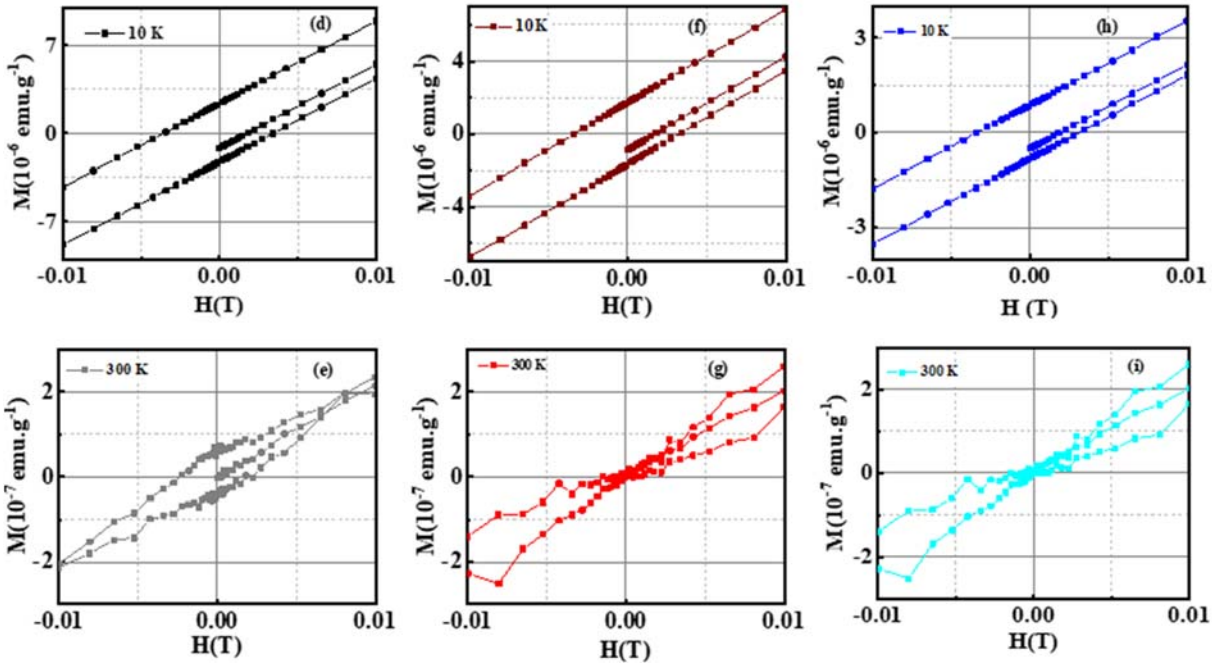

Figure III.15 : Magnetization (M) versus applied magnetic field (H) measured at 10 and 300 K for $Bi_{25}Fe_{1-x}Al_xO_{40}$, for (a) x = 0.00, (b) x = 0.20, and (c) x = 0.50. (d–h) and (e–i) give the zoom view of the magnetic hysteresis loops for x = 0.00, 0.20, and 0.50, at 10 K and 300 K, respectively.

6. Optical characterization of Al/Fe-sillenites

The optical band gap of γ-$Bi_{25}FeO_{40}$ material was determined based on optical reflectance measurements. That recorded at room temperature by means of a Specord ®210 Plus–Analytik Jena UV-Visible spectrometer, equipped with a 150 mm ILN-925 integrating sphere.

The optical absorption coefficient (α) is calculated from the reflectance data according to the Kubelka-Munk equation [125]:

$$F(R) = \alpha = \frac{(1-R)^2}{2R} \qquad \text{(III.9)}$$

where R is the diffuse reflectance and F(R) is the Kubelka-Munk function.The optical band gap energy is calculated based on Tauc's equation [194]:

$$(\alpha h\nu) = A(h\nu - E_g)^n \qquad \text{(III.10)}$$

where $h\nu$ is the photon energy, A is a constant of proportionality depending on the nature of the material, and n is equal to 1/2 for a direct allowed transition or 2 for an

indirect one. The diffuse reflectance spectrum (DRS) and optical bandgap energy of γ-$Bi_{25}FeO_{40}$ are illustrated in Figures III.16 (a) and (b), respectively.

From Figure III.16 (a) one can notice five clear absorption bands, that shift to high wavenumber values with increasing of Al-substitution ratio. The first one located at 351 nm is due to the d-d electron transition of Fe^{3+} on tetrahedral sites ($^6A_1(^6S) \rightarrow {}^4T_1(^4P)$) [195,196]. In addition to that, it is attributed to the $^1S_0 \rightarrow {}^3P_1$ electronic transitions of Bi^{3+} [199,200]. The second and the third ones observed at about 474 nm 640 nm, respectively. Moreover, the second one is due to the ligand-field transitions of Fe^{3+} cations from ligand to metal [199]. Besides to $^3P_1 \rightarrow {}^1S_0$ electronic transitions of Bi^{3+} on the octahedral site [198,200]. The latest bands situated at 624, 825, and 852 nm is assigned to the d-d ($^6A_1(^6S) \rightarrow {}^4T_2(^4P)$) transition of Fe^{3+} cations [199,201].

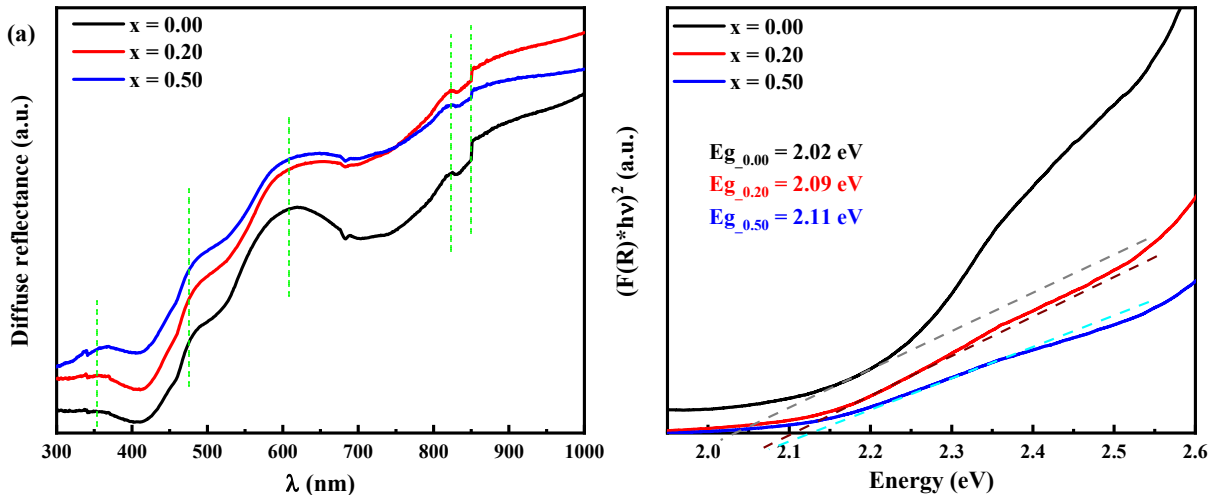

Figure III.16: (a) Diffuse reflectance spectrum measured at 300 K and (b) Tauc plot of $Bi_{25}Fe_{1-x}Al_xO_{40}$ (x = 0.00, 0.20, and x = 0.50) compounds.

The studied materials exhibit a direct band gap with energies of 2.02, 2.09, and 2.11 eV, in accordance with the literature [16,66]. The increasing behavior of band gap energies as a function of the substitution ratio is due to the dielectric behavior of aluminium. Moreover, previous works reported the dielectric behavior of Al_2O_3 with a direct band gap of about 4.90 eV, which decreases to 3.40 eV with a Bi_2O_3 addition of 3%, and asserted their photocatalytic activities [180]. Furthermore, the narrow band gap energies and the high absorption bands in the visible area of $Bi_{25}Fe_{1-x}Al_xO_{40}$ (x = 0.00, 0.20, and x = 0.50), provide them to be promising candidate for the photodegradation of pollution and colorants.

7. Conclusions

In this chapter, we presented the experimental investigation of New Sillenite materials $Bi_{25}Fe_{1-x}Al_xO_{40}$ ($x = 0.00$, 0.20, and $x = 0.50$) powders. The first section of this chapter was devoted to the description of the synthesis method of $Bi_{25}FeO_{40}$, followed by structural study, that achieved via the XRD pattern, SEM, FT-IR, and Raman analysis. $Bi_{25}Fe_{1-x}Al_xO_{40}$ ($x = 0.00$, 0.20, and $x = 0.50$) were synthesized using the conventional solid–state reaction process. The recorded XRD patterns show that these sillenite materials crystallize in a body-centered cubic structure (I23 space group). The decrease of the cell parameters as a function of the substitution ratio is explained based on the relative difference in ionic radii of Al^{3+} and Fe^{3+} ions. SEM morphological analysis reveals the formation of irregular agglomerated grains with a decrease in grain size when increasing the Al-doping rate. The insertion of Al in the sillenite matrix and its effect on vibrational properties have been highlighted and discussed through Raman and FT–IR spectroscopies. The DSC analysis highlighted the occurrence of various phenomena related to the onset of structural transitions and dielectric features. The frequency and temperature dependent dielectric behavior have been studied. The frequency dependence of electrical conductivity is analyzed using Jonscher's law, and the conductivity process is confirmed by the correlated barrier hoping mechanism. Besides, the temperature dependence of electrical conductivity allows the estimation of activation energies and suggests that the conduction process is governed by the motion of oxygen vacancies at high temperatures. The impedance spectroscopy results confirm the appearance of the relaxation phenomenon in these samples exhibiting semiconductor behavior with both positive temperature of resistance coefficient (PTCR) and negative temperature of resistance coefficient (NTCR). The temperature dependence of ZFC, FC magnetization, and the inverse of the magnetic susceptibility highlight the antiferromagnetic behavior below T_N of about 268 and 265 K, for $x = 0.00$ and 0.20, respectively. $Bi_{25}Fe_{0.50}Al_{0.50}O_{40}$ sample shows paramagnetic behavior. These results are claimed using the M–H hysteresis measurements and the negative value of the Weiss constant (θ_{CW} ($x = 0.00$) = –150 K and θ_{CW} ($x = 0.20$) = –182 K). The narrow bandgap and the high absorption in the UV and visible ranges make these materials suitable candidates for photocatalysis applications. For more understanding the mechanism of pollution degradation using the photocatalytic application, we will implement a theoretical study of $Bi_{25}FeO_{40}$ (Chapter IV).

Chapter IV

Theoretical investigation of iron-sillenite $Bi_{25}FeO_{40}$: DFT and MCs

To better understand and compare the obtained physicochemical properties of the studied compound which were calculated and measured experimentally, we will describe the theoretical investigation of iron-sillenite. The first section is devoted to the description of the computational method used for the simulation of $Bi_{25}FeO_{40}$, followed by the structural properties and the magnetic stability of $Bi_{25}FeO_{40}$, which will be discussed in the second section. Then, the electronic and optical properties of the studied compound will be described in sections three and four, respectively. The photocatalytic properties (PEC) will be studied with and without pH effect and described in the section 6. The electrical and the magnetic properties will be presented in the latest sections.

1. Computational method for calculation of iron-sillenite $Bi_{25}FeO_{40}$

1.1. Computational details

To study the physicochemical properties of $Bi_{25}FeO_{40}$, we will use the Wien2k [156] and Quantum Espresso (QE) [202] packages. The structural property was performed using the Full-Potential Linearized Augmented Plane Wave method (FP-LAPW) [155] and realized in Wien2k package, using the non-magnetic structure. Furthermore, the magnetic stability, electronic properties, and the magnetic moments will be calculated via QE package, and the optical properties will be calculated using Yambo code [203]. The PEC properties will be calculated by the QE and Yambo codes. The BoltzTraP code based on the Boltzmann equations [163], has been employed to determine the thermoelectric (TEC) properties. The magnetic properties were calculated using the Monte-Carlo simulation (MCs).

The projector augmented wave pseudopotentials were used for the description of the electron-ion interactions. As well as a functional type Perdew-Burke Ernzerhof (PBE) exchange correlation nonlinear [204], as it gives precise results that match the experimental data (Chapter III). The valence wave functions were expanded on a plane-wave basis with cut-off energy of 65 Ry. The Brillouin zones of the unit cells are presented by a Monkhorst-pack special k-point scheme with 3×6×6 grid meshes and the atomic displacement distance of 0.01 Å.

1.2. Monte-Carlo simulation

The Monte-Carlo simulation (MCs) combined with the Metropolis algorithm were adopted [205], to investigate the magnetic properties of iron-sillenite. The Hamiltonian

energy equation of the studied system, follows the Ising model, and described in the equation above:

$$H = -J_1 \sum_{<i,j>} S_i S_j - J_2 \sum_{<i,j>} S_i S_j - \Delta \sum_i S_i^2 - h \sum_i S_i \quad \text{(IV.1)}$$

where; <i,j>, J_1, J_2, Δ, and h, represent the close neighbours, the magnetic exchange couplings between the first nearest neighbours and the second ones of the Fe atoms, the crystal field, and the external magnetic field applied on all system sites, respectively. The magnetic properties are calculated using unit cell of 32×32×32.

The iron spins (S_i(Fe)) take values equal to ± 2, $\pm$ 1, and 0. The applied Metropolis algorithm is applied to impose the cyclic boundary conditions on the lattice and create configurations by crossing consecutively over the lattice and doing single-spin-flip tries. The flip of spin is selected depending on the difference of energy between the studied spin and its neighbors. The spin will flip directly if the difference in energy is negative. Otherwise, it will flip if the number chosen randomly is smaller than the Boltzmann factor $e^{-\beta H}$. At 10^5 MCs (Monte Carlo steps) per spin, the data was generated by rejecting the first 10^4 Monte Carlo steps. Various iterations were performed to reach thermal equilibrium, followed by further iterations conducted to investigate some physical parameters such as magnetization and magnetic susceptibility.

2. Structural properties and magnetic stability of iron-sillenite $Bi_{25}FeO_{40}$

2.1. Structural properties

To study the structural properties of iron-sillenite (Figure IV.1), we start with the optimization of the crystalline structure of $Bi_{25}FeO_{40}$ (Figure IV.2). The structural optimization was achieved using a non-magnetic structure, to obtain the optimal lattice parameters that correspond to the equilibrium state of the system. For this reason, we computed the total energy as a function of the unit cell volume as shown in Figure IV.2. Murnaghan's equation [206] was used to fit the obtained data and determine the equilibrium cell volume and lattice parameters, V = 1082.07 (6) Å^3 and a = 10.26 (1) Å, respectively. The obtained results are in good agreement with the previous experimental values [68] and with the affined cell parameters mentioned in chapter III (Section 2.1). These correspond to a unit cell volume 0.60% larger than that reported at room temperature, as determined through previous works [16,18,68].

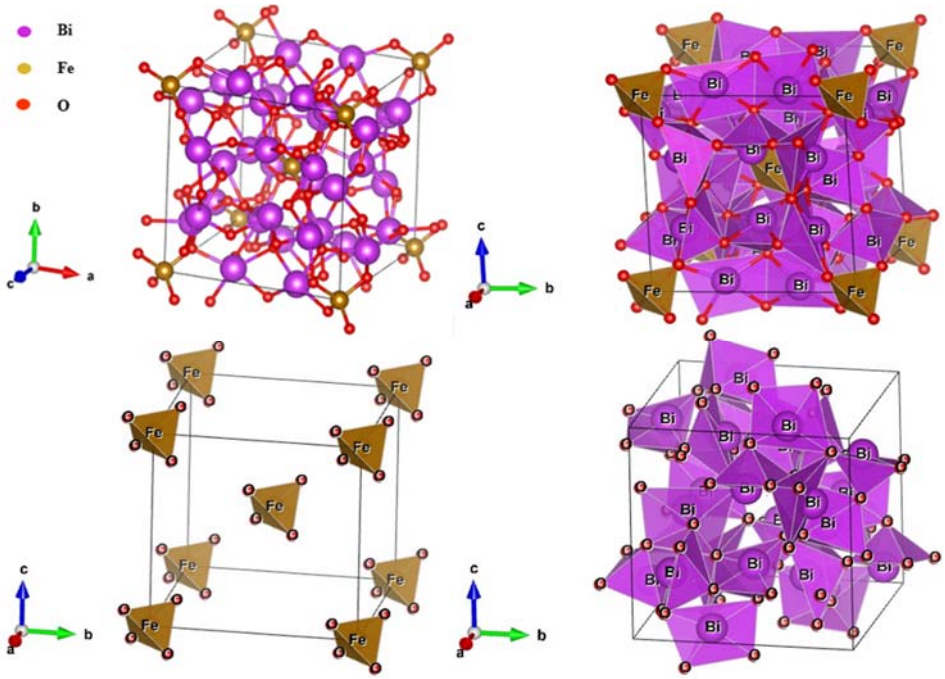

Figure IV.1: Illustration of the crystalline structure of $Bi_{25}FeO_{40}$ [16,18,68].

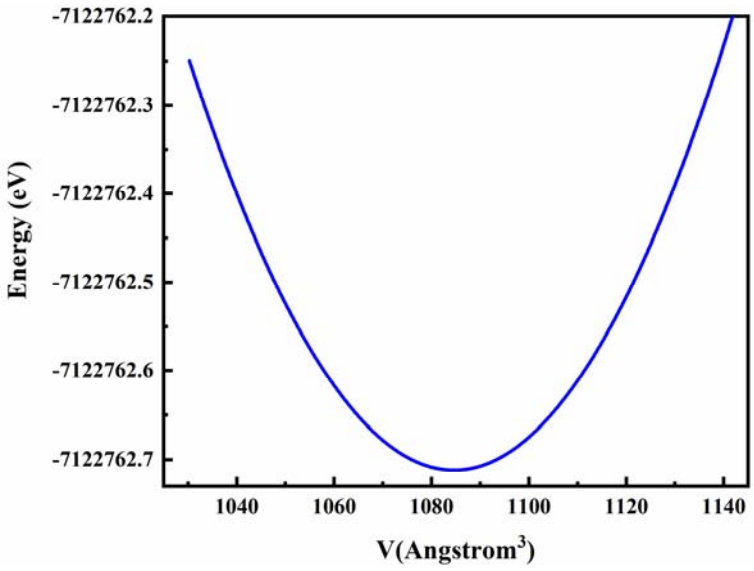

Figure IV.2: The unit cell volume depends on the total energy of $Bi_{25}FeO_{40}$.

It is obvious that there is an increase in the theoretical volumes is expected since the GGA tends to expand lattice constants in comparison with the experimental values. Therefore, we used the optimized lattice parameters for the rest of our theoretical calculations.

2.2. Magnetic stability

The structural magnetic stability has been performed by calculating the total energy as a function of three different magnetic configurations, as presented in Figure IV.3 (FM, AFM1, and AFM2), using a 2×1×1 supercell (132 atoms). The most stable magnetic structure is the AFM2. The obtained results agreed well with the findings in magnetic properties measured experimentally and presented in Chapter III.6. For this reason, we will continue our investigation with the selected antiferromagnetic structure (AFM2).

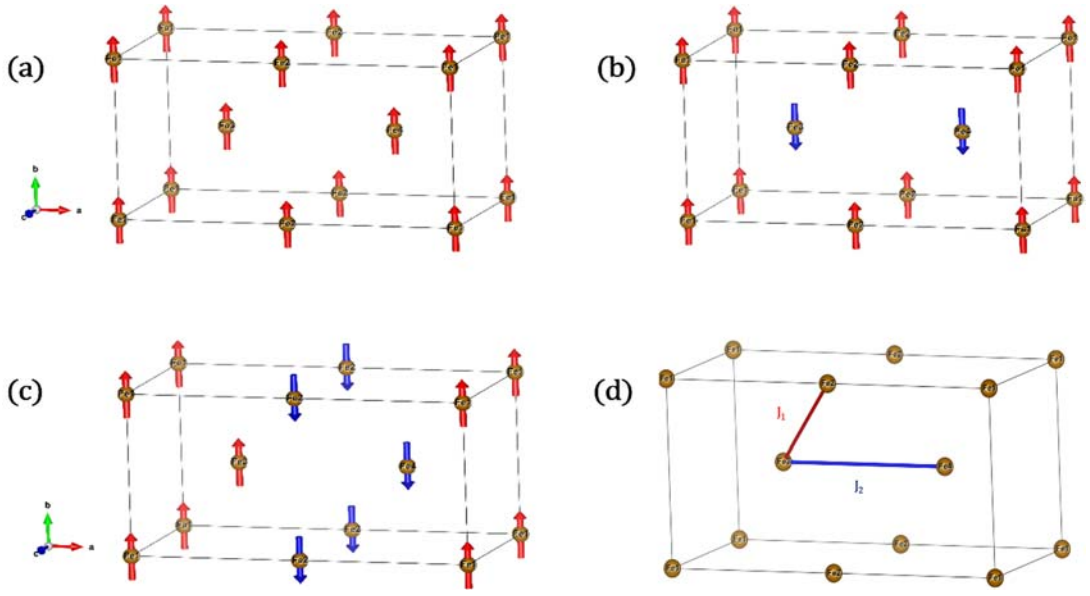

Figure IV.3: Magnetic configurations used for the exchange coupling calculation of $Bi_{25}FeO_{40}$ in; (a) FM, (b) AFM1, (c) AFM2. The magnetic couplings in $Bi_{25}FeO_{40}$ (made with Vesta software [207]) are presented in (d).

3. Electronic properties of iron-sillenite $Bi_{25}FeO_{40}$

To analysis the physical properties of the studied compound, the electronic band structure, and the density of states (DOS) will be implemented in this section, utilizing the QE due to the computational burden (132 atoms) compared to the unit cell calculations (66 atoms). These allow to explore and understand the nature of the bonds formed between the different elements. The electronic properties of $Bi_{25}FeO_{40}$ are clarified employing the band structure (BS) and both total and partial density of states (TDOS and PDOS) calculated within optimized values.

3.1. Band structure calculation

The band structure calculation is plotted in Figure IV.4. The $Bi_{25}FeO_{40}$ is found to present a p-type semiconducting with a direct bandgap along the Γ point. The electronic band gap energy is 1.87 eV.

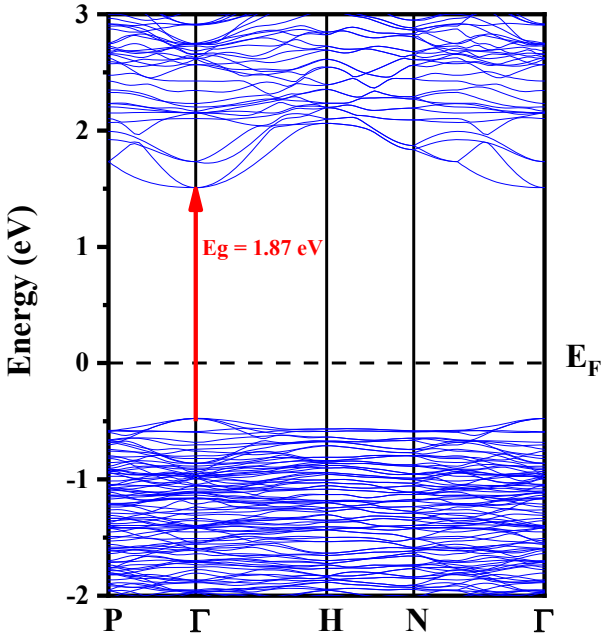

Figure IV.4: Band structure of iron-sillenite.

3.2. Density of state calculation

The origin of computed BS is further analyzed based on the investigation of the density of state plot (Figure IV.5). From Figure IV.5, one can notice a minor increase of the VB towards the Fermi level. This can be explained by the hybridization between Fe-3d and O3-2p orbitals forming tetrahedral coordination and a fewer mixing of Bi-6p and Bi-6s orbitals with O1-2p and O2-2p orbitals. Furthermore, the lowest energies of the VB as well as the conduction band are mainly occupied by the Fe-3d states. Moreover, the total and partial densities of iron-sillenite assert the p-type semiconducting behavior of iron-sillenite, as mentioned before in previous section in this chapter (Section 3.1).

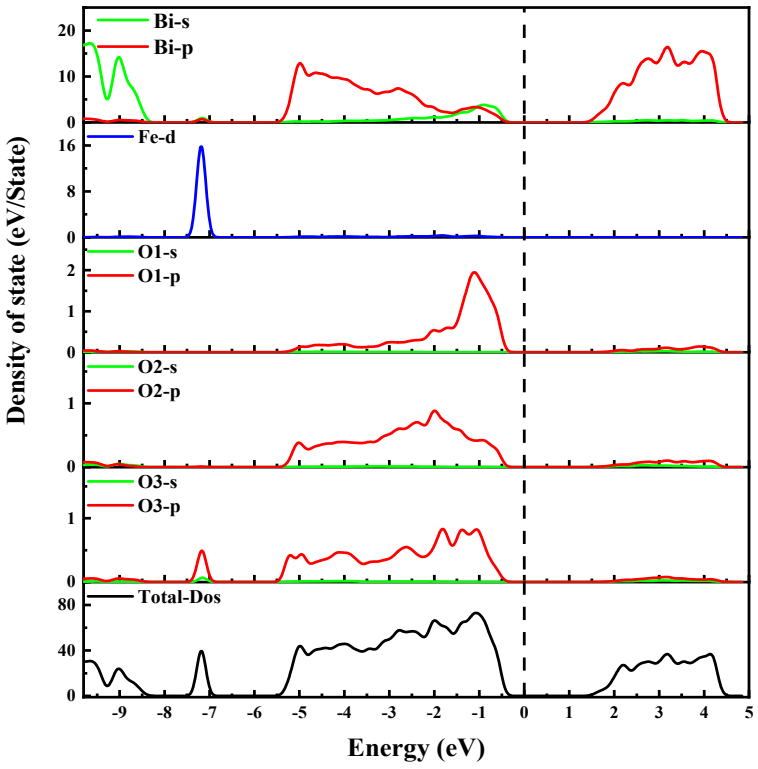

Figure IV.5: Total and partial DOS of iron-sillenite.

4. Optical properties of iron-sillenite $Bi_{25}FeO_{40}$

The optical properties were investigated via the calculation of the absorption coefficient α(ω), reflectivity R(ω), transmittance T(ω), and the optical band gap energy E_g following [100] direction, due to the optical isotropy behavior which is attributed to the cubic symmetry of $Bi_{25}FeO_{40}$. Those parameters can be described following below equations:

$$\alpha(\omega) = \frac{2\pi\omega}{C} k(\omega) \quad \text{(IV.2)}$$

$$R(\omega) = \left|\frac{1 - n(\omega)}{1 + n(\omega)}\right|^2 \quad \text{(IV.3)}$$

where, $k(\omega)$ and n(ω) are the extinction and the refractive index, respectively. Moreover, the transmittance (T) was calculated based on reflectivity (R) and absorption coefficient (A) using the following formula:

$$A + R + T = 100\ \% \quad \text{(IV.4)}$$

All these parameters are expressed in %. The extinction and the refractive indexes were calculated based on the real and imaginary parts of dielectric function $\varepsilon_1(\omega)$ and $\varepsilon_2(\omega)$, respectively, following below equations:

$$n(\omega) = \left[\frac{\sqrt{\varepsilon_1^2(\omega) + \varepsilon_2^2(\omega)} + \varepsilon_1(\omega)}{2}\right]^{1/2} \quad \text{(IV.5)}$$

$$k(\omega) = \left[\frac{\sqrt{\varepsilon_1^2(\omega) + \varepsilon_2^2(\omega)} - \varepsilon_1(\omega)}{2}\right]^{1/2} \quad \text{(IV.6)}$$

The real part of the dielectric function $\varepsilon_1(\omega)$ describes the polarization of a medium crossed by a light beam of an energy hν. Although, the imaginary part $\varepsilon_2(\omega)$ depicts the absorption of a material. They are calculated via the Ehrenreich and Cohen formalism as follow:

$$\varepsilon(\omega) = \varepsilon_1(\omega) + i\,\varepsilon_2(\omega) \quad \text{(IV.7)}$$

$$\varepsilon_1(\omega) = 1 + \frac{2}{\pi}\int_0^{\infty} \frac{\varepsilon_2(\omega')\omega' d\omega'}{\omega'^2 - \omega^2} \quad \text{(IV.8)}$$

$$\varepsilon_2(\omega) = \frac{4\pi^2 e^2}{m^2\omega^2}\sum_{i,j} |< i|M|j >|^2 \times \left(f_i(1-f_i)\right)\delta\left(E_f - E_i - \hbar\omega\right)d^3k \quad \text{(IV.9)}$$

where M represents the matrix elements for the transitions between the valence band and the conduction band, e and m are the charge and the mass of the electrons, respectively. ω represents the frequency of the incident photon, f_i is the Fermi distribution function for the state, E_i the energy of the electron in the i^{th} state, i and j are initial and final states, respectively.

Figure IV.6 ((a) and (b)) presents the absorption coefficient and the variation of $(F(R)\,h\upsilon)^{1/2}$ as a function of hν, respectively. From the absorption coefficient plot of iron-sillenite (Figure IV.6 (a)) is low in the region from 0.00 to 2.00 eV, and the absorption process starts from 1.63 eV. The optical band gap energy is calculated using the straightforward extrapolation method [208]. As a results, the value of the band gap energy is 2.38 eV. These findings are closed to the value presented in Chapter III (Section 7), and results given by Sun et al. [74], Senuliene et al. [209], Kargin and Skorikov [210], and Zhang et al. [42]. On the other hand, band gap values between 1.68 eV and 2.00 eV were also reported in previous frameworks [17,66,74]. The wide-ranging variation of the optical band gap is probably caused by different methods to determine the band gap energy [211], different syntheses and/or different particle sizes. The obtained optical features allow the $Bi_{25}FeO_{40}$ compound to be considered a good coating material and a potential candidate for Dye-Sensitized Solar Cells applications (DSSC) [23,24].

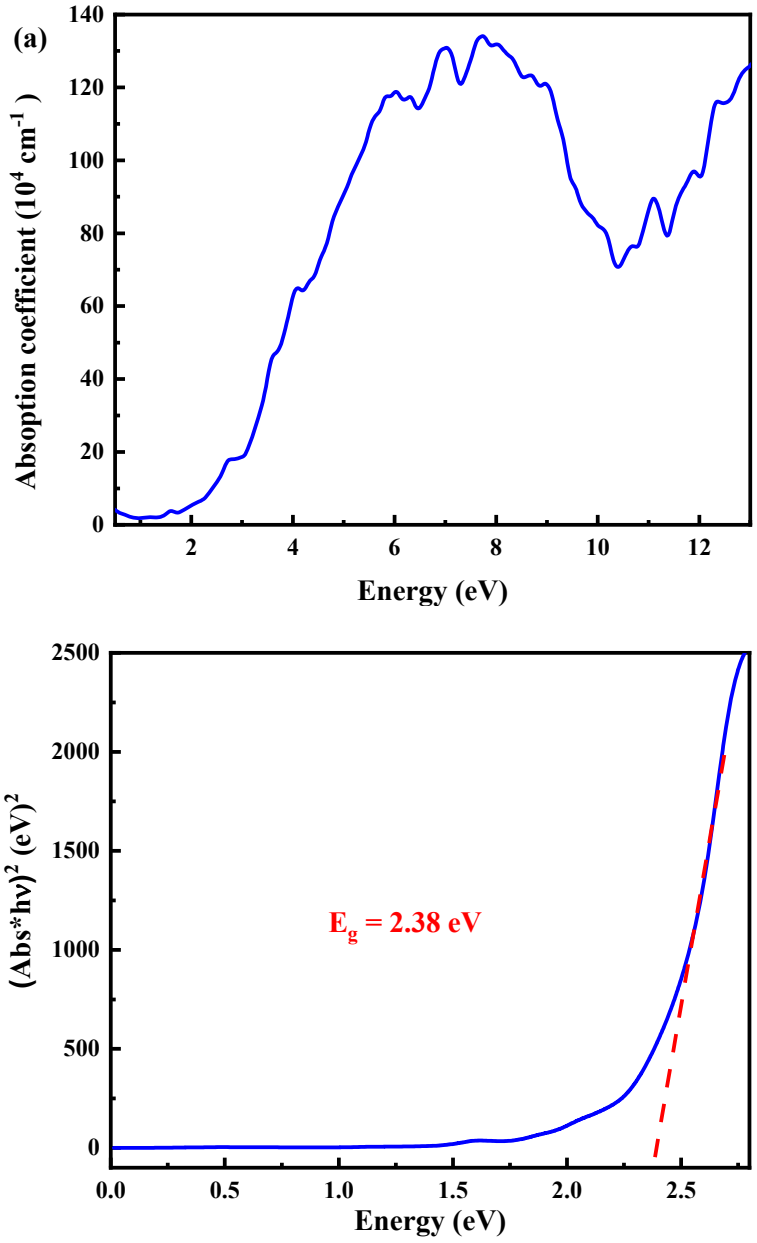

Figure IV.6: a) Absorption coefficient of iron-sillenite and b) variation of $(Abs \times h\upsilon)^2$, of iron-sillenite as function of hυ.

The simulated compound displays a good absorption of about 78.00% ($1.35\ 10^6$ cm^{-1}) in the UV range till reaching a value of 27.00 % ($4.57\ 10^5$ cm^{-1}) at a wavenumber of 345 nm. It exhibits a weak absorption in the visible range 11.00% ($1.20\ 10^5$ cm^{-1}). While the reflectivity begins with the value of 73.00%, then decreases to reach a value of 54.00% at a wavenumber of 447 nm (Visible range). Further, the reflectivity of iron-selenite, stabilized in a ratio of 47.00 % in the IR area. $Bi_{25}FeO_{40}$ shows low transmittance in the UV, then increases to a ratio ranging from 36.00% to 53.00% in

the visible region and stabilizes in the IR region below 57.00%. The obtained optical properties allow the $Bi_{25}FeO_{40}$ compound to be considered as a good coating material.

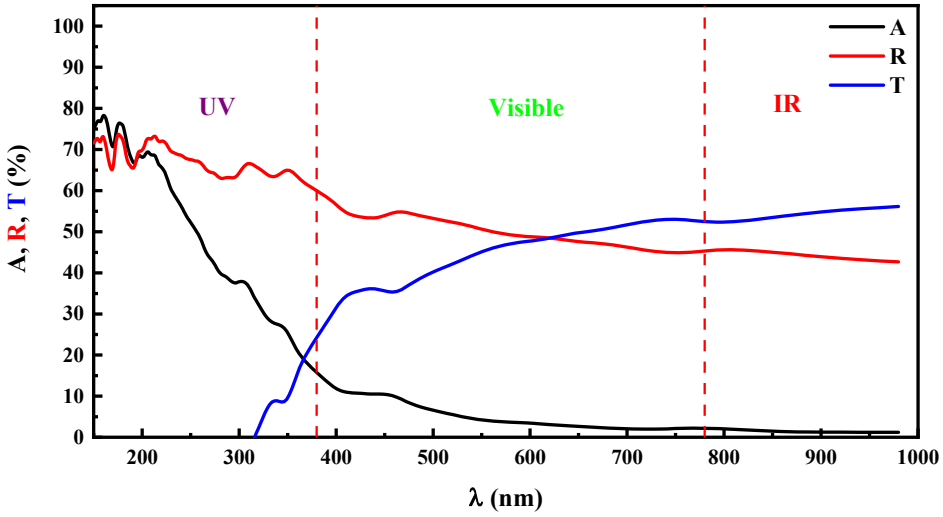

Figure IV.7: Absorption coefficient (A), reflectivity (R) and transmittance (T) evolution as function of wave number of iron-sillenite.

5. Photocatalytic properties of iron-sillenite $Bi_{25}FeO_{40}$

Among the photocatalysis application characteristic parameters, the optical band gap energy, and the valence band maxima (VBM) as well as the conduction band minima (CBM) edges, are considered as typical parameters for photocatalysis application. These parameters play a significant roles in the redox reactions in the electrolyte system [25]. For this purpose, we have investigated the improvement of photocatalytic properties of irons-sillenite under pH effect (pH varying from 0 to 14).

5.1. Photocatalytic properties of $Bi_{25}FeO_{40}$ without pH effect

The band-edge potential levels of $Bi_{25}FeO_{40}$ photocatalysis without pH effect, are identified by using the well-known Mulliken electronegativity theory [44]. The value of valence band maxima (VB) and conduction band minima (CB) energies can be calculated using the following equations:

$$E_{VB}^{0} = \chi_e - E_0 + 0.5E_g \quad \text{(IV.10)}$$

$$E_{CB}^{0} = E_{VB}^{0} - E_g \quad \text{(IV.11)}$$

where, E_{VB}^{0} and E_{CB}^{0} are the valence band and the conduction band edge potential at pH = 0, respectively. χ_e is the absolute electronegativity of a semiconductor, and take value of

6.24 for $Bi_{25}FeO_{40}$, and E_0 is the energy of free electrons on the hydrogen scale ($E_0 = 4.5eV$) [25]. The calculated band gap energy (E_g) of the studied compound is 2.16 eV.

The electrons and holes effective masses (m_h^* and m_e^*) at the band edges of the studied compound, were calculated based on their k-vector band structures, which were obtained from the first-principale calculation DFT/GGA-PBE method, using the following expression:

$$\left(\frac{1}{m^*}\right)_{i,j} = \frac{1}{\hbar^2}\frac{\partial^2 E_n(k)}{\partial k_i k_j} \ (i,j = x,y,z), \qquad \text{(IV.12)}$$

where i and j represent reciprocal components and E(k) is the dispersion relation for the n-band. The values of these effective masses are presented in Table IV.1.

The relative effective mass ratio (D) of photogenerated electrons and holes was calculated to estimate the charge separation efficiency [11]. This parameter playing a significant role in photocatalysis and can be evaluated via the following formula:

$$\mathrm{D} = m_h^*(\mathrm{m_0}) \,/\, m_e^*(\mathrm{m_0}) \qquad \text{(IV.13)}$$

Generally, a higher D value implies a higher probability of photo-induced electron-hole pairs separation, thereby a lower recombination rate to promote the photocatalytic activity. The relative ratio of effective mass is greater than unity (Table IV.1), highlighting the reduction of generation recombination of electron-hole pairs, affirm the high performance of Iron-sillenite in the PEC application [79]. These results are found to be better than that reported for $SrTiO_3$ (2.17), $NaTaO_3$ (2.29), and $KTaO_3$ (2.25), considered as the most promising candidates for environmental remediation and solar energy conversion [11].

Table IV.1: Carrier effective masses and the relative ratio (D) of the effective masses

$m_h^*(\mathrm{m_0})$	$m_e^*(\mathrm{m_0})$	D
14.12	6.15	2.30

Adding to the high absorption in the UV and visible range, narrow band gap energy, and the high value of the relative ratio of effective masses of $Bi_{25}FeO_{40}$. The photocatalytic reaction mechanism has been investigated to allow further comprehension of the mechanism of dyes photodegradation and/or water treatment using $Bi_{25}FeO_{40}$ as a catalyst.

The photocatalytic reaction mechanism is shown in Figure IV.8. When the incident photon is equal to or greater than the bandgap energy of Iron-Sillenite, the electrons gain energy. As a result, these electrons transfer from the valence band (VB) to the conduction one (CB), generating holes (h^+) in the VB and electrons (e^-) in the CB. According to the NHE (normal hydrogen electrode), the CB and VB edge potentials of $Bi_{25}FeO_{40}$ are calculated and take values of 0.66 eV and 2.82 eV, respectively. Consequently, the photoinduced holes in the valence band can oxidize water (H_2O) and generate hydroxyl radicals O_2, H_2O_2, and O_3. These radicals can reduce, decompose, and/or remediate the organic pollutants, dye molecules and dyes under solar UV, or visible light irradiation [5,7,46].

The photocatalytic mechanism of the studied compound can be described as follow.

$$4\mathrm{H}^+ + O_2 + 4e^- \rightarrow 2H_2O \quad \text{(IV.14)}$$

$$H_2O_2 + 2\mathrm{H}^+ + 2e^- \rightarrow 2H_2O \quad \text{(IV.15)}$$

$$O_3 + 2\mathrm{H}^+ + 2e^- \rightarrow O_2 + H_2O \quad \text{(IV.16)}$$

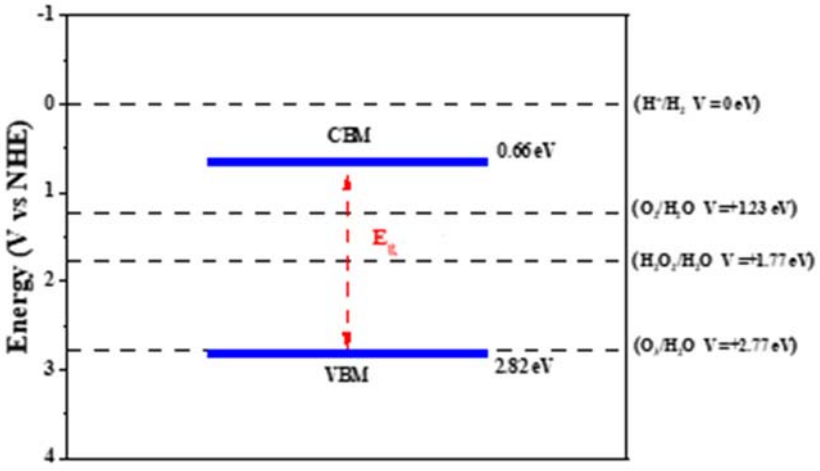

Figure IV.8: Schematic illustration for the calculated energy band diagram of $Bi_{25}FeO_{40}$ for the photocatalytic property without pH effect (pH = 0).

5.2. Photocatalytic properties of $Bi_{25}FeO_{40}$ under pH effect

In this section we will study the effect of pH on the photocatalytic mechanisms since it is based on the separation of water. And the water splitting process is widely affecting by the pH of the solutions. By variation of the solution pH, the conduction and valence band edges can be calculated as follows [212]:

$$E_{VB}^{pH} = E_{VB}^{0} - 0.05911 \times (pH - pH_{pzc}) \quad \text{(IV.18)}$$

$$E_{CB}^{pH} = E_{VB}^{pH} - E_g \quad \text{(IV.19)}$$

where pH_{pzc} is the pH value at the point of zero charge ($pH_{pzc} = 0$).

Table IV.2: Effect of pH on the band-edge potential levels of $Bi_{25}FeO_{40}$.

pH	0	1	2	3	4	5	6	7
E_{VB}	2.82	2.76	2.70	2.64	2.58	2.53	2.46	2.41
E_{CB}	0.66	0.60	0.54	0.48	0.42	0.37	0.3	0.25
pH	**8**	**9**	**10**	**11**	**12**	**13**	**14**	
E_{VB}	2.35	2.29	2.23	2.17	2.11	2.05	1.99	
E_{CB}	0.19	0.13	0.07	0.01	-0.06	-0.11	-0.17	

From Figure Table IV.2 and Figure IV.9, one can notice the shift of CB and VB edges towards up along with the variation of pH values from 0 to 14. These results allow the studied compound to be applied for the H_2 production in solutions with pH of 11, 12, 13, and 14. This is due to CB edge becoming more negative than the reduction potential of H^+/H_2(0 eV vs. NHE), and the VBM potential should be more positive than the oxidation potential of O_2/H_2O (1.23 eV vs. NHE) as it is illustrated in Figure IV.9.

The process of hydrogen production via the photocatalytic water splitting is similar to the photodegradation mechanism. Otherwise, under illumination the photogenerated electron-hole pairs migrate to the surface of the photocatalyst, allowing the oxydo-reduction reactions with the adsorbed water molecules in the active sites. Subsequently, the production of the dihydrogen H_2 and di-oxygen O_2, according to the equations below:

$$Bi_{25}FeO_{40} + h\nu \rightarrow Bi_{25}FeO_{40} + e^- + h^+ \quad \text{(IV.20)}$$

$$2h^+ + H_2O \rightarrow \frac{1}{2}O_2 + 2H^+ \quad \text{(IV.21)}$$

$$2H^+ + 2e^- \rightarrow H_2 \quad \text{(IV.22)}$$

$$H_2O \rightarrow \frac{1}{2}O_2 + H_2 \quad \text{(IV.23)}$$

Equations (IV.21) and (IV.22) express the half equation for oxidation and reduction, respectively. The overall equation for water splitting is given in the equation (IV.23).

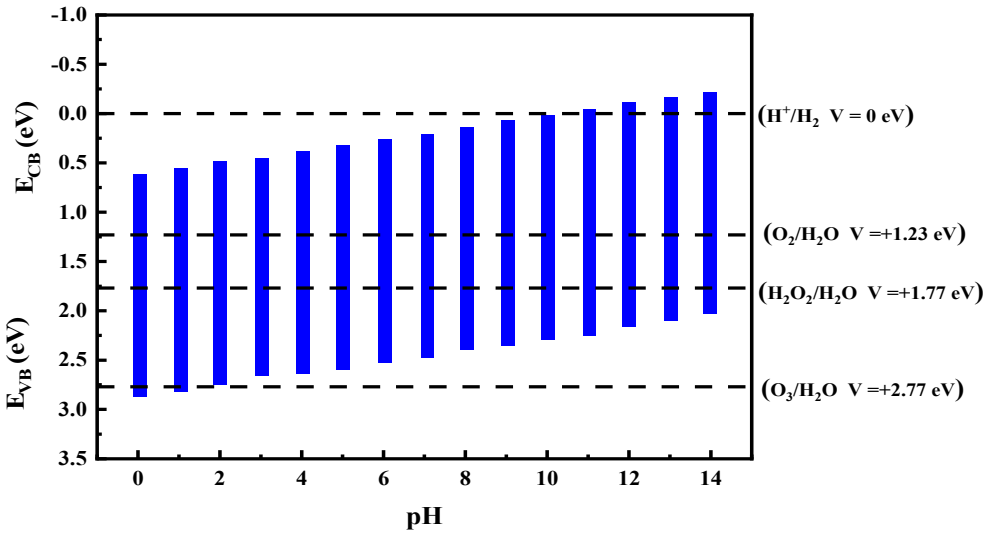

Figure IV.9: Schematic illustration for the photocatalytic mechanism diagram of $Bi_{25}FeO_{40}$ under pH effect from 0 to 14.

6. Electrical properties of iron-sillenite $Bi_{25}FeO_{40}$

To more understand the effect of temperature on the electrical and thermoelectrical properties, we accomplish a theoretical investigation of the electrical conductivity, electrical resistivity, thermal conductivity, Seebeck coefficient, carrier mobility, constant relaxation-time, carrier concentration p [213] at various temperatures (200, 300, 500, 700, and 800 K) dependent in relaxation time τ using the BoltzTrap code combined with the QE package [163,202]. The relaxation time τ values (Table IV.3) were calculated using the flowing formulas to evaluate the real value of the characterizes parameters of the transport properties [214];

$$\tau = \frac{\sigma_{exp}}{(\sigma/\tau)_{theo}} \quad \text{(IV.24)}$

where τ is the relaxation time, σ_{exp} is the experimental electrical conductivity determined by dielectric measurement (Chapter III) and $(^{\sigma}/_{\tau})_{theo}$ is the electrical conductivity divided by relaxation time calculated by the BoltzTraP package.

The electrical resistivity was calculated based on the following equation:

$$\rho = 1/\sigma \qquad \text{(IV.25)}$$

Table IV.4 presents the relevant thermoelectric parameters. The Seebeck coefficient (S) indicates the predominant type of charge carrier. The negative sign indicates the predominance of electrons for which the compound is an N-type semiconductor, while the positive sign highlights the predominance of holes and thus the p-type semiconductor. Therefore, the positive sign of S for all temperatures indicates that $Bi_{25}FeO_{40}$ is a p-type semiconductor, as already mentioned through both BS and DOS studies. (Section 3.1 and Section 3.2).

Table IV.3: Carrier mobility, constant relaxation-time, and the carrier concentration of iron-sillenite $Bi_{25}FeO_{40}$

μ_p ($m^2.V^{-1}.s^{-1}$)	τ_p (s)	p (cm^{-3})
$3.00\ 10^{-11}$	$2.41\ 10^{-21}$	$1.79\ 10^{21}$

Table IV.4: Transport properties of iron-sillenite $Bi_{25}FeO_{40}$ calculated via PBE-GGA at various temperature.

	200	300	500	700	800
S ($V.K^{-1}$)	$2.53\ 10^{-3}$	$1.73\ 10^{-3}$	$1.08\ 10^{-3}$	$8.06\ 10^{-4}$	$7.19\ 10^{-4}$
σ ($S.cm^{-1}$)	$3.32\ 10^{-13}$	$4.57\ 10^{-9}$	$1.00\ 10^{-5}$	$2.76\ 10^{-4}$	$7.85\ 10^{-4}$
ρ (Ω.cm)	$3.01\ 10^{12}$	$2.19\ 10^{8}$	$1.01\ 10^{5}$	$3.62\ 10^{3}$	$1.27\ 10^{3}$
K_{el} ($W.m^{-1}.K^{-1}$)	$1.03\ 10^{-16}$	$9.98\ 10^{-13}$	$1.42\ 10^{-9}$	$3.07\ 10^{-8}$	$7.96\ 10^{-8}$

This semiconductor shows low electrical conductivities, high Seebeck coefficient values, and low thermal conductivities, and high resistivity. Furthermore, the figure of merit decreases slightly as function of temperature.

7. Magnetic properties of iron-sillenite $Bi_{25}FeO_{40}$

Magnetic properties of $Bi_{25}FeO_{40}$ were implemented in this section, by means of the MCs combined with the Metropolis algorithm [205]. The magnetic anisotropy value of the studied compound is determined based on the calculation of the total energy difference relative to the ground state ΔE following the seven directions for $Bi_{25}FeO_{40}$. As a result, the easy magnetization of the c-axis is proven (Table IV.6). For this reason, we will adopt the discrete Ising-like model with an anisotropic factor for the magnetic investigation (Equation IV.1).

The exchange-coupling parameters (J_1 and J_2) (Figure IV.3) and the crystal field (Δ) are evaluated using the first-principal calculations at T = 0 K following the equations:

$$J_1 = \frac{E_{AFM3} - E_{AFM1}}{S_i S_j Z_1} \quad \text{(IV.26)}$$

$$J_2 = \frac{E_{AFM3} - E_{AFM2}}{S_i S_j Z_2} \quad \text{(IV.27)}$$

$$\Delta = \frac{E_a}{\sum_i (S_i)^2} \quad \text{(IV.28)}$$

where, E_{AFM1}, E_{AFM2}, E_{AFM3}, E_a, Z_1, and Z_2 are the energies of the antiferromagnetic configuration types (Table IV.1), the magnetic anisotropic energy which is equal to the difference of the energy between the low and high energy positions, Z_1 and Z_2 represent the number of the first and second nearest neighbors ions for every sublattice ($Z_1 = 8$ and $Z_2 = 6$), respectively. The obtained value of the exchange-coupling interactions of the compound are $J_1 = -1.656$ meV, $J_2 = -0.134$ meV, and $\Delta = -0.001$ meV.

The magnetic properties of Iron-Sillenite, including the magnetization μ and the magnetic susceptibility χ are calculated using the free boundary conditions. We will consider the average size of the nanoparticles ranging from 8.21 nm to 36.94 nm is corresponding to unit cells ranging from L = 8 to L = 36, where the nanoparticle size is the product of the lattice constant a = 10.26 Å and the finite size system L (Figure IV.10).

The total magnetization, the magnetic susceptibility, and the specific heat are described as follows:

$$M = \frac{1}{N}\sum_{i=1}^{N} S_i \quad \text{(IV.29)}$$

$$\chi = \frac{1}{K_B T}(< m^2 > - < m >^2) \quad \text{(IV.30)}$$

where, K_B is the Boltzmann constant, and T is the temperature. From Figure IV.11, one can notice that the total magnetization starts with null value of the magnetization. Then, the magnetization curve increases till reaches a maximum, corresponding to the antiferromagnetic-paramagnetic transition. This is asserted via the magnetic susceptibility plot. From Figure IV.10 ((a) and (b)), one can notice that the magnetization and the magnetic susceptibility curves stabilize for $L = 32$. Otherwise, the magnetic susceptibility increases as a function of temperature and then decreases after crossing over the $T_N = 255K$, which corresponds to the maximum susceptibility χ_{Max}. This feature is attributed to the antiferromagnetic–paramagnetic phase transition (Figure IV.11).

Table IV.5: Total energy difference relative to the ground state ΔE following the seven directions for $Bi_{25}FeO_{40}$.

Directions	ΔE (J/m^3)
(100)	$0.1039\ 10^{-12}$
(001)	**$-0.4644\ 10^{-13}$**
(010)	$-0.1303\ 10^{-12}$
(110)	$0.3908\ 10^{-12}$
(011)	$0.5329\ 10^{-12}$
(101)	$0.2771\ 10^{-12}$
(111)	$0.4050\ 10^{-12}$

The calculated total, atom-resolved magnetic moments, values of spin polarization for $Bi_{25}FeO_{40}$ calculated within the GGA–PBE approximations are shown in Table IV.7. One can observe from Table IV.7, that the largest contribution of the total magnetic moment comes from Fe atoms. This is due to the large exchange splitting between spin-up and spin-down states of Iron atoms, with a week contribution of Bismuth and Oxygen elements (O_1, O_2 and O_3).

The total spin magnetic moment obtained from spin polarized calculations of $Bi_{25}FeO_{40}$ is approximately 0 μ_B, this value confirms the antiferromagnetic behaviour of the studied compound. Further, the calculated magnetic moment of Fe^{3+} ions is about 3.84 μ_B, which is less than the experimental effective magnetic moment of iron (5.95 μ_B. mol^{-1}, 6.07 μ_B.mol^{-1}, and 6.37 μ_B) [16] and only slightly different from the theoretical value of 5.92 μ_B of free Fe^{3+} ion in its high spin configuration [215].

It can be also observed from Figures IV.10, that the magnetization is in good agreement with the corresponding spin-state calculated using the first principal calculation, especially at $T = 0$ K ($S = 2$; see Table IV.7).

Moreover, the maximum of the magnetic susceptibility and magnetic-specific heat peaks (Figure IV.11) are detected at around Neel temperature of $T_N = 255$ K. These is in good agreement with experimental finding, that mentioned in the previous chapter (Chapter III), asserting that Iron-Selenite exhibited a antiferromagnetic–paramagnetic phase transition at $T_N = 268$ K. Likewise, by Wu et al. [216] who prove that Iron-Sillenite exhibit a weak ferromagnetic behavior without mentioned the critical temperature of the studied compound.

Table IV.6: Spin magnetic moments of iron-sillenite calculated via GGA-PBE.

M_{Bi}	M_{Fe}	M_{O1}	M_{O2}	M_{O3}	M_{Cell}
0.0007	3.8400	0.0022	0.0001	0.0990	0.0000

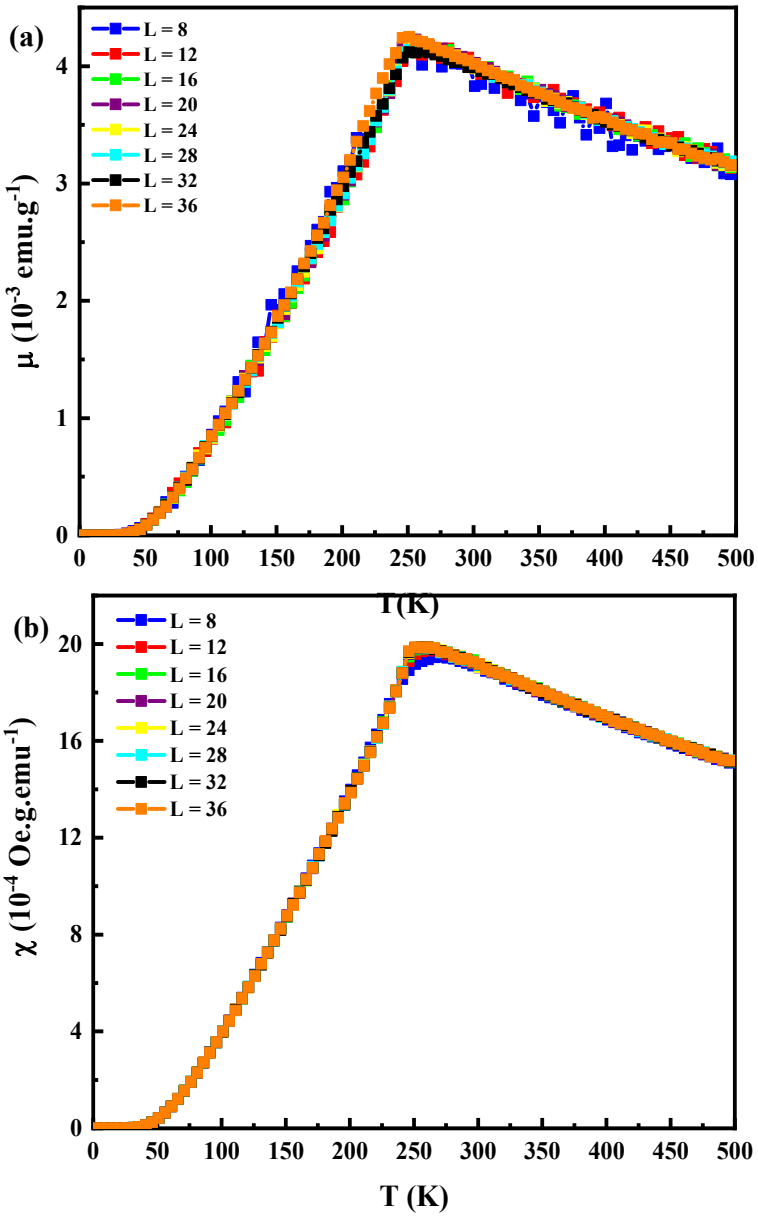

Figure IV.10: Temperature dependents on (a) Magnetization and (b) magnetic susceptibility behaviour of the $Bi_{25}FeO_{40}$ for various system sizes, using Monte Carlo Simulation.

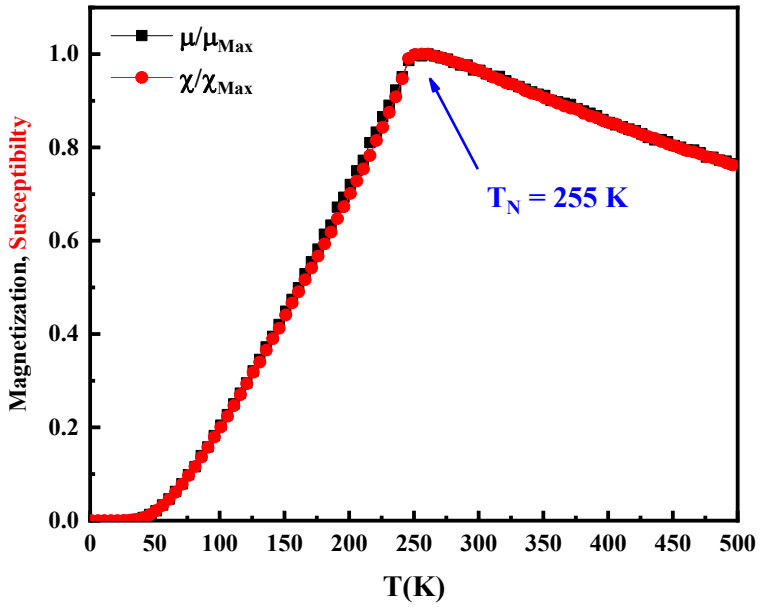

Figure IV.11: Temperature dependents on magnetization, susceptibility, and specific heat behaviour of the $Bi_{25}FeO_{40}$ for L = 32, using Monte–Carlo Simulation.

8. Conclusions

In this chapter, we conduct a theoretical investigation of the studied properties in the previous chapter for Iron-Sillenite $Bi_{25}FeO_{40}$ by means of DFT and MCs. The optimized cell parameters were agreed well with the obtained experimental results (Chapter III. Section 2.1). The electronic properties indicate the p-type semiconducting of $Bi_{25}FeO_{40}$, with a direct band gap energy of 1.87 eV. The calculated optical band gap energy was found to be 2.38 eV. Furthermore, Iron-sillenite exhibits a good absorption in both regions, UV, and Visible areas. The presented optical properties reveal the possibility of using Iron-sillenite as a good coating material in the UV and Visible regions, also for Dye-Sensitized Solar Cells applications (DSSC). The magnetic moment and the exchange-coupling interactions of the $Bi_{25}FeO_{40}$ compound are calculated by the first principal calculations. The critical temperature of the Iron-Sillenite compound is determined from the magnetic susceptibility (T_N = 255K), in good agreement with the experimental value of 268 K (Chapter III. Section 6.2).

Chapter V

Triaxial strain effect on the structural, electronic, magnetic, and electrical properties of iron-sillenite $Bi_{25}FeO_{40}$

In this chapter, we will investigate the triaxial strain effect on the structural, electronic, and electrical properties of Iron-Sillenite $Bi_{25}FeO_{40}$, preceding the same route of the previous chapter (Chapter IV). The computational details used for studying the strained Iron-Sillenite is presented in the first section, then the structural properties and magnetic properties will be presented in next section (Section 2). Afterward, the electronic properties will be described in the following sections (Section 3). Moreover, the triaxial effect on the electrical properties will be studied in the last section (Section 4).

1. Computational details for calculation of the strained iron-sillenite

The structural, electronic properties, and magnetic properties will be calculated using the QE package [202]. The thermoelectric properties will be calculated via the BoltzTraP code based on the Boltzmann equations [163].

The projector augmented wave pseudopotentials were used for the description of the electron-ion interactions. As well as a functional type Perdew-Burke Ernzerhof (PBE) exchange correlation nonlinear [204]. The valence wave functions were expanded on a plane-wave basis with cut-off energy of 65 Ry. The Brillouin zones of the unit cells are presented by a Monkhorst-pack special k-point scheme with 3×6×6 grid meshes and the atomic displacement distance of 0.01 Å.

In this chapter, we will discuss the obtained results concerning the strain effect on the structural, electronic, magnetic, and electrical properties of Iron-Sillenite. The Strain effect will be applied from -3% to +3% along x, y, and z axis, and defined as follows:

$$\varepsilon = \frac{a - a_0}{a_0} \times 100\ \% \qquad \text{(V.1)}$$

where ε, a, and a_0 are the strain ratio, lattice parameter of Iron-Sillenite with and without strain effect, respectively. Herein, the negative value of ε indicates the compressive strain, while the positive one implies the application of the tensile strain.

2. Structural and the magnetic properties of the strained iron-sillenite

2.1. Structural properties

The structural properties of iron-sillenite under triaxial strain effect will be studied in this section. $Bi_{25}FeO_{40}$ adopts a cubic centred structure (I23, No. 197), in which Bi and Fe atoms are situated at (0.1764; 0.3180; 0.0141) and (0.0000; 0.0000; 0.0000),

respectively, with an optimized cell parameters of a = 10.26 Å [16,68,219]. Where Iron-atoms forming tetrahedral coordination with oxygen atoms and Bismuth-atoms occupied octahedral positions [68]. Figure V.1 presents the crystalline structure of the Iron-Sillenite unit cell, the tetrahedral and octahedral coordination of iron and Bismuth atoms. The bond length Bi-O1, Bi-$O2^{(i)}$, Bi-$O2^{(ii)}$, Bi-$O2^{(iii)}$, Bi-O3, Bi-Bi, and Fe-O3 take values of 2.451, 2.427, 2.052, 2.442, 3.796, and 1.894 Å, respectively (Table V.1). These parameters are in good agreements with the previous experimental results [18].

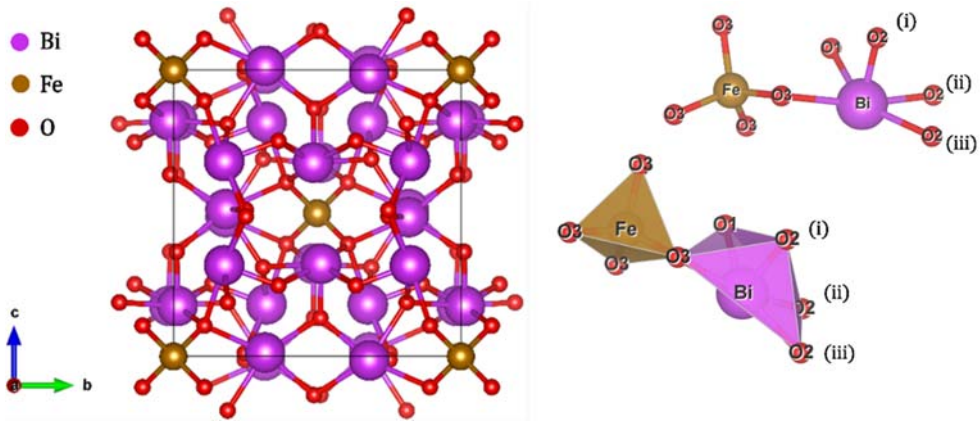

Figure V.1: Crystallin structure of iron-sillenite $Bi_{25}FeO_{40}$ [16,18,68].

Figure V.2 shows that after compressive strain along the x-axis, the bond length between the Bi-Bi atoms gradually increases until it reaches a first maximum at the unstressed compound. Then $d_{Bi\text{-}Bi}$ decreases under +1% and continues to increase to the second maximum at +3% under a tensile effect along the x-axis. Otherwise, this parameter exhibits the same behavior under strain effect along y and z axis, which present a constant value under tensile and compressive effects (Figure V.2 and Table V.1). Furthermore, the other bond length; $d_{Bi\text{-}O1}$, $d_{Bi\text{-}O2(i)}$, $d_{Bi\text{-}O2(ii)}$, $d_{Bi\text{-}O2(iii)}$, $d_{Bi\text{-}O3}$, $d_{Bi\text{-}Bi}$, and $d_{Fe\text{-}O3}$ shown the same behavior along the x-axis, they increase linearly with the increase of the deformation rate.

Under strain effect along y-axis and z-axis, the bond length between Bi-O3 ad Fe-O3 increase gradually with the strain ratio. Otherwise, the other bond lengths changed slightly or doesn't affect, producing a symmetry breaking of the studied structure after a strain effect along the y and z axes as presented in the XRD patterns using the VESTA package (Figure V.3).

Table V.1: Selected geometric parameters (Å) of $Bi_{25}FeO_{40}$ under triaxial strain.

		Bi-O1	Bi-O2(i)	Bi-O2(ii)	Bi-O2(iii)	Bi-O3	Bi-Bi	Fe-O3
	0%	2.451	2.427	2.052	2.442	2.451	3.796	1.894
	0% [18]	2.214	2.263	2.069	2.599	2.572	3.602	1.894
x-axis	**-3%**	2.388	2.373	2.006	2.396	2.396	3.629	1.851
	-2%	2.412	2.398	2.027	2.421	2.420	3.666	1.870
	-1%	2.437	2.422	2.048	2.446	2.445	3.721	1.890
	+1%	2.486	2.471	2.089	2.495	2.495	3.779	1.928
	+2%	2.516	2.511	2.110	2.516	2.519	3.816	1.947
	+3%	2.535	2.544	2.131	2.520	2.544	3.853	1.966
y-axis	**-3%**	2.443	2.418	2.068	2.418	2.459	3.741	1.890
	-2%	2.449	2.428	2.068	2.435	2.462	3.741	1.896
	-1%	2.455	2.437	2.068	2.453	2.466	3.741	1.902
	+1%	2.468	2.456	2.0684	2.488	2.474	3.741	1.915
	+2%	2.474	2.466	2.068	2.505	2.477	3.742	1.921
	+3%	2.480	2.475	2.068	2.523	2.481	3.742	1.928
z-axis	**-3%**	2.454	2.439	2.014	2.470	2.464	3.741	1.890
	-2%	2.457	2.442	2.032	2.470	2.466	3.741	1.896
	-1%	2.459	2.444	2.050	2.470	2.468	3.741	1.902
	+1%	2.464	2.449	2.087	2.470	2.472	3.741	1.915
	+2%	2.466	2.451	2.105	2.470	2.474	3.741	1.921
	+3%	2.469	2.454	2.123	2.470	2.476	3.741	1.928

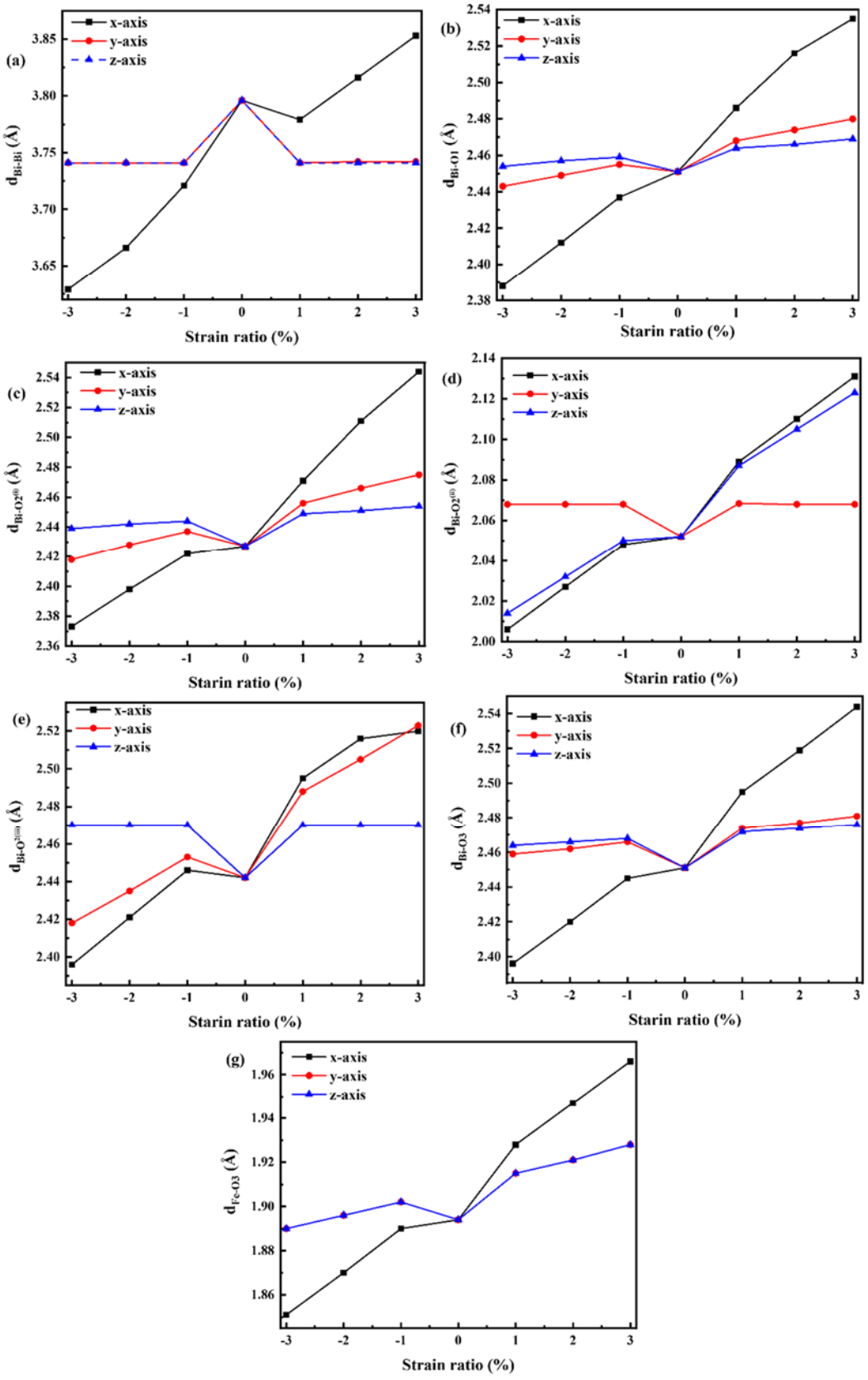

Figure V.2: Triaxial strain effect on the bond-length of iron-sillenite $Bi_{25}FeO_{40}$.

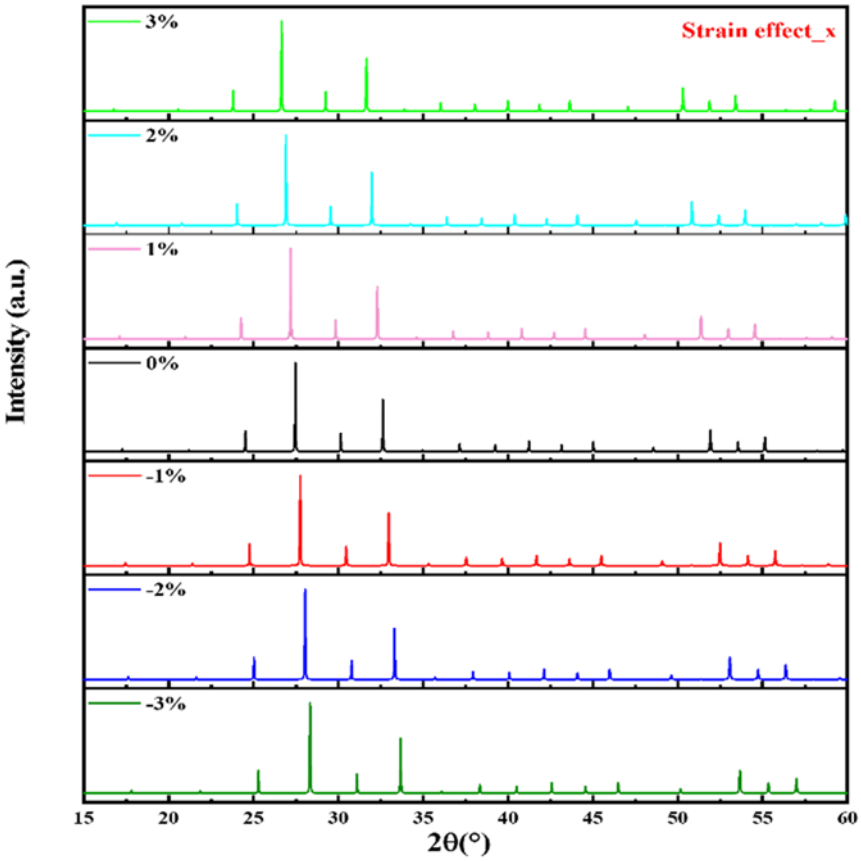
Strain effect_x
3%
2%
1%
0%
-1%
-2%
-3%
Intensity (a.u.)
15
20
25
30
35
40
45
50
55
60
2θ(°)

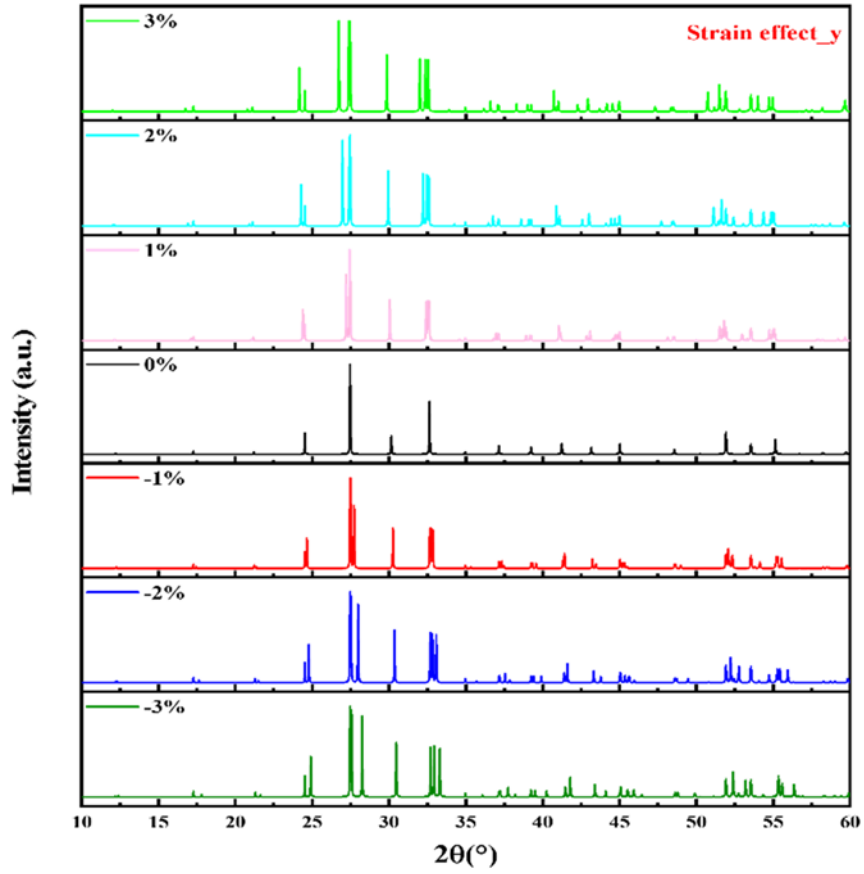
Strain effect_y
3%
2%
1%
0%
-1%
-2%
-3%
Intensity (a.u.)
10
15
20
25
30
35
40
45
50
55
60
2θ(°)

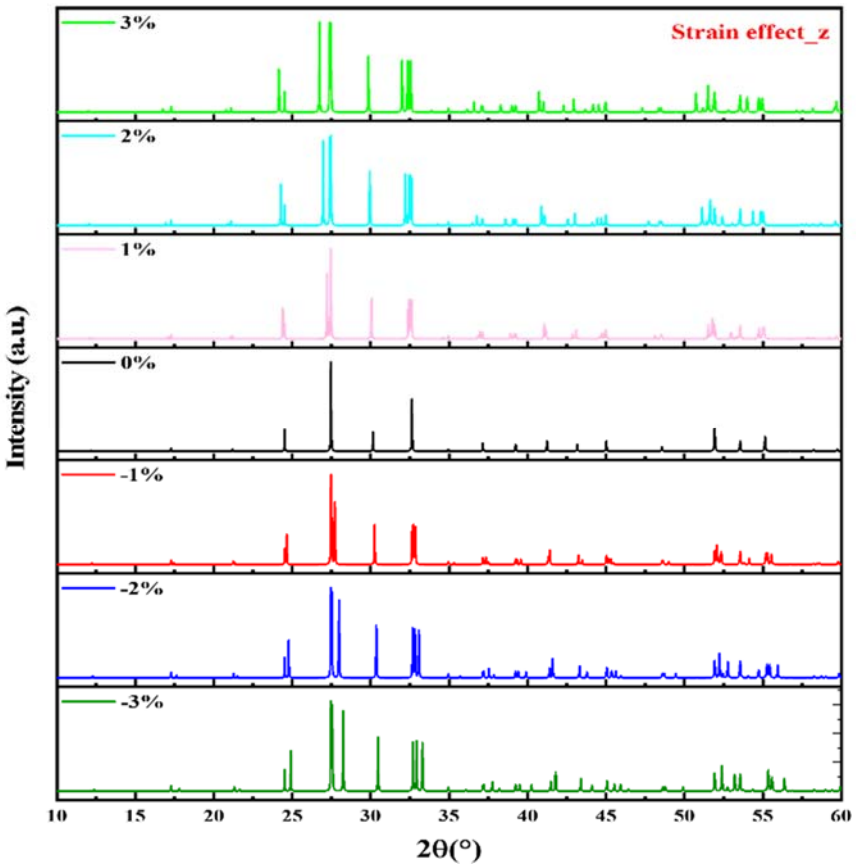

Figure V.3: XRD patterns of iron-sillenite $Bi_{25}FeO_{40}$ under triaxial effect.

2.2. Magnetic properties

Iron-Sillenite is an antiferromagnetic material, with the c-axis easy magnetization and a Neel temperature ranging from 246 to 265 K (Chapter III and IV, respectively). As presented in the previous chapter, that the largest contribution of the total magnetic moment comes from the Iron-atoms. This is due to the large exchange between spin-up and spin-down states of Iron atoms, with a week contribution of Bismuth and Oxygen elements (O_1, O_2 and O_3). Table V.2 presents, the total and partial magnetic moments without and under triaxial strain effect along x, y, and z-axis.

From Table V.2, one can notice strain effect have no effect on the magnetic behaviour of the studied compound, and this is asserted via the null value of the total magnetic moments. In addition to that, the magnetic moment of Fe^{3+} is slightly changed under tensile and compressive effect along x-axis (Table V.2).

Table V.2: Spin magnetic moments of iron-sillenite under triaxial strain effect (μ_B).

		μ_{Bi}	μ_{Fe}	μ_{O1}	μ_{O2}	μ_{O3}	μ_{T_Cell}
	0%	0.00	3.84	0.00	0.00	0.10	0.00
x-axis	**-3%**	0.00	3.73	0.00	0.0	0.10	0.00
	-2%	0.00	3.77	0.00	0.00	0.10	0.00
	-1%	0.00	3.81	0.00	0.00	0.10	0.00
	+1%	0.00	3.87	0.00	0.00	0.10	0.00
	+2%	0.00	3.91	0.00	0.00	0.10	0.00
	+3%	0.00	3.93	0.00	0.00	0.10	0.00
y-axis	**-3%**	0.00	3.81	0.00	0.00	0.10	0.00
	-2%	0.00	3.82	0.00	0.00	0.10	0.00
	-1%	0.00	3.83	0.00	0.00	0.10	0.00
	+1%	0.00	3.85	0.00	0.00	0.10	0.00
	+2%	0.00	3.86	0.00	0.00	0.10	0.00
	+3%	0.00	3.87	0.00	0.00	0.10	0.00
z-axis	**-3%**	0.00	3.81	0.00	0.00	0.10	0.00
	-2%	0.00	3.82	0.00	0.00	0.10	0.00
	-1%	0.00	3.83	0.00	0.00	0.10	0.00
	+1%	0.00	3.85	0.00	0.00	0.10	0.00
	+2%	0.00	3.86	0.00	0.00	0.10	0.00
	+3%	0.00	3.87	0.00	0.00	0.10	0.00

3. Electronic properties

In this section, we will investigate the strain effect on the electronic properties of Iron-Sillenite, analysing the electronic band structure, the density of states (DOS), and the electronic density of charge.

3.1. Band structure calculation

The calculated band structures of the $Bi_{25}FeO_{40}$ under various strains are shown in Figure V.4, in which the band structure for the pristine compound (Chapter IV.3.1) is also presented for comparison. Figure V.4 displays that the applied strains does not change the allowed direct transition nature of the studied material, and the profile of entire band structure still almost unchanged. It seems that the bandgap of the unstrained iron-sillenite presents a sensitivity with the applied strain, and it behaves differently under the compression and tensile effects.

The bandgap energies $Bi_{25}FeO_{40}$ decrease with the application of a compressive effect from -1% to -3%, till reaching minimum values of 1.38, 1.65, and 1.65 eV along x, y, and z axis, respectively. Further, this parameter increases after a tensile effect from +1% to +3%, till reaching a maximum value of 2.27 eV under tensile effect of +3% along x axis. Otherwise, the bandgap energy behaves similarly along y and z axis and take the same values under +1% and +3% of 1.85 and 1.94 eV, respectively (Figure V.6).

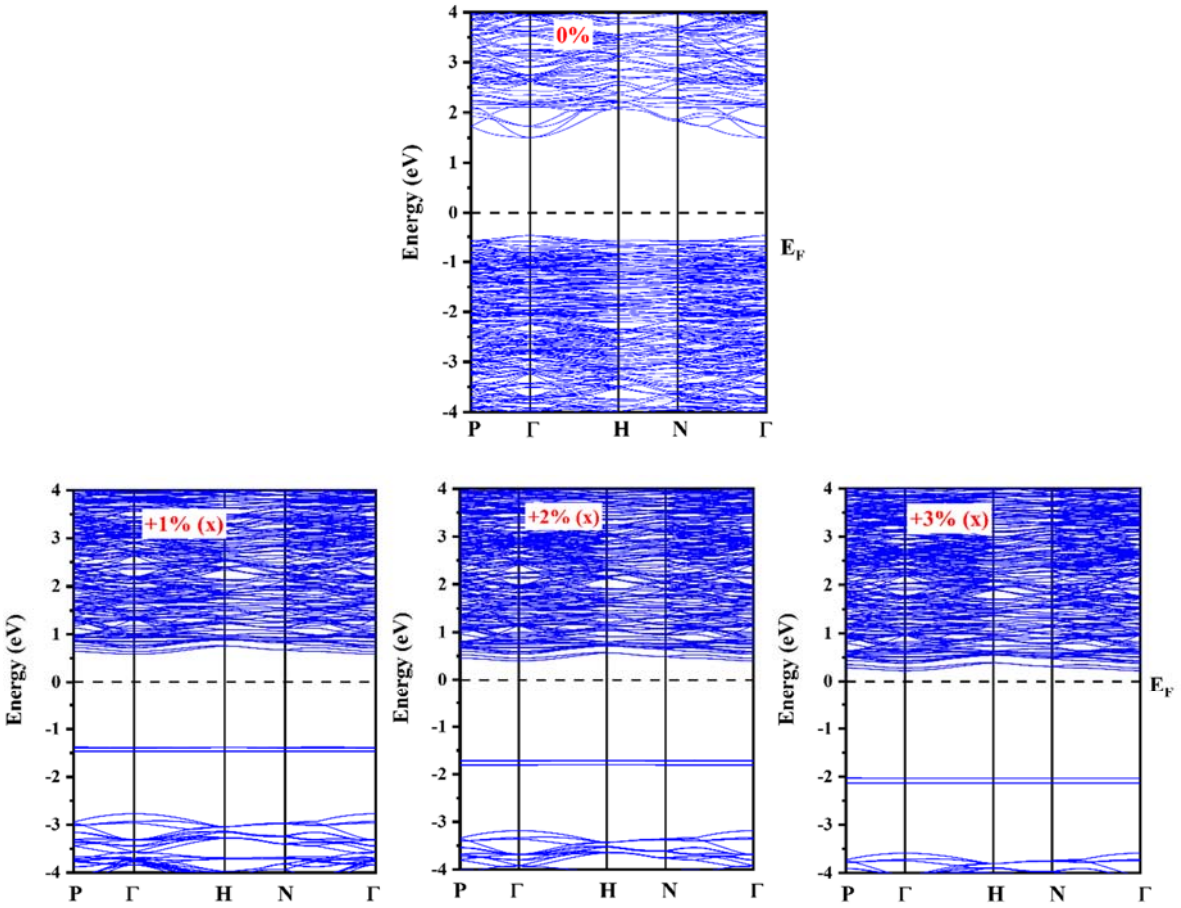

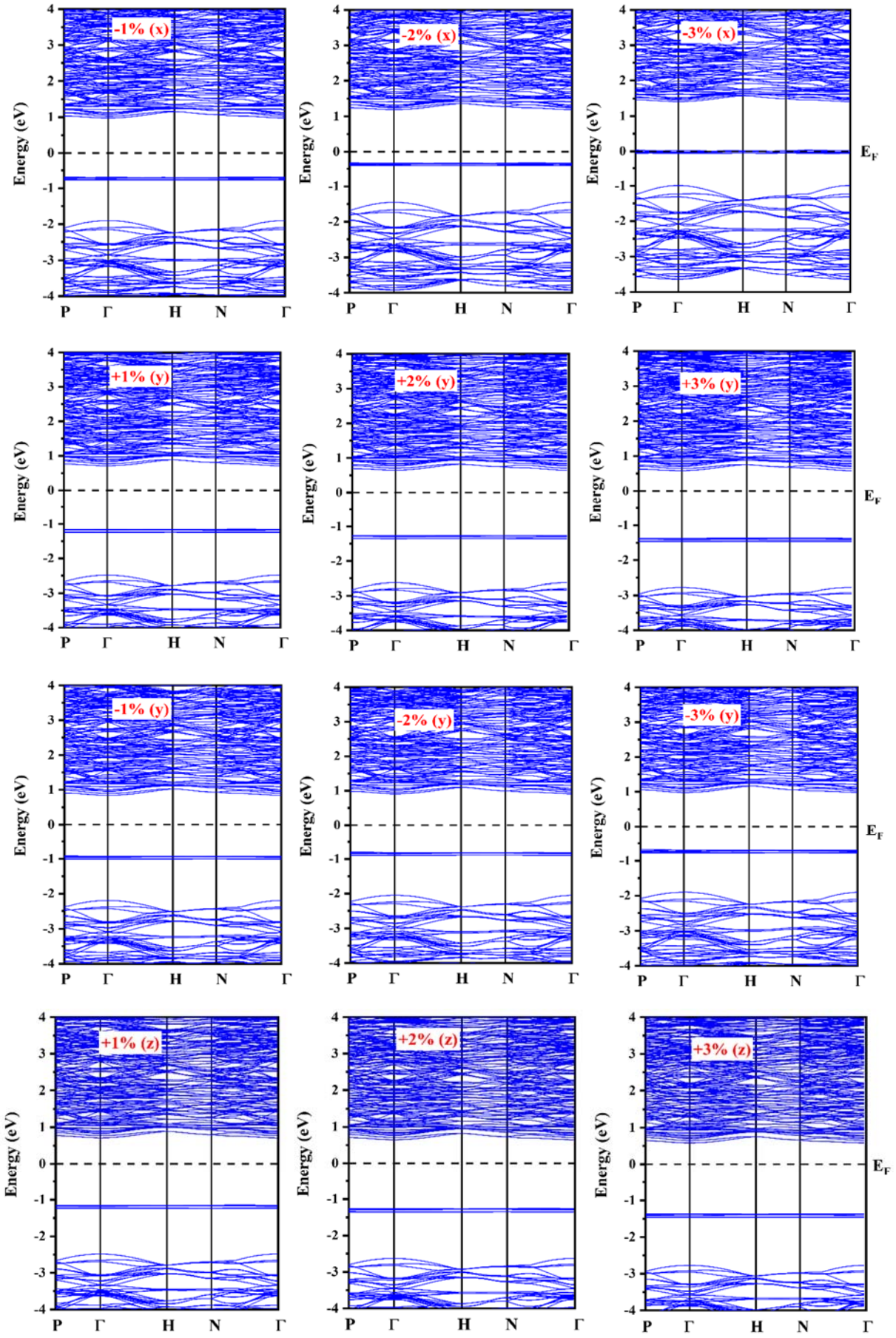
-1% (x)
-2% (x)
-3% (x)
+1% (y)
+2% (y)
+3% (y)
-1% (y)
-2% (y)
-3% (y)
+1% (z)
+2% (z)
+3% (z)
Energy (eV)
P Γ H N Γ
E_F

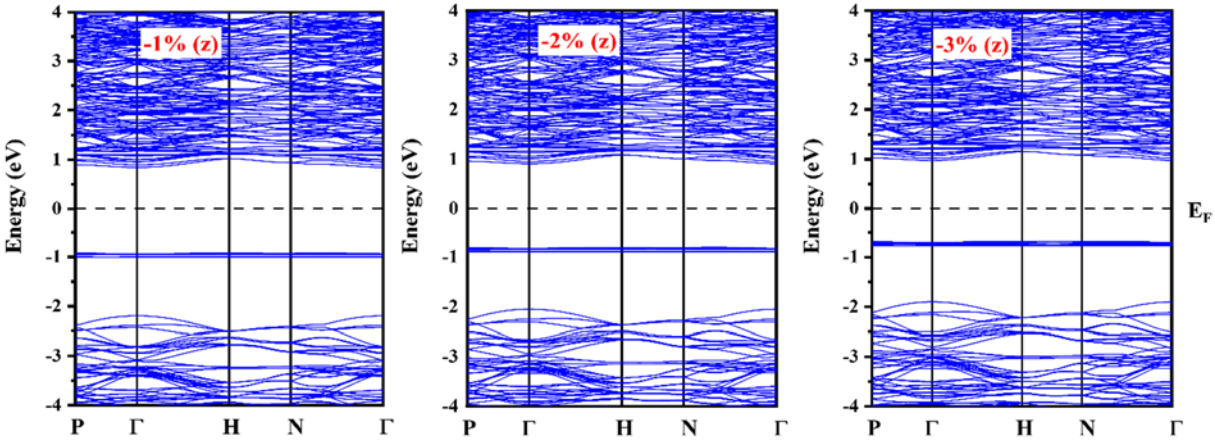

Figure V.4: Band structure of iron-sillenite under triaxial strain effect.

3.2. Density of state calculation

The electronic densities of state were calculated for the overall unit cell and for the partial atoms (Bi, Fe, O1, O2, and O3), with and without triaxial strain effect and presented in Figure V.5. We can notice from Figure V.5, that the lower part (between -6.5 and 8.0 eV) of the density of state, is principally produced via the hybridisation between the Fe-3d and O3-2p orbitals. Furthermore, the VB nearby the fermi level (between -5.8 and 0.0 eV) and the CB parts (between 1.0 and 5.0 eV) are formed via the hybridisation between the Bi-6s and 6p orbitals and the O-2s and 2p orbitals.

One can observe from Figure V.5, that after tensile effect along the x-axis, the conduction band shifts to low energies and increasing the value of the bandgap energies, which attributed to linear increasing behavior of the bond length between Bi-Bi, Bi-O1, Bi-$O2^{(i)}$, Bi-$O2^{(ii)}$, Bi-$O2^{(iii)}$, Bi-O3. Thus, after the compressive effect along the same axis, the valance and conduction bands shift to high energies and decreasing the value of the band gap energies. This is due to linear decreasing behavior of the same band length.

Moreover, after tensile and compressive effect along y and z axis, we can notice that the total and partial densities of state behave approximately in the same way, and this is due to slightly change in the bond length.

One can conclude that the responsible on the profile of band structure and the density of state nearby the fermi level, is the hybridization between the Bi-6s and 6p orbitals and the O-2s and 2p orbitals. Thus, the change in the bond length related to the bismuth atoms, allowing the modification of the bandgap energies.

Table V.3: Electronic bandgap energies E_g(eV) of iron-sillenite under triaxial strain effect.

	-3%	-2%	-1%	0%	+1%	+2%	+3%
x-axis	1.38	1.50	1.65	1.87	1.94	2.22	2.27
y-axis	1.65	1.68	1.71	1.87	1.85	1.88	1.94
z-axis	1.65	1.71	1.77	1.87	1.85	1.91	1.94

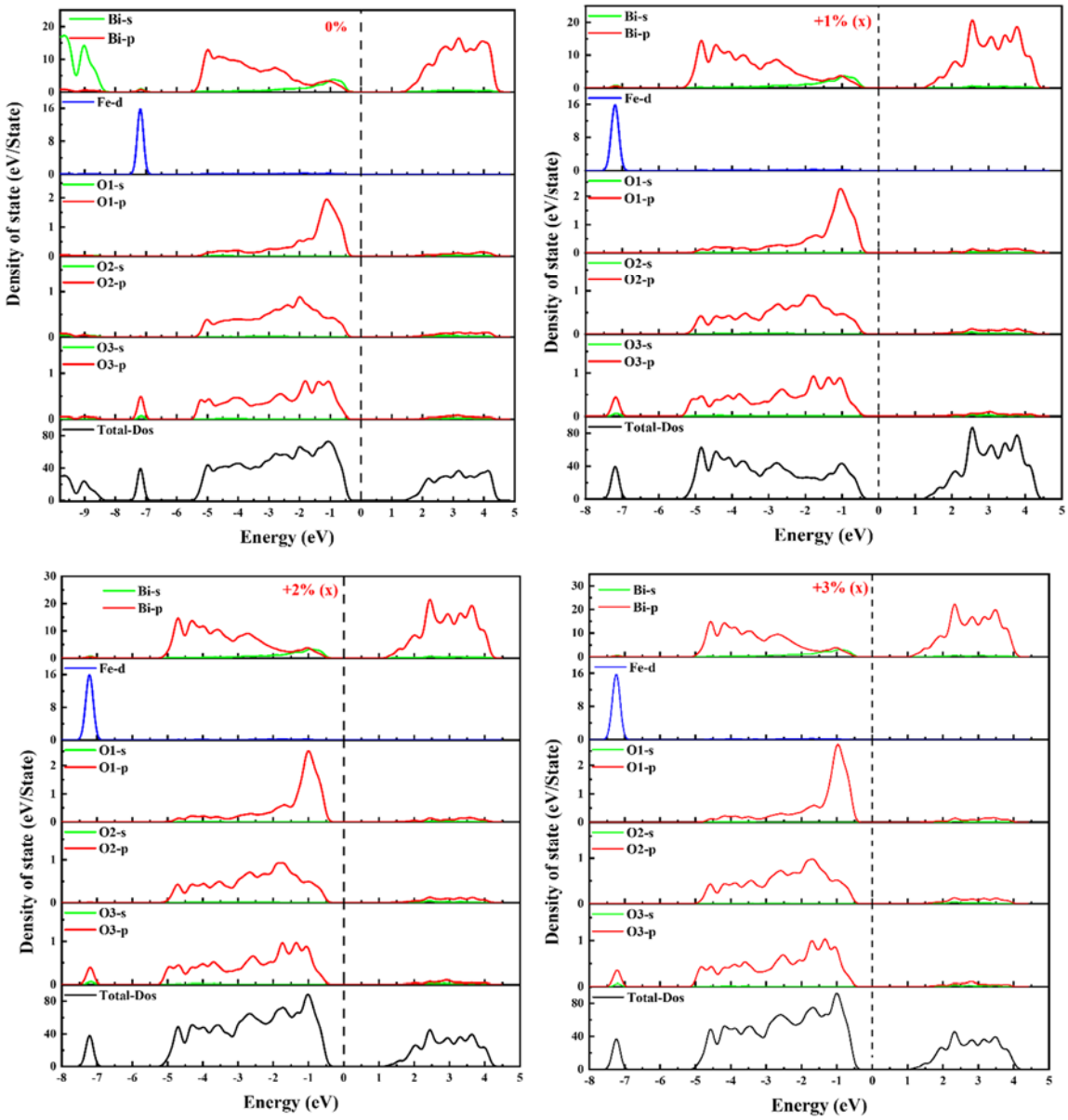

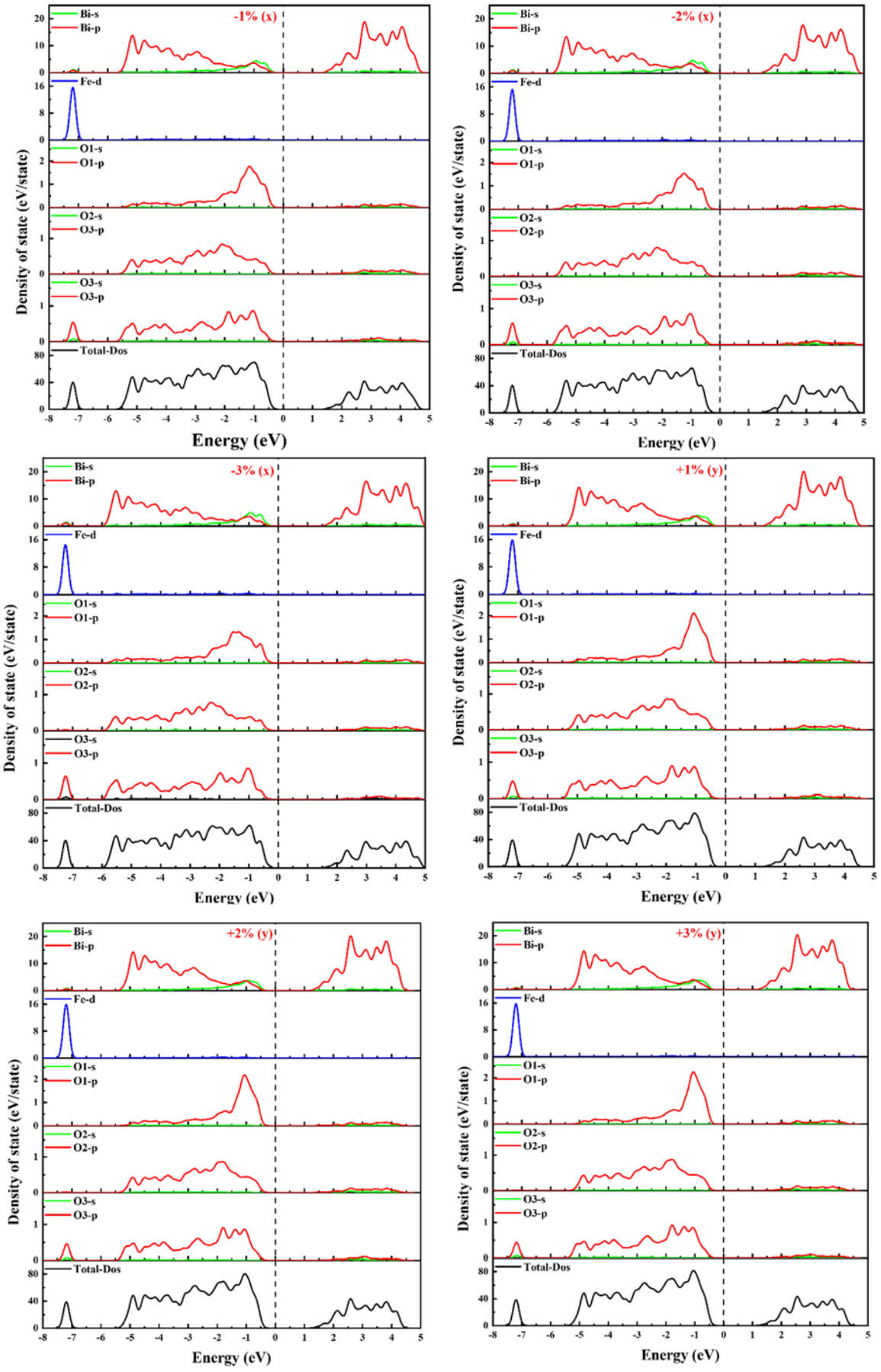
-1% (x)
-2% (x)
-3% (x)
+1% (y)
+2% (y)
+3% (y)
Bi-s
Bi-p
Fe-d
O1-s
O1-p
O2-s
O2-p
O3-s
O3-p
Total-Dos
Density of state (eV/state)
Energy (eV)

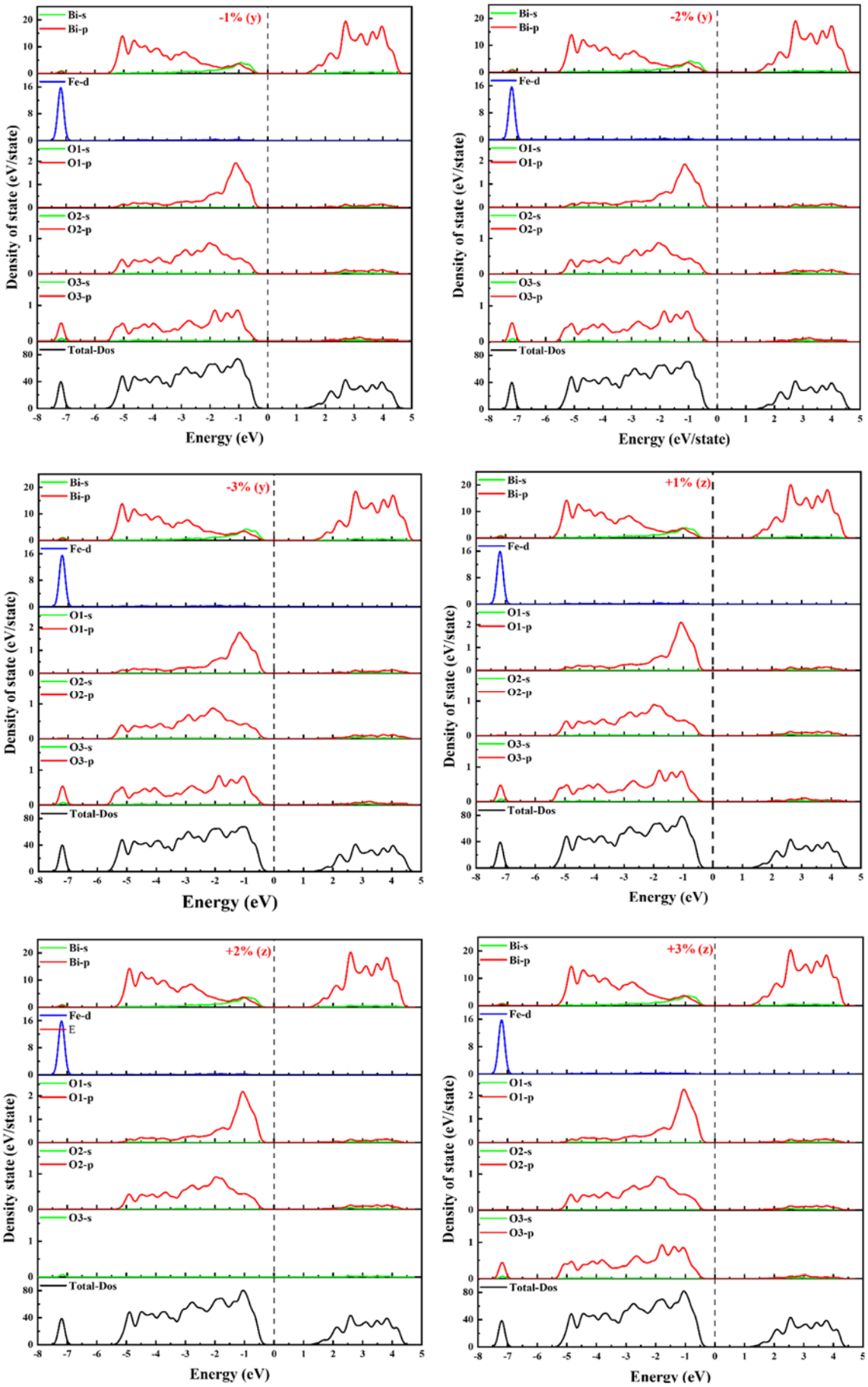
-1% (y)
-2% (y)
-3% (y)
+1% (z)
+2% (z)
+3% (z)
Bi-s
Bi-p
Fe-d
O1-s
O1-p
O2-s
O2-p
O3-s
O3-p
Total-Dos
Density of state (eV/state)
Energy (eV)
Energy (eV/state)

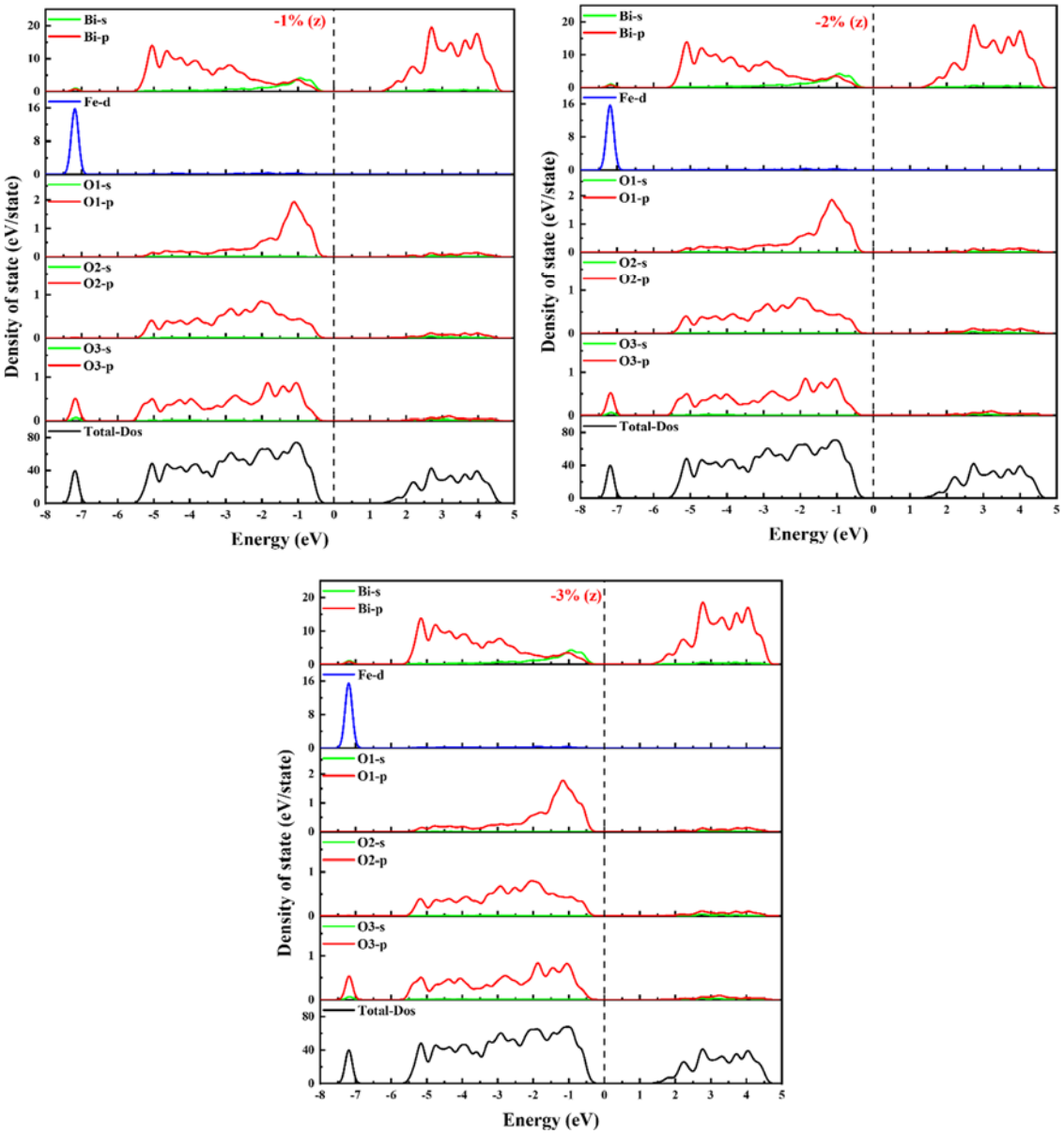

Figure V.5: Total and partial DOS of iron-sillenite under triaxial strain effect.

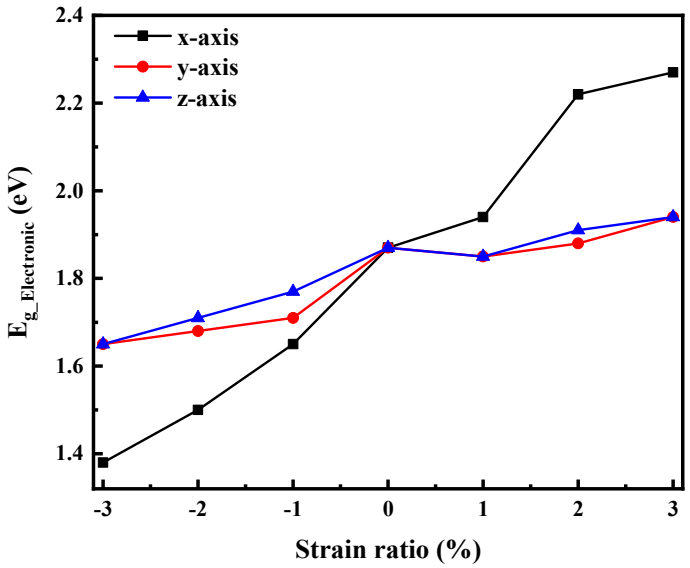

Figure V.6: Electronic bandgap energies of iron-sillenite under triaxial strain effect.

3.3. Electronic density of charge calculation

The calculation of the electronic charge density, which is usually presented in a plane or along a direction, gives us information about the charge transfer and consequently about the ionic or covalent nature of the bond. Thus, to visualize the nature of the bonding character of the pristine and strained iron-sillenite from -3% to +3% along x, y, and z axis, we calculated the electronic density of charge in the (011) plane (Figure V.7).

The Bi atoms are wider with many valence electrons compared to the Fe atoms. Further, O atoms have more core electrons that accumulate near the nucleus, resulting in a higher charge density near the nucleus. The large difference in electronegativity between Fe and O, and between Bi and O results in a charge transfer between Iron (cation) and oxygen (anion), thus, between Bismuth (cation) and oxygen (anion). From Figure V.7, one can conclude the ionic bond between Bi and O atoms. Besides, the distribution between Fe and O atoms seems to be homogenous, revealing that Fe and O atoms are covalently bonded. The electronic charges are accumulated along Fe-O bond and increase with the strain effect along x–axis. Thus, it decreases with the strain effect along y and z axis.

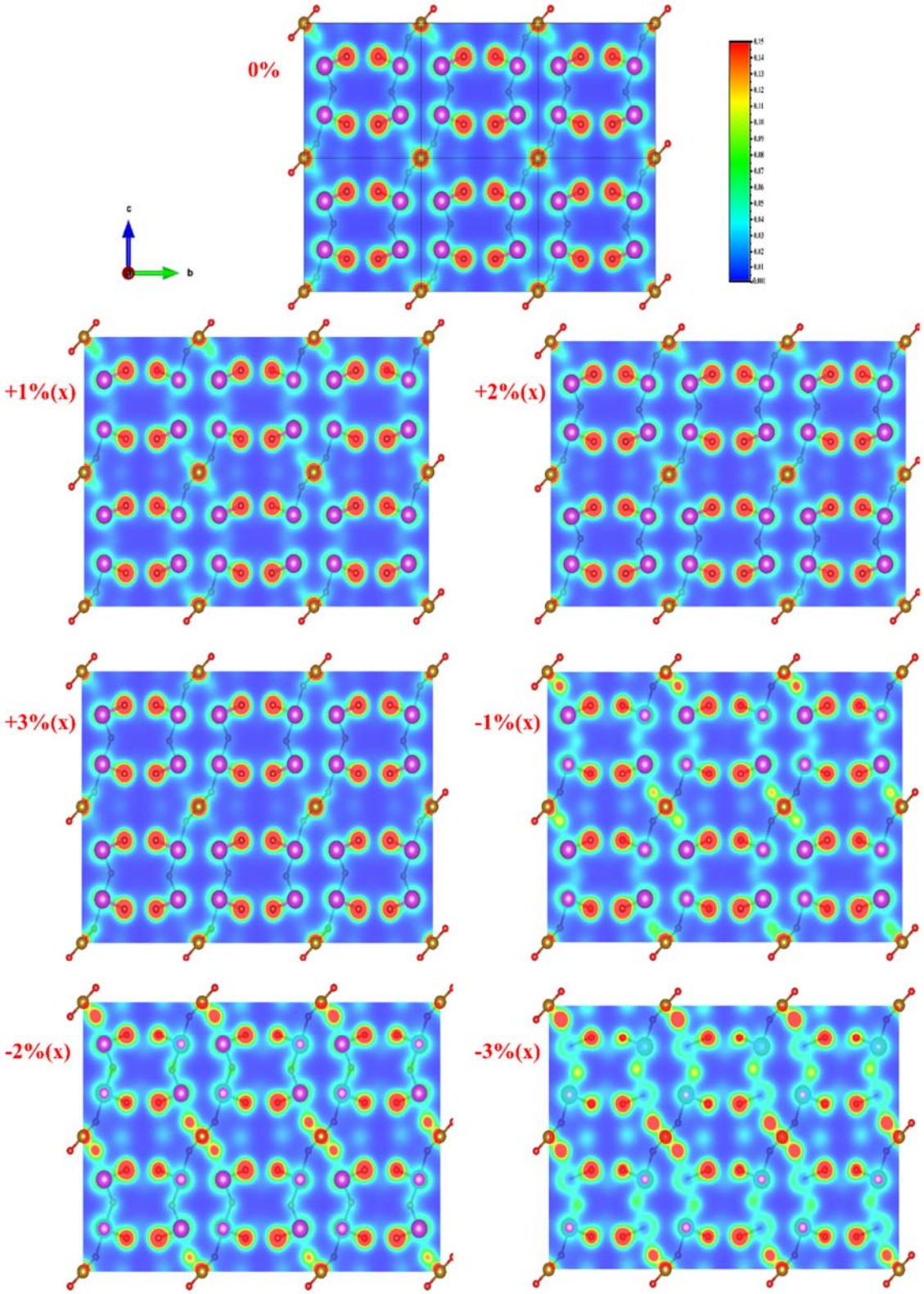
0%
c
b
+1%(x)
+2%(x)
+3%(x)
-1%(x)
-2%(x)
-3%(x)

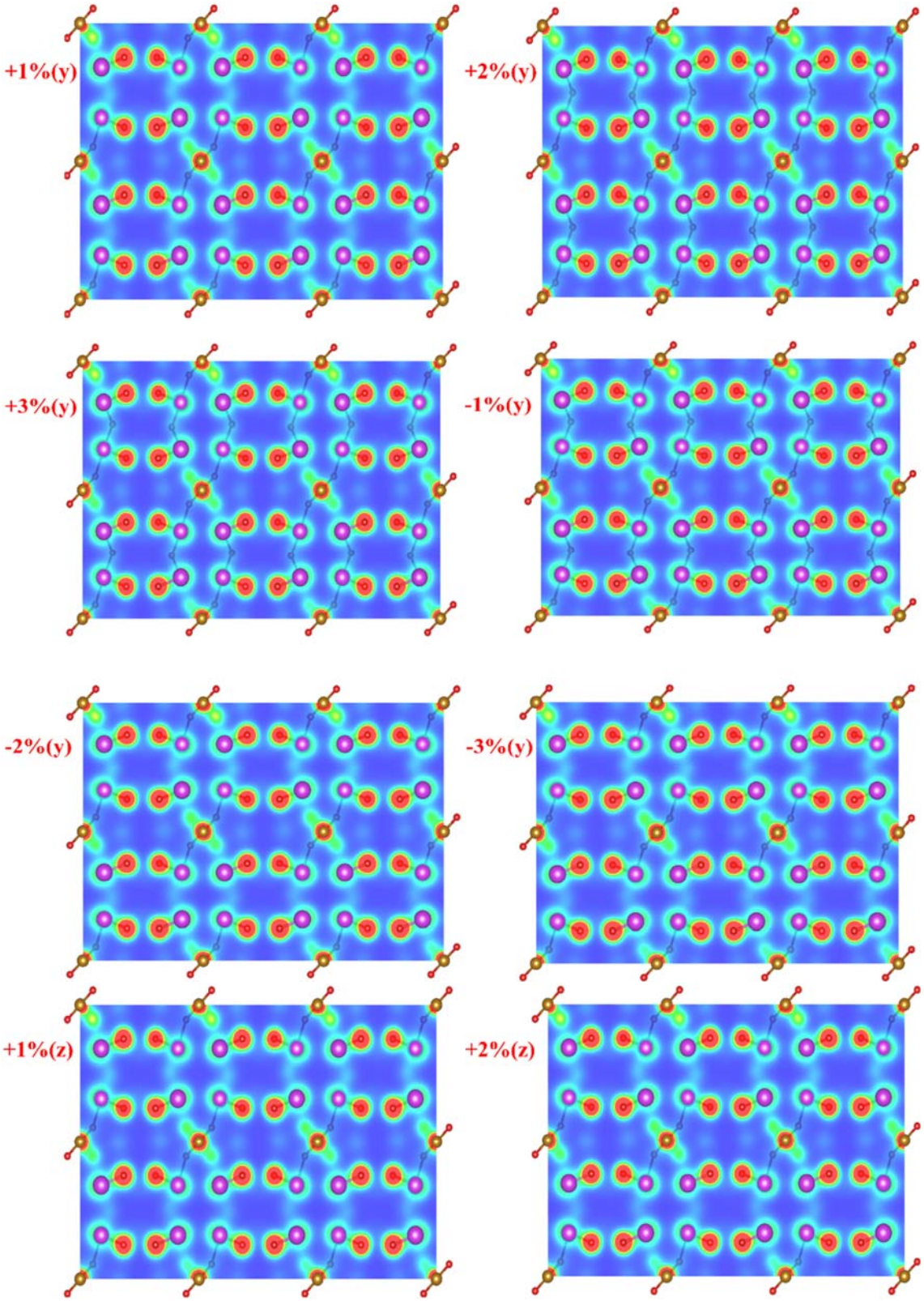
+1%(y)
+2%(y)
+3%(y)
-1%(y)
-2%(y)
-3%(y)
+1%(z)
+2%(z)

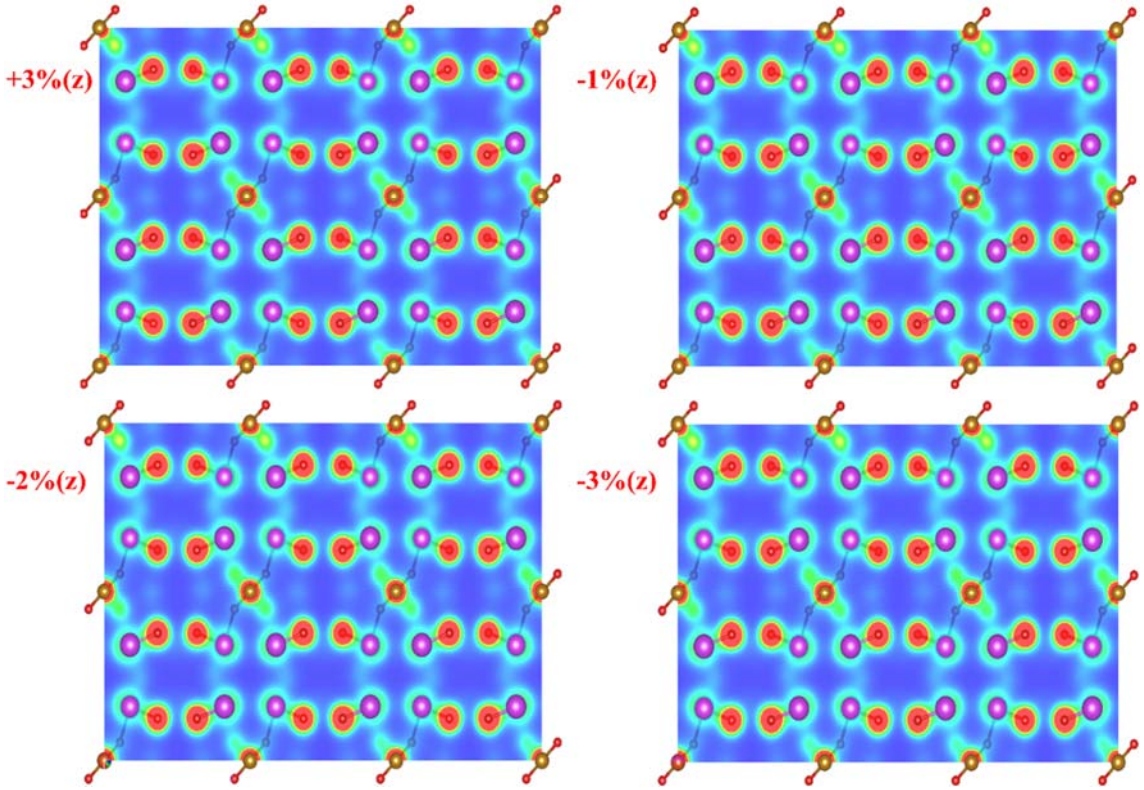

Figure V.7: Electronic density of charge of iron-sillenite under triaxial strain effect.

4. Electrical properties of iron-sillenite $Bi_{25}FeO_{40}$ under strain effect

The electrical properties of the strained iron-sillenite, will be calculated using the BoltzTraP package based on the Boltzmann model via the Boltzmann transport equation [163]. Boltzmann transport theory has proven its validity in many applications where the calculated transport coefficients can be easily compared with experimental results. The calculation of electrical properties was achieved at room temperature, by the calculation of the Seebeck coefficient S, electrical conductivity σ, electrical resistivity ρ, and electrical thermal conductivity K_{el} (Figure V.8 and Table V.4).

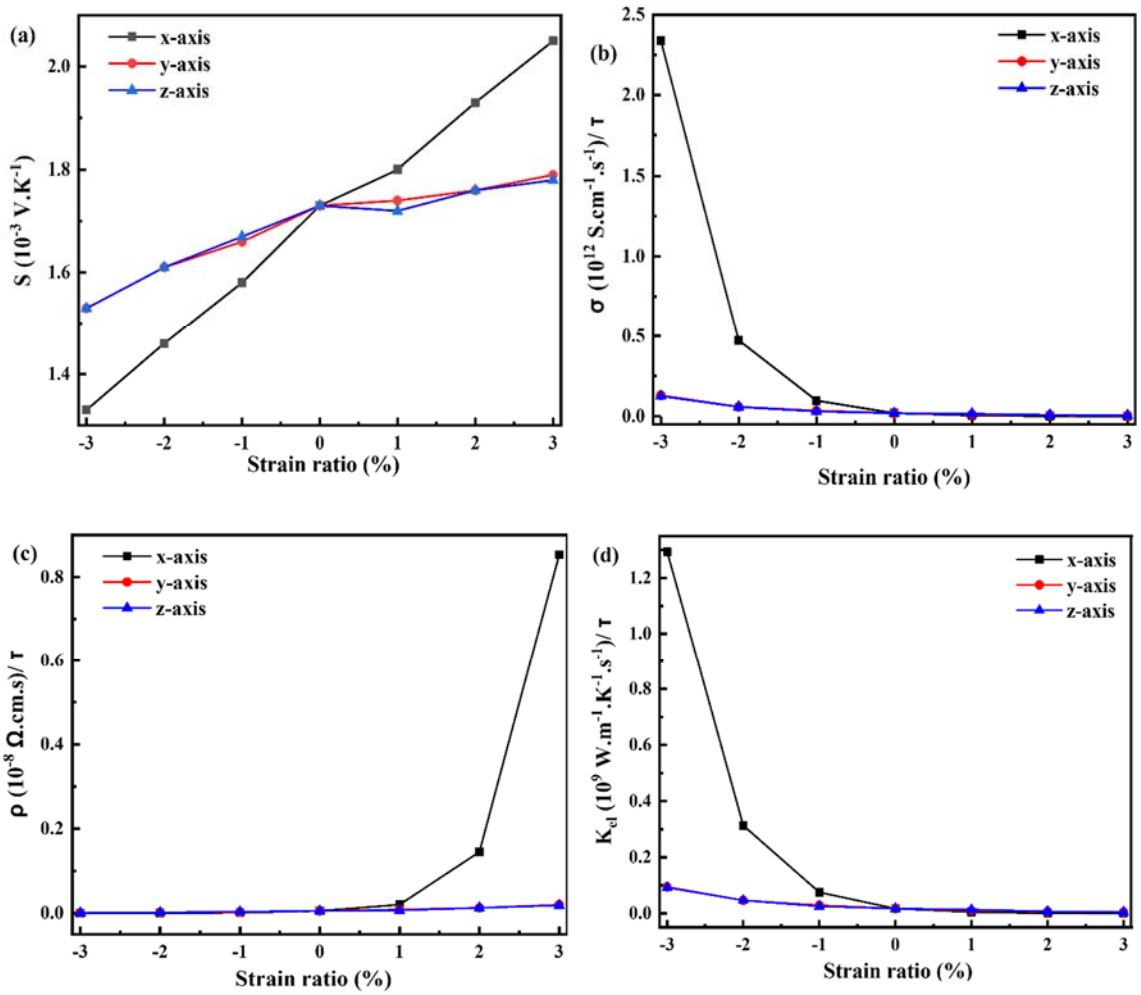

Figure V.8: Electrical properties of iron-sillenite under triaxial strain effect.

4.1. Seebeck coefficient

The calculation of the Seebeck coefficient allows to quantify the ratio between the electric potential and the thermal potential. It was established by the experiment that the values for the usual materials are of the order of the μV. K^{-1}.

Figure V.8(a), illustrates the evolution of the Seebeck coefficient (S) under compressive and tensile effect, calculated in room temperature. The evolution of the Seebeck coefficient reveals that it increases progressively as a function of the strain ratio from -3% to +3% along x. However, the strain effect along y and z-axis have the same effect on S, that become approximately constant under tensile effect from +1% to +3%.

Indeed, the positive sign of the Seebeck coefficient suggests a conduction of the material through positive charge carriers (holes), so this material is a P-type. Likewise, the Seebeck coefficient exhibits a positive sign after an application of the tensile and

compressive effect. This is revealing that the strain along x, y, and z-axis from -3% to +3% has no effect on the conduction mechanism.

Table V.4: Electrical properties of $Bi_{25}FeO_{40}$ under triaxial strain effect, calculated at room temperature.

		S ($V.K^{-1}$)	σ ($S.cm^{-1}.s^{-1}$)/ τ	ρ ($\Omega.cm.s$)/ τ	K_{el} ($W.m^{-1}.K^{-1}.s^{-1}$)/ τ
	0%	$1.73\ 10^{-3}$	$1.90\ 10^{10}$	$5.27\ 10^{-11}$	$1.72\ 10^{7}$
x-axis	**+1%**	$1.80\ 10^{-3}$	$4.97\ 10^{9}$	$2.01\ 10^{-10}$	$4.92\ 10^{6}$
	+2%	$1.93\ 10^{-3}$	$6.89\ 10^{8}$	$1.45\ 10^{-9}$	$7.83\ 10^{5}$
	+3%	$2.05\ 10^{-3}$	$1.17\ 10^{8}$	$8.53\ 10^{-9}$	$1.49\ 10^{5}$
	-1%	$1.58\ 10^{-3}$	$9.70\ 10^{10}$	$1.03\ 10^{-11}$	$7.53\ 10^{7}$
	-2%	$1.46\ 10^{-3}$	$4.74\ 10^{11}$	$2.11\ 10^{-12}$	$3.13\ 10^{8}$
	-3%	$1.33\ 10^{-3}$	$2.34\ 10^{12}$	$4.28\ 10^{-13}$	$1.29\ 10^{9}$
y-axis	**+1%**	$1.74\ 10^{-3}$	$1.15\ 10^{10}$	$8.68\ 10^{-11}$	$1.07\ 10^{7}$
	+2%	$1.76\ 10^{-3}$	$7.90\ 10^{9}$	$1.27\ 10^{-10}$	$7.55\ 10^{6}$
	+3%	$1.79\ 10^{-3}$	$5.01\ 10^{9}$	$2.00\ 10^{-10}$	$4.94\ 10^{6}$
	-1%	$1.66\ 10^{-3}$	$3.45\ 10^{10}$	$2.90\ 10^{-11}$	$2.92\ 10^{7}$
	-2%	$1.61\ 10^{-3}$	$5.82\ 10^{10}$	$1.72\ 10^{-11}$	$4.66\ 10^{7}$
	-3%	$1.53\ 10^{-3}$	$1.30\ 10^{11}$	$7.72\ 10^{-12}$	$9.45\ 10^{7}$
z-axis	**+1%**	$1.72\ 10^{-3}$	$1.50\ 10^{10}$	$6.65\ 10^{-11}$	$1.36\ 10^{7}$
	+2%	$1.76\ 10^{-3}$	$7.86\ 10^{9}$	$1.27\ 10^{-10}$	$7.49\ 10^{6}$
	+3%	$1.78\ 10^{-3}$	$5.38\ 10^{9}$	$1.86\ 10^{-10}$	$5.24\ 10^{6}$
	-1%	$1.67\ 10^{-3}$	$2.98\ 10^{10}$	$3.36\ 10^{-11}$	$2.56\ 10^{7}$
	-2%	$1.61\ 10^{-3}$	$5.82\ 10^{10}$	$1.72\ 10^{-11}$	$4.66\ 10^{7}$
	-3%	$1.53\ 10^{-3}$	$1.26\ 10^{11}$	$7.96\ 10^{-12}$	$9.22\ 10^{7}$

4.2. Electrical conductivity and electrical resistivity

The electrical conductivity as function of the strain ratio is presented in Figure V.8(b). From this figure, one can notice that σ/τ decreases slightly under tensile effect along x-axis. Otherwise, it increases till reaching a maximum value of 2.34 10^{12} S. cm^{-1}. s^{-1}, following the same direction. Similarly, the strain effect has the same impact along y and z-axis. In addition to that, the electrical conductivities along the y-axis are approximately equal to those calculated along the z-axis.

Contrariwise, the electrical resistivity varies inversely to the electrical conductivity (Figure V.8(c)), which increases under tensile strain, till reached a maximum value of 8.53 10^{-9}, 2.00 10^{-10}, and 1.86 10^{-10} Ω.cm.s along x, y, and z-axis, respectively. Besides, ρ decreases under compressive effect.

4.3. Electrical thermal conductivity

The thermal conductivity curves versus the strain ratio are illustrated in Figure V.8 (d). One can notice that the evolution of the thermal conductivity is the same as that of the electrical conductivity, which decreases slightly under tensile effect. Otherwise, it increases after an application of the compressive effect from -1% to -3%, till reaching a maximum value of 1.29 10^{9}, 9.45 10^{7}, 9.22 10^{7} $W.m^{-1}.K^{-1}.s^{-1}$, along x, y, and z-axis, respectively.

5. Conclusions

In this chapter, we investigate the triaxial strain effect on the structural, magnetic, electronic, and electrical properties, by means of the density functional theory (DFT). After studying the physical properties of iron-sillenite, theoretically and experimentally in chapter IV and III, respectively, we are examined in this chapter, the effect of the tensile and the compressive effect, allowing the enhancement of the electronic band gap energies under a negative strain effect, that reached a minimum value of 1.38 eV under a compressive strain of -3% along x-axis. This is due to the bond length change between Bi-Bi, Bi-O1, Bi-$O2^{(i)}$, Bi-$O2^{(ii)}$, Bi-$O2^{(iii)}$, Bi-O3 under the strain effect along x-axis. Afterward, this is produced modification on the mechanism of the s-p hybridisation between Bi-6s and 6p orbitals and the O-2s and 2p orbitals, allowing the improvement of the value of bandgap energy. The electrical and thermal conductivities behave similarly under tensile

and compressive effect, that improved at -3%. Contrariwise, the electrical resistivity enhanced under +3% tensile effect. Based on the positive sign of the Seebeck coefficient suggests a conduction of the material through holes, allowing the P-type direct semiconductor behavior of $Bi_{25}FeO_{40}$ with and without strain effect. This is revealing that the strain along x, y, and z-axis from -3% to +3% has no impact on the conduction mechanism of iron-sillenite, similarly, to the magnetic properties, that remain unchanged under tensile and compressive strain.

General conclusion

In this thesis, we aim to investigate and understand the characteristics of the photocatalysis process for water treatment, pollutant and/or dye degradation, as these are the main applications of $Bi_{25}FeO_{40}$. Iron-sillenite has been considered as a promising candidate for the photodegradation of dyes and pollutants, that can be easily recycled and collected by magnetic separation. $Bi_{25}FeO_{40}$ contains many oxygens and ionic vacancies, leading to reduction of the recombination of electron–hole pairs, responsible for the enhancement of photocatalytic activity.

The main idea of this manuscript is the combination of experimental and theoretical studies on the physicochemical properties of iron-sillenite. We aimed to understand the mechanism of photocatalytic activity of $Bi_{25}FeO_{40}$, as well as the origin of the magnetic properties of this material, using theoretical methods such as the density functional theory and the Monte-Carlo simulation. Moreover, we have studied the effect of aluminum substitution and the triaxial strain on structural stability, thus on the physicochemical properties of iron-sillenite using experimental and theoretical methods, respectively.

Indeed, we initiated our thesis work by studying of new sillenites $Bi_{25}Fe_{1-x}Al_xO_{40}$, where x takes values of 0%, 20%, and 50%. They are synthesized using the conventional solid-state reaction process. Physicochemical characterizations of these compounds revealed a set of interesting results.

The structural analysis of the $Bi_{25}Fe_{1-x}Al_xO_{40}$ systems showed that all these phases represent a common cubic structure (I23, N°197). The decrease of the cell parameters as a function of the substitution ratio is explained by the relative difference of the ionic radii of Al^{3+} and Fe^{3+} ions. A structural transition from a centred cubic structure (γ-$Bi_{25}FeO_{40}$) to a monoclinic one (α-$Bi_{25}FeO_{40}$) is observed at 700 K, that affirmed by the X-ray diffraction spectra recorded at high temperature (XRD-HT). The influence of aluminium size on vibrational properties is also studied. Thermal analysis by differential scanning calorimetry revealed the appearance of various phenomena related to the structural transition characteristic of sillenite materials and to the structural transition observed by HT–XRD.

The frequency and temperature dependent dielectric behavior are also studied in this manuscript. The frequency dependence of the electrical conductivity is analyzed using Jonscher's law, and the conductivity process is confirmed by the correlated barrier hoping mechanism. Besides, the temperature dependence of the electrical conductivity is used to estimate the activation energies. It suggests that the conduction process is governed by the motion of oxygen vacancies at high temperatures. Impedance spectroscopy results confirm the appearance of the relaxation phenomenon in these samples, exhibiting semiconductor behavior with both a positive temperature of resistance coefficient (PTCR) and negative temperature of resistance coefficient (NTCR).

The magnetic properties reveal the antiferromagnetic-paramagnetic transition of $Bi_{25}FeO_{40}$ and $Bi_{25}Fe_{0.80}Al_{0.20}O_{40}$ below Neel temperature of about 268 and 265 K, respectively. Otherwise, $Bi_{25}Fe_{0.50}Al_{0.50}O_{40}$ sample shows paramagnetic behavior. The narrow band gap and the high absorption in the UV and visible ranges make these materials suitable candidates for photocatalysis and for dye dye-sensitized solar cells applications.

On the other hand, we performed a theoretical investigation of the structural, electronic, optical, photocatalytic, electrical, and magnetic properties of the pristine compound $Bi_{25}FeO_{40}$ by means of DFT and MCs. It was found that the optimized cell parameters were agreed well with the obtained experimental results. Furthermore, the p-type semiconductor behavior of $Bi_{25}FeO_{40}$ with a direct allowed transition was asserted using the electronic and electrical properties. The optical properties disclose that iron-sillenite exhibits good absorption in UV and Visible regions. The calculated optical bandgap energy is about 2.38 eV, which is in accordance with the experimental results. In addition, the magnetic properties indicate that the transition from the ordered magnetic state to the paramagnetic state occurs below T_N of about 255 K, that is in good agreement with the experimental value of 268 K.

After studying the physicochemical properties of iron-sillenite, theoretically and experimentally in Chapters IV and III, respectively, we examine in the las chapter the strain effect along x, y, and z axis. Electronic bandgap energies are enhanced and reached a minimum value of 1.38 eV under a compressive strain of -3% along x-axis. This is due to the change of the bond length between Bi-Bi, Bi-O1, Bi-$O2^{(i)}$, Bi-$O2^{(ii)}$, Bi-$O2^{(iii)}$, Bi-O3 under the strain effect along x-axis. Afterward, a change in the s-p hybridisation between

Bi-6s and 6p orbitals and the O-2s and 2p orbitals is produced, that improves the bandgap energy value. The electrical properties indicate that the electrical conductivity improved at -3%. Contrariwise, the electrical resistivity enhanced under +3% tensile effect.

Moreover, the positive sign of the Seebeck coefficient suggests conduction of the material through the holes, allowing us to state that $Bi_{25}FeO_{40}$ is a direct p-type semiconductor, with and without strain effect. This reveals that strain along x, y, and z-axis from -3% to +3% has no impact on the conduction mechanism of iron-sillenite, as well as on the magnetic properties, that remain unchanged under tensile and compressive strain.

In perspective, there was not enough time to present the theoretical results of the new synthesized sillenite materials. Thus, to implement the results related to the triaxial effect on the optical and photocatalytic properties. For this reason, we intend to complete our thesis work by:

- Introduction of a theoretical investigation of the $Bi_{25}Fe_{1-x}Al_xO_{40}$ systems, using various substitution ratio.
- Accomplish the optical, and the photocatalytic properties of the strained iron-sillenite, and thus examine the effect of the compression and tensile effect on the mechanism of the photocatalytic activity.

Bibliography

[1] M. A. Montgomery, J. Bartram, and M. Elimelech, "Increasing Functional Sustainability of Water and Sanitation Supplies in Rural Sub-Saharan Africa", Environmental Engineering Science, 26 (2009) 1017–1023.

[2] M. A. Shannon, P. W. Bohn, M. Elimelech, J. G. Georgiadis, B. J. Mariñas, and A. M. Mayes, "Science and technology for water purification in the coming decades", in Nanoscience and Technology, Co-Published with Macmillan Publishers Ltd, UK (2009) 337–346.

[3] F. Han, V. S. R. Kambala, M. Srinivasan, D. Rajarathnam, and R. Naidu, "Tailored titanium dioxide photocatalysts for the degradation of organic dyes in wastewater treatment: A review", Applied Catalysis A: General, 359 (2009) 1–2.

[4] N. Le-Minh, S. J. Khan, J. E. Drewes, and R. M. Stuetz, "Fate of antibiotics during municipal water recycling treatment processes", Water Research, 44 (2010) 4295–4323.

[5] Y. Huang, L. Nengzi, X. Li, L. Meng, Q. Song, and X. Cheng, "Fabrication of $Cu_2O/Bi_{25}FeO_{40}$ nanocomposite and its enhanced photocatalytic mechanism and degradation pathways of sulfamethoxazole", Materials Science in Semiconductor Processing, 109 (2020) 104932.

[6] V. Polshettiwar, R. Luque, A. Fihri, H. Zhu, M. Bouhrara, and J.-M. Basset, "Magnetically Recoverable Nanocatalysts", Chem. Rev., 111 (2011) 3036–3075.

[7] A. Sun, H. Chen, C. Song, F. Jiang, X. Wang, and Y. Fu, "Magnetic $Bi_{25}FeO_{40}$-graphene catalyst and its high visible-light photocatalytic performance", RSC Adv., 3 (2013) 4332, 2013.

[8] A. Fujishima and K. Honda, "Electrochemical Photolysis of Water at a Semiconductor Electrode", Nature, 238 (1972) 5358.

[9] K. H. Ng, K. Chen, C. K. Cheng, and D.-V. N. Vo, "Elimination of energy-consuming mechanical stirring: Development of auto-suspending ZnO-based photocatalyst for organic wastewater treatment", Journal of Hazardous Materials, 409 (2021) 124532.

[10] S. Wang, H. Gao, L. Fang, Q. Hu, G. Sun, X. Chen et al., "Synthesis of novel $CQDs/CeO_2/SrFe_{12}O_{19}$ magnetic separation photocatalysts and synergic adsorption-photocatalytic degradation effect for methylene blue dye removal", Chemical Engineering Journal Advances, 6 (2021) 100089.

[11] F. Opoku, K. K. Govender, C. G. C. E. van Sittert, and P. P. Govender, "Enhancing Charge Separation and Photocatalytic Activity of Cubic $SrTiO_3$ with Perovskite-Type Materials $MTaO_3$ (M=Na, K) for Environmental Remediation: A First-Principles Study", ChemistrySelect, 2 (2017) 6304–6316.

[12] W. Feng Yao, H. Wang, X. Hong Xu, X. Feng Cheng, J. Hunag, S. Xia Shang et al., "Photocatalytic property of bismuth titanate $Bi_{12}TiO_{20}$ crystals", Applied Catalysis A: General, 243 (2003) 185–190.

[13] M. Devalette, J. Darriet, M. Couzi, C. Mazeau, and P. Hagenmuller, "Caracterisation physique de l'environnement tetraedrique des cations A et B dans les phases de structure sillenite", Journal of Solid State Chemistry, 43 (1982) 45–50.

[14] X. Lin, F. Huang, W. Wang, and J. Shi, "Photocatalytic activity of $Bi_{24}Ga_2O_{39}$ for degrading methylene blue", Scripta Materialia, 56 (2007) 189–192.

[15] W. F. Yao, X. H. Xu, J. T. Zhou, X. N. Yang, Y. Zhang, S. X. Shang et al., "Photocatalytic property of sillenite $Bi_{24}AlO_{39}$ crystals", Journal of Molecular Catalysis A: Chemical, 212 (2004) 323–328.

[16] R. Köferstein, T. Buttlar, and S. G. Ebbinghaus, "Investigations on $Bi_{25}FeO_{40}$ powders synthesized by hydrothermal and combustion-like processes", Journal of Solid State Chemistry, 217 (2014) 50–56.

[17] T. Tong, W. Cao, H. Zhang, J. Chen, D. Jin, and J. Cheng, "Controllable phase evolution of bismuth ferrite oxides by an organic additive modified hydrothermal method", Ceramics International, 41 (2015) S106–S110.

[18] D. C. Craig and N. C. Stephenson, "Structural studies of some body-centered cubic phases of mixed oxides involving Bi_2O_3: The structures of $Bi_{25}FeO_{40}$ and $Bi_{38}ZnO_{60}$", Journal of Solid State Chemistry, 15 (1975) 1–8.

[19] A. Harriman, J. M. Thomas, W. Zhou, and D. A. Jefferson, "A new family of photocatalysts based on Bi_2O_3", Journal of Solid State Chemistry, 72 (1988) 126–130.

[20] X. Xing, L. Du, D. Feng, C. Wang, M. Yao, X. Huang et al., "Individual gas sensor detecting dual exhaled biomarkers via a temperature modulated n/p semiconducting transition", J. Mater. Chem. A, 8 (2020) 26004–26012.

[21] M. Gao, D. Zhu, X. Zhang, Y. Liu, X. Gao, X. Zhou et al., "In Situ Studies of 30% Li-Doped $Bi_{25}FeO_{40}$ Conversion Type Lithium Battery Electrodes", ACS Omega, 4 (2019) 2344–2352.

[22] Y. Zhang, S. Cao, C. Liang, J. Shen, Y. Chen, Y. Feng et al., "Electrocatalytic performance of Sb-modified $Bi_{25}FeO_{40}$ for nitrogen fixation", Journal of Colloid and Interface Science, vol. 593, pp. 335–344, Jul. 2021.

[23] A. Muthu Kumar, V. Ragavendran, J. Mayandi, K. Ramachandran, and K. Jayakumar, "Influence of PVP on $Bi_{25}FeO_{40}$ microcubes for Supercapacitors and Dye-Sensitized Solar Cells applications", J Mater Sci: Mater Electron, 33 (2022) 9512–9524.

[24] A. M. Kumar, V. Ragavendran, J. Mayandi, K. Ramachandran, and K. Jayakumar, "Phase dependent electrochemical characteristics of bismuth ferrite: A bifunctional electrocatalyst for Supercapacitors and Dye-Sensitized Solar Cells", Colloids and Surfaces A: Physicochemical and Engineering Aspects, 656 (2023) 130529.

[25] M. A. Basith, R. Ahsan, I. Zarin, and M. A. Jalil, "Enhanced photocatalytic dye degradation and hydrogen production ability of $Bi_{25}FeO_{40}$-rGO nanocomposite and mechanism insight", Sci Rep, 8 (2018) 11090.

[26] M. Lv, H. Yang, Y. Xu, Q. Chen, X. Liu, and F. Wei, "Improving the visible light photocatalytic activities of $Bi_{25}FeO_{40}$/MIL-101/PTH via polythiophene wrapping", Journal of Environmental Chemical Engineering, 3 (2015) 1003–1008.

[27] L. Zhang, Y. Zou, J. Song, C.-L. Pan, S.-D. Sheng, and C.-M. Hou, "Enhanced photocatalytic activity of $Bi_{25}FeO_{40}$–Bi_2WO_6 heterostructures based on the rational design of the heterojunction interface", RSC Adv., 6 (2016) 26038–26044.

[28] Z.-P. Ma, L. Zhang, X. Ma, Y.-H. Zhang, and F.-N. Shi, "Design of Z-scheme g-C_3N_4/BC/$Bi_{25}FeO_{40}$ photocatalyst with unique electron transfer channels for efficient degradation of tetracycline hydrochloride waste", Chemosphere, 289 (2022) 133262.

[29] S. Li, Y. Wu, H. Zheng, Y. Zheng, T. Jing, J. Tian et al., "High microwave responsivity Co–$Bi_{25}FeO_{40}$ in synergistic activation of peroxydisulfate for high efficiency pollutants degradation and disinfection: Mechanism of enhanced electron transfer", Chemosphere, 288 (2022) 132558.

[30] X. Li, Y. Qiu, Z. Zhu, H. Zhang, and D. Yin, "Novel recyclable Z-scheme g-C_3N_4/carbon nanotubes/$Bi_{25}FeO_{40}$ heterostructure with enhanced visible-light photocatalytic

performance towards tetracycline degradation", Chemical Engineering Journal, 429 (2022) 132130.

[31] S. Huang, L. Li, N. Zhu, Z. Lou, W. Liu, J. Cheng et al., "Removal and recovery of chloride ions in concentrated leachate by Bi(III) containing oxides quantum dots/two-dimensional flakes', Journal of Hazardous Materials, 382 (2020) 121041.

[32] Y. Ni, D. Shi, B. Luo, Z. Yang, Z. Xiong, C. Lu et al., "Tailoring Morphologies, Photocatalytic Activity, and Energy Bands of $Bi_{25}FeO_{40}$ via Valence State Transformation of Doped V Ions", Inorg. Chem., 58 (2019) 6966–6973.

[33] Z. Xiong and L. Cao, "Tailoring morphology, enhancing magnetization and photocatalytic activity via Cr doping in $Bi_{25}FeO_{40}$", Journal of Alloys and Compounds, 773 (2019) 828–837.

[34] Y. Liu, H. Guo, Y. Zhang, W. Tang, X. Cheng, and W. Li, "Heterogeneous activation of peroxymonosulfate by sillenite $Bi_{25}FeO_{40}$: Singlet oxygen generation and degradation for aquatic levofloxacin", Chemical Engineering Journal, 343 (2018) 128–137.

[35] F. Sharmin and M. A. Basith, "Simple Low Temperature Technique to Synthesize Sillenite Bismuth Ferrite with Promising Photocatalytic Performance", ACS Omega, 7 (2022) 34901–34911.

[36] Y. Wu, H. Luo, X. Jiang, H. Wang, and J. Geng, "Facile synthesis of magnetic $Bi_{25}FeO_{40}$/rGO catalyst with efficient photocatalytic performance for phenolic compounds under visible light", RSC Adv., 5 (2015) 4905–4908.

[37] R. Zhang, C. Zhao, T. Zhang, Q. Han, Y. Li, Y. Liu et al., "Ternary Z-Scheme Heterojunction of Bi_2WO_6 with Reduced Graphene Oxide (rGO) and $Bi_{25}FeO_{40}$ for Enhanced Visible-Light Photocatalysis", J Inorg Organomet Polym, 30 (2020) 2152–2162.

[38] Y. Huang, X. Zhang, G. Zhu, Y. Gao, Q. Cheng, and X. Cheng, "Synthesis of silver phosphate/sillenite bismuth ferrite/graphene oxide nanocomposite and its enhanced visible light photocatalytic mechanism", Separation and Purification Technology, 215 (2019) 490–499.

[39] D. S. Vavilapalli, A. A. Melvin, F. Bellarmine, R. Mannam, S. Velaga, H. K. Poswal et al., "Growth of sillenite $Bi_{12}FeO_{20}$ single crystals: structural, thermal, optical, photocatalytic features and first principle calculations", Sci Rep, 10 (2020) 22052.

[40] S. M. Shandarov, A. O. Zlobin, A. A. Shmidt, N. I. Burimov, et al., "Determination of Material Parameters of Photorefractive Crystals Using Adaptive Holographic Interferometry", Opt. Spectrosc., 129 (2021) 576–580.

[41] T. Jiang, Y. Wang, Z. Guo, H. Luo, C. Zhang, Y. Wang et al., "$Bi_{25}FeO_{40}/Bi_2O_2CO_3$ piezoelectric catalyst with built-in electric fields that was prepared via photochemical self-etching of $Bi_{25}FeO_{40}$ for 4-chlorophenol degradation", Journal of Cleaner Production, 341 (2022) 130908.

[42] C. Y. Zhang, H. J. Sun, W. Chen, J. Zhou, B. Li, and Y. B. Wang, "Hydrothermal synthesis and photo-catalytic Property of $Bi_{25}FeO_{40}$ powders", in 2009 18th IEEE International Symposium on the Applications of Ferroelectrics, (2009) 1–3.

[43] Y. Wu, Y. Chen, S. Huang, G. Li, S. Sun, Y. Jinag et al., "Comparison of bismuth ferrites for chloride removal: Removal efficiency, stability, and structure", Applied Surface Science, 576 (2022) 151804.

[44] G. Wang, D. Cheng, T. He, Y. Hu, Q. Deng, Y. Mao et al., "Enhanced visible-light responsive photocatalytic activity of $Bi_{25}FeO_{40}/Bi_2Fe_4O_9$ composites and mechanism investigation", J Mater Sci: Mater Electron, 30 (2019) 10923–10933.

[45] L. Ren, S. Y. Lu, J. Z. Fang, Y. Wu, D. Z. Chen, L. Y. Huang et al., "Enhanced degradation of organic pollutants using $Bi_{25}FeO_{40}$ microcrystals as an efficient reusable heterogeneous photo-Fenton like catalyst", Catalysis Today, 281 (2017) 656–661.

[46] S. Kalikeri and V. Shetty Kodialbail, "Solar light-driven photocatalysis using mixed-phase bismuth ferrite ($BiFeO_3/Bi_{25}FeO_{40}$) nanoparticles for remediation of dye-contaminated water: kinetics and comparison with artificial UV and visible light-mediated photocatalysis', Environ Sci Pollut Res, 25 (2018) 13881–13893.

[47] X. Wu, M. Li, J. Li, G. Zhang, and S. Yin, "A sillenite-type $Bi_{12}MnO_{20}$ photocatalyst: UV, visible and infrared lights responsive photocatalytic properties induced by the hybridization of Mn 3d and O 2p orbitals", Applied Catalysis B: Environmental, 219 (2017) 132–141.

[48] S. F. Radaev, M. Trömel, Y. F. Kargin, A. A. Marin, E. E. Rider, and V. A. Sarin, "$Bi_{12}(Bi_{0.5}^{III}Ti_{0.5}^{III})O_{19.50}$", Acta Crystallogr C Cryst Struct Commun, 50 (1994) 656–659.

[49] H. A. Harwig and A. G. Gerards, "Electrical properties of the α, β, γ, and δ phases of bismuth sesquioxide", Journal of Solid State Chemistry, 26 (1978) 265–274.

[50] V. M. Skorikov, Yu. F. Kargin, A. V. Egorysheva, V. V. Volkov, and M. Gospodinov, "Growth of Sillenite-Structure Single Crystals", Inorg Mater, 41 (2005) S24–S46.

[51] C. A. Scurti, N. Auvray, M. W. Lufaso, S. Takeda, H. Kohno, and D. J. Arenas, "Electron diffraction study of the sillenites $Bi_{12}SiO_{20}$, $Bi_{25}FeO_{39}$ and $Bi_{25}InO_{39}$: Evidence of short-range ordering of oxygen-vacancies in the trivalent sillenites", AIP Advances, 4 (2014) 087125.

[52] M. Isik, S. Delice, N. M. Gasanly, N. H. Darvishov, and V. E. Bagiev, "Trapping centers in $Bi_{12}TiO_{20}$ single crystals by thermally stimulated current", Optical Materials, 122 (2021) 111797.

[53] O. Baaloudj, N. Nasrallah, and A. A. Assadi, "Facile synthesis, structural and optical characterizations of $Bi_{12}ZnO_{20}$ sillenite crystals: Application for Cefuroxime removal from wastewater", Materials Letters, 304 (2021) 130658.

[54] M. K. Verma, L. Singh, A. Kumar, V. Kumar, N. B. Singh, and K. D. Mandal, "Dielectric studies of polycrystalline bismuth titanate $Bi_{12}TiO_{20}$ ceramic synthesized via economical chemical route", Indian J Phys, 95 (2021) 2661–2666.

[55] G. Surucu, M. Isik, A. Gencer, and N. Gasanly, "Experimental and theoretical investigation of the mechanical characteristics of sillenite compound: $Bi_{12}GeO_{20}$', Journal of Alloys and Compounds, 882 (2021) 160686.

[56] H. Sekhar and D. Narayana Rao, "Preparation, structural and linear optical properties of zinc sillenite ($Bi_{12.66}Zn_{0.33}O_{19.33}$) nanocrystals", J Mater Sci: Mater Electron, 24 (2013) 1569–1574.

[57] A. F. Lima and M. V. Lalic, "First-principles study of the Bi_MO_4 antisite defect in the $Bi_{12}MO_{20}$ (M=Si, Ge, Ti) sillenite compounds", J. Phys.: Condens. Matter, 25 (2013) 495505.

[58] O. Baaloudj, N. Nasrallah, R. Bouallouche, H. Kenfoud, L. Khezami, and A. A. Assadi, "High efficient Cefixime removal from water by the sillenite $Bi_{12}TiO_{20}$: Photocatalytic mechanism and degradation pathway", Journal of Cleaner Production, 330 (2022) 129934.

[59] J. Zhao, H. Zhang, and J. Xue, "Hierarchical manganese sillenite $Bi_{12}MnO_{20}$ microparticles assembled by nanocubes with microwave absorption enhancement", Ceramics International, 46 (2020) 4700–4706.

[60] E. Medina, V. H. Pathirana, J. Li, A. P. Ramirez, and M. A. Subramanian, "Tetrahedral Mn^{4+} as chromophore in sillenite-type compounds", Journal of Solid State Chemistry, 289 (2020) 121463.

[61] H. Kenfoud, O. Baaloudj, N. Nasrallah, R. Bagtache, A. A. Assadi, and M. Trari, "Structural and electrochemical characterizations of $Bi_{12}CoO_{20}$ sillenite crystals: degradation and reduction of organic and inorganic pollutants", J Mater Sci: Mater Electron, 32 (2021) 16411–16420.

[62] C. Pan, Z. Wang, Y. Lou, Y. Zhang, Y. Dong, and Y. Zhu, "The construction of a wide-spectrum-responsive and high-activity photocatalyst, $Bi_{25}CoO_{40}$, via the creation of large external dipoles", J. Mater. Chem. A, 9 (2021) 3616–3627.

[63] V. Raja Preethi, R. Radha, R. K. Vinod, S. Balakumar, B. Gupta, and S. Singh, "Controlled synthesis of photoactive gallium based sillenite single crystal and its application in environmental remediation", Solar Energy, 220 (2021) 890–900.

[64] J. Lu, L. J. Qiao, P. Z. Fu, and Y. C. Wu, "Phase equilibrium of Bi_2O_3–Fe_2O_3 pseudo-binary system and growth of $BiFeO_3$ single crystal", Journal of Crystal Growth, 318 (2011) 936–941.

[65] Y. Xie, C. Zhang, D. Wang, J. Lu, Y. Wang, J. Wang et al., "Catalytic performance of a Bi2O3–Fe2O3 system in soot combustion", New J. Chem., 43 (2019) 15368–15374.

[66] G.-Q. Tan, Y.-Q. Zheng, H.-Y. Miao, A. Xia, and H.-J. Ren, "Controllable Microwave Hydrothermal Synthesis of Bismuth Ferrites and Photocatalytic Characterization", Journal of the American Ceramic Society, 95 (2012) 280–289.

[67] D. H. Haneberg, "A Finite-Size Study on Samarium-Substituted Bismuth Ferrite: Multiferroic and Lead-Free Piezoelectric Materials", Master thesis, Institutt for materialteknologi, 2011.

[68] C. E. Infante and B. Carrasco, "Stoichiometry and oxygen structure of Fe sillenite", Materials Letters, 4 (1986) 194–197.

[69] M. Valant and D. Suvorov, "A Stoichiometric Model for Sillenites", Chem. Mater., 14 (2002) 3471–3476.

[70] P. Suresh and S. Srinath, "A Comprative Study of Sol-gel And Solid-state Prepared La^{3+} Doped Multiferroic $BiFeO_3$', Advanced Materials Letters, 5 (2014) 127–130.

[71] M. M. de Góis, W. de Paiva Araújo, R. B. da Silva, G. E. da Luz, and J. M. Soares, "$Bi_{25}FeO_{40}$—Fe_3O_4—Fe_2O_3 composites: Synthesis, structural characterization, magnetic and UV–visible photocatalytic properties", Journal of Alloys and Compounds, 785 (2019) 598–602.

[72] S. Bu, D. Cai, J. Li, S. Yu, D. Jin, and J. Cheng, "Structure and photocatalytic properties of $Bi_{25}FeO_{40}$ crystallites derived from the PEG assisted sol-gel methods", MRS Online Proceedings Library (OPL), 1324 (2011) mrss11.

[73] P. Kumari and N. Khare, "Structural, Optical and Magnetic Properties of $Bi_{25}FeO_{40}$ Nanoparticles Synthesized by Hydrothermal Method", in Recent Trends in Materials and Devices, V. K. Jain, S. Rattan, and A. Verma, Eds., in Springer Proceedings in Physics, 178 (2017) 139–143.

[74] Y. Sun, X. Xiong, Z. Xia, H. Liu, Y. Zhou, M. Luo et al., "Study on visible light response and magnetism of bismuth ferrites synthesized by a low temperature hydrothermal method", Ceramics International, 39 (2013) 4651–4656.

[75] F. Li, J. Zhou, G. Gao, H. Qiu, Y. Gong, J. Gao et al., "A green method to prepare magnetically recyclable Bi/$Bi_{25}FeO_{40}$-C nanocomposites for photocatalytic hydrogen generation", Applied Surface Science, 521 (2020) 146342.

[76] J. Li, J. Song, J. Chen, S. Yu, D. Jin, and J. Cheng, "PVA(Polyvincyl Acohol)-assisted Hydrothermal Preparation of $Bi_{25}FeO_{40}$ and Its Photocatalytic Activity", MRS Online Proceedings Library, 1217 (2010) 322.

[77] M. K. Verma, A. Kumar, L. Singh, R. K. Sonwani, T. Das, S. Sing et al., "$Bi_{25}feO_{40}$ polycrystalline ceramic as highly efficient photocatalyst synthesised via economical chemical route", Materials Technology, 35 (2020) 483–493.

[78] M. A. Basith, N. Yesmin, and R. Hossain, "Low temperature synthesis of $BiFeO_3$ nanoparticles with enhanced magnetization and promising photocatalytic performance in dye degradation and hydrogen evolution", RSC Adv., 8 (2018) 29613–29627.

[79] P. Arunachalam, K. Nagai, M. S. Amer, M. A. Ghanem, R. J. Ramalingam, and A. M. Al-Mayouf, "Recent Developments in the Use of Heterogeneous Semiconductor Photocatalyst Based Materials for a Visible-Light-Induced Water-Splitting System—A Brief Review", Catalysts, 11 (2021) 160.

[80] H. C. Ørsted, Selected Scientific Works of Hans Christian Orsted: Princeton University Press, (1998).

[81] P. G. Paul G. Huray, "Maxwell's Equations", John Wiley&Sons, (2011).

[82] B. Barbara, Y. Imry, G. Sawatzky, and P. C. E. Stamp, "Quantum Magnetism", Springer Science & Business Media, (2008).

[83] J. M. D. Coey, "Magnetism and Magnetic Materials", Cambridge University Press, (2010).

[84] E. D. T. de Lacheisserie, J. Fourier, D. Gignoux, and M. Schlenker, "Magnetism", Springer Science & Business Media, (2005).

[85] A. Tanto, "Etude et modélisation d'un micro-résonateur : résonateur micro bande en anneau, pour la caractérisation de ferrites en hyperfréquences", Thesis, (2018).

[86] I. S. Tereshina, A. P. Pyatakov, E. A. Tereshina-Chitrova, Y. Skourski, J. M. Law, M. A. Paukov, "Probing the exchange coupling in the complex modified Ho-Fe-B compounds by high-field magnetization measurements", AIP Advances, 8 (2018) 5223.

[87] R. L. Carlin and A. J. van Duyneveldt, "Paramagnetism: The Curie Law", Springer, (1977) 1–22.

[88] T. Miyazaki and H. Jin, "The Physics of Ferromagnetism", Springer Science & Business Media, (2012).

[89] A. Goldman, "Handbook of Modern Ferromagnetic Materials", Springer Science & Business Media, (2012).

[90] D. Jiles and D. Atherton, "Ferromagnetic hysteresis", IEEE Transactions on Magnetics, 19 (1983) 2183–2185.

[91] A. López-Ortega, M. Estrader, G. Salazar-Alvarez, A. G. Roca, and J. Nogués, "Applications of exchange coupled bi-magnetic hard/soft and soft/hard magnetic core/shell nanoparticles", Physics Reports, 553 (2015) 1–32.

[92] A. Aharoni and R. K. P. of T. M. A. Aharoni, "Introduction to the Theory of Ferromagnetism", Oxford University Press, (2000).

[93] A.-Y. Hu and H.-Y. Wang, "The exchange interaction values of perovskite-type materials $EuTiO_3$ and $EuZrO_3$", Journal of Applied Physics, 116 (2014) 193903.

[94] J.-Q. Yan, Y. H. Liu, D. S. Parker, Y. Wu, A. A. Aczel, M. Matsuda et al., "A-type antiferromagnetic order in $MnBi_4Te_7$ and $MnBi_6Te_{10}$ single crystals", Phys. Rev. Materials, 4 (2020) 054202.

[95] R. Pöttgen, H. Borrmann, and R. K. Kremer, "Ferromagnetic ordering in CeAuGe", Journal of Magnetism and Magnetic Materials, 152 (1996) 196–200.

[96] A. I. Kurbakov, I. A. Abdel-Latif, M. R. Ahmed, H. U. Habermeier, A. Al-Hajry, A. L. Malyshev et al., "C-type and Γ2 antiferromagnetic orders in the complex magnetic ordering of $Yb_{0.6}Sr_{0.4}MnO_3$", Eur. Phys. J. Plus, 137 (2022) 658.

[97] S. S. Subramanian, S. Anandan, and B. Natesan, "Stabilization of E-type antiferromagnetic ordering in La and Y substituted orthorhombic $LuMnO_3$: A first-principles study", Physics Letters A, 383 (2019) 125950.

[98] M. Ciomaga Hatnean, O. A. Petrenko, M. R. Lees, T. E. Orton, and G. Balakrishnan, "Optical Floating Zone Crystal Growth of Rare-Earth Disilicates, $R_2Si_2O_7$ (R = Er, Ho, and Tm)", Crystal Growth & Design, 20 (2020) 6636–6648.

[99] J.-M. Lee, S.W. Huang, H. T. Jeng, Y. C. Shao, L. A. Wray, J. M. Chen et al., "The magnetic order in multiferroic $DyMnO_3$", Journal of Electron Spectroscopy and Related Phenomena, 246 (2021) 147013.

[100] M. Ni, S. Zhang, S. Han, X. Liu, H. Lu, S. Zhou et al., "G-type antiferromagnetism of Mn ions in A-site-ordered perovskite $LaMn_3Rh_4O_{12}$ and $La_{0.8}Ca_{0.2}Mn_3Rh_4O_{12}$', Physics Letters A, 397 (2021) 127258.

[101] Q.-P. Ding, S. Pakhira, N. S. Sangeetha, E. H. Krenkel, E. I. Timmons, M. A. Tanatar et al., "Itinerant G-type antiferromagnet studied by magnetization, heat capacity, electrical resistivity, and NMR measurements", Phys. Rev. B, 105 (2022) 134408, Apr. 2022.

[102] S. F. A. Kettle, "Physico-chimie inorganique: Une approche basée sur la chimie de coordination", De Boeck Supérieur, (1999).

[103] L. Néel, "Antiferromagnetism and Ferrimagnetism", Proc. Phys. Soc. A, 65 (1952) 869–885.

[104] C. Kittel and P. McEuen, "Introduction to Solid State Physics", John Wiley & Sons, (2018).

[105] J. S. Smart, "The Néel Theory of Ferrimagnetism", American Journal of Physics, 23 (1955) 356–370.

[106] L. Néel, "Propriétés magnétiques des ferrites ; ferrimagnétisme et antiferromagnétisme", Annales De Physique, 12 (1948) 137–198.

[107] G. Guiot-Guillain and H. Forestier, "Les ferrites des terres rares : influence de l'ion de terre rare sur la température de curie", In Colloque national de magnétisme commémoratif de l'oeuvre de Pierre Weiss, CNRS= Centre National de la Recherche Scientifique, 233 (1958).

[108] V. E. Dmitrienko, E. N. Ovchinnikova, S. P. Collins, G. Nisbet, Y. O. Kvashnin, V. V. Mazurenko et al., "Measuring the Dzyaloshinskii–Moriya interaction in a weak ferromagnet", Nature Phys, 10 (2014).

[109] I. Dzyaloshinsky, "A thermodynamic theory of weak ferromagnetism of antiferromagnetics", Journal of Physics and Chemistry of Solids, 4 (1958) 241–255.

[110] T. Moriya, "Anisotropic Superexchange Interaction and Weak Ferromagnetism", Phys. Rev., 120 (1960) 91–98.

[111] M. A. S. Rivera, "Operating the Siemens XRD Diffraktometer D5000", 34.

[112] N. Iwashita, "Chapter 2 - X-ray Powder Diffraction", in Materials Science and Engineering of Carbon, M. Inagaki and F. Kang, Eds., Butterworth-Heinemann, (2016) 7–25.

[113] C. G. Pope, "X-Ray Diffraction and the Bragg Equation", J. Chem. Educ., 74 (1997) 129.

[114] F.-E. N'faoui, M. Taibi, J. Aride, A. Boukhari, H. Saadaoui, and M. Rouziéres, "Spectroscopic, optical, magnetic and dielectric investigation of the orthoborate $Ba_2Co(BO_3)_2$ nanopowder", J Mater Sci: Mater Electron, 31 (2020) 16678–16687.

[115] H. Pedersen, "Chloride-based Silicon Carbide CVD", (2008) 52.

[116] Mohammad J Jafari, "Application of Vibrational Spectroscopy in Organic Electronics", (2017).

[117] C. V. Raman and K. S. Krishnan, "The Optical Analogue of the Compton Effect", Nature, 121 (1928) 3053.

[118] N. Egeland, "MSc Thesis: Raman Spectroscopy Applied to Enhanced Oil Recovery Research", (2015).

[119] M. Shawky, El-Said El-Said El-Shereafy, I. Ahmed, and A. Y. Shenouda, "A Study on Synthesis and Characterization of Some (I-IV-VI) Groups Compounds for Solar Cells Energy Application For Partial Fulfillment of the Requirements for The Master Degree of science in Chemistry (Physical Chemistry) The Former CMRDI President", (2016).

[120] A. El kissani, D. Ait elhaj, S. Drissi, A. Abali, A. Agdad, H. Ait dads et al., "Structural, optical and electrical properties of Cu_2CoSnS_4 thin film solar cells prepared by facile sol-gel route", Thin Solid Films, 758 (2022) 139430.

[121] V. M. Nakaguchi and T. Ahamed, "Development of an Early Embryo Detection Methodology for Quail Eggs Using a Thermal Micro Camera and the YOLO Deep Learning Algorithm", Sensors, 22 (2022).

[122] T. J. Dursch, M. A. Ciontea, G. J. Trigub, C. J. Radke, and A. Z. Weber, "Pseudo-isothermal ice-crystallization kinetics in the gas-diffusion layer of a fuel cell from differential scanning calorimetry", International Journal of Heat and Mass Transfer, 60 (2013) 450–458.

[123] A. Lasia, "General Method of Obtaining Impedance of Complex Reactions", in Electrochemical Impedance Spectroscopy and its Applications, Springer, (2014) 147–153.

[124] J. R. Dygas, "Dielectric function of ionic conductors studied by impedance spectroscopy", Solid State Ionics, 176 (2005) 2065–2078.

[125] Lahcen BOUDAD, "Élaboration, caractérisations physico-chimiques des pérovskites simples mixtes et de nouvelles doubles pérovskites à base de terres rares", 2020.

[126] M. Abatal, V. García-Vázquez, E. Chavira, G. González, and A. Tejeda, "The Interplay Among Electrical, Magnetic, and Structural Properties in the Non-superconducting $Ru(Sr_{2-x}Ba_x)GdCu_2O_{8\pm z}$ System", J Low Temp Phys, 168 (2012) 69–83.

[127] D. Hurt, S. Li, and A. Amann, "Versatile SQUID Susceptometer With Multiple Measurement Modes", IEEE Trans. Magn., 49 (2013) 3541–3544.

[128] L. H. Thomas, "The calculation of atomic fields", Math. Proc. Camb. Phil. Soc., 23 (1927) 542–548.

[129] D. Shechtman, I. Blech, D. Gratias, and J. W. Cahn, "Metallic Phase with Long-Range Orientational Order and No Translational Symmetry", Phys. Rev. Lett., 53 (1984) 1951–1953.

[130] P. A. M. Dirac, "Generalized Hamiltonian Dynamics", Can. j. math., 2 (1950) 129–148.

[131] R. Thomas, C. Kharif, and M. Manna, "A nonlinear Schrödinger equation for water waves on finite depth with constant vorticity", Physics of Fluids, 24 (2012) 127102.

[132] R. K. Nesbet, "Thomas-Fermi theory revisited", Int. J. Quantum Chem., 90 (2002) 262–265.

[133] M. Murata, "Asymptotic expansions in time for solutions of Schrödinger-type equations", Journal of Functional Analysis, 49 (1982) 10–56.

[134] CHRISTOPHER K. R. T. JONES, "Instability of standing waves for non-linear Schrödinger-type equations", Ergod. Th. Dynam. Sys., 8 (1988) 119–138.

[135] V. I. Karpman and A. G. Shagalov, "Stability of solitons described by nonlinear Schrödinger-type equations with higher-order dispersion", Physica D: Nonlinear Phenomena, 144 (2000) 1–2.

[136] S. Ichi Doi, "Remarks on the cauchy problem for schrödinger-type equations", Communications in Partial Differential Equations, 21 (1996) 1–2.

[137] A. Savin, C. J. Umrigar, and X. Gonze, "Relationship of Kohn–Sham eigenvalues to excitation energies", Chemical Physics Letters, 288 (1998) 2–4.

[138] H. Essén, "The physics of the born-oppenheimer approximation: BORN-OPPENHEIMER APPROXIMATION", Int. J. Quantum Chem., 12 (1977) 721–735.

[139] J. M. Combes, P. Duclos, and R. Seiler, "The Born-Oppenheimer Approximationz, in Rigorous Atomic and Molecular Physics, Springer (1981) 185–213.

[140] H. J. Schnitzer, "Hartree approximation in relativistic field theory", Phys. Rev. D, 10 (1974) 2042–2046.

[141] F. Reines and H. W. Sobel, "Test of the Pauli Exclusion Principle for Atomic Electrons", Phys. Rev. Lett., 32 (1974) 954–954.

[142] P. Lykos and G. W. Pratt, "Discussion on The Hartree-Fock Approximation", Rev. Mod. Phys., 35 (1963) 496–501.

[143] A. Dalgarno, G. A. Victor, and D. R. Bates, "The time-dependent coupled Hartree-Fock approximation", Proceedings of the Royal Society of London. Series A. Mathematical and Physical Sciences, 291 (1966) 291–295.

[144] M. Moshinsky, "How Good is the Hartree-Fock Approximation", American Journal of Physics, 36 (1968) 52–53.

[145] E. H. Lieb and B. Simon, "The Thomas-Fermi theory of atoms, molecules and solids", Advances in Mathematics, 23 (1977) 22–116.

[146] P. A. M. Dirac, "Note on Exchange Phenomena in the Thomas Atom", Math. Proc. Camb. Phil. Soc., 26 (1930) 376–385.

[147] A. Görling, "Density-functional theory beyond the Hohenberg-Kohn theorem", Phys. Rev. A, 59 (1999) 3359–3374.

[148] P. Hohenberg and W. Kohn, "Inhomogeneous Electron Gas", Phys. Rev., 136 (1964) B864–B871.

[149] W. Kohn and L. J. Sham, "Self-Consistent Equations Including Exchange and Correlation Effects", Phys. Rev., 140 (1965) A1133–A1138.

[150] W. Kohn and L. J. Sham, "Quantum Density Oscillations in an Inhomogeneous Electron Gas", Phys. Rev., 137 (1965) A1697–A1705.

[151] R. J. Furnstahl, "EFT for DFT", in Renormalization Group and Effective Field Theory Approaches to Many-Body Systems, Eds., in Lecture Notes in Physics, Springer, 852 (2012) 133–191.

[152] Z. Wu and R. E. Cohen, "More accurate generalized gradient approximation for solids", Phys. Rev. B, 73 (2006) 235116.

[153] M. Causà and A. Zupan, "Density-FunctionalLCAO calculations for solids: Comparison between Hartree-Fock and Kohn-Sham structural properties", Int. J. Quantum Chem., 52 (1994).

[154] M. M. Saffren and J. C. Slater, "An Augmented Plane-Wave Method for the Periodic Potential Problem. II", Phys. Rev., 92 (1953) 1126–1128.

[155] M. Petersen, F. Wagner, L. Hufnagel, M. Scheffler, P. Blaha, and K. Schwarz, "Improving the efficiency of FP-LAPW calculations", Computer Physics Communications, 126 (2000) 294–309.

[156] K. Schwarz, P. Blaha, and G. K. H. Madsen, "Electronic structure calculations of solids using the WIEN2k package for material sciences", Computer Physics Communications, 147 (2002) 71–76.

[157] R. Yu, D. Singh, and H. Krakauer, "All-electron and pseudopotential force calculations using the linearized-augmented-plane-wave method", Phys. Rev. B, 43 (1991) 6411–6422.

[158] D. M. Bylander and L. Kleinman, "Exact Phillips-Kleinman-like pseudopotential for transition metals", Phys. Rev. B, 46 (1992) 9837–9840.

[159] C. J. Smallwood, C. N. Mejia, W. J. Glover, R. E. Larsen, and B. J. Schwartz, "A computationally efficient exact pseudopotential method. II. Application to the molecular pseudopotential of an excess electron interacting with tetrahydrofuran (THF)", The Journal of Chemical Physics, 125 (2006) 074103.

[160] R. Atkins, S. Disch, Z. Jones, I. Haeusler, C. Grosse, S. F. Fischer et al., Synthesis, structure and electrical properties of a new tin vanadium selenide", Journal of Solid State Chemistry, 202 (2013) 128–133.

[161] A. H. Reshak and S. Auluck, "Theoretical investigations of the electronic and optical properties of pure and alkali metal intercalated 1T-VSe_2', Physica B: Condensed Matter, 349 (2004) 310–315.

[162] J. M. Ziman, "Electrons and Phonons: The Theory of Transport Phenomena in Solids", OUP Oxford, (2001).

[163] G. K. H. Madsen and D. J. Singh, "BoltzTraP. A code for calculating band-structure dependent quantities", Computer Physics Communications, 175 (2006) 67–71.

[164] K. Binder, D. Heermann, L. Roelofs, A. J. Mallinckrodt, and S. McKay, "Monte Carlo Simulation in Statistical Physics", Comput. Phys., 7 (1993) 156, 1993.

[165] A. Howard and C. Wohlgamuth, "Applications of Monte Carlo Methods to Statistical Physics", (2009).

[165] A. Howard and C. Wohlgamuth, "Applications of Monte Carlo Methods to Statistical Physics", (2009).

[166] K. Binder, "Applications of Monte Carlo methods to statistical physics", Rep. Prog. Phys., 60 (1997) 487–559.

[167] S. Zhang and Y. Tan, "Risk assessment of earth dam overtopping and its application research", Nat Hazards, 74 (2014) 717–736.

[168] I. Buvat and D. Lazaro, "Monte Carlo simulations in emission tomography and GATE: An overview", Nuclear Instruments and Methods in Physics Research Section A: Accelerators, Spectrometers, Detectors and Associated Equipment, 569 (2006) 323–329.

[169] D. Landau and K. Binder, "A Guide to Monte Carlo Simulations in Statistical Physics. Cambridge University Press", (2021).

[170] I. Beichl and F. Sullivan, "The Metropolis Algorithm", Computing in Science & Engineering, 2 (2000) 65–69.

[171] H. J. Herrmann, "Fast algorithm for the simulation of Ising models", J Stat Phys, 45 (1986) 145–151.

[172] G. Bhanot, D. Duke, and R. Salvador, "Finite-size scaling and the three-dimensional Ising model", Phys. Rev. B, 33 (1986) 7841–7844.

[173] H. Oudghiri-Hassani, S. Rakass, F. T. Al Wadaani, K. J. Al-ghamidi, A. Omer, M. Messali et al., "Synthesis, characterization and photocatalytic activity of α-Bi_2O_3 nanoparticles", Journal of Taibah University for Science, 9 (2015) 508–512.

[174] Z. Gargar, A. Zegzouti, M. Elaatmani, A. Tachafine, D. Fasquelle, A. Outzourhit et al., "Structure, electrical, and dielectric properties of $Ba_{1-x}Y_xTi_{(1-x/4)}O_3$ ceramics sintering at low temperature", J. Korean Ceram. Soc., 60 (2023) 52–61.

[175] P. Kumar, C. Panda, and M. Kar, "Effect of rhombohedral to orthorhombic transition on magnetic and dielectric properties of La and Ti co-substituted $BiFeO_3$", Smart Mater. Struct., 24 (2015) 045028.

[176] R. R. Toledo, V. R. Santoyo, C. D. M. Sánchez, and M. M. Rosales, "Effect of aluminum precursor on physicochemical properties of Al_2O_3 by hydrolysis/precipitation method", Nova Scientia, 10 (2018) 20.

[177] L. Boudad, M. Taibi, A. Belayachi, and M. Abd-Lefdil, "Sol-gel synthesis and characterization of novel double perovskites $RBaFeTiO_6$ (R= Pr, Nd)", Ceramics International, 48 (2022) 6087–6096.

[178] Q. Hang, X. Zhu, J. Zhu, and Z. Liu, "Sillenite-type Bismuth Ferric Nanocrystals: Microwave Hydrothermal Synthesis, Structural Characterization, and Visible-Light Photocatalytic Properties", Procedia Engineering, 27 (2012) 616–624.

[179] F. Gyakwaa, T. Alatarvas, Q. Shu, M. Aula, and T. Fabritius, "Characterization of Synthetic Non-Metallic Inclusions Consisting of TiN, Ti_2O_3, and Oxides of Al_2O_3 and $MgO{\cdot}Al_2O_3$ Spinel Using Raman Spectroscopy", Metals, 11 (2021) 1549, Sep. 2021.

[180] M. Hakimi, M. Morvaridi, H. A. Hosseini, and P. Alimard, "Preparation, characterization, and photocatalytic activity of Bi_2O_3–Al_2O_3 nanocomposite", Polyhedron, 170 (2019) 523–529.

[181] F. Oudich, N. David, S. Mathieu, and M. Vilasi, "Phase equilibria investigations and thermodynamic modeling of the system Bi_2O_3–Al_2O_3", Journal of Nuclear Materials, 457 (2015) 72–79.

[182] K. C. Kao, "Dielectric Phenomena in Solids", Elsevier, (2004).

[183] R. Mazumder, S. Ghosh, P. Mondal, D. Bhattacharya, and S. Dasgupta, "Particle size dependence of magnetization and phase transition near TN in multiferroic $BiFeO_3$", (2006) 033908.

[184] D. Adler and J. Feinleib, "Electrical and Optical Properties of Narrow-Band Materials", Phys. Rev. B, 2 (1970) 3112–3134.

[185] K. Funke, "Jump relaxation in solid electrolytes", Progress in Solid State Chemistry, 22 (1993) 111–195.

[186] L. Boudad, M. Taibi, A. Belayachi, and M. Abd-Lefdil, "Dielectric relaxation, electrical conductivity and optical studies of solid-state synthesized $EuCrO_3$", J Mater Sci: Mater Electron, 31(2020) 354–360.

[187] L. Boudad, M. Taibi, A. Belayachi, and M. Abd-lefdil, "Structural, morphological, thermal, and oxygen-vacancy-related dielectric relaxation behaviors in $EuFeO_3$ perovskite", Materials Today: Proceedings, 58 (2022) 1028–1032.

[188] L. Boudad, M. Taibi, A. Belayachi, and M. Abd-lefdil, "Structural, morphological, dielectric and optical properties of double perovskites $RBaFeTiO_6$ (R = La, Eu)', RSC Adv., 11 (2021) 40205–40215.

[189] M. Taheri, F. S. Razavi, Z. Yamani, R. Flacau, P. G. Reuvekamp, A. Schulz et al., "Magnetic structure, magnetoelastic coupling, and thermal properties of $EuCrO_3$ nanopowders", Phys. Rev. B, 93 (2016) 104414.

[190] A. A. Zatsiupa, L. A. Bashkirov, I. O. Troyanchuk, G. S. Petrov, A. I. Galyas, L.S. Lobanovsky et al., "Magnetization, magnetic susceptibility, effective magnetic moment of Fe^{3+} ions in $Bi_{25}FeO_{39}$ ferrite", Journal of Solid State Chemistry, 212 (2014) 147–150, Apr. 2014.

[191] H.-J. Feng, "The reversal of magnetization driven by the Dzyaloshinskii–Moriya interaction in Bi_2FeMnO_6", Journal of Magnetism and Magnetic Materials, 324 (2012) 178–182.

[192] J. Junquera, "Dzyaloshinskii–Moriya interaction turns electric", Nat. Mater., 20 (2021) 291–292.

[193] J. Tauc, "Optical properties and electronic structure of amorphous Ge and Si", Materials Research Bulletin, 3 (1968) 37–46.

[194] L. P. Sosman, T. Abritta, M. R. Amaral, N. Cella, and H. Vargas, "Optical properties of $LiGaTiO_4$: Fe^{3+}", Solid State Communications, 105 (1998) 135–138.

[195] Y. Liu, T. Zhang, S. Li, K. Zhang, X. Wang, Y. Zhang et al., Geometric and electronic modification of the active Fe^{3+} sites of α-Fe_2O_3 for highly efficient toluene combustion", Journal of Hazardous Materials, 398 (2020) 123233.

[196] H. Arfin, J. Kaur, T. Sheikh, S. Chakraborty, and A. Nag, "Bi^{3+}-Er^{3+} and Bi^{3+}-Yb^{3+} Codoped $Cs_2AgInCl_6$ Double Perovskite Near-Infrared Emitters", Angew. Chem. Int. Ed., 59 (2020) 11307–11311.

[197] J. Li, J. Liu, and X. Yu, "Synthesis and luminescence properties of Bi^{3+}-doped YVO_4 phosphors", Journal of Alloys and Compounds, 509 (2011) 9897–9900.

[198] K. Narasimharao, A. Al-Shehri, and S. Al-Thabaiti, "Porous Ag–Fe_2O_3 nanocomposite catalysts for the oxidation of carbon monoxide", Applied Catalysis A: General, 505 (2015) 431–440.

[199] J. Han, D. C. Sinclair, "Redefinition of Crystal Structure and Bi^{3+} Yellow Luminescence with Strong Near-Ultraviolet Excitation in La_3BWO_9 :Bi^{3+} Phosphor for White Light-Emitting Diodes", ACS Appl. Mater. Interfaces, 10 (2018) 13660–13668.

[200] T. R. N. Kutty and M. Nayak, "Cationic distribution and its influence on the luminescent properties of Fe^{3+}-doped $LiAl_5O_8$ prepared by wet chemical methods", Journal of Alloys and Compounds, 269 (1998) 75–87, May.

[201] P. Giannozzi, S. Baroni, N. Bonini, M. Calandra, R. Car, C. Cavazzoni et al., "QUANTUM ESPRESSO: a modular and open-source software project for quantum simulations of materials", J. Phys.: Condens. Matter, 21 (2009) 395502.

[202] D. Sangalli, A. Ferretti, H. Miranda, C. Attaccalite, I. Marri, E. Cannucia et al., "Many-body perturbation theory calculations using the yambo code", J. Phys.: Condens. Matter, 31 (2019) 325902.

[203] J. P. Perdew, K. Burke, and M. Ernzerhof, "Generalized Gradient Approximation Made Simple", Phys. Rev. Lett., 77 (1996) 3865–3868.

[204] N. Metropolis and S. Ulam, "The Monte Carlo Method", Journal of the American Statistical Association, 44 (1949) 335–341.

[205] V. G. Tyuterev and N. Vast, "Murnaghan's equation of state for the electronic ground state energy", Computational Materials Science, 38 (2006) 350–353.

[206] K. Momma and F. Izumi, "VESTA 3 for three-dimensional visualization of crystal, volumetric and morphology data", J Appl Cryst, 44 (2011).

[207] O. Schevciw and W. B. White, "The optical absorption edge of rare earth sesquisulfides and alkaline earth-rare earth sulfides", Materials Research Bulletin, 18 (1983) 1059–1068.

[208] D. B. Senulene, G. A. Babonas, E. I. Leonov, I. Muminov, and V. M. Orlov, "Limite d'absorption des cristaux de $Bi_{25}FeO_{40}$", Fiz. tverd. tela, 26 (1984) 1281–1284.

[209] Yu. F. Kargin and V. M. Skorikov, "Photorefractive crystals of the sillenite structure", Ferroelectrics, 167 (1995) 257–265.

[210] M. Nowak, B. Kauch, and P. Szperlich, "Determination of energy band gap of nanocrystalline SbSI using diffuse reflectance spectroscopy", Rev. Sci. Instrum., 80 (2009) 046107.

[211] F. Mezzat, H. Zaari, A. El Kenz, and A. Benyoussef, "Enhanced visible light photocatalytic activity of $KTaO_3$ (Se,V): DFT investigation", Computational Condensed Matter, 30 (2022) e00648.

[212] O. Rubel, F. Tran, X. Rocquefelte, and P. Blaha, "Perturbation approach to ab initio effective mass calculations", Computer Physics Communications, 261 (2021) 107648.

[213] A. Dutta, T. P. Sinha, and S. Shannigrahi, "Dielectric relaxation and electronic structure of $Ca(Fe_{1/2}Sb_{1/2})O_3$", Phys. Rev. B, 76 (2007) 155113.

[214] E. Ressouche, V. Simonet, B. Canals, M. Gospodinov, and V. Skumryev, "Magnetic Frustration in an Iron-Based Cairo Pentagonal Lattice", Phys. Rev. Lett., 103 (2009) 267204.

[215] L. Wu, C. Dong, H. Chen, J. Yao, C. Jiang, and D. Xue, "Hydrothermal Synthesis and Magnetic Properties of Bismuth Ferrites Nanocrystals with Various Morphology", J. Am. Ceram. Soc., 95 (2012) 3922–3927.

List of publications

1. Submitted

1. **H. Jebari**, H. Mouatassim, Y. Kaddar, L. Boudad, M. Boujnah, N. Tahiri, O. El Bounagui, M. Taibi, and H. Ez-Zahraouy, 'DFT study of the physical properties of the Iron-sillenite as a multifunctional material', article submitted.
2. **H. Jebari**, L. Boudad, M. Taibi, M. Boujnah, A. El Mansouri, H. Labrim, N. Tahiri, O. El Bounagui, and H. Ez-Zahraouy,'Effect of aluminum substitution on physical-chemical properties of novel Iron-Sillenite $Bi_{25}Fe_{1-x}Al_xO_{40}$ (x = 0.00, 0.20, 0.50)', article submitted.
3. **H. Jebari**, H. Mouatassim, L. Boudad, M. Boujnah, N. Tahiri, O. El Bounagui, M. Taibi, and H. Ez-Zahraouy, 'Triaxial strain effect on the structural, electronic, and electrical properties of the Iron-sillenite $Bi_{25}FeO_{40}$', article submitted.
4. F. Z. Nainaa, **H, Jebari**, N. Bekkioui, and H. Ez-Zahraouy, 'Photovoltaic and thermoelectric properties of Ag_2MnGeS_4_Kesterite: First-principal investigations', article submitted.
5. **H. Jebari**, A. El Mansouri, N. Hadik, N. Tahiri, O. El Bounagui, A. El kissani, H. Ez-Zahraouy, and A. Outzourhit, 'Impact of conducting polymer interlayer and iodine doping on the electronic properties of hybrid solar cells based on alkylated sexithiophene and nanostructured zinc oxide', article submitted.

2. Published

1. A.Ouasri, I. Hamideddine, **H. Jebari**, A. Rhandour, N. Tahiri, O. El Bounagui, and H. Ez-Zahraouy, 'Structural, Infrared and Raman Spectroscopy Reinvestigation, and Theoretical Optoelectronic Properties of Hydrazinium (1+) Hexafluorosilicate $(N_2H_5)_2SiF_6$, Biointerface Research in Applied Chemistry, vol. 13, 2023.
2. **H. Jebari**, H. Ouichou, I. Hamideddine, L. Boudad, N. Tahiri, A. El Mansouri, O. El Bounagui, M. Taibi, and H. Ez-Zahraouy, 'First-principles calculations to investigate structural, electronic, optical, thermoelectric, magnetic, and magnetocaloric properties of the orthochromite $EuCrO_3$', Computational and Theoretical Chemistry, vol. 1220, p. 113993, Feb. 2023.
3. **H. Jebari**, N. Tahiri, M. Boujnah, O. El Bounagui, L. Boudad, M. Taibi, and H. Ez-Zahraouy, 'Structural, optical, dielectric, and magnetic properties of iron-sillenite $Bi_{25}FeO_{40}$', Appl. Phys. A, vol. 128, no. 9, p. 842, Sep. 2022.
4. I. Hamideddine, **H. Jebari**, N. Tahiri, O. El Bounagui, and H. Ez-Zahraouy, 'The investigation of the electronic, optical, and thermoelectric properties of the Ge-based halide perovskite $AGeI_2Br$ (a = K, Rb, Cs) compound for a photovoltaic application: First principles calculations', Intl J of Energy Research, p. er.8372, Jul. 2022.
5. **H. Jebari**, N. Tahiri, M. Boujnah, O. El Bounagui, M. Taibi, and H. Ez-Zahraouy, 'Theoretical investigation of electronic, magnetic and magnetocaloric properties of Bi_{25} FeO_{40} compound', Phase Transit., pp. 1–12, May 2021.

PHASE TRANSITIONS
https://doi.org/10.1080/01411594.2021.1931690

Taylor & Francis
Taylor & Francis Group

Theoretical investigation of electronic, magnetic and magnetocaloric properties of $Bi_{25}FeO_{40}$ compound

H. Jebari[a], N. Tahiri[a], M. Boujnah[b], O. El Bounagui [a], M. Taibi[c] and H. Ez-Zahraouy[a]

[a]Laboratory of Condensed Matter and Interdisciplinary Sciences, Faculty of Sciences, Mohammed V University, Rabat, Morocco; [b]Instituto de Investigacionesen Materiales, Universidad Nacional Autónoma de México, Mexico City, Mexico; [c]Laboratory of Physics and Chemistry of Inorganic and Organic Materials (LPCMIO), Materials Science Research Center, Ecole Normale Supérieure, Mohammed V University, Rabat, Morocco

ABSTRACT

The electronic, magnetic and magnetocaloric properties of the Iron-Selenite $Bi_{25}FeO_{40}$ compound have been investigated using first-principles calculations and Monte Carlo simulations (MCs). It was found that $Bi_{25}FeO_{40}$ is a *p*-type semiconductor with an indirect bandgap of about 2.16 eV which is in good agreement with the previous experimental and theoretical results. The studied compound displays a ferromagnetic behaviour with a spin moment of the unit cell of about 4.06 μ_B. The $Bi_{25}FeO_{40}$ compound exhibits a weak ferromagnetic behaviour around $T_C = 271.96$ K; this value is in good agreement with experimental results. In addition, it shows a magnetocaloric effect (MCE) around the Curie temperature (T_C), with the maximum values of the magnetic entropy change (ΔS_m^{Max}) and relative cooling power (RCP) are 2.56 J.kg^{-1}.K^{-1}and 55.01 J/Kg, respectively, under applied an external magnetic field of $h = 5.00$ T. The good magnetocaloric properties reveal the applicability of $Bi_{25}FeO_{40}$ compound to the magnetic refrigeration around T_C.

ARTICLE HISTORY
Received 8 January 2021
Accepted 13 May 2021

KEYWORDS
Ab initio calculations; magnetocaloric properties; magnetic properties; Monte Carlo simulations

1. Introduction

Bismuth-based oxides (BO) have been used in many applications in environmental pollution remediation, among them; bismuth-based iron oxides (BFO). Compared to perovskite-type $BiFeO_3$, there were a few works focused on Selenite bismuth ferrite $Bi_{25}FeO_{40}$ [1]. Selenites are a large group of compounds with interesting physical and chemical properties: photorefractive, piezoelectric, electro-optic, and photoconductive properties; formed by doping Bi_2O_3 with metal oxides [2]. In addition, a new field of application for Iron-Selenite was assumed based on the reflectivity spectra, which is coating materials [3]. $Bi_{25}FeO_{40}$ is isostructural to γ-Bi_2O_3, which crystallizes a body-centred cubic system with a space group I 2 3 (N° 197). In the previous study, Infante et al. has provided two possible chemical formulas for bismuth Iron-Selenite $Bi_{25}FeO_{40}$ and $Bi_{25}FeO_{39}$ [4]. According to Craig et al. [5] and Devalette et al. [6] one Bi ion per unit cell exists in the oxidation state 5+ resulting in the formula $Bi_{24}^{3+}(Bi^{5+}Fe^{3+})O_{40}$. Further, the Bi^{3+} ions occupy the octahedral positions forming a BiO_5E-polyhedrons (E = inert $6s^2$ electron pair), whereas Bi^{5+} and Fe^{3+} ions are sharing the tetrahedral positions [5]. Contrariwise, Radaev et al. [7] suggest that Bi^{3+} is located in the tetrahedral position accompanied by oxygen vacancies. Moreover, Sun, Xiong et al. [8] using UV-visible absorption spectroscopy, found that the $Bi_{25}FeO_{40}$ has more visible light absorption compared to $BiFeO_3$. In addition, $Bi_{25}FeO_{40}$ is considered a promising photocatalyst due to its

CONTACT N. Tahiri tahiri.najim@gmail.com

Applied Physics A (2022) 128:842
https://doi.org/10.1007/s00339-022-05973-4

Applied Physics A
Materials Science & Processing

Structural, optical, dielectric, and magnetic properties of iron-sillenite $Bi_{25}FeO_{40}$

H. Jebari[1] · N. Tahiri[1] · M. Boujnah[2] · O. El Bounagui[1] · L. Boudad[3] · M. Taibi[3] · H. Ez-Zahraouy[1]

Received: 10 May 2022 / Accepted: 16 August 2022

Abstract
The iron-sillenite $Bi_{25}FeO_{40}$ has been synthesized using the solid-state reaction route. The elaborated material crystallizes in a cubic structure. The studied material exhibits an anomaly, noticed via the DSC analysis and dielectric measurements at 671 K. This anomaly can be attributed to the occurrence of a thermally activated relaxation in the $Bi_{25}FeO_{40}$ sample. Besides, the magnetic study revealed the antiferromagnetic behaviour of γ-$Bi_{25}FeO_{40}$ sillenite, with a 240 K of Neel temperature T_N, Curie constant of 9.18 10^{-8} m^3.K/mol, resulting in a magnetic moment of 6.37 μ_B. Furthermore, the band gap of $Bi_{25}FeO_{40}$ is about 2.02 eV and the magnetic behavior makes it an appropriate candidate as a photocatalyst for water and/or wastewater treatment, and degradation of pollutants, that can be simply recycled by magnetic separation.

Keywords Iron-sillenite · Optical properties · DSC · Dielectric · Magnetic measurement · Antiferromagnet

1 Introduction

Among different phases of Bismuth ferrites, iron-sillenite $Bi_{25}FeO_{40}$ has attracted much interest due to its physical/chemical properties and high-tech applications such as; gas sensing, digital memory, piezoelectric, photorefractive, photoconductive, and electro-optic properties [1, 2]. $Bi_{25}FeO_{40}$ is widely investigated via several synthesis methods such as solid-state reaction [3, 4], hydrothermal method [1, 2, 5–7], combustion-like process [1], molten salt growth [8], and co-precipitation method [9], producing $Bi_{25}FeO_{40}$ with a particle size ranging from 25 nm [10] to 10 µm [2]. Iron-sillenite $Bi_{25}FeO_{40}$ is similar to γ-Bi_2O_3 formed by doping γ-Bi_2O_3 with iron metal oxides; γ-Fe_2O_3 [7]. iron-sillenite crystallizes in a body-centered cubic structure (space group I23 (No 197)) with a cell parameter of 10.18 Å. This structure includes a lot of oxygen and ionic vacancies [11]. Overall, an ideal sillenite is characterized by the general formula $Bi_{12}MO_{20}$, where the Bi^{3+} occupy the octahedral positions, and the M atoms occupy the tetrahedral positions with a tetravalency of M, as in Mn^{4+} and Fe^{4+} forming ideal sillenites, such as $Bi_{12}MnO_{20}$ [12], and $Bi_{12}FeO_{20}$ [13]. Furthermore, Valant et al. [14] developed the general formula of sillenite materials, $Bi_{12}(Bi_{4/5\text{-}nx}M_{n+5x})O_{19.2+nx}$, describing the possible homogeneity area depending on the charge of the tetrahedral M^{n+} cations. According to Infante et al. [15] iron-sillenite exhibit two possible chemical formulas; $Bi_{25}FeO_{40}$ and $Bi_{25}FeO_{39}$. Contrariwise, Craig et al. [11] and Devalette et al. [17] revealed that one Bi cation per unit cell exists in the oxidation state 5 + follow-on the formula $Bi_{24}^{3+}(Bi^{5+}Fe^{3+})O_{40}$. Moreover, the octahedral sites were occupied by the Bi^{3+} creating BiO_5E-polyhedrons (E = inert $6s^2$ electron pair). While the tetrahedral sites were shared by Bi^{5+} and Fe^{3+} cations [11]. Lu et al. [17] and Harwig [18] report from the DSC measurements a phase transition of Bi_2O_3 from monoclinic phase (α-Bi_2O_3) to face-centered cubic phase (δ-Bi_2O_3) at 1030 K. Besides, and during cooling under the melting point, two types

✉ H. Jebari
houda_jebari2@um5.ac.ma

✉ M. Boujnah
boujnah.mourad@gmail.com

[1] Laboratory of Condensed Matter and Interdisciplinary Sciences, Unite de Recherche Labelliseìe CNRST, URL-CNRST-17, Faculty of Sciences, Mohammed V University of Rabat, Rabat, Morocco

[2] Instituto de Investigaciones en Materiales, Universidad Nacional Autónoma de México, Mexico City, Mexico

[3] Laboratory of Physics and Chemistry of Inorganic and Organic Materials (LPCMIO), Materials Science Research Center, Ecole Normale Supérieure, Mohammed V University in Rabat, Rabat, Morocco

Published online: 31 August 2022

Received: 9 January 2022 | Revised: 24 May 2022 | Accepted: 29 June 2022

DOI: 10.1002/er.8372

SPECIAL ISSUE RESEARCH ARTICLE

INTERNATIONAL JOURNAL OF ENERGY RESEARCH WILEY

The investigation of the electronic, optical, and thermoelectric properties of the Ge-based halide perovskite $AGeI_2Br$ (a = K, Rb, Cs) compound for a photovoltaic application: First principles calculations

I. Hamideddine | **H. Jebari** | **N. Tahiri** | **O. El Bounagui** | **H. Ez-Zahraouy**

Laboratory of Condensed Matter and Interdisciplinary Sciences, Unite de Recherche Labelliseìe CNRST, URL-CNRST-17, Faculty of Sciences, Mohammed V University of Rabat, Morocco, Mohammed V University in Rabat, Rabat, Morocco

Correspondence
I. Hamideddine, Laboratory of Condensed Matter and Interdisciplinary Sciences, Faculty of Sciences, Mohammed V University in Rabat, Rabat, Morocco.
Email: imane.hamideddine@gmail.com

Summary

The electronic, optical, photocatalytic, and thermoelectric properties of inorganic halide cubic perovskite $AGeI_2Br$ (A = K, Rb, Cs) are investigated using the density functional theory, in order to use these compounds in different fields. The aim of our investigation is to bring a prediction of the free lead halide mixed compound which is still not synthesized until now, and show the potential use of these materials in the solar field. The results show that the studied compounds exhibit remarkable properties like their high absorption coefficient (over 10^5 cm^{-1}) in the visible range, but the only inconvenience of these materials is that they have slightly low bandgap energy. For this purpose, the tensile effect is investigated to recognize its effect on the bandgap values and how it can be helpful to be more useful for photovoltaic application. Besides, the mechanism of photocatalytic water-splitting was studied based on the calculated bandgap energy, relative ratios of effective mass, and the valence band and the conduction band edge potential.

KEYWORDS

bandgap energy, optical properties, perovskite $AGeI_2Br$ compound, solar cell, thermoelectric properties

1 | INTRODUCTION

The increase in economic development and energy insufficiencies are resulting in the exhausting of fossil fuels and increasing global environmental issues. Nowadays, numerous candidates are offered, such as nuclear power, wind force, and hydraulic power. The solar energy is mostly focused in the near-infrared, ultraviolet, and visible area from 1.03 to 4.13 eV (ie, [300-1200 nm]). As though, a year's worth of sunlight supplies more than 100 times the energy of the world's entire known fossil fuel reserves. Clean and inexhaustible solar energy has attracted much interest. Therefore, requiring renewable and clean energy has been getting considerable interest.[1] For this reason, photocatalysis and photovoltaic are two of the more important process used for solar energy. The production of hydrogen from photocatalysis by water splitting was a promising economic and friendly environment process.[1,2] The photocatalysis mechanism is based on converting solar energy to produce H_2 as a potential clean energy vector using a semiconductor that possesses small bandgap energy, redshift absorption, as well as appropriate sites of the conduction band (CB) and valence band (VB) edges for reduction and oxidation reactions respectively.[3] Currently, lead halide perovskites are known for their potential application, likewise, for

Computational and Theoretical Chemistry 1220 (2023) 113993

Contents lists available at ScienceDirect

Computational and Theoretical Chemistry

journal homepage: www.elsevier.com/locate/comptc

First-principles calculations to investigate structural, electronic, optical, thermoelectric, magnetic, and magnetocaloric properties of the orthochromite $EuCrO_3$

H. Jebari [a,*], H. Ouichou [a], I. Hamideddine [a], L. Boudad [b], N. Tahiri [a], A. El Mansouri [a,c,d], O. El Bounagui [a], M. Taibi [b], H. Ez-Zahraouy [a,*]

[a] Laboratory of Condensed Matter and Interdisciplinary Sciences, Unite de Recherche Labelliseìe CNRST, URL-CNRST-17, Faculty of Sciences, Mohammed V University of Rabat, Morocco
[b] Mohammed V University of Rabat, Laboratory of Physics and Chemistry of Inorganic and Organic Materials (LPCMIO), Materials Science Research Center, Ecole Normale Supérieure, Morocco
[c] Nanomaterials, Energy and Environment Laboratory, Faculty of Sciences Semlalia, Cadi Ayyad University, Marrakech, Morocco
[d] Higher Institute of Audiovisual and Film Professions, Rabat, Morocco

ARTICLE INFO

Keywords:
Orthochromite
G_y-AFM
Photovoltaic
Thermoelectric
Magnetocaloric properties

ABSTRACT

A comparative study of the structural and electronic properties of the orthorhombic and cubic structure of $EuCrO_3$ has been performed in this manuscript. The stability of the orthorhombic structure with respect to the cubic one has been studied. The calculated optical band gap energies were determined to be 2.09 eV, 1.95 eV and 2.02 eV along the [100], [010], and [001] directions, respectively, and are in good agreement with previous work. The studied material exhibits the behavior of a P-type semiconductor. $EuCrO_3$ is a G_y-antiferromagnetic semiconductor with a partial magnetic moment of 2.18 μ_B induced by the $3d^3$ orbital of Cr^{3+} electrons and a Neel temperature of 195 K. This behavior is attributed to the super-exchange mechanisms between Cr^{3+}-Cr^{3+} cations via O^{2-} ions. Optical, thermoelectric and magnetocaloric studies revealed that europium chromite $EuCrO_3$ is a promising candidate for photovoltaic, thermoelectric, and magnetic refrigeration devices.

1. Introduction

Owing to the strong coupling between their structural, magnetic, and electrical properties, rare earth chromates ($RCrO_3$) represent one of the most important families of multiferroic perovskite oxides [1-23]. It has been reported that the properties of these materials such as weak ferromagnetism, ferroelectricity, as well as optical properties, are likely to be critically controlled by their crystal lattice structure and distortion [24]. In addition, among orthochromites, special features are their strong magnetocaloric effect at low temperature, their semiconducting behavior at room temperature and their high conductivity at high temperature [25-27].

One interesting member of the $RCrO_3$ family is the europium chromite ($EuCrO_3$). This P-type semiconductor material, which crystallizes in a distorted orthorhombic perovskite structure isostructurally with $GdFeO_3$ [23-25] exhibits a direct band gap with an energy of 2.4 eV [26]. Magnetic studies have revealed that the $EuCrO_3$ perovskite exhibits a canted antiferromagnetic structure below the Neel temperature (T_N) where the canting weak ferromagnetism arises from the antisymmetric Dzyaloshinskii–Moriya (DM) (ranging from 162 to 182 K) [30,31]. Besides, room temperature ferroelectricity, characterized by two Curie temperatures of about 353 K and 425 K, has also been reported for the europium chromite [22]. Based on dielectric measurements, Boudad et al. reported that the $EuCrO_3$ displays a heterogeneous electrical response where the difference in conductivity between the grains and the grain boundaries results in the establishment of a Maxwell–Wagner type relaxation [26]. Moreover, both magnetodielectric and magnetoelastic effects have been evidenced [26,28].

These interesting features have motivated researchers to conduct a series of theoretical studies on this material by means of Density Functional Theory (DFT), where magnetic, electronic, elastic, thermoelectric, and optical, etc. properties have been investigated [14,15,29-33]. According to Ullah et al. [29], $EuCrO_3$ perovskite is considered as a cubic phase of ferromagnetic and half-metallic nature. The calculation of the

* Corresponding authors.
E-mail addresses: houda_jebari2@um5.ac.ma (H. Jebari), h.ezzahraouy@um5r.ac.ma (H. Ez-Zahraouy).

https://doi.org/10.1016/j.comptc.2022.113993
Received 19 August 2022; Received in revised form 13 December 2022; Accepted 15 December 2022
Available online 18 December 2022

Biointerface Research in Applied Chemistry
Open-Access Journal (ISSN: 2069-5837)

Article
Volume 13, Issue 5, 2023, 498
https://doi.org/10.33263/BRIAC135.498

Structural, Infrared and Raman Spectroscopy Reinvestigation, and Theoretical Optoelectronic Properties of Hydrazinium (1+) Hexafluorosilicate $(N_2H_5)_2SiF_6$

Ali Ouasri [1,2,*], Imane Hamideddine [3], Houda Jebari [3], Ali Rhandour [2], Najim Tahiri [3], Omar El Bounagui [3], Hamid Ez-Zahraouy [3]

[1] Laboratoire (ReSIP), Centre Régional des Métiers de l'Education et de la Formation, Madinat Al Irfane, Souissi, B.P. 6210 Rabat, Morocco
[2] Equipe de Physico-Chimie des Matériaux Inorganiques, Université Ibn Tofail, Faculté des Sciences, B.P. 133, 14000 Kenitra, Morocco
[3] Laboratory of Condensed Matter and Interdisciplinary Sciences, Unite de Recherche Labelliseìe CNRST, URL-CNRST-17, Faculty of Sciences, Mohammed V University of Rabat, Morocco
* Correspondence: aouasri@yahoo.fr (A.O.);

Scopus Author ID 56001570100
Received: 12.09.2022; Accepted: 30.10.2022; Published: 6.01.2023

Abstract: The material $(N_2H_5)_2SiF_6$ was reinvestigated by XRD, IR, and Raman spectroscopy. It crystallizes in the monoclinic space group $P2_1/n$ (Z=2). The characteristic bands in FT-IR (450-4000) cm^{-1} and FT-Raman (50-3500) cm^{-1} spectra were interpreted using factor group analysis considering the D_2 factor group, in which SiF_6^{2-} anions and $N_2H_5^+$ cations occupied C_i and C_1 symmetry sites, respectively. Against the previous assignment, the Infrared bands (651, 474, 435 cm^{-1}) are not due to the Raman active modes [ν_1 (Si-F), ν_2 (Si-F), and ν_5 (F-Si-F)] of SiF_6^{2-} anion, theoretically not infrared active in the $P2_1/n$ space group. The electronic structure, optical, photocatalytic, and thermoelectric properties of $(N_2H_5)_2SiF_6$ are investigated using the Full-Potential Linearized Augmented Plane Wave (FP-LAPW) method based on the density functional theory (DFT) as implemented in Wien2k package. Hence, the direct band gap energy, with valence band (VB) maximum and conduction band (CB) minimum too located at point Γ, is calculated at 7.04 eV. The photocatalytic reaction mechanism of $(N_2H_5)_2SiF_6$ is described. The optical properties comprising absorption, conductivity, reflectivity, and refractivity index (1.2 for $\lambda > 200$ nm), were evaluated versus wavelength (100-1000 nm). The high absorption coefficient (50×10^4 cm^{-1} in small wavelength) indicates absorption in the ultraviolet range. The optical conductivity, decreasing to zero for $\lambda > 200$ nm, implies a very high conductivity of this salt for high wavelength applications. The transport properties studied at ambient temperature show high electrical conductivity ($2.04\ 10^{18}$ $S.cm^{-1}.s^{-1}$), high thermal conductivity ($2.81\ 10^{13}$ $W.m^{-1}.K^{-1}.s^{-1}$), and low and positive Seebeck coefficient ($1.67\ 10^{-4}$ $V.K^{-1}$) of the perspective material $(N_2H_5)_2SiF_6$.

Keywords: IR; Raman; FP-LAPW method; optoelectronic; photocatalytic; thermoelectric properties.

1. Introduction

Hybrid materials have attracted more attention to research merging characteristics of both organic and inorganic components [1-9]. Especially, 2D perovskites were investigated for

Abstract

This thesis presents a combination of experimental and theoretical results on the physicochemical properties of iron sillenite. It is considered a promising candidate for wastewater treatment and/or photodegradation of pollutants and dyes. In addition, we explore the aluminium substitution and the effect of triaxial deformation on the physicochemical properties of $Bi_{25}FeO_{40}$ using experimental and theoretical methods, respectively. Experimentally, we successfully synthesized new $Bi_{25}Fe_{(1-x)}Al_xO_{40}$ sillenite compounds ($x = 0.00$, 0.20, and $x = 0.50$) at 750°C using the solid state route. Next, we prove the structural stability of $Bi_{25}FeO_{40}$ and $Bi_{25}Fe_{0.80}Al_{0.20}O_{40}$. The pure compound exhibits a structural transition from a cubic-centred phase to a monoclinic ($\gamma \rightarrow \alpha$) phase at high temperatures. This phenomenon was observed by HT–XRD and confirmed by DSC analyses and dielectric measurements. Moreover, this anomaly is also found for $x = 0.20$ and 0.50. Magnetic measurements revealed the antiferromagnetic behavior of $Bi_{25}FeO_{40}$ and $Bi_{25}Fe_{0.80}Al_{0.20}O_{40}$ below T_N. On the other hand, a paramagnetic behavior is observed for $Bi_{25}Fe_{0.50}Al_{0.50}O_{40}$. The optical properties make these materials suitable candidates for photocatalysis and photovoltaic applications. Moreover, the theoretical study based on DFT, and MCs confirms the obtained magnetic and optical results. Theoretically, we prove that $Bi_{25}FeO_{40}$ can also be used for hydrogen production in a basic solution with a pH higher than 11. To evaluate the effect of triaxial deformation on the structural, magnetic, electronic, and electrical properties, we perform a theoretical study using DFT. This allows us to predict the decrease of the electronic bandgap energy, electrical, and thermal conductivities under a compression effect of -3%. On the contrary, the electrical resistivity increases under a traction effect of +3%.

Keywords: Aluminum/Iron Sillenite; Solid-State reaction; Neel temperature; AFM; HT-XRD; FTIR; Raman; DSC; Dielectric; Photodegradation; H_2 production; DFT; MCs; Three-axial strain.

Résumé

Cette thèse présente une combinaison de résultats expérimentaux et théoriques sur les propriétés physicochimiques de la sillénite de fer. Elle est considérée comme un candidat prometteur pour le traitement des eaux usées et/ou la photo-dégradation des polluants et des colorants. En outre, nous explorons la substitution de l'aluminium et l'effet de la déformation triaxiale sur les propriétés physicochimiques de $Bi_{25}FeO_{40}$ en utilisant des méthodes expérimentales et théoriques, respectivement. Expérimentalement, nous avons synthétisé avec succès de nouveaux composés de sillénite $Bi_{25}Fe_{(1-x)}Al_xO_{40}$ ($x = 0{,}00$, 0,20, et $x = 0{,}50$) à 750°C en utilisant la voie de l'état solide. Ensuite, nous prouvons la stabilité structurelle de $Bi_{25}FeO_{40}$ et $Bi_{25}Fe_{0.80}Al_{0.20}O_{40}$. Le composé pur présente une transition structurelle d'une phase cubique centrée à une phase monoclinique ($\gamma \rightarrow \alpha$) à haute température. Ce phénomène a été observé par XRD-HT et confirmé par des analyses DSC et des mesures diélectriques. En outre, cette anomalie est également constatée pour $x = 0{,}20$ et 0,50. Les mesures magnétiques ont révélé le comportement antiferromagnétique de $Bi_{25}FeO_{40}$ et $Bi_{25}Fe_{0.80}Al_{0.20}O_{40}$ sous T_N. D'autre part, un comportement paramagnétique est observé pour $Bi_{25}Fe_{0.50}Al_{0.50}O_{40}$. Les propriétés optiques font de ces matériaux des candidats appropriés pour la photocatalyse et les applications photovoltaïques. De plus, l'étude théorique basée sur la DFT et les MCs confirme les résultats magnétiques et optiques obtenus. Théoriquement, nous démontrons que $Bi_{25}FeO_{40}$ peut également être utilisé pour la production d'hydrogène dans une solution basique avec un pH supérieur à 11. Afin d'évaluer l'effet de la déformation triaxiale sur les propriétés structurelles, magnétiques, électroniques et électriques, nous réalisons une étude théorique à l'aide de la DFT. Ceci nous permet de prédire la diminution de gap énergétique électronique, du conductivité électrique et thermique sous un effet de compression de -3%. Au contraire, la résistivité électrique augmente sous un effet de traction de +3%.

Mots clés : Sillénite de Fer/Aluminium ; Réaction à l'état solide ; Température de Néel ; AFM ; HT-XRD ; FT-IR ; Raman ; DSC ; diélectrique ; photo-dégradation ; production de H_2 ; DFT ; MCs ; déformation triaxiale.